ISTANBUL TECHNICAL UNIVERSITY ★ GRADUATE SCHOOL

DEVELOPMENT AND CHARACTERIZATION OF HIGH ENTROPY $(HfTiZrMn/Cr)B_2$ BASED CERAMICS

M.Sc. THESIS

İlayda SÜZER

Department of Metallurgical and Materials Engineering

Materials Engineering Programme

DECEMBER 2022

ISTANBUL TECHNICAL UNIVERSITY ★ GRADUATE SCHOOL

DEVELOPMENT AND CHARACTERIZATION OF HIGH ENTROPY (HfTiZrMn/Cr)B_2 BASED CERAMICS

M.Sc. THESIS

İlayda SÜZER
(506201403)

Department of Metallurgical and Materials Engineering

Materials Engineering Programme

Thesis Advisor: Assoc. Prof. Dr. Duygu AĞAOĞULLARI

DECEMBER 2022

İSTANBUL TEKNİK ÜNİVERSİTESİ ★ LİSANSÜSTÜ EĞİTİM ENSTİTÜSÜ

YÜKSEK ENTROPİ (HfTiZrMn/Cr)B_2 BAZLI SERAMİKLERİN GELİŞTİRİLMESİ VE KARAKTERİZASYONU

YÜKSEK LİSANS TEZİ

İlayda SÜZER
(506201403)

Metalurji ve Malzeme Mühendisliği Anabilim Dalı

Malzeme Mühendisliği Programı

Tez Danışmanı: Doç. Dr. Duygu AĞAOĞULLARI

ARALIK 2022

İlayda Süzer, a M.Sc. student of ITU Graduate School student ID 506201403, successfully defended the thesis entitled "DEVELOPMENT AND CHARACTERIZATION OF HIGH ENTROPY $(HfTiZrMn/Cr)B_2$ BASED CERAMICS", which she prepared after fulfilling the requirements specified in the associated legislations, before the jury whose signatures are below.

Thesis Advisor : **Assoc. Prof. Dr. Duygu AĞAOĞULLARI** ....
Istanbul Technical University

Jury Members : **Prof. Dr. M. Lütfi ÖVEÇOĞLU** ....
Istanbul Technical University

Assoc. Prof. Dr. Özge BALCI-ÇAĞIRAN ....
Koç University

Date of Submission : 16 December 2022
Date of Defense : 26 December 2022

To my family,

FOREWORD

In this thesis, there are many valuable people who support me. First of all, I would like to give my biggest thanks to my thesis advisor, Assoc. Prof. Dr. Duygu AĞAOĞULLARI for her help, sincerity, encouragement, knowledge, support, motivation and for being with me both in my thesis and in my life.

In addition, I would like to thank Prof. Dr. M. Lütfi ÖVEÇOĞLU, who provided invaluable assistance and knowledge throughout all scientific processes.

I would also like to acknowledge Assoc. Prof. Dr. Erhan AYAS from Eskişehir Technical University for allowing us to use the laboratory in the SPS process. I would like to thank Prof. Dr. Hüseyin ÇİMENOĞLU, Assoc. Prof. Dr. Nazlı AKÇAMLI and Asst. Prof. Dr. C. Fahir ARISOY for using the laboratory facilities in mechanical tests.

I would like to express my sincere thanks to Res. Asst. Sıddıka MERTDİNÇ-ÜLKÜSEVEN for motivating, supporting and helping in all my studies and at every moment when I needed her. I would also like to express my sincere to Res. Asst. Semih ATEŞ for his support and help, especially with my experimental studies. Thank you both for their valuable friendship.

I would like to thank my project colleagues Esin AYSEL and Amir AKBARİ (M.Sc) for their support during the experimental studies. I am also thankful to Res. Asst. Kübra GÜRCAN BAYRAK, who always helped the SPS experiments, Res. Asst. Berk ŞENYURT for his help in mechanical tests and Res. Asst. Faruk KAYA for his help in the thermochemical calculations. I would also like to thank my dear friends with whom I work, for creating the perfect working environment at ITU PML.

This thesis was supported by the "TENMAK National Boron Research Institute (BOREN)" with the project title of "Sintering of High-Entropy Boride Ceramics from High-Purity Metal Boride (Ti, Zr, Hf, Ta, Mo, W, Cr, Mn Borides) Powders Produced from Cheap Oxide Raw Materials via Mechanochemical Synthesis Method and Related Characterization Studies" with the project number of 2019-31-07-15-001. It was also funded by "Istanbul Technical University Scientific Research Projects (BAP)" with the project number of MYL-2022-43543.

Apart from all these, I would like to express my sincere thanks to Cem ÇİÇEK, who has always been by my side during my work, always making me feel his support and motivation in every moment of life.

Finally, I would like to thank, my father İsmail SÜZER, my brother Kazım SÜZER and especially my mother Ayşen SÜZER, for their support.

December 2022

İlayda SÜZER
(Metallurgical and Materials Engineer)

TABLE OF CONTENTS

ABBREVIATIONS

BCC	: Body-Centered Cubic
BCTR	: Boro/carbothermal Reduction Method
BPR	: Ball-to-Powder Weight Ratio
DC	: Direct Current
EDS	: Energy Dispersive Spectroscopy
FCC	: Face-Centered Cubic
h	: Hour
HCP	: Hexagonal Close-Packed
HEA	: High-Entropy Alloy
HEB	: High-Entropy Boride
HEBM	: High-Energy Ball Milling
ICDD	: International Center for Diffraction Data®
MA	: Mechanical Alloying
MEB	: Medium-Entropy Alloys
MCS	: Mechanochemical Synthesis
Min	: Minute
UHTC	: Ultra-High Temperature Ceramics
OM	: Optical Microscope
PSA	: Particle Size Analyses
RPM	: Rotation per Minute
SEM	: Scanning Electron Microscope
SHS	: Self-Propagating High-Temperature Synthesis
SPS	: Spark Plasma Sintering
SS	: Solid-Solution
XRD	: X-ray Diffractometer
VEC	: Valence Electron Concentration
wt	: Weight

SYMBOLS

ΔG	: Changing of Gibbs free energy
ΔH	: Changing of enthalpy
ΔH_{mix}	: Enthalpy of Mixing
ΔS	: Changing of entropy
ΔS_{conf}	: Configurational Entropy
ΔS_{mix}	: Entropy of Mixing
µm	: Micrometer
°C	: Degree of Celcius
c	: Number of Components
G	: Gibbs Free Energy
H	: Enthalpy
HV	: Vickers Hardness
i	: Molar Ratio of the Elements
M	: Molarity
n	: Number of Elements/Freedoms
p	: Phase
S	: Entropy
T	: Temperature
T_m	: Melting Temperature
δ	: Atomic Size Differences
Ω	: Omega Parameter

LIST OF TABLES

Page

LIST OF FIGURES

Page

DEVELOPMENT AND CHARACTERIZATION OF HIGH ENTROPY $(HfTiZrMn/Cr)B_2$ BASED CERAMICS

SUMMARY

Materials are divided into four groups: metals/alloys, ceramics, polymers and composites. Materials science includes the study of the physical, mechanical, thermal, chemical and many other properties of materials and the development of new materials. Advanced ceramic materials, including transition metal borides, carbides and nitrides, have attracted attention in recent years compared to traditional ceramics. Transition metal borides are characterized by a high melting point, high strength, high hardness, high wear and corrosion resistance, good thermal shock resistance, high chemical and thermal stability and high transmission stability. Thanks to all these superior properties, transition metal borides can be used as catalysts, refractory parts, sensors in high resolution detectors, decorative coatings, abrasive materials, coatings on cathodes, neutron absorption materials, sanding and polishing processes and in the aerospace industry, defense industry and nuclear technology. Various methods have been used to synthesize transition metal borides until today. The thermal plasma method, self-propagating high-temperature synthesis, metallothermic or carbothermic/borothermic reduction, autoclave synthesis, molten salt electrolysis and solid-state synthesis methods are the main ones. Another method used in the synthesis of metal borides, different from the methods mentioned, is the mechanochemical synthesis process, which has been used for other material groups for the last 20 years and is still being developed. Mechanochemical synthesis is a powder metallurgy production method that allows for the production of composite metal powders with small crystal grains and controlled microstructures at room temperature, using a cold welding-fracturing-rewelding mechanism and starting from easily accessible raw materials, as opposed to high reaction temperature production methods.

In recent years, it has been necessary to develop new materials to meet the needs of many sectors, such as medicine, biomedicine, energy, aerospace technologies, automotive and electronics. High-entropy alloys (HEA) are one of the materials developed to meet these needs. Traditional alloying includes combining two or more elements. In high-entropy alloys, four or more elements are combined in equimolar ratios. Contrary to expectations, solid-solutions are formed instead of intermetallic compounds. In this way, HEAs have a single-phase structure even though they contain more than one element. Although there are many elements in the structure, high-entropy alloys mostly have body-centered cubic or face-centered cubic crystal structures. Recent studies have shown that such alloys may also have a hexagonal close-packed structure. Along with solid-solutions, high-entropy alloys also show four different core effects. The high-entropy effect explains its relationship with thermodynamic properties. The sluggish diffusion effect explains the kinetic state. The severe-lattice distortion effect represents both the crystal structure and the formation of mechanical properties. The effect of all the elements added to the alloy is examined under the cocktail effect. High-entropy alloys have high thermal and chemical resistance, good wear, oxidation and corrosion resistance, and mechanical properties

such as high hardness, fracture toughness, and strength due to the elements in the alloy, the solid-solutions formed, and the four core effects. Thanks to its superior properties, it is used in the nuclear industry, shipping, the production of refractory materials, the aerospace industry, and cutting tool tips. Many methods are preferred in the production of high-entropy alloys, but arc melting, mechanical alloying, pressureless sintering and pressure sintering are the most common ones.

The production of high-entropy ceramics, which is a new class based on high-entropy alloys, is a subject that has been studied in recent years. High-entropy ceramics include oxides, borides, carbides, nitrides and silicides. The idea of producing high-entropy metal borides, which is considered a new type of high-entropy materials and a new class of ultra-high-temperature ceramics, also has been emerged in 2016. High-entropy diboride ceramics have a *P6/mmm* space group and a hexagonal close-packed structure. In this structure, there are metal-boron, boron-boron and metal-metal bonds. It is characterized by superior properties as it contains metallic, ionic and covalent bonds together. High-entropy metal borides have the combination of superior properties of ceramics, such as low density, excellent high temperature strength, high hardness and strength, high wear and corrosion resistances and specific physical (optical, electrical and magnetic) properties. Due to these superior properties, it can be used in aviation, the solar and nuclear energy sectors, cutting edges and microelectronic systems. Many methods are used in the synthesis of high-entropy metal boride ceramics, a material group that has attracted attention recently due to its high thermal stability, improved mechanical properties, high oxidation resistance, and radiation damage tolerance. Mechanical alloying, boro/carbothermal reduction, self-propagating high-temperature synthesis, pressureless sintering, pressure sintering like spark plasma sintering or hot pressing are the main ones. In cases where a single-phase high-entropy diboride structure cannot be obtained, two consequent methods can be used. Mechanical alloying is a powder metallurgical production method and has the advantages of being carried out at room temperature, using cheap starting materials and inexpensive equipment. In the spark plasma sintering method, single-phase structure can be obtained with high temperature and high pressure.

Within the scope of this study, HfB_2, TiB_2, ZrB_2, TaB, Mn boride, Cr boride, Mo boride and W boride powders were synthesized by a mechanochemical route and purified by leaching in the lab-scale using the optimum conditions. Boride powders synthesized without any by-products were synthesized from optimum ones. The reproduced powders were blended in an equimolar ratio of consisting three to eight components. The three-component $(Hf_{0.33}Ti_{0.33}Zr_{0.33})B_2$ medium-entropy alloy was chosen as the main alloy. The selected composition was first synthesized in a planetary ball mill for 30 h, 60 h or 100 h at ball-to-powder weight ratios of 10:1, 20:1 and 30:1. Then, the same composition was milled in a high-energy ball mill at a ball-to-powder weight ratio of 10:1 for 6 h, 10 h, 15 h and 20 h. In the high-energy ball mill, a ball-to-powder weight ratio of 10:1 and a milling time of 6 h were chosen as the optimum conditions. All prepared compositions were synthesized under optimum situation. For the characterization of powder samples, X-ray diffractometry, particle size measurement and density measurement with pycnometer were performed. Single-phase high-entropy diboride could not be obtained after mechanical alloying. The highest density was observed at 7.1379 ± 0.0057 g/cm^3 $(Hf_{0.142}Ti_{0.142}Zr_{0.142}Mn_{0.142}Cr_{0.142}W_{0.142}\ Ta_{0.142})B_2$ composition, while the lowest density was observed in the $(Ti_{0.25}Zr_{0.25}Mn_{0.25}Cr_{0.25})B_2$ compositions at 4.9708 ± 0.005 g/cm^3.

A single phase high-entropy structure was synthesized by spark plasma sintering after milling. In addition, low intensity (Hf, Zr) oxide phases were observed. Again, secondary phases with low intensity were formed in five different compositions. X-ray diffractometer, scanning electron microscope/energy dispersive spectrometer, hardness measurement with the Vickers method, dry-sliding wear test and density measurement with the Archimedes method were used for characterization of sintered samples. The composition $(Hf_{0.125}Ti_{0.125}Zr_{0.125}Mn_{0.125}Cr_{0.125}Mo_{0.125}W_{0.125}Ta_{0.125})B_2$ has the highest density value of 7.4794 ± 0.0065 g/cm^3, while the composition $(Ti_{0.25}Zr_{0.25}Mn_{0.25}Cr_{0.25})B_2$ has the lowest density value of 4.7517 ± 0.0015 g/cm^3. When all samples were examined, the hardness values ranged from 17.08 ± 2.32 GPa to 26.74 ± 1.85 GPa. The average hardness value of all samples was calculated at about 24 GPa. $(Hf_{0.125}Ti_{0.125}Zr_{0.125}Mn_{0.125}Cr_{0.125}Mo_{0.125}W_{0.125}Ta_{0.125})B_2$ has the lowest wear resistance and $(Hf_{0.166}Ti_{0.166}Zr_{0.166}Mn_{0.166}Cr_{0.166}Mo_{0.166})B_2$ has the highest wear resistance.

YÜKSEK ENTROPİ $(HfTiZrMn/Cr)B_2$ BAZLI SERAMİKLERİN GELİŞTİRİLMESİ VE KARAKTERİZASYONU

ÖZET

Malzemeler metaller/alaşımlar, seramikler, polimerler ve kompozitler olmak üzere dört gruba ayrılmaktadır. Malzeme bilimi malzemelere ait fiziksel, mekanik, termal, kimyasal ve diğer pekçok özelliğin incelenmesini ve yeni malzemelerin geliştirilmesini kapsamaktadır. Geçiş metal borür, karbür ve nitrürlerini de içeren ileri teknoloji seramik malzemeler, özellikle son yıllarda geleneksel seramiklere göre oldukça yoğun ilgi görmektedir. Geçiş metal borürleri, yüksek ergime noktası, yüksek dayanım, yüksek sertlik, yüksek aşınma ve korozyon direnci, iyi termal şok dayanımı, yüksek kimyasal ve termal kararlılık, yüksek iletim kararlılığı ile karakterize edilirler. Tüm bu üstün özellikleri sayesinde geçiş metal borürleri katalizörler olarak, refrakter parçalar olarak, yüksek çözümlemeli dedektörlerde sensörler olarak, dekoratif kaplama olarak, aşındırıcı malzeme olarak, katodlarda kaplama olarak, nötron absorplama malzemesi olarak, zımpara ve parlatma proseslerinde, havacılık endüstrisinde, savunma sanayasinde ve nükleer teknoloji alanında kullanılmaktadır. Bugüne kadar geçiş metal borürlerinin sentezlenmesinde çeşitli yöntemler kullanılmıştır. Termal plazma yöntemi, kendiliğinden ilerleyen yüksek sıcaklık yanma sentezi, karbotermik/borotermik/metalotermik redüksiyon, otoklavda sentezleme, ergimiş tuz elektrolizi ve katı-hal sentezleme yöntemleri bunlardan başlıcalarıdır. Belirtilen yöntemlerden farklı olarak metal borür sentezlenmesinde kullanılan bir başka yöntem ise, son 20 yıldır başka malzeme grupları için kullanılmakta ve halen geliştirilmekte olan mekanokimyasal sentezleme prosesidir. Mekanokimyasal sentezleme, yüksek reaksiyon sıcaklığı gerektiren üretim yöntemlerinden farklı olarak, kolay ulaşılabilir hammaddelerden yola çıkarak, küçük kristal tanelere ve kontrollü mikroyapılara sahip kompozit metal tozlarını, tekrarlı kırma-öğütme-kaynaklama mekanizmasına dayanarak oda sıcaklığında sentezlemeye imkan tanıyan toz metalurjisi üretim yöntemidir.

Son yıllarda tıp, biyomedikal, enerji, havacılık uzay teknolojileri, otomotiv, elektronik gibi pek çok sektörün ihtiyaçlarını karşılamak için yeni malzemeler geliştirilmesi gerekmektedir. Yüksek entropili alaşımlar (YEA) da bu ihtiyaçları karşılamaya yönelik geliştirilmiş malzemelerden biridir. Geleneksel alaşımlama, iki veya daha fazla elementin bir araya getirilmesidir. Yüksek entropi alaşımlarında ise eşmolar oranlarda dört veya daha fazla element bir araya getirilmektedir. Beklenenin aksine intermetalik bileşiklerin yerine katı çözeltiler oluşmaktadır. Bu sayede, birden çok element içermesine rağmen YEAlar tek fazlı yapıya sahiptir. Yapıda birçok element bulunmasına rağmen, yüksek entropi alaşımları çoğunlukla hacim merkezli kübik veya yüzey merkezli kübik kristal yapılarına sahiptir. Son yıllarda yapılan çalışmalar bu tür alaşımların ayrıca hegzagonal sıkı paket yapısına da sahip olabileceğini göstermektedir. Katı çözeltilerle beraber, yüksek entropi alaşımlarında dört farklı çekirdek etkisi de oluşmaktadır. Yüksek entropi etkisi, termodinamik özelliklerle ilişkisini ifade etmektedir. Yavaş difüzyon etkisi, kinetik durumu açıklamaktadır. Kafes bozunması etkisi, hem kristal yapıyı hem de mekanik özelliklerin oluşumunu

temsil etmektedir. Alaşıma katılan tüm elementlerin etkisi ise kokteyl etkisi altında incelenmektedir. Alaşıma katılan elementlerin, oluşan katı çözeltilerin ve dört çekirdek etkisinin sayesinde, yüksek entropi alaşımları; yüksek termal ve kimyasal dayanıklılık, yüksek sertlik, kırılma tokluğu, dayanım gibi mekaniksel özellikler, iyi aşınma, oksidasyon ve korozyon direnci gibi özelliklerle karakterize edilir. Üstün özellikleri sayesinde, nükleer sanayide, gemicilikte, refrakter malzemelerin üretiminde, havacılık ve uzay endüstrisinde, kesici takım uçlarında kullanılmaktadır. Yüksek entropi alaşımlarının üretiminde birçok yöntem tercih edilmektedir, fakat ark ergitme, mekanik alaşımlama, basınçsız sinterleme ve basınçlı sinterleme yöntemleri en çok kullanılan methodlardır.

Yüksek entropili alaşımlarını temel alan yeni bir sınıf olan yüksek entropili seramiklerin üretimi ise son yıllarda çalışılmakta olan bir konudur. Yüksek entropili seramikler, oksitleri, borürleri, karbürleri, nitrürleri ve silisidleri içermektedir. Yüksek entropi malzemelerinin yeni tipi olarak ve ultra-yüksek sıcaklık seramiklerinin yeni bir sınıfı olarak kabul edilen yüksek entropi metal borürlerin üretilmesi fikri de 2016 yılında ortaya çıkmıştır. Yüksek entropi borür seramikleri, *P6/mmm* uzay grubuna ve hegzagonal sıkı paket yapısına sahiptir. Bu yapının içerisinde metal-bor, bor-bor ve metal-metal bağları bulunmaktadır. Metalik, iyonik ve kovalent bağları bir arada içerdiği için üstün özellikler ile karakterize edilmektedir. Yüksek entropi metal borürler, seramiklerin düşük yoğunluk, mükemmel yüksek sıcaklık mukavemeti, yüksek sertlik ve dayanım, yüksek aşınma ve korozyon direnci, spesifik fiziksel (optik, elektriksel ve manyetik) özellikler gibi üstün özelliklerinin kombinasyonuna sahiptir. Bu üstün özelliklerinden dolayı havacılıkta, güneş enerjisi ve nükleer enerji sektörlerinde, kesici uçlarda ve mikroelektronik sistemlerde kullanılabilmektedir. Yüksek termal kararlılık, gelişmiş mekanik özellikler, yüksek oksidasyon direnci, radyasyon hasarı toleransı nedeniyle son zamanlarda dikkat çeken bir malzeme grubu olan yüksek entropi metal borür seramiklerinin sentezlenmesinde birçok yöntem kullanılmaktadır. Mekanik alaşımlama, boro/karbotermal indirgeme ile sentezleme, kendiliğinden ilerleyen yüksek sıcaklık yanma sentezi, basınçsız sinterleme, spark plasma sinterleme veya sıcak presleme gibi basınçlı sisterleme yöntemleri bunlardan başlıcalarıdır. Tek fazlı yüksek entropi borür yapısının elde edilemediği durumlarda birbirini takip eden iki yöntem kullanılabilir. Mekanik alaşımlama, toz metalurjisi ile üretim yöntemidir ve oda sıcaklığında gerçekleşme, ucuz başlangıç malzemeleri ve ucuz ekipmanlar kullanma gibi avantajlara sahiptir. Spark plazma sinterleme yönteminde ise yüksek sıcaklık ve yüksek basınç ile tek fazlı yapı elde edilebilmektedir.

Bu çalışma kapsamında ilk olarak belirlenen optimum koşullar üzerinden laboratuvar ortamında HfB_2, TiB_2, ZrB_2, TaB, Mn borür, Cr borür, Mo borür, W borür tozları mekanokimyasal yöntem ile sentezlenmiş ve liç işlemi ile saflaştırılmıştır. Herhangi bir yan ürün içermeden sentezlenen borür tozları optimum koşullar üzerinden çoğaltılmıştır. Çoğaltılan tozlar üç bileşenden sekiz bileşene kadar eşmolar oranda harmanlanmıştır. Üç bileşenli $(Hf_{0.33}Ti_{0.33}Zr_{0.33})B_2$ orta-entropi alaşımı ana alaşım olarak seçilmiştir. Seçilen kompozisyon, öncelikle gezegen tipi bilyalı öğütücüde 30 saat, 60 sa veya 100 sa boyunca, 10:1, 20:1 ve 30:1 bilya-toz ağırlık oranlarında sentezlenmiştir. Daha sonra aynı kompozisyon yüksek enerjili bilyalı değirmende 10:1 bilya-toz ağırlık oranında 6 sa, 10 sa, 15 sa ve 20 sa boyunca öğütülmüştür. Yüksek enerjili bilyalı değirmende bilya-toz oranı 10:1 ve 6 saatlik öğütme süresi optimum koşul olarak seçilmiştir. Hazırlanan tüm yüksek entropi borür kompozisyonlar optimum koşul üzerinden sentezlenmiştir. Toz numunelerin karakterizasyonu için X-ışınları difraktometresi, partikül boyut ölçümü ve piknometre ile yoğunluk ölçümü yapılmıştır. Mekanik alaşımlama sonrasında tek fazlı yüksek entropi borür yapısı elde edilememiştir. En yüksek toz yoğunluğu 7.1379 ± 0.0057 g/cm^3 ile $(Hf_{0.142}Ti_{0.142}Zr_{0.142}Mn_{0.142}Cr_{0.142}W_{0.142}Ta_{0.142})B_2$ bileşiminde gözlenirken en düşük toz yoğunluğu ise 4.9708 ± 0.005 g/cm^3 ile $(Ti_{0.25}Zr_{0.25}Mn_{0.25}Cr_{0.25})B_2$ bileşiminde gözlenmektedir.

Spark plazma sinterleme ile tek fazlı yüksek entropi yapısı sentezlenmiştir. Ayrıca, düşük şiddette (Hf, Zr) oksit fazları görülmüştür. Yine beş farklı kompozisyonda düşük şiddete sahip ikincil fazlar oluşmuştur. X-ışınları difraktometresi, taramalı elektron mikroskobu/enerji dağılım spektroskopisi, Vickers yöntemi ile sertlik ölçümü, aşınma testleri ve Arşimed yöntemi ile yoğunluk ölçümü sinterlenen numunelerin karakterizasyonu için uygulanmıştır. En yüksek yoğunluk değeri 7.4794 ± 0.0065 g/cm^3 ile $(Hf_{0.125}Ti_{0.125}Zr_{0.125}Mn_{0.125}Cr_{0.125}Mo_{0.125}W_{0.125}Ta_{0.125})B_2$ bileşiminde, en düşük yoğunluk değeri ise 4.7517 ± 0.0015 g/cm^3 ile $(Ti_{0.25}Zr_{0.25}Mn_{0.25}Cr_{0.25})B_2$ bileşiminde görülmüştür. Tüm numuneler incelendiğinde, sertlik değerleri 26.74 ± 1.85 GPa ile 17.08 ± 2.32 GPa arasında değişmektedir. Tüm numunelerin ortalama sertlik değeri yaklaşık 24 GPa olarak hesaplanmıştır. Aşınma direnci en düşük bileşim $(Hf_{0.125}Ti_{0.125}Zr_{0.125}Mn_{0.125}Cr_{0.125}Mo_{0.125}W_{0.125}Ta_{0.125})B_2$'dir; en yüksek bileşim ise $(Hf_{0.166}Ti_{0.166}Zr_{0.166}Mn_{0.166}Cr_{0.166}Mo_{0.166})B_2$'dir.

1. INTRODUCTION

Advanced ceramics are frequently preferred due to their superior properties in different applications. Transition metal borides, carbides and nitrides, which are belong to advanced ceramics, draw attention with their outstanding characteristics. Transition metal borides, on the other hand, stand out with their characteristics such as high melting temperature, high temperature strength, good electrical conductivity and high hardness and strength. With their superior properties, they are used in many areas like cutting tools and refractory parts. Self-propagating high-temperature synthesis (SHS), carbothermic/borothermic/metallothermic reduction and mechanochemical synthesis (MCS) are some of the methods of synthesizing transition metal borides. The MCS process is a powder metallurgy synthesis method. Production takes place at room temperature in the presence of a reducing agent, with no need for an initial temperature. MCS has become increasingly popular in recent years.

Materials have continued to be developed in recent years using alloying, which can combine two classes of materials to form different composites. Today, alloying, as claimed, forms the basis of materials science and metallurgy. In traditional alloying, basically two elements come together and the main element creates the properties of composites. On the other hand, the need for alloys with superior properties has increased. Therefore, traditional alloys have been developed with more than two elements. In 2004, a new term has been defined as high-entropy alloys (HEA). Simultaneously, "multicomponent alloys" has been defined in the same year. HEA simply refers to the alloys formed by combining four or more elements in an equimolar ratio (between 5 % and 35 %). Contrary to the Gibbs phase rule, high-entropy alloys have a single phase structure even though they contain more than one element. This is explained by four different core effects, independent of the Gibbs rule. Contrary to expectations, solid-solutions are formed instead of intermetallic phases, which allows a single-phase structure to be obtained. However, when solid-solutions occur, all four core effects, namely high-entropy, sluggish diffusion, severe-lattice distortion and cocktail effects are combined in HEA. The high-entropy effect is associated with thermodynamic properties; the sluggish diffusion effect explains the kinetics; the severe-lattice distortion effect is mostly identified with both structure and mechanical properties; the cocktail effect defines the combination properties of all alloying elements in the composition. Due to these core effects, HEAs have superior properties: high thermal stability (high melting point), outstanding mechanical properties (high hardness, strength and fracture toughness), good oxidation, corrosion and wear resistance. These features provide many areas of use, from shipping to nuclear power plants, from cutting blades to aircraft materials. Although there are many elements in the structure, HEAs only have face-centered cubic, body-centered cubic or sometimes hexagonal close-packed (HCP) crystal structures.

The development of high-entropy alloys continues with high-entropy ceramics. Firstly, high-entropy oxide composition has been synthesized in 2015. Then high-entropy ceramics continued as carbides, borides, sulfides, silicides and nitrides. In 2016, a new high-entropy ceramic has been explained as high-entropy diborides. The two primary criteria in the formation of high-entropy are enthalpy of mixing and atomic size difference. However, when it comes to HEB ceramics, these two effects are insufficient to explain, so lattice constant differences are used. Unlike HEAs, HEB ceramics have an AlB_2 type, a *P6/mmm* space group and hexagonal close-packed crystal structure. HEBs only show this structure. Inside the HCP structure, there are metal-boron, metal-metal and boron-boron layers; thus, the structure includes ionic, covalent and metallic bonds at the same time. With this combining of the bonds, HEB ceramics exhibit outstanding characteristics like high melting point, very high hardness and strength, good wear and corrosion resistance and excellent chemical stability. HEBs are highly resistant to extreme environmental conditions due to these properties, so they are used in many fields. Many production methods have been developed for HEBs. Mechanical alloying (MA), boro-carbothermal reduction (BCTR) and pressure sintering (spark plasma sintering, hot pressing) are the most common routes. Basically, in the MA process, the synthesis process can be carried out at room temperature. Single-phase structure cannot be obtained with the MA or BCTR methods, so a second method is needed. Here, pressure sintering methods are often preferred. Single-phase is obtained with the effect of pressure and high temperature. Today, studies for the development of high-entropy borides continue using different compositions, production methods and starting materials. The synthesis and reproduction of metal borides used as starting materials under laboratory conditions are almost nonexistent when previous studies are examined. Again, there are no studies on HEB ceramics containing Mn-B phase. This study aims to show the possibility of synthesizing high-entropy (HfTiZrMn/Cr)B_2 based ceramics via high-energy ball milling assisted spark plasma sintering (SPS). During this production, metal boride powders synthesized under laboratory conditions were used as starting materials. Detailed physical, microstructure and mechanical characterization of high-entropy boride ceramics has been completed.

This study includes the following steps:

- First of all, metal borides (HfB_2, TiB_2, ZrB_2, TaB, Mn-B, Cr-B, W-B and MoB) were produced by mechanochemical synthesis from metal oxides, native boron oxides and magnesium as a reducing agent under optimum conditions.
- The synthesized metal borides were hybridized by mixing equimolar ratios of three components to eight. Meanwhile, the $(Hf_{0.33}Ti_{0.33}Zr_{0.33})B_2$ composition was chosen as the main component considering the superior properties of each individual metal boride.
- The main component was milled in both planetary ball milling and high-energy ball milling (HEBM) for varying durations and ball-to-powder weight ratios. After that, BPR of 10:1 and 6 h milling were chosen as the optimum conditions in HEBM.
- All compounds were synthesized under optimum conditions. However, single-phase structure could not be obtained.
- After high-energy ball milling, powders were sintered with spark plasma sintering method at 2000°C and under 30 MPa.
- X-ray diffractometer, density measurement with a pycnometer and particle size analyzer were used for powder characterization. On the other hand, X-ray diffractometry, scanning electron microscopy/energy dispersive spectroscopy, density measurement with Archimedes' method and mechanical tests (Vickers hardness and dry-sliding wear tests) were performed for sintered specimen characterization.

2. LITERATURE REVIEW

2.1 Metal Boride Powders

The development of human history since ancient times began with the discovery of pure metals such as gold and copper. Today, numerous types of materials such as ceramics, composites, metals and polymers are used (Murty et al, 2014). These four different material groups continue to develop within themselves. For example, ceramics are classified into two groups: traditional ceramics and advanced ceramics. The first one is made up of inorganic solids like clay, silica and feldspar. Glass, porcelain and tiles are some examples of traditional ceramics. The second one is made up of metallic and non-metallic elements like B, O, C and N. Advanced ceramics are also called as engineering ceramics, high-technology ceramics, high-performance ceramics. In recent years, advanced ceramics have started to be widely preferred over traditional ceramics due to their higher mechanical properties, high thermal stability, high density and good thermal conductivity. Moreover, advanced ceramics outperform in terms of quality and offer new applications that traditional ones do not. Several methods are used for preparing ceramic components, like casting, solid-state reactions, sol-gel technique, pressure sintering routes, presureless sintering and chemical vapor deposition. AlON, Si_3N_4, B_4C, Al_2O_3 and silica are the most common examples of advanced ceramics. Except these, transition metal borides, carbides, silicides, oxides and nitrides are subgroups (Otitoju et al, 2020). Among these, transition metal borides attract attention with their different crystal structures and superior properties (Ağaoğulları et al, 2012a). Borides have a very large group of compounds. Metal borides have been the subject of numerous studies throughout history. In this part of the thesis, the crystal structures, characteristics, usage areas and production methods of metal borides will be explained with the support of the literature studies.

2.1.1 Crystal structures and phase diagrams of metal borides

Metal borides constitute a class of materials with wide application fields and different physical properties. The various physical ones are due to the variety of crystal structures of each boride compound. It can be said that metal borides have several crystal structures for varying metal-boron ratios. In this thesis, eight different metal borides were synthesized with multi-phase. The crystal structures, structure types and space groups of some of the synthesized borides are given in Table 2.1.

Table 2.1 : Crystal structures, structure types and space groups of metal borides (Akopov et al, 2017).

Compound	Crystal Structure	Structure Type	Space Group
HfB_2	Hexagonal	AlB_2	*P6/mmm*
TiB_2	Hexagonal	AlB_2	*P6/mmm*
ZrB_2	Hexagonal	AlB_2	*P6/mmm*
Cr_3B_4	Orthorhombic	Ta_3B_4	*Immm*
CrB	Orthorhombic	CrB	*Cmcm*
CrB_2	Hexagonal	AlB_2	*P6/mmm*
Cr_2B	Orthorhombic	Mn_4B	*Fddd*
TaB	Orthorhombic	CrB	*Cmcm*
Mo_2B	Tetragonal	$CuAl_2$	*I4/mcm*
α-MoB	Tetragonal	MoB	$I4_1/amd$
β-MoB	Orthorhombic	CrB	*Cmcm*
MoB_2	Hexagonal	AlB_2	*P6/mmm*
MoB_4	Hexagonal	$Mo_{0.8}B_3$	$P6_3/mmc$
WB_2	Hexagonal	W_2B_4	$P6_3/mmc$
W_2B	Tetragonal	$CuAl_2$	*I4/mcm*
WB	Orthorhombic	CrB	*Cmcm*
Mn_2B	Tetragonal	$CuAl_2$	*I4/mcm*
Mn_2B	Orthorhombic	o-Mn_2B	*Fddd*
MnB	Orthorhombic	FeB	*Pmma*
Mn_3B_4	Orthorhombic	Ta_3B_4	*Immm*
MnB_2	Hexagonal	AlB_2	*P6/mmm*
MnB_4	Monoclinic	MnB_4	*Cmcm*

Almost all of the diboride phases are in hexagonal close-packed structures of the AlB_2 structure type. In the AlB_2 type, the metal atoms are located at the corners, while the boron atoms are located in the middle. Within the trigonal prisms, there are graphite-like boron networks (Akopov et al, 2017). Each boron is surrounded by six metals and three boron atoms, and each metal is surrounded by six metals and twelve boron atoms. A representation of the AlB_2 type is given in Figure 2.1a (Akopov et al, 2017; Merz et al, 2014). Boron atoms are represented by gray and metal atoms by blue. CrB, FeB and α-MoB types, which are also tetragonal and orthorhombic crystal structures, have a zigzag-shaped boron atom chain (Albert & Hillebrecht, 2009; Iyer et al, 2019). It is shown representatively in Figure 2.1b. Boron atoms are represented by gray and metal atoms by pink spheres.

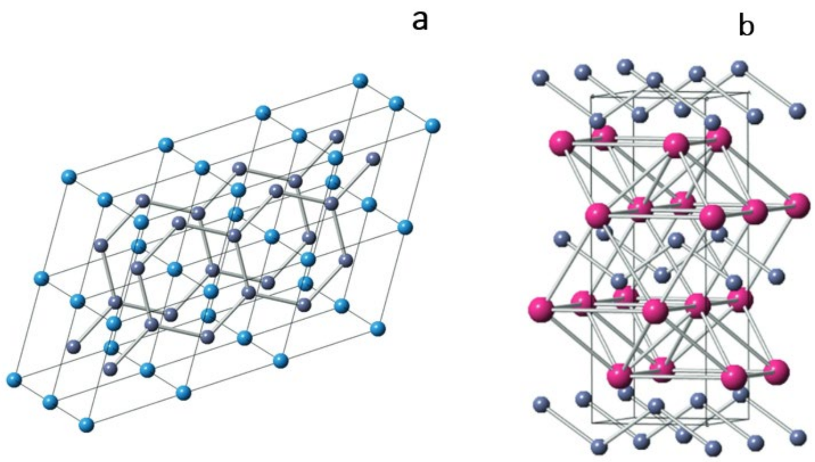

Figure 2.1 : Crystal structure of AlB_2 type (Akopov et al, 2017; Merz et al, 2014).

Figure 2.2a-b include phase diagrams of the Hf-B and Zr-B systems, respectively. As it can be seen from the Hf-B phase diagram, there are just two boride phases: HfB and HfB_2. HfB phases are stable until 2100 ℃; on the other hand, HfB_2 phases persist up to very high temperatures (nearly 3380 ℃). Also, it is seen that Hf in the elemental state can also occur up to about 2200 ℃ (Gigolotti et al, 2012). The phase diagram of the Zr-B system shows the presence of phases ZrB_2 (3500 K), peritectic ZrB_{12} (2400 K), and unstable ZrB (1600 K). Among these phases, ZrB_2 is the most resistant to high temperatures and the most stable phase (Tokunaga et al, 2008).

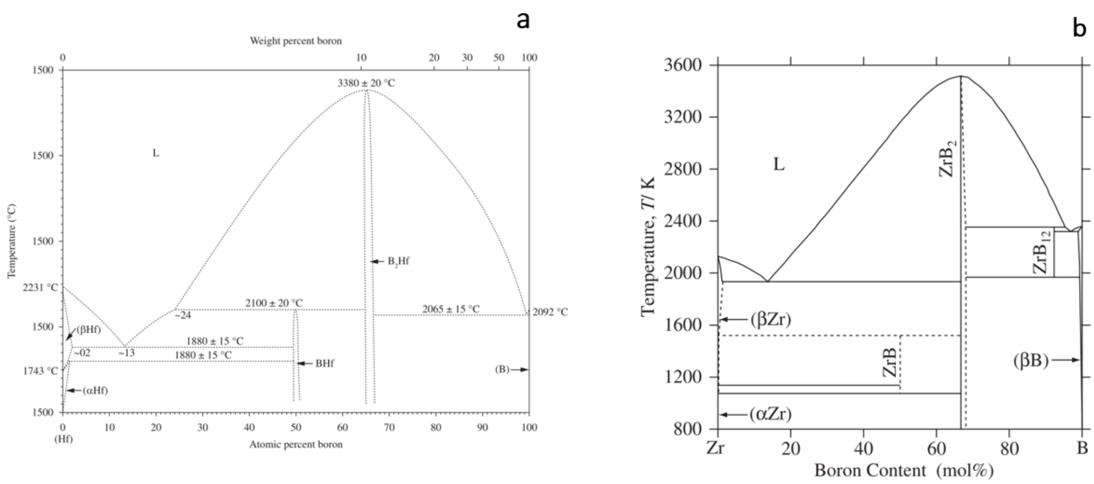

Figure 2.2 : The binary phase diagrams of (a) Hf-B (Gigolotti et al, 2012) and (b) Zr-B (Tokunaga et al, 2008).

On the basis of Figure 2.3a, intermetallic TiB, peritectic Ti_3B_4 and TiB_2 phases are observed. Both TiB and Ti_3B_4 are stable until 2200 ℃. However, The TiB_2 phase is in the structure up to ~ 3225℃, which indicates that the TiB_2 phase is more stable (Euh et al, 2001). In the Mn-B system, as seen in Figure 2.3b, there are unstable and various peritectic phases. To begin, the peritectic phases Mn_2B, MnB, Mn_3B_4, MnB_2 and MnB_4 form at temperatures of 1580 °C, 1890 °C, 1827 °C and 1375 °C, respectively. Also, unstable MnB_4 phase is seen at nearly 1120 °C. In this case, it can be said that the most stable phase is MnB, but it is seen that the melting temperatures of the phases are quite close to each other. As a result of this, it is understood that not a single stable phase but more than one phase can be seen in the Mn-B system (Spear & Liao, 1986).

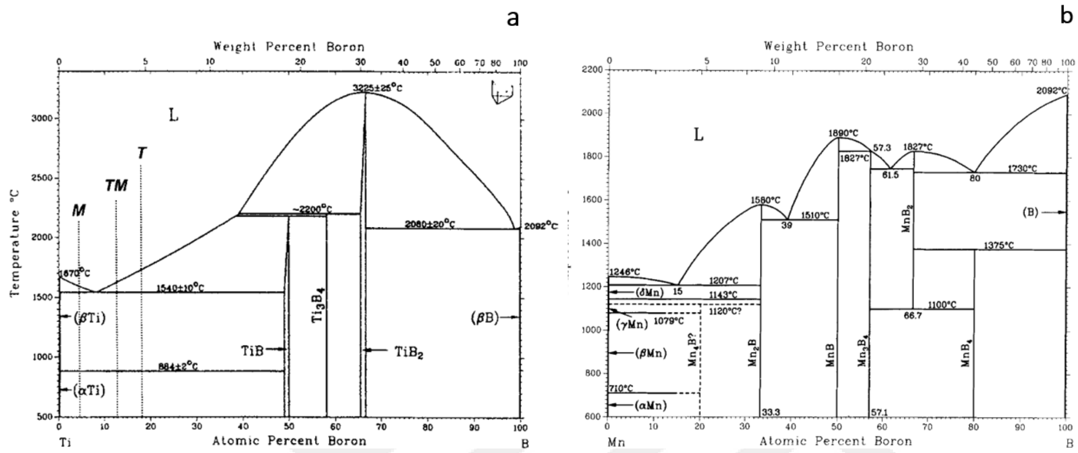

Figure 2.3 : The binary phase diagrams of (a) Ti-B (Euh et al, 2001) and (b) Mn-B (Spear & Liao, 1986).

Figure 2.4a represents the phase diagram of the Cr-B system. Like the Mn-B system, there are various peritectic Cr-B phases. At 1870 °C, Cr_2B and Cr_5B_3 are stable. The system also contains CrB (at 2100 °C), Cr_3B_4 (at 2070 °C), CrB_2 (at 2200 °C) and CrB_4 (at 1500 °C) phases. Among these ones, CrB_2 is the most stable phase. However, the temperatures at which the phases can be stable are very close to each other, except for the CrB_4 one. Consequently, more than one Cr-B phase is expected to be seen (Spear & Liao, 1986). According to the phase diagram of the Mo-B binary system (Figure 2.4b), there are MoB, Mo_2B, MoB_2, Mo_2B_5 and MoB_4 phases. Besides, MoB has two allotropic transformations: α-MoB which is a low temperature phase and β-MoB which is a high temperature phase. The MoB_2, which is a high temperature one, exists between 1800±80 °C and 2375±15 °C. Mo_2B, Mo_2B_5 and MoB_4 are stable the end of the 2280±12 °C, 2140±15 °C and 1807±50 °C, respectively. It can be seen that the element Mo can still be found at high temperature (Spear & Liao, 1988).

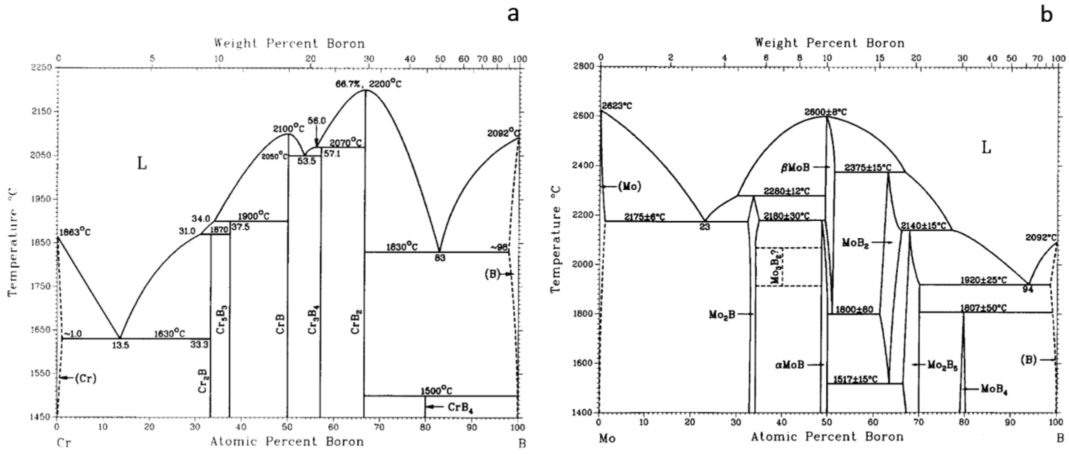

Figure 2.4 : The binary phase diagrams of (a) Cr-B (Spear & Liao, 1986) and (b) Mo-B (Spear & Liao, 1988).

The binary phase diagram of W-B is exhibited in Figure 2.5a. W_2B (~ 2700 °C), W_2B_5 (~ 2350 °C), WB_4 (~ 2000 °C) and WB which consists of α-WB (~ 2550 °C) and β-WB (~ 2700 °C) are formed. WB_2 phase are not stable according to the phase diagram. Furthermore, because the temperatures at which the phases can remain stable are similar, it is normal to see more than one different W-B phase at high temperatures (Kieffer & Benesovsky, 1958). Otherwise, there are four peritectic phases in the Ta-B phase diagram (Figure 2.5b). Ta_3B_2, TaB, Ta_3B_4 and TaB_2 ones are formed at nearly 2100 °C, 2400 °C, 2650 °C and 3100 °C, respectively. TaB_2 is the most stable phase, yet, the stability temperatures of the other ones are close to each other (Usta et al, 2005).

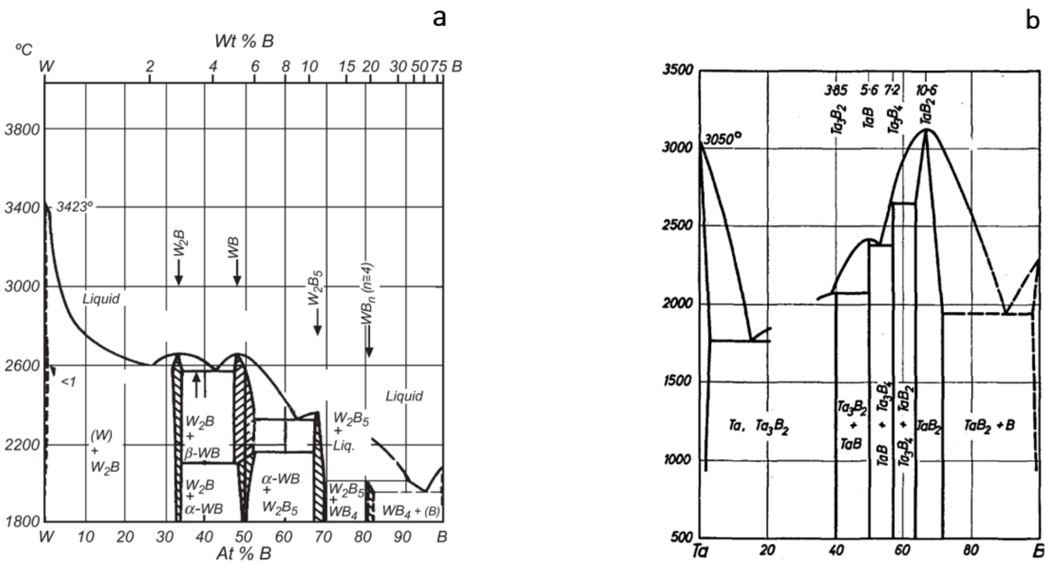

Figure 2.5 : The binary phase diagrams of (a) W-B (Usta et al, 2005) and (b) Ta-B (Kieffer & Benesovsky, 1958).

2.1.2 Properties and application areas of metal borides

Metal boride compounds own their strong properties to strong ionic and covalent bonds between elements. These alloys have superior thermal properties like high melting point (more than 3000 °C), thermal stability, thermal expansion coefficient, thermal shock resistance and thermal conductivity (Ağaoğulları et al, 2015, 2019; Fahrenholtz et al, 2007; Yao et al, 2012). Also metal borides have good mechanical features such as high Young's modulus and high hardness, so some of these alloys are called superhard materials (Altıntaş et al, 2021; Qi et al, 2014; L. Xu et al, 2012). Besides, this type of boride contains good electrical properties, such as high electrical conductivity. In addition, they exhibit low density and are chemically unaffected by strong oxidants (Ağaoğulları et al, 2015, 2019; Balcı et al, 2012; Friedrich et al, 2011).

Table 2.2 includes the properties of the some metal borides. According to the table, HfB_2, TiB_2 and ZrB_2 are stable at very high temperatures. The melting temperatures of the other phases are similar to each other. When the density values are compared with each other, it is seen that the W-B phases, TaB_2 and HfB_2 structures have the highest density values. Therefore, compositions containing these phases are expected to have higher density values. On the other hand, TiB_2, MnB_2 and CrB_2 phases have low densities. The hardness values of metal borides change between 11 and 28 GPa (Reddy et al, 2015; Xu et al, 2017). It is understood that boride compounds have various values different from each other. Having several values shows that when the boride compositions are brought together, they will affect the hardness value of the alloy differently. Also, not only thermal but also electrical conductivities are not similar. The fact that the features are different from each other allows them to be used in a wide variety of application areas (Reddy et al, 2015; Xu et al, 2017; Url-1, Url-2, Url-3, Url-4, Url-5, Url-6; Yamada et al, 2003; Zapata-Solvas et al, 2013).

With these outstanding features, metal borides are used in various high temperature applications, especially in the defense industry and nuclear industries, and in various industrial applications (low weight armor ceramic, neutron absorption material, wear resistant parts, abrasive material in polishing and grinding processes, building material in molds, nozzles and shaft bearings, electrodes (Otitoju et al, 2020). Refractory materials are used in a variety of applications (e.g., material and cutting tip, grain reducer in metal matrices, cathode coating and thermocouple sheath in aluminum electrolysis, jet engines and nozzles, crucibles and rolling bits for molten metals, etc.)

(Balcı et al, 2016; Xu et al, 2012). They also have potential applications as catalysis supports, lithium-ion battery materials and thermoionic electron sources. In addition to all these, metal boride compounds are also used in many electrical applications such as automotive, telecommunications, power electronics, oscillators, and various radar and sensor systems (Ağaoğulları et al, 2012a, 2015, 2019; Otitoju et al, 2020; Xu et al, 2012).

Table 2.2 : Properties of metal borides (Reddy et al, 2015; Xu et al, 2017; Url-1, Url-2, Url-3, Url-4, Url-5, Url-6; Yamada et al, 2003; Zapata-Solvas et al, 2013).

Compound	Melting Temperature (°C)	Density (g/cm^3)	Hardness (GPa)	Thermal Conductivity ($W.(cm.K)^{-1}$)	Electrical Conductivity ($10^4.\ \Omega^{-1}.\ m^{-1}$)
HfB_2	3380	11.2	15-28	0.51	944
TiB_2	3225	4.53	-	0.664	1110
ZrB_2	3245	6.09	13-23	0.579	1030
MnB_2	1827	5.57	22.5	-	-
MoB	2600	8.67	23	-	223
Mo_2B_5	2140	7.48	23	0.502	385
WB	2550	15.73	-	-	-
W_2B_5	2350	11.76	26.1	0.25	455
TaB_2	2650	12.62	24.5	0.16	308
CrB_2	2200	5.6	11-13	0.318	333

2.1.3 Production methods of metal boride powders

Various methods are used in the production of metal borides with high melting temperatures, chemical and thermal stability properties, higher hardness and thermal conductivity than oxide ceramics, and high corrosion, abrasion and thermal shock resistance (Ağaoğulları et al, 2012a, 2016). Thermal plasma method, self-propagating high temperature synthesis (SHS), carbothermic/borothermic/metallothermic reduction, autoclave synthesis, molten salt electrolysis and solid-state synthesis are the most common methods for obtaining metal borides (Ağaoğulları et al, 2012a; Balcı et al, 2016; Mertdinç et al, 2018; Popov et al, 2007).

Another method used in the synthesis of metal borides, different from the routes mentioned, is the mechanochemical synthesis (MCS) process, which has been used for other material groups for the last twenty years and is still being developed. Mechanochemistry is defined as a form of chemistry activated by non-hydrostatic mechanical stress (Suryanarayana, 2001). It has been used in the synthesis of a wide variety of stable and semi-stable phases, supersaturated solid-solutions, nanocrystalline and semi-crystalline intermediate phases and amorphous alloys in the microstructure of the material since the mid-nineties. MCS involves reacting, mechanically activating and alloying the products of the reaction with a suitable reductant or reducing agent. The energy obtained from plastic deformation, fracture and friction during alloying is transformed into different types of energies, and these energies accumulate in the system. The accumulated energy creates new, wide and active surfaces, increasing chemical reactivity (Chen et al, 1997). Along with all these, mechanical deformation in the crystal structure increases chemical reactivity and disrupts the thermodynamic equilibrium. The new surfaces allow reactions to take place at lower temperatures, without the need for external heat, with increased reactivity. In addition, the diffusion distance decreases due to the increase in the surface area of the powder particles, which brings a decrease in the reaction temperature (Chen et al, 1997; Levitas, 2003; Suryanarayana, 2001; Suryanarayana et al, 2001).

The MCS process, which takes place under the influence of two different kinetic mechanisms, is generally based on the replacement of metal oxides, chlorides or sulfides with a more active metal (a reductant or reducing agent) to obtain pure metal and/or other related metal compounds. In the first of these kinetic mechanisms, the reaction takes place slowly and gradually. In the second type, when the reaction enthalpy is sufficient, the reaction starts and continues on its own without the need for any external heat. Here, duration is the critical parameter. The temperature increases after a certain period of time and the reaction takes place within seconds at the end of this period (Wieczorek-Ciurowa, 2013; Wieczorek-Ciurowa et al, 2007). The reaction kinetics are affected by milling parameters such as milling time, ball-to-powder weight ratio, type and size of milling balls and vials, type of milling, process control agent, preparation of starting powders in stoichiometric or excess amounts (Suryanarayana, 2001). By changing one or more of these parameters, many different results can be obtained experimentally.

Undesirable by-products or oxidized phases can be expected as a result of MCS, in which case the by-products can be removed by leaching or vacuum distillation. Some studies on the production of Ti, Zr, Hf, Ta, Mo, W, Cr, Mn boride by mechanochemical synthesis and mechanical alloying methods are as follows:

Çelik et al. (2022) synthesized the TiB_2 phase with a size of 50.2 nm from the TiO_2-B_2O_3-Mg system with the leaching process followed by the MCS (4 h) method. Bilgi et al. (2008) produced TiB_2 with an efficiency of 89.6 % from a mixture of 30 g powder containing B_2O_3, TiO_2 and metallic Mg in a planetary type ball mill and a ball-powder ratio of 10:1 for a time period of 5-15 h. Coşkun and Öveçoğlu (2013) obtained nanometric W_2B_5 powder from $WO_{2.72}$/B_2O_3/Mg powders by MCS (30 h) and purification (7 M HCl). Şenyurt et al. (2021) synthesized W-B phases from the WO_3-B_2O_3-Mg-C quaternary system mechanochemically. They determined that the products formed as a result of the synthesis were significantly affected by the process parameters. Akgün et al. (2011) synthesized ZrB_2 separately from ZrO_2/B_2O_3/Mg powder raw materials by combustion synthesis and MCS (30 h) methods. They applied leaching process with HCl to both products, but they also detected ZrO_2 phase besides ZrB_2 phase in both products. Ağaoğulları et al. (2012b) synthesized ZrB_2/ZrC powders in the particle size range of 50-250 nm with the mechanical alloying process lasting 2 h, starting from Zr/B/C mixtures in different mole ratios. TaB/TaB_2 powders were produced by MCS followed by leaching process using Ta_2O_5, B_2O_3 and Mg starting powders by Mertdinç et al. (2019). When the blends prepared in stoichiometric ratio were milled, a large amount of TaB phase was formed. It was observed that the TaB_2 phase was dominant when the blend mixture contained excess B_2O_3. Kudaka et al. (2001) synthesized MoB_2 and Mo_2B_5 powders by mechanochemical routes. Blends with Mo/B mole ratios of 1/2 and 2/5 were milled under Ar atmosphere for 10-40 h. The milled powders were annealed at 1000 °C and 1500 °C. Single-phase MoB_2 could not be synthesized, but single-phase Mo_2B_5 synthesis was carried out by annealing the powders in the ratio Mo/B:2/5 at both temperatures. In the study by Yamauchi et al. (2007), MoB, MoB_2 and Mo_2B phases were obtained together with ball milling and annealing process. In another study, ferromagnetic Mn_2B powders were synthesized by milling the blend prepared with Mn and B powders in a high-energy ball milling (400 rpm) with a ball-to-powder weight ratio of 40/1 for 10 h (Şimşek et al., 2019). In their study, Iizumi et al. (2011) synthesized CrB_2 powders by milling the blend of Cr/B (1:2) powders for 10, 20 and 30 h, and then annealing at 900 °C for 2 h. In the same study, the powder ratio was changed to Cr/B:1/1, and after 20 and 40 h of milling, annealing was conducted at 1000 °C, and CrB powders were obtained.

2.2 High-Entropy Alloys (HEAs)

In the past, the story of humanity began with the discovery of pure metals such as gold and copper. Today, however, there is access to hundreds of elements and countless materials. The increasing diversity of materials can be seen from the strength-density Ashby diagrams in Figure 2.6. Engineering materials can be divided into four groups as ceramics, polymers, composites and metals. In fact, the revolution that began in England in the 18th century led to the discovery of new elements. Various engineering materials and alloys have been developed with these new elements. According to many, alloying forms the basis of materials science and metallurgy. In fact, alloying was discovered by accidently. Early humans formed the basis of alloying by combining arsenic and copper by chance. It is clear that these groups have developed from the past to the present, new materials have been synthesized and will continue to develop (Murty et al, 2014).

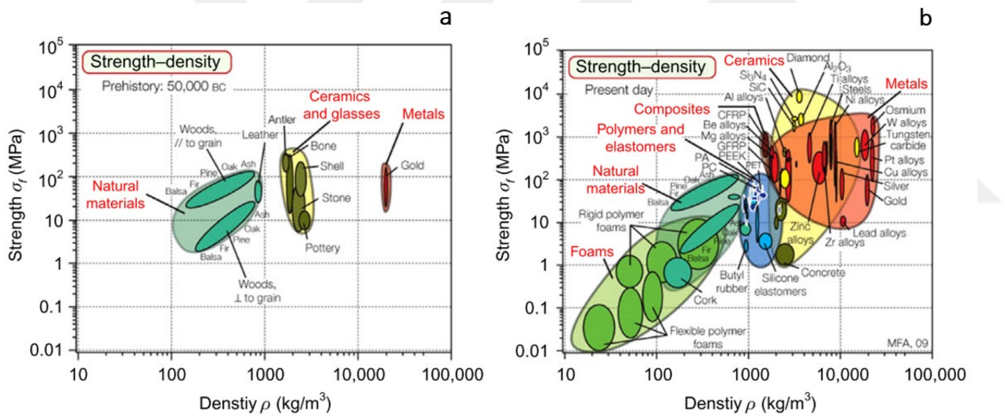

Figure 2.6 : Diversity of materials: (a) prehistoric era, (b) current (Murty et al, 2014).

According to the Cantor (2021), all materials are alloys, which means that all materials consist of one or more different starting materials. Alloying has been used for about 5000 years, from the past to the present. In the bronze, copper or iron age, alloys were used in the production of jewelry, weapons and tools with metals such as gold, copper, silver, iron, lead, tin, zinc and mercury (Cantor, 2021; Murty et al, 2014). In addition, alloys were used in their daily lives in ancient times. For example, bronze was used in the making of mirrors (Murty et al, 2014). Today, metal alloys are preferred in many applications due to their advanced mechanical, thermal and physical properties (Kumar et al, 2022). The historical development of metals and their alloys are shown in Figure 2.7.

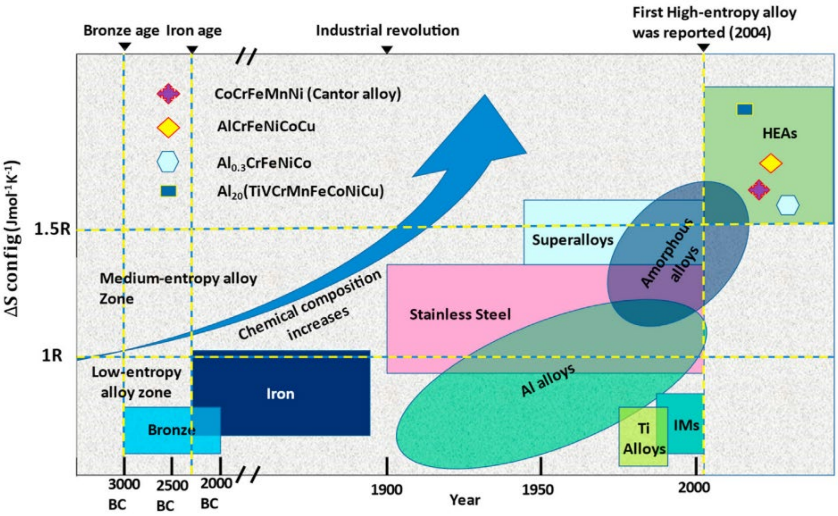

Figure 2.7 : Historical development of metals and their alloys (He et al, 2017).

Alloy design is a very difficult and complex subject. The production of metal alloys is traditionally based on one or two elements (Cantor, 2021; Miracle & Senkov, 2017). Typically, the major element determines the chemistry of the alloy and mostly its properties, while the second element, and sometimes the third element, affect the characteristics in small amounts (Cantor, 2021; Cho et al, 2022; Miracle & Senkov, 2017; Tsai & Yeh, 2014). With the development of modern technology, new materials are needed. In the last 18 years, efforts have been made to obtain superior properties by expanding the concept of alloying to more than two or three elements. This new alloy group is called "High-Entropy Alloy (HEA)" (Yeh et al, 2004).

The concept of HEA was first introduced in 2004 by Yeh et al. In addition to the definition of high-entropy, Cantor et al. used the term "multicomponent alloys" in their study published in 2004. High-entropy alloys consist of four, five or more elements in an equimolar ratio. This definition has been expanded to require that the concentration of each principal element is between 5 % and 35 % (Yeh et al, 2004). As it can be understood from the definition that it refers only to the concentrations of the elements, and does not contain a statement about the magnitude or range of entropy. Looking at the entropy-based definition, three different areas emerge. There is a first low-entropy area ($\Delta S_{conf} \leq 0.69R$), second medium-entropy area ($0.69R < \Delta S_{conf} < 1.61R$) and third high-entropy area ($\Delta S_{conf} \geq 1.61R$). ΔS_{conf} represents the total configurational molar entropy in an perfect solid-solution and R is the gas constant (Miracle and Senkov, 2017; Yeh, 2007). This fields are summarized in Figure 2.8a. The calculations of configurational entropy expressions are explained under the core effects. Figure 2.8b shows the materials classification based on the configurational entropy, except composite materials (Murty et al, 2014). The low-entropy alloys includes traditional alloys, polymers and ceramics. The medium-entropy alloys consist of 2-4 principal elements and high-entropy alloys include at least five elements (Tsai & Yeh, 2014). The high-entropy group consists of ceramics and mostly alloys (Kumar et al, 2022).

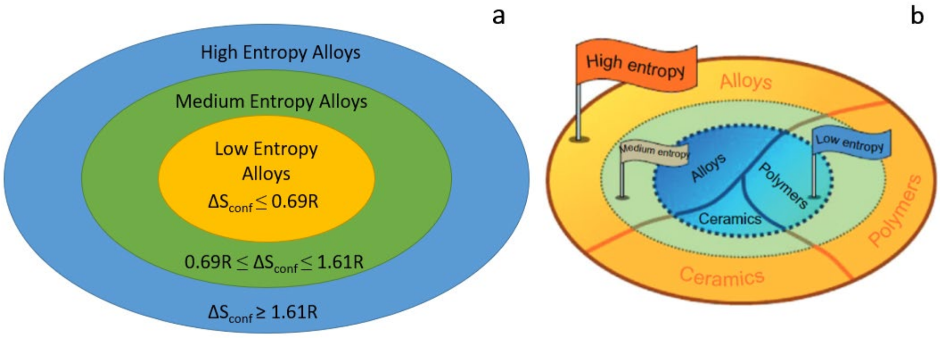

Figure 2.8 : (a) Entropy based definition of HEAs and (b) classification of materials based on the configurational entropy, adapted from Murty et al. (2014).

Currently, more than four hundred high-entropy alloys have been developed (Cantor, 2021). Today, however, it is observed that high-entropy alloys expand with additions of nitride, oxide, boride, carbide, sulphide, fluoride, silicide (Musicó et al, 2020). The historical evolution of high-entropy alloys is clearly represented in Figure 2.9.

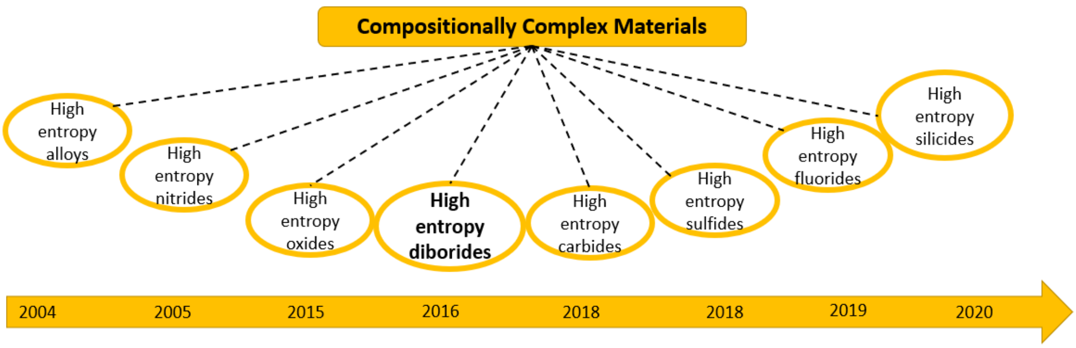

Figure 2.9 : Historical evolution of HEAs, adapted from Kumar et al. (2022) and Musicó et al. (2020).

The random distribution of atoms in the lattice according to their entropy class is stated in Figure 2.10a-c. Figure 2.10a represents the high-entropy alloys. Contains five elements and atoms are located at the same points relative to each other. In medium-entropy alloys schematized in Figure 2.10b, there are three different atoms and they are in the same position relative to each other, similar to high-entropy alloys. In traditional alloying (Figure 2.10c), there are two atoms of different sizes. It is known that the difference between atomic number and radius affects the properties of alloys (Kumar et al, 2022).

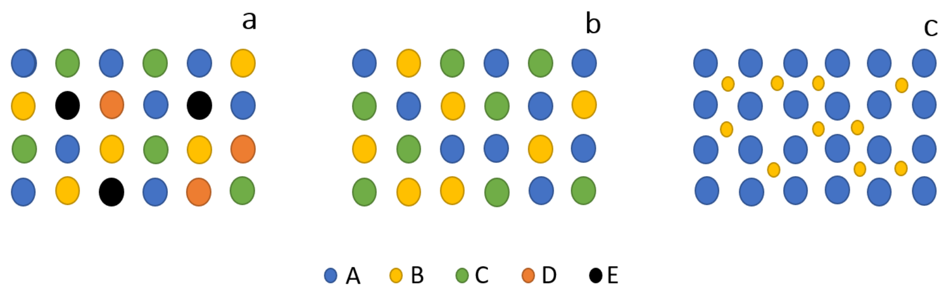

Figure 2.10 : Schematic representation of (a) high-entropy, (b) medium-entropy and (c) low-entropy alloys distributed randomly on a lattice, adapted from Kumar et al. (2022).

Although they contain more than one principal element, high-entropy alloys are single-phase and have a single crystal structure. They are mostly in face-centered cubic (FCC) or body-centered cubic (BCC) (Guo et al, 2011; Li & Tsai, 2020; Yin et al, 2022). However, in different studies, it has been observed that it also has a hexagonal close-packed (HCP) structure (Feuerbacher et al, 2015; Youssef et al, 2015). A rule or parameter is needed to determine these structures. According to the revised Hume-Rothery rule (Battezzati, 2019), the valence electron concentration (VEC) of an alloy is another Critical parameter that affects the crystallization of the solid-solution phase when atomic size effects are not significant and valance electron concentration (VEC) plays an important role for specifying structures. Guo and his teammates (2011) calculated the VEC parameter according to equation (2.1).

$$VEC = \sum_{i=1}^{n} c_i \, (VEC)_i \tag{2.1}$$

Here, $(VEC)_i$ is the valence electron density of element i. When the VEC is 8, a single-phase FCC structure is expected; additionally, when the VEC is 6.87, a single-phase BCC structure is desired. FCC and BCC structures were obtained together if the VEC value was between 6.87 and 8 (Guo et al, 2011; Y. Zhang et al, 2014b). So, it can be said that since FCC phases are stable at high VECs, BCC phases are stable at low VECs. Although there are exceptions, the VEC value defines the crystal structure limit precisely. For example, while the CoCrCuFeNi high-entropy alloy has the FCC structure, the AlCoCrFeNi high-entropy alloy has the BCC structure. Figure 2.11 represents a schematic illustration showing the relation between lattice structure and high-entropy alloys, and also the relationship between lattice structures and VEC (Guo et al, 2011).

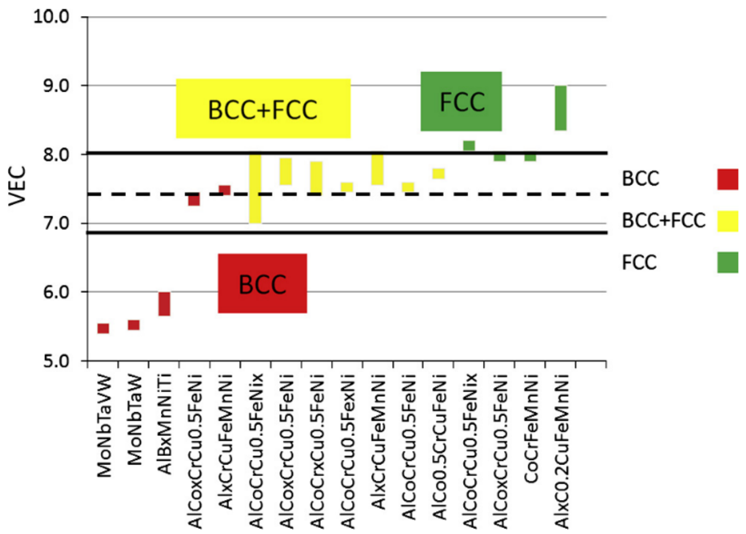

Figure 2.11 : Relationship between VEC and FCC/BCC phases of different high-entropy alloys (Y. Zhang, et al, 2014b).

2.3 Core Effects of HEAs

High-entropy alloys show distinctive mechanical, physical and chemical differences from traditional alloying elements. These differences are attributed to the four different core effects. The high-entropy effect changes the thermodynamic properties. Sluggish diffusion effect makes a difference in kinetics. Severe-lattice distortion affects both structure and mechanical properties. The cocktail effect combines all of the characteristics of the elements (Kumar et al, 2022; Tsai & Yeh, 2014).

2.3.1 High-entropy effect

The Gibbs phase rule giving the relationship between composition and phases of the system under equilibrium conditions is shown in equation (2.2). Where p is phases, c is number of components and n is the number of freedom of the system (Cantor, 2014, 2021).

$$p + n = c + 1 \tag{2.2}$$

When the number of free variables is zero as given in equation (2.3), the maximum number of phases are determinded under equilibrium (Cantor, 2014, 2021).

$$p_{max} = c + 1 \tag{2.3}$$

The production of the most of the materials differs from equilibrium conditions. This indicates that the maximum number of phases will be greater than that determined by the Gibbs phase rule. This situation is explained in equation (2.4) (Cantor, 2014, 2021).

$$p_{max} > c + 1 \tag{2.4}$$

For example, in a binary system (c = 2), the maximum equilibrium number of phases is 3. Another example about ternary system, when (c = 3), the maximum equilibrium number of phases are four (Cantor, 2014, 2021). High-entropy alloys are contrary to the Gibbs phase rule. Although they contain more than one element, there is only one phase in the structure. High-entropy alloys form a solid-solutions (SS) instead of intermetallic phases. Elements that are randomly brought together in an equimolar ratio cannot form a solid-solution; they must meet the HEA formation conditions in order to form the SS phase. The high-entropy effect reduces the free energy of the solid-solution phases, thus facilitating the formation of SS, especially at high temperatures (Cantor, 2014, 2021; Yeh, 2013). In this way, a single-phase structure compared to the Gibbs phase rule can be obtained. Generally, as can be seen from Figure 2.12, the entropy of the mixture takes its maximum value when the elements are added in equimolar ratios in binary alloys, and the entropy increases as the number of components increases in binary alloys (Murty et al, 2014).

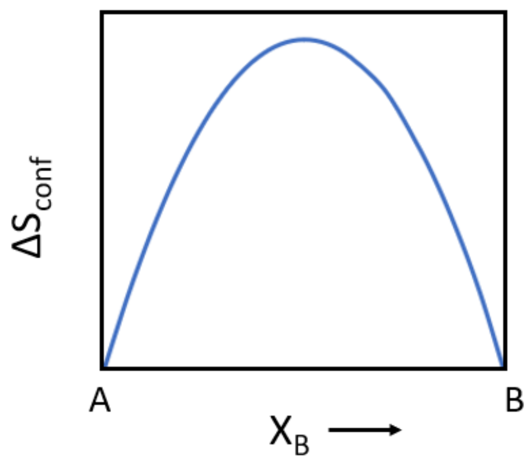

Figure 2.12 : Changing of the configurational entropy in the binary system, adapted from Murty et al. (2014).

The energy of solid-solutions can be reduced by increasing entropy. In a thermodynamic equilibrium, the entropy (S) depending on the Gibbs free energy (G), enthalpy (H) and temperature (T) is explained as given in equation (2.5) (Murty et al, 2014).

$$G = H - TS \tag{2.5}$$

For alloy systems, the Gibbs free energy change is defined as shown in equation (2.6). (Murty et al, 2014).

$$\Delta G = \Delta H - T\Delta S \tag{2.6}$$

When the number of elements increases the mixing of Gibbs free energy change has negative values in the traditional alloys (Tong et al, 2005). However, in high-entropy alloys, equimolar elements reduce the Gibbs free energy, and it is seen that solid-solutions are formed. In addition to Gibbs free energy, it affects solid-solution formation in high-entropy alloys in selected elements according to Hume-Rothery rules (Y. Zhang et al, 2014b). These rules include: (a) the difference between the radii of the solvent and solute atoms should not exceed 15 %; (b) the electronegativity values of the solute and solvent atoms should be similar to each other; (c) solute and solvent atoms have the same crystal structure; (d) solute and solvent atoms should have similar valence values (Battezzati, 2019; Y. Zhang et al, 2014b). High-entropy alloys meet the first two of these, but not the last two. Accordingly, the formation of high-entropy alloys cannot be explained by Hume-Rothery's rules, which are valid for intermetallic phases. Different parameters should be studied to explain the formation of high-entropy alloys (Battezzati, 2019; Tong et al, 2005; Y. Zhang et al, 2014b).

In terms of thermodynamic equilibrium conditions, three important parameters have been determined for the formation of solid-solution phases in YEAs. These are ΔH_{mix} (enthalpy of mixing) and δ (atomic size difference), and are defined in equations (2.7)-(2.8) (C. Zhang et al, 2012).

$$\Delta H_{mix} = 4 \sum_{i=j,i\neq j}^{n} \Delta H_{ij}^{mix} \, c_i \, c_j \tag{2.7}$$

$$\delta = \sqrt{\sum_{i=1}^{n} X_i \, (1 - \frac{r^i}{\bar{r}})^2}, \bar{r} = \sum_{i=1}^{n} X_i r_i \tag{2.8}$$

Enthalpy of mixing between elements i and j is represented by ΔH_{ij}^{mix}, molar ratio of element *i* is shown by X_i, atomic radius of element *i*, is represented by r_i and $\bar{r}$ is the mean radius of the alloy. ΔH_{mix} refers to the tendency to form stable intermetallic compounds (Fang et al, 2003). The parameter δ in equation (2.7) defines the effect of atomic size difference in an alloy with *n* elements.

In addition to these criteria, a new empirical parameter Ω is defined in equation (2.9), taking into account the effect of entropy for HEA (Guo & Liu, 2011; Y. Zhang, et al, 2014a).

$$\Omega = \frac{T_m \, \Delta S_{mix}}{|\Delta H_{mix}|} \tag{2.9}$$

For the formation of stable solid-solution phases in high-entropy alloys, empirically the δ value should be less than 6.6 % ($\delta \leq 6.6$ %), the ΔH_{mix} value should be between -15 kJ/mol and 15 kJ/mol (-15 kJ/mol ≤ ΔH_{mix} ≤ 15 kJ/mol), and the Ω value should be greater than 1.1 (Ω ≥ 1.1) (X. Yang & Zhang, 2012).

In here, T_m and ΔS_{mix} are identified in equation (2.10) and (2.11), respectively (Yeh, 2013; Y. Zhang et al, 2014b).

$$T_m = 4 \sum_{i=1}^{n} X_i \, (T_m)_i \tag{2.10}$$

$$\Delta S_{mix} = -R \sum_{i=1}^{n} X_i \, ln X_i \tag{2.11}$$

T_m is the mean melting temperature, ΔS_{mix} is the mixing entropy of the alloy systems, and R (8.314 J/mol) is the gas constant (Yeh, 2013; Zhang et al, 2014a). At the same time, in alloys to which equimolar elements are added, the configuration entropy can be calculated according to the Boltzmann hypothesis as given in equation (2.12) (Zhang et al, 2014a):

$$\Delta S_{mix} = R \ln n \tag{2.12}$$

The total mixing entropy under the effects of four conditions, like configurational, vibrational, magnetic dipole, and electronic randomness. On the other hand, configurational entropy is the dominant one (Yeh, 2013). The calculation of configuration entropy for up to 13 elements according to the equation (2.12) in equimolar alloys is given in Table 2.3. It is clear that the configuration entropy rises above one after three elements and exceeds $1.61R$ after five elements. After the addition of eleven elements, the increase slowed down and became almost linear. The entropy classification based on these calculations is illustrated in Figure 2.8. The configuration entropy of five elements determined for high-entropy alloys was calculated at $1.61R$. Two elements and below are expressed as low-entropy alloys and the configuration entropy is $0.69R$. Finally, the configuration entropy of medium-entropy alloys was calculated between $0.69R$ and $1.61R$ (Yeh, 2013).

Table 2.3 : Calculation of configurational entropy for up to 13 elements in equimolar alloys, adapted from Yeh (2013).

n	1	2	3	4	5	6	7	8	9	10	11	12	13
ΔS_{mix}	0	0.69 *R*	1.1 *R*	1.39 *R*	1.61 *R*	1.79 *R*	1.95 *R*	2.08 *R*	2.2 *R*	2.3 *R*	2.4 *R*	2.49 *R*	2.57 *R*

Figure 2.13 graphically illustrates the data shown in Table 2.3. The relationship between the entropy of the mixing and the number of elements is given in the graph. In this way, the difference between high-entropy and medium-entropy alloys is clearly seen. The entropy stabilization seen here not only shows the formation of high-entropy phases, but also changes parameters that affect properties such as cocktail effect, sluggish diffusion, and valence electron distribution (Akrami et al, 2021).

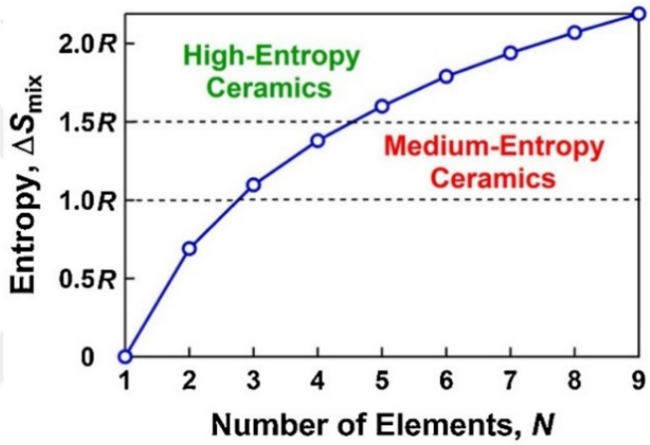

Figure 2.13 : The relationship between the entropy of the mixing and the number of elements (Akrami et al, 2021).

2.3.2 Sluggish diffusion effect

As it is clear, phase transformations and diffusion are very slow in high-entropy alloys compared with traditional alloys. These two factors have led to this conclusion. First of all, HEAs have different atoms in the structure. As a result of this, each atom has various neighbors. When an atom jumps to a low-energy point, it gets trapped and the energy required to move from that point to another point decreases and cannot be moved. Contrarily, when the atom moves to a high-energy state, the atom has a better chance of returning to its place. Both of these scenarios decreases the diffusion process (Tsai & Yeh, 2014; Yeh, 2013; Y. Zhang et al, 2014a).

Secondly, each element in high-entropy alloys has a different diffusion coefficient. Some elements have low diffusion coefficients, while others have high diffusion coefficients (Tsai & Yeh, 2014; Yeh, 2013). Elements with high melting points are less active and are very difficult to move into atomic spaces compared to other elements. In addition, elements must move together during phase transformations. Nucleation and growth of a new phase, reaching the desired composition, and moving all the elements together to the grain boundaries are difficult in cases with different kinetics. As a result, HEAs have a single-phase structure (Tsai & Yeh, 2014; Yeh, 2013; Y. Zhang et al, 2014b).

Tsai et al. (2013) investigated the activation energies of Cr, Fe, Mn, Co and Ni elements in different matrices and elemental states (Figure 2.14). Here, it is seen that the lowest diffusion coefficient is in high-entropy CoCrFeMnNi alloy. It also has the largest Q/T_m (activation energy normalized by melting point). The lowest value is seen in metals. This is direct evidence of the diffusion effect in HEAs. It is also seen that there is a relationship between the number of elements in the matrix and the diffusion rate. As the number of elements in the matrix increases, the diffusion rate slows down (K.-Y. Tsai et al, 2013).

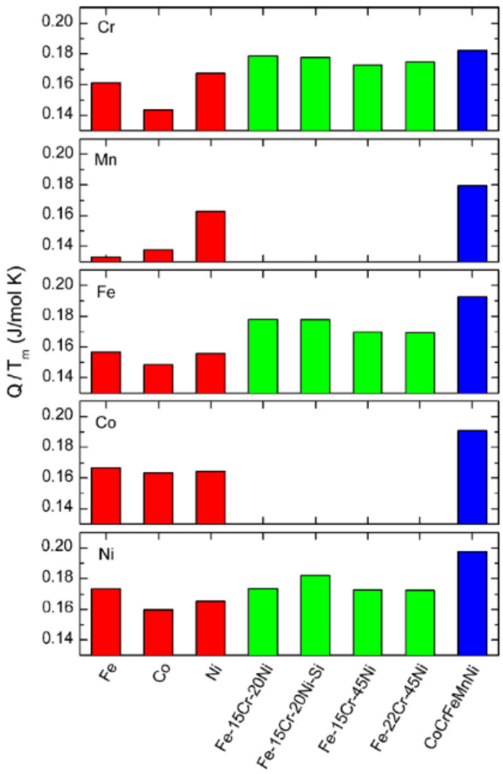

Figure 2.14 : Activation energies of Cr, Fe, Mn, Co and Ni elements in different matrices and elemental states (K.-Y. Tsai et al, 2013).

It is clearly understood that sluggish diffusion affects the phase nucleation, growth, distribution, and also microstructure is controlled by this effect (Murty et al, 2014).

2.3.3 Severe-lattice distortion effect

As mentioned before, HEAs contain more than one kind of atom, which causes the neighbors of each atom to be different from each other (Tsai & Yeh, 2014). There are also differences in size between atoms, which cause large lattice strain and lattice stress (Yeh, 2013). Figure 2.15a illustrates the severe-lattice distortion effect on the crystal structure. The lattice-distortion effect also varies according to the crystal structure. FCC alloys show less solution hardening than BCC alloys due to the fact that the FCC structure has 12 neighboring atoms while the BCC lattice has 8 neighboring atoms. The FCC lattice has a smaller fraction on the nearest neighboring atoms as opposed to different pairs, resulting in lower distortion stress and solution hardening (Murty et al, 2014). Figure 2.15b shows the effect of the lattice-distortion on the BCC structure. There are huge distortions in the crystal structure.

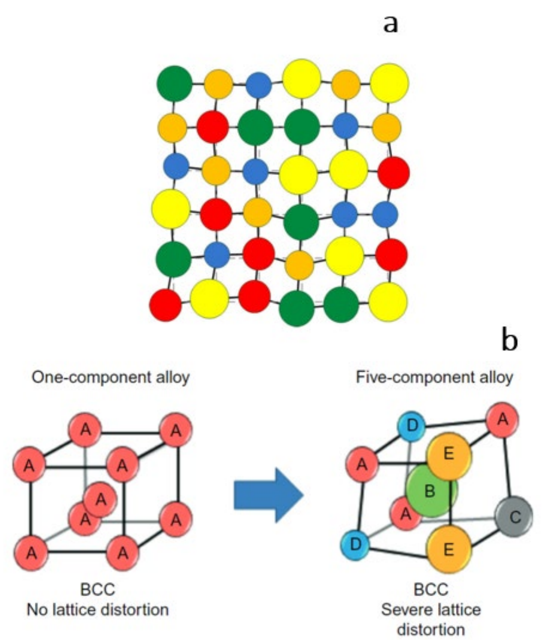

Figure 2.15 : (a) Lattice distortion effect on the crystal structure (Yeh, 2013), (b) lattice distortion of BCC structure (Murty et al, 2014).

Thermal properties are also affected by lattice distortion. Furthermore, there are unsymmetrical bonds between each atom and its neighbors. Besides, the electronic connections are not symmetrical either (Tsai & Yeh, 2014). As a result, electron scattering and electrical conductivity are reduced. As a result, the electron contribution to thermal conductivity and electrical conductivity decreases. In addition, phonon scattering becomes larger in the distorted lattice and decreases the thermal conductivity. Also, the thermal vibrations of atoms are quite small compared to lattice distortion. Therefore, the thermal conductivity coefficient is low in HEAs (Murty et al, 2014). As a result, it is thought that not only different binding energies but also crystal structure tendencies cause even higher lattice distortion (R. Wang et al, 2020; Yeh et al, 2007).

2.3.4 Cocktail effect

The "cocktail effect" was first named by Ranganathan (2003). All the characteristics of HEAs are related to the properties of the elements in the structure (Tsai & Yeh, 2014). Phase size, shape, distribution, phase boundaries and properties of each phase affect the composition. Each one is a multi-element solid-solution as well. It changes the properties of the HEAs under the influence of individual elements (Yeh, 2013; Yin et al, 2022). However, the interactions of the elements with each other also affect the properties and lattice structure. For example, aluminum (Al) is ductile and has a low melting point, yet in a high-entropy alloy, it can increase HEA's hardness (Yeh, 2013). As can be seen, the cocktail effect directly affects and/or changes the qualifications of the alloy and even its crystal structure (Ranganathan, 2003; Tsai & Yeh, 2014; Yeh, 2013; Y. Zhang et al, 2014b).

As a result, four core effects significantly affect the properties, crystal structures and microstructure of HEAs. Furthermore, as a result of these combined effects, the design, understanding and explanation of HEAs are now more clear. A summary representation of the core effects schematized by Kumar et al. (2022) is given in Figure 2.16.

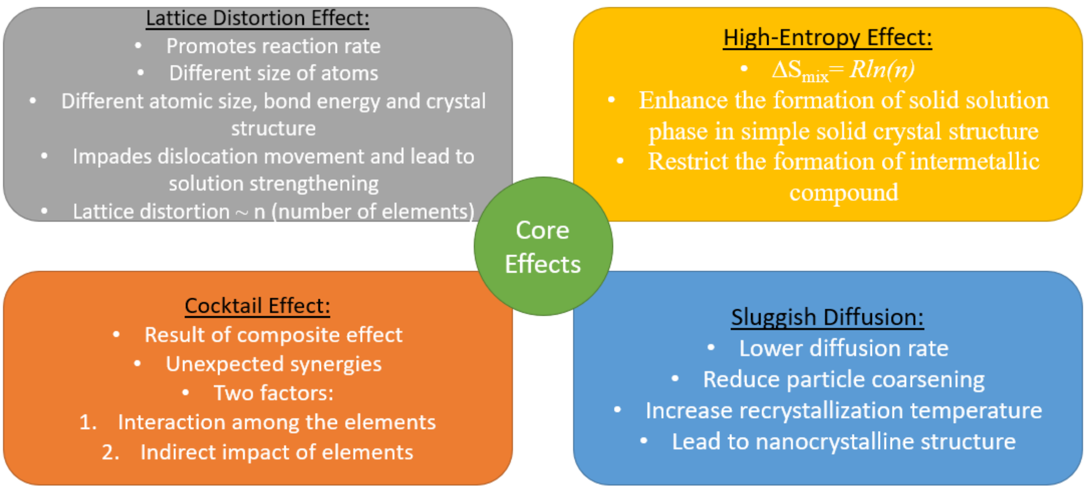

Figure 2.16 : Schematic representation of core effects, adapted from Kumar et al. (2022).

2.4 Properties of HEAs

Elements, fractions and phases of elements in the structure of high-entropy alloys directly affect their properties (Miracle & Senkov, 2017). High-entropy alloys have superior properties because they have four core effects and contain different elements. These are outstanding mechanical properties under extreme environment like high hardness and strength, good resistance to wear, exceptional fracture toughness and fatigue resistance (F. Li et al, 2022; R. Wang et al, 2020; Y. Yang et al, 2020); excellent thermal characteristics such as melting point and thermal stability (Cho et al, 2022; J. Li & Tsai, 2020; Y.Yang et al, 2020); perfect corrosion and oxidation resistance (Kumar et al, 2016; Senkov et al, 2013; Shuang et al, 2020; R. Wang et al, 2020); superior magnetic and electrical specialities (Tsai, 2013). The improvement of oxidative resistance is highly dependent on element selection. While elements such as Al, Ti, Cr improve oxidation resistance, metals such as V, Mo decrease the resistance (Senkov et al, 2018). Production and post-production methods, dislocation movements between atoms also change the properties (Kang et al, 2018). The process temperature also affects the mechanical properties (Senkov et al, 2018). In addition to all these, the presence of intermetallic phases such as Laves or the atomic sizes of the elements in the alloy also have an effect on the properties (Miracle & Senkov, 2017). Good mechanical properties are based on the severe-lattice distortion effect. The fact that there is more than one atom, and they are in different orders makes it difficult for the dislocations to glide, which causes high strength and hardness (Y.-C. Yang et al, 2020). Also, crystal structures affect the mechanical properties. BCC structures are more stronger than FCC structures because they have non-planar screw dislocations for shear. In addition, the electrical and thermal conductivity are significantly reduced due to scattering (electron and phonon) that occurs in the lattice distortion. As described before in the sluggish diffusion effect, high-entropy alloys are supersatured, high temperature strength and structural stability due to slow kinetics. As a result of this, this type of alloy has superior creep resistance (Tsai & Yeh, 2014; Yeh, 2013). Again, the slow diffusion effect explains the thermal stability at high temperatures. It has been explained in the previous sections that it is difficult for atoms of different weights and sizes to move together. This makes phase transformation difficult. In addition, the lattice structure, which deteriorates due to different atomic sizes, ensures that the lattice does not decompose at high temperatures (Tsai & Yeh, 2014; Yeh, 2013). The schematic representation of the effects of four core effects on the properties and microstructure of high-entropy alloys is given in Figure 2.17. From this, it is seen that the crystal structure and thermodynamic equilibria significantly affect the microstructure and properties of the alloys.

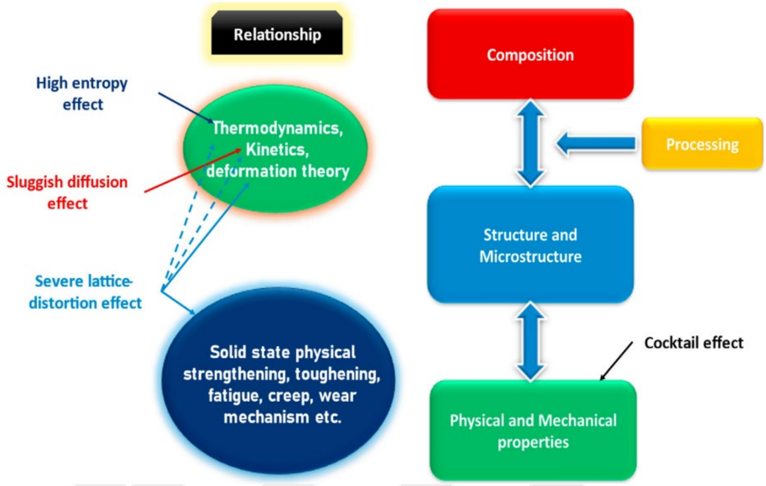

Figure 2.17 : Four core effects and connections between microstructure and properties (Kumar et al, 2022).

2.5 Application Areas and Production Methods of HEAs

High-entropy alloys are used in many fields and for various applications because of their superior features. With their high mechanical properties, like good fracture toughness and wear resistance, high cycle fatigue (Cantor, 2021; Miracle & Senkov, 2017; Tsai & Yeh, 2014), HEAs are used in aircraft components or aerospace, engine materials (Dai et al, 2016). Also, HEAs have superior thermal characteristics (Cho et al, 2022), so they are a potential candidate for thermal power generation, boiling pipes, tubes of heat exchangers and chemical plants (Gorsse et al, 2017; Kumar et al, 2022). It can also be preferred in marine applications due to its high corrosion, oxidation and wear resistance (Y. Liu et al, 2015; Shuang et al, 2020). Furthermore, HEAs are preferred for nuclear components and energy sectors due to their superior corrosion and irradiation resistance. In addition, refractory high-entropy alloys, like those used as thermal barrier coatings or cutting tools (R. Wang et al, 2020). Thanks to their outstanding physical properties, alloys such as these are excellent candidates for electronic and magnetic applications.

A wide variety of methods are preferred in the production of high-entropy alloys. These are solid-state production methods like powder metallurgy methods, especially mechanical alloying (MA), pressureless sintering, pressure sintering methods such as spark plasma sintering or hot pressing/hot isostatic pressing, liquid-state production methods like vacuum arc melting or self-propagating high-temperature synthesis (SHS) and gas-state production methods like sputtering (Cantor, 2021; Kumar et al, 2016). Also, induction furnaces, additive manufacturing and casting are the most common production methods (Kumar et al, 2022; Li et al, 2022). All methods have their own advantages and disadvantages. For example, in the MA process mostly need a second method for obtaining single-phase structure. Therefore, contamination can occur from the balls and/or vials during the process (Suryanarayana, 2022). In addition, intractable morphology is the main disadvantage of the vacuum arc melting method (Singh et al, 2011). The appropriate production method should be selected based on the composition.

2.6 High-Entropy Borides (HEBs)

A subgroup of ultra-high temperature ceramics (UHTC), transition metal borides have been used in many areas due to their outstanding properties, as mentioned before. Refractory borides like HfB_2, TiB_2 and ZrB_2, which are among the transition metal borides, draw attention because they have different application areas and much stronger properties. It has been tried to enhance the application fields and features with metal borides combined with traditional alloying. Metal borides combined with traditional alloying have been tried to improve application fields and features. The material's application fields have become even more diverse as technology has developed. For example, technological advances have resulted in the development of materials that are resistant to higher temperatures, and have higher mechanical strengths. As a result of this, both the need for improved properties and the need for new materials have increased. Based on this, “multicomponent alloys” have been proposed (Cantor et al, 2004). High-entropy alloys are one example of multicomponent systems. Single-phase HEAs have magnificent characteristics compared to traditional ones (Miracle & Senkov, 2017). Similarly, the development of HEAs continued and accordingly, high-entropy ceramic materials emerged. First of all, Chen et al. produced high-entropy nitride films in 2005. Then, in this content, Rost et al. synthesized high-entropy ($Mg_{0.2}Zn_{0.2}Co_{0.2}Cu_{0.2}Ni_{0.2}$) oxide in bulk form for the first time in 2015. So, high-entropy ceramics expanded to include oxides (Rost et al, 2015), carbides (Castle et al, 2018; Kavak et al, 2022a), borides (Gild et al, 2016; Mayrhofer et al, 2018), sulfides (C. Zhang et al, 2018), silicides (Gild et al, 2019a) and nitrides (Chen et al, 2004). Figure 2.9 shows the historical development of high-entropy alloys (Kumar et al, 2022). When it came to the 2016, a new term was defined by Gild and his team: high-entropy boride (HEB) ceramics. Especially, high-entropy metal diborides are identified as a new class of UHTCs.

In the formation of high-entropy alloys, ΔH_{mix} (enthalpy of mixing) and δ (atomic size difference), which are given in the calculations in equation (2.7) and equation (2.8), are shown as two basic criteria. On the other hand, enthalpy of mixing is not convenient equation for HEB ceramics (Gild et al, 2016). For this reason, equation (2.13) and equation (2.14) are defined by considering the relationship between Hume-Rothery solid-solution rules and atomic size differences. These equations are based on the calculation of the atomic size differences using the lattice constant differences of individual metal diborides (Gild et al, 2016; Wang et al, 2018).

$$\delta_a = \sqrt{\sum_{i=1}^{n} X_i \left[1 - a_i / \left(\sum_{i=1}^{n} X_i a_i\right)\right]^2} \tag{2.13}$$

$$\delta_c = \sqrt{\sum_{i=1}^{n} X_i \left[1 - c_i / \left(\sum_{i=1}^{n} X_i c_i\right)\right]^2} \tag{2.14}$$

In here, a_i and c_i represent the lattice parameters of the metal diborides (Gild et al, 2016; Wang et al, 2018). By calculating δ_a and δ_c values, information can be obtained about whether a single-phase or not single-phase structure will form. When the δ value gets smaller, solid-solution was generally obtained. On the other hand, this is not a certain method (Gild et al, 2016; D. Liu et al, 2020; Wang et al, 2018).

In contrast to HEAs, HEB ceramics have just an AlB_2 type (space group: *P6/mmm*) hexagonal close-packed structure (Barbarossa et al, 2021a; Chen et al, 2019; Gu et al, 2019; Mitra et a., 2022; Wang et al, 2018; X. Zhang et al, 2022). Metal diborides with hexagonal AlB_2 structure have a highly anisotropic layered (Feng et al, 2021; Liu et al, 2019; Monteverde et al, 2022; Wang et al, 2021; Y. Zhang, et al, 2021a). Each metal atom is surrounded by two electrons and metal-boron bonds, in addition, there are two-dimensional (2D) metal and boron layers. In consequence of ionic, covalent and metallic bonds are together and also do not explain atomic size differences. It is more correct to explain the difference between the lattice parameters given in equation (2.13) and equation (2.14) instead of the atomic size (Gild et al, 2016). Figure 2.18 depicts an AlB_2 type crystal structure.

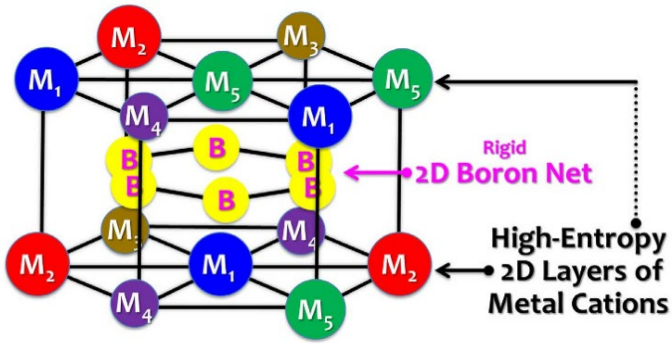

Figure 2.18 : Illustration of the crystal structure of the HEB ceramics (Gild et al, 2016).

2.7 Properties and Application Areas of HEBs

There are various studies about the synthesis of high-entropy boride ceramics. Many superior properties have been discovered with the HEB ceramics produced. HEBs have outstanding mechanical stabilities like very high hardness (~ 24 GPa), elastic modulus and wear resistance (Feng et al, 2021; Kirnbauer et al, 2020; Monteverde et al, 2022; Smith et al, 2022). Basically, it is thought that solid-solution hardening increases the hardness of materials. In addition, solid-solution occurs between four or more elements in the HEB ceramics (Feng et al, 2021). It is stated that high hardness is the result of this situation. Besides, they have good electrical conductivities at ambient pressure (Liu et al, 2020; X. Zhang et al, 2022). In the HEBs, there is stronger electron and phonon scattering compared with individual diborides due to the severe-lattice distortion effect and high-entropy effect, which are the two core effects. Under the influence of this, HEB ceramics have higher room-temperature resisitivities and lower temperature coefficients (X. Zhang et al, 2022). In addition to all these, it is seen that they have a very high melting point (Feltrin et al, 2021; Y. Gao et al, 2022; B. Ye et al, 2020). Moreover, they exhibit superior chemical stabilities (Feltrin et al, 2021; Ma et al, 2020). All these properties are affected by the four core effects, which are high-entropy, severe-lattice distortion, sluggish diffusion and cocktail, as explained in previous chapters. It is clear that the properties of HEB ceramics are greatly improved when compared with traditional binary boride alloys or individual transition metal borides.

HEB ceramics have begun to be preferred in many fields or extreme environmental conditions due to this combination of not only physical but also chemically outstanding properties. Ultra-high temperature insulation applications are one of the most common

(Chen et al, 2019). They are also preferred in the aerospace industry due to their high mechanical properties (Gu et al, 2019). Thanks to their good electrical conductivity, HEB ceramics are used in microelectronics (X. Zhang et al, 2022). They are also possible to be preferred in the production of both renewable energy sources, like the solar energy sector and non-renewable energy sources, such as nuclear reactors (Liu et al, 2019). Moreover, HEB ceramics can be used for cutting tools (Ma et al, 2020).

2.8 Production Methods of HEBs

Like high-entropy alloys, high-entropy boride ceramics have various production methods. First of all, it is aimed at hybridizing of HEB powders. For the hybridization, high-energy ball milling (HEBM) (Gild et al, 2016), borothermal reduction, boro/carbothermal reduction process (BCTR) (Smith et al, 2022), self-propagating high-temperature synthesis (SHS) (Gu et al, 2019) are the most common routes. After that, compaction and densification of hybridized powders are considered. For compaction and densification, spark plasma sintering (SPS) is the most preferred method. Pressureless sintering and hot pressing (or hot isostatic pressing) are alternatives to SPS (Akrami et al, 2021). On the other hand, during the synthesis of HEB ceramics, the raw materials contain differences. Some of the processes start with metal diborides (Gild et al, 2019b), the others use elemental powders and boron (Tallarita et al, 2020) as starting materials. Metal oxide raw materials and boron carbide (B_4C) are mostly preferred in the BCTR process (Gild et al, 2020). The synthesis method should also vary according to the raw materials (Barbarossa et al, 2021b).

Each production method has its own positive and negative characteristics. Taking place at room temperature is one of the biggest advantages of the HEBM process. On the contrary, the main disadvantages are the long milling time and the possibility of contamination in the resulting powders (Gild et al, 2016; Qin et al, 2020a). Another example about the BCTR process, it is mostly used for the cheap oxide raw materials; however, high temperatures (1600-1700 °C), remaining oxide raw materials and long times negatively affect the process (Gu et al, 2019; Y. Zhang et al, 2019b; Y. Zhang et al, 2021a). Another method is the SHS process, which takes place in a few minutes, yet it is important to select suitable compounds for exothermic initiation (Barbarossa et al, 2021a; Tallarita et al, 2020).

2.8.1 Boro/carbothermal reduction method (BCTR)

This process basically consists of two steps and a second step is needed to obtain high-entropy boride phases. Generally, starting materials, which are reactants and reducing agents, are mixed with the mechanical alloying process in the first stage. Then, it is heated to thousands of degrees. During the BCTR process, mostly boron carbide (B_4C) is used as a reducing agent due to the low price of starting materials, low processing temperature and lack of need for forming and sintering agents. With the reducing agent, metal oxides are also used as starting materials. In the theoretical reaction with the reactions of boron carbide and metal oxides, high-entropy boride compounds, boron oxide (B_2O_3) and carbon monoxide (CO) gases are formed as products. Since high volumes of carbon monoxide and boron oxide gases are formed during the reaction, HEB in a porous structure is formed (Akrami, 2021).

2.8.2 Self-propagating high-temperature synthesis (SHS)

In the SHS process, the reaction starts with the heat given to the mixture. Then, the product emerges with the heat released as a result of the exothermic reaction. In the SHS method, the reactions proceed spontaneously without the need for any energy other than the initial heat given in the amount that will bring the mixture to the ignition temperature. The heat released as a result of the reaction in the first layer passes to the unreacted mixture layer, and provides the first heat for the ignition of that area. The most important advantages of the process are that the reaction takes place very quickly and progresses by itself, it can be applied easily, it does not need high energy, it offers the opportunity to work with low-cost raw materials, and it provides the opportunity to obtain products in different shapes and sizes. The high thermal energy released as a result of the process increases the reaction rate and provides fast, economical and efficient production (Munir & Tamburini, 1989).

2.8.3 Mechanical alloying (MA)

Mechanical alloying is a powder metallurgy production method in which powders can also be synthesized, consisting of repeated cold welding, fracturing and re-welding processes in a high-energy ball mill (Suryanarayana, 2001). During the MA process, powders were mixed homogenously in milling media like balls and vials. MA was first defined in the 1960s at the International Nickel Company's (INCO) Paul D. Merica Research laboratories to disperse oxides that do not disperse in the liquid phase in nickel-based superalloys in the solid phase (Benjamin & Volin, 1974). Although the production from the liquid phase is cheap, homogeneous alloys can be obtained as a result of the production carried out in the solid phase (Lü & Lai, 1998; Suryanarayana et al, 2001).

In the mechanical alloying process, plastic deformation occurs with the applied force of the powder particles and the particles break as a result of the deformation hardening (Gutman, 1998; Levitas, 2003). Many collisions occur between the ball, powder and the walls of the containers. As a result of these collisions, mechanical stress occurs (Suryanarayana, 2001). The interaction of the powders with the ball is shown schematically in Figure 2.19.

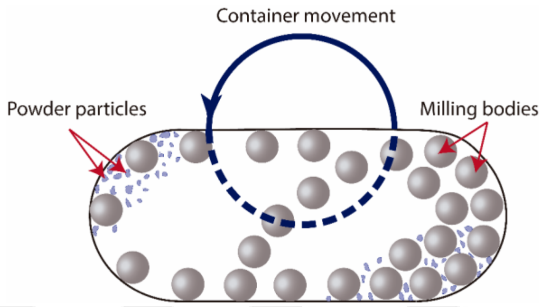

Figure 2.19 : Schematic representation of relationship between balls and powders (Rios et al, 2001).

The powders are cold worked, welded and fragmented repeatedly, thus achieving a homogeneous distribution. (Delogu & Mulas, 2010; Gilman & Benjamin, 1983). New metal surface layers emerge with the broken particles. During continued deformation, after a while, fracture becomes more dominant than cold welding. Re-welding occurs with the formation of new surfaces (Suryanarayana, 2001). Plastic deformation occurs at high rates in the powder particles, while the particle size is expected to decrease. The mechanical energy generated is mostly converted into heat, and some of it is stored in the material (Rigney & Hammerberg, 1999; Kim et al, 2007). As a result, the equilibrium is disturbed and chemical reactivity increases.

Examples of potential materials that can be mechanically alloyed are pure metals, nanostructured materials, sensors, catalysts, superalloys, carbides, nitrides, silicides etc. (Suryanarayana et al, 2001). In recent years, high-entropy alloys have also been produced by MA. During the MA, process parameters, which are the type of mill, milling vials, milling energy/speed, milling time, size distribution of balls, ball-to-powder weight ratio, extent of vial filling, milling atmosphere and process control agent, affect not only the final product but also the properties of the final product (Suryanarayana, 2022).

2.8.3.1 Types of mill

Different types of millers are used for the mechanical alloying of powders. They differ in their efficiency, capacity, speed of operation and functions for controlling the milling temperature and contamination of powders (Baláž et al, 2008). Choosing a suitable miller affects the final product and the quality of the final product (Suryanarayana, 2022).

SPEX-type millers are the most widely used milling type. Approximately 10-15 g of powders are mechanically alloyed. One or two vials are placed in the miller. Powder and/or balls are placed inside the containers. With the shaking action, the containers start to rotate at a specific rpm (almost 1200 rpm). During rotation, the powders hit both the balls and the vials, so they are mixed and milled. Due to the speed of 1200 rpm, the collision energy of the balls is quite high. Therefore, SPEX-type milling is defined as high-energy ball milling (Suryanarayana, 2001). Planetary ball mills are also equipment used for MA processes. They have the capacity to mill several hundred grams of powder at one time. However, when compared to SPEX type millers, they are called low energy ones (Suryanarayana, 2001). In a planetary ball mill, the vials rotate around their own axis. Since the disc rotates in a different direction, the balls collide with the effect of the centrifugal force (El-Eskandarany, 2015). The schematic representation of the planetary ball milling movements is given in Figure 2.20.

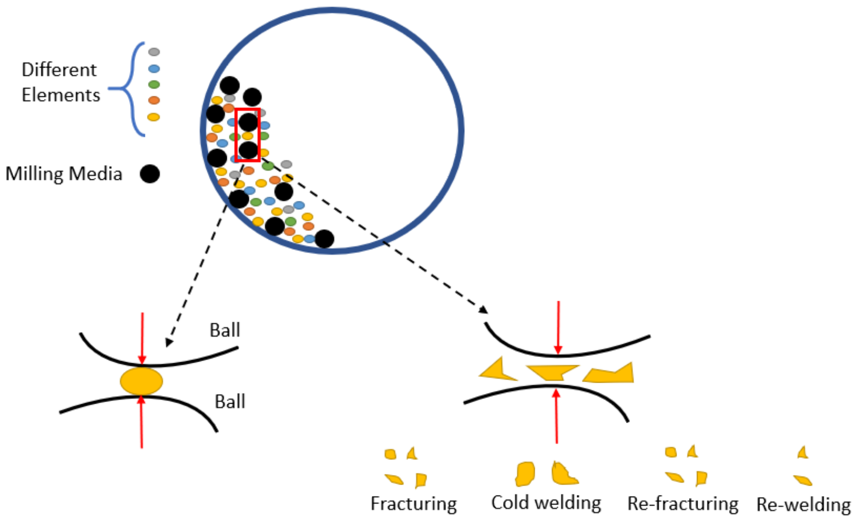

Figure 2.20 : Movement mechanism of planetary ball milling, adapted from Kumar et al. (2022).

An attritor-type miller has a vertical shaft and arms radiating from it. The cylindrical milling media is located in the shaft (Soni, 2001). When the shaft rotates, the arms strike the milling balls and energize them. In this way, the powder size is reduced due to impact between the balls, between the balls and the vial wall, and between the balls, the mixer shaft and the arms. It has a speed of about 250 rpm. Therefore, it has lower efficiency than SPEX-type milling or planetary ball milling. It is possible to mill up to 40 kilograms of powder at one time (Suryanarayana, 2001). The attritor-type miller is shown schematically in Figure 2.21.

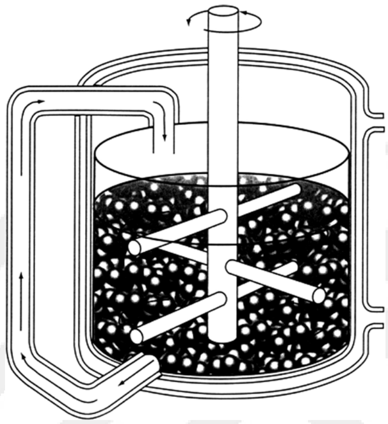

Figure 2.21 : The attritor type miller (Baláž et al, 2008).

2.8.3.2 Material of milling media

The milling media consist of the milling vials and balls. The balls and vials used vary according to the starting materials. Incorrect material selection can cause contamination or impurities, which affect the final product. Therefore, starting raw materials and milling materials should be as similar as possible. Different kinds of steels (hardened, stainless steel, tempered, etc.), alumina, tungsten carbide, zirconia, stainless steel, plastic can be used as milling containers. Incorrect material selection can also result in wear or damage (Suryanarayana, 2001). In addition to the containers, the choice of balls is also very important. The balls and vials must be the same. In addition, the size and density of the balls also have a significant impact on the final product. The density of them is higher than the material to be milled (Baláž et al, 2008).

2.8.3.3 Milling speed and temperature

The milling speed is one of the most important parameters in the MA process, but the maximum milling speed depends on the design of the miller (Suryanarayana, 2022). The required force cannot be applied to the powders above a critical speed. If the speed of the process is low, alloying cannot occur or be completed, and homogeneity does not obtain (Suryanarayana, 2001).

As the speed increases, the temperature increases; however, the increase in temperature is moderate (Baláž et al, 2013). The changing temperature allows different phases to form. There are two types of temperatures in the MA process. These are the temperatures between the balls when they collide, as well as the overall temperature of the vial. In addition, powders have different temperatures. The powder one affects the diffusion, powder concentration and thus the phase transformations (Baláž et al, 2008, 2013; Suryanarayana, 2022).

2.8.3.4 Milling time and atmosphere

Milling duration is one of the most important parameters in the MA process. It directly affects the final product. Insufficient time causes the homogenity to be incomplete and the desired phases not to be formed. On the other hand, the long milling time increases the contamination, and causes the formation of undesirable phases (Baláž et al, 2008; Suryanarayana, 2001, 2022). In general, particle size decreases as milling time increases (Ağaoğulları et al, 2012a), as it can be seen from Figure 2.22.

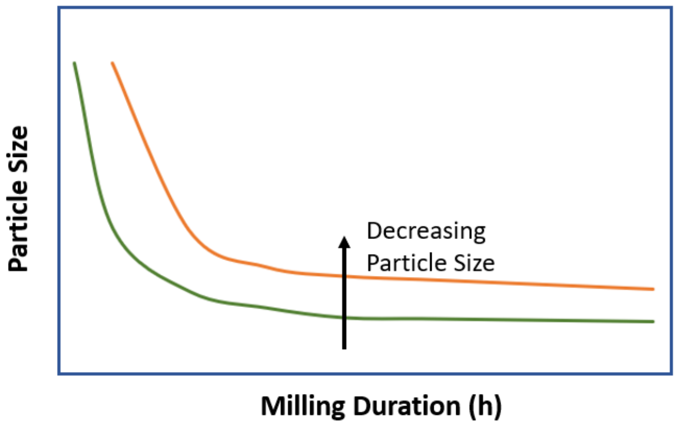

Figure 2.22 : Relationship between milling duration and particle size, adapted from Suryanarayana (2001).

During mechanical alloying, the powders get finer, and accordingly, the surface of the powders expands. Powders become open to reacting with various gases, especially oxygen. Therefore, this process should be completed in an oxygen-free atmosphere when placing the powders in the vials. Although different atmospheres are used, the most commonly preferred milling atmosphere is inert gas such as argon (Suryanarayana, 2001).

2.8.3.5 Ball-to-powder weight ratio (BPR) and extent of filling the vial

The ball-to-powder weight ratio is a critical parameter for the mechanical alloying process. When the BPR is low, the collision frequency decreases; in the contrary situation, when the BPR is high, the movement of the particles is restricted and amorphization begins (Soni, 2001; Suryanarayana, 2001). In the Spex Mixer/Miller, BPR is typically selected at a 10:1 ratio (Suryanarayana, 2001).

The impact force applied to the powder particles ensures that the mechanical alloying is completed. If there is not enough space in the containers, the balls and powders cannot move freely and collisions cannot occur. Therefore, the vials should not be overfilled; a sufficient amount of space should be optimized (Suryanarayana, 2001).

2.8.3.6 Process control agents

The fact that at least one of the starting materials used during mechanical alloying is ductile which prevents the powders from being damaged by extreme cold welding. Cold welding is excessive in brittle-brittle systems, and it is attempted to be kept to a minimum by the addition of a process control agent (PCA). The process control agent acts as a lubricant and reduces cold welding (Chen & Chen, 2012). There are many PCAs, but stearic acid, oxalic acid and hexane are the most preferred. It is usually added in amounts ranging from 1 % to 5 %. Much or little few added PCA directly affects the alloy and the final product, so the amount of PCA must be optimized. In addition, PCA suitable for the powder mixtures used should be selected (Balaz, 2008; Suryanarayana, 2001).

One of the main disadvantages is powder contamination during the MA process. This contamination can come from balls, vials and milling atmospheres. Many precautions can be taken to prevent contamination. The milling media should be harder than the starting powders. The milling atmosphere must be suitable to prevent the powders from reacting with oxygen and becoming contaminated. Choosing the right process parameters is important to prevent contamination (Suryanarayana, 2001, 2022; Suryanarayana et al, 2001).

2.8.4 Hot-pressing

Hot pressing is based on the simultaneous application of uniaxial pressure (typically 20–50 MPa) and heat to powder mixtures to obtain dense bodies. Powder materials are heated to high temperatures (up to ~2500 °C) with sufficient residence times. The powder to be condensed is filled into the appropriate mold (usually graphite or the material that can withstand high temperatures and pressures without reacting with powders) and pressure is applied to the powder using punches. Heating coils are used to heat the mold. The graphite mold is enclosed in a protective atmosphere or vacuum chamber to prevent damage to the used mold. Loading is done along the vertical axis in punches pressurized from an external hydraulic system. Although the pressure is applied along the vertical axis, there is a radial pressure against the die wall. The differential stress between the axial and radial directions creates the shear stress effective in particle bonding. This shear stress is the applied stress. Initial densification involves particle rearrangement and plastic flow, and as densification progresses, grain boundary diffusion and volume diffusion and creep become controlled. The simultaneous application of high pressure and temperature causes the particles to rearrange and allows plastic deformation at the contact points and finally eliminates porosity, resulting in compact structures (German, 2014).

2.8.5 Spark plasma sintering (SPS)

The condensation of traditional or advanced ceramics, composite materials, biomaterials or wear-resistant materials by homogeneous densification is called spark plasma sintering (SPS) (Tokita, 2013). Especially in the ceramic industry, production with the SPS method has become quite common in recent years. The short duration of the process and its energy efficiency play an important and a major role in its widespread use (Kardashova, 2020; Munir et al, 2006). Production with a technique similar to SPS was first carried out in Germany in 1910. Sintering was achieved by applying electrical energy to the powder materials (Tokita, 2013). Later, in 1933 G.F. Tayler received a patent for the first resistive sintering method, followed by G.D. Cremer, who received a patent for the sintering of different metals and alloys. The known SPS technique was developed by Dr. Japax in Japan in 1962. It was discovered by Kiyoshi Inoue. Dr. Inoue called this system "spark sintering". The SPS we use today was introduced in Japan in 1989 by the Sumitomo Coal Mining Company. Until today, different SPS devices with different technologies that were suitable for mass production have been produced. A fifth generation advanced SPS was developed after the 2010s (Tokita, 2013).

The basic illustration of SPS is given in Figure 2.23. Basically, a SPS system consists of uniaxial pres, graphite punches, electrodes, a vacuum and water cooling chamber, a DC pulse generator, a control unit which belongs to vacuum/gas/air atmosphere, position, temperature and pressure regulating systems with software (Matizamhuka, 2016).

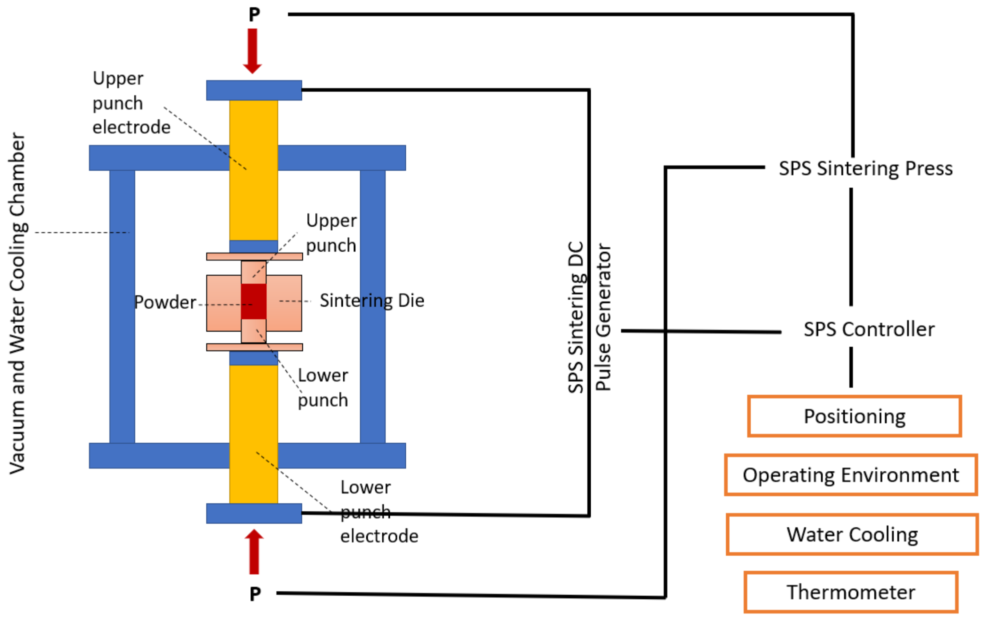

Figure 2.23 : Basic illustration of SPS system, adapted from Chen et al. (2005).

The powder placed in the sintering die is fixed by the upper and lower punches. The sintering process is completed with direct current. Direct current is applied simultaneously to the both die and sample. Figure 2.24 shows how the pulse current circulates through the powder particles in the SPS sintering die. In this way, the mold acts as a heating resistor. The current sent through the sample causes rapid condensation. In this system, four factors contribute to rapid condensation: fast heat transfer, applied pressure, high heating/cooling rates, and the use of pulsed direct current; thus, exposure of the sample to direct current (Suárez et al, 2013). In this way, short circuits, arcs and plasmas are formed between the powder grains. Thanks to these driving forces, sintering takes place and then the system is cooled with the help of water. The control panels form the connection between the SPS system and the computer give instantaneous values of current, voltage, temperature, pressure, displacement, vacuum and various cooling water temperatures (Dobodoe et al, 2013).

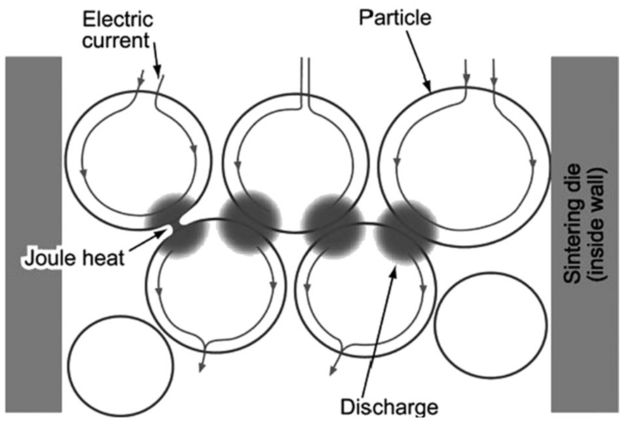

Figure 2.24 : Pulsed current flow between particles (Suárez et al, 2013).

There are various parameters in the SPS process, like the heating rate, maximum temperature, cooling rate, load application rate, maximum hold load and load removal rate. Certain operating conditions are required for the SPS system to work. For electrical conditions, low voltage (10 V) and high currents (1-10 kA) are generally preferred. The experiments were done up to 2400 °C with the graphite tools. In addition, the heating rate can be 1000 °C/min, so the process completes in a short time. The cooling rates change from 150 °C/min up to 400 °C/min (Guillon et al, 2014). The temperatures can be measured with pyrometer or thermocouple. A pyrometer is a remote sensing thermometer that measures the temperature of distant objects by calculating the surface temperature from the amount of thermal radiation emitted. On the other hand, it is generally not used below 600 °C. Operating temperature range, spot size, focus distance, emissivity of the sample and response time are the characteristics of the pyrometer. A thermocouple is an electrical junction formed by two different electrical conductors that generates a temperature-dependent voltage and is used to measure temperature. When using a thermocouple, it should be protected from conductive and reactive materials (Guillon et al, 2014; Tokito, 2013). The pressure is applied between 50-250 kN (Guillon et al, 2014). In the SPS process, the powders are condensed under pressure and temperature in the currently-passed system. While pressure is applied to the powders placed in the mold, DC current passes and the temperature increases. During sintering with SPS, three important points stand out: a high heating rate, the applied pressure and the current effect (Munir et al, 2006).

SPS includes mechanical, electrical and thermal effects (Guillon et al, 2014). The mechanical effect is due only to the applied uniaxial pressure. Mostly graphite molds are used in the SPS system because of their ease of machinability, low cost and resistance to high temperatures in the inert atmosphere. However, the yield strength of graphite at high temperatures limits the mechanical stress. More expensive and better creep resistance, high fracture toughness and electrical conductivity molds (like Si_3N_4 or WC) can be used instead of graphite ones (Matizamhuka, 2016). The thermal effect is of high importance throughout the entire process. Grain growth under pressure cannot be completely prevented. At high temperatures, densification mechanisms occur together with the creep mechanism. In addition, microstructure coarsening is prevented by rapid cooling/heating. The process reaches the sintering temperature in a short time (Matizamhuka, 2016). ON-OFF DC pulse mechanism creates electrical effects like spark plasma generation, spark pulse pressure, joule heating and the electric field diffusion effect. In the SPS process, the surfaces of the powder particles become active more easily than in traditional sintering processes that do not use pulsed direct current. It is possible to obtain materials with dense structures at low temperatures and in short times, as material transport at micro and macro levels is facilitated. When the pulsed current starts to discharge, the temperature rises suddenly, and thus evaporation and melting begin on the surface of the powder particles. This provides necking between particles. In the SPS system, the surfaces of the particles are activated more easily, and the material transfer becomes easier compared to traditional alloys. Thus, time is getting shorter (Guillon et al, 2014; Tokita, 2013). The basic mechanism of neck formation is shown in Figure 2.25.

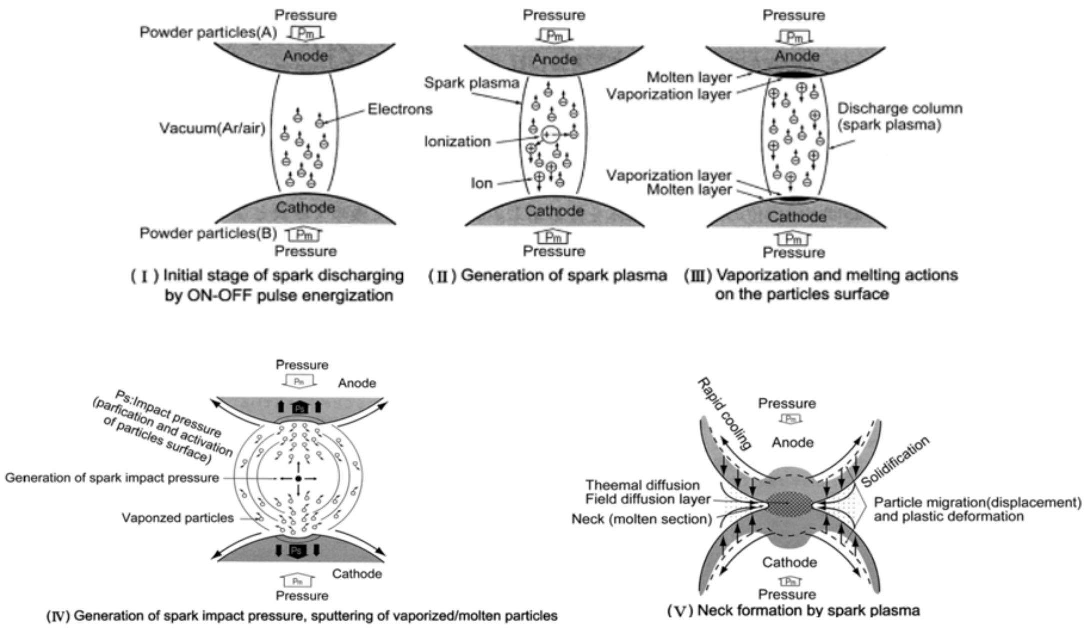

Figure 2.25 : The basic mechanism of neck formation by SPS (Tokita, 2013).

Figure 2.26 represents the four stages of SPS. During the first stage, gases are removed, and a vacuum is created. At the second stage, the pressure increases. It is followed by resistance heating as the third stage. In this duration, the sample is heated by increasing the intensity of the pulsed current applied to the graphite molds. After the device warms up, the temperature continues to increase at a certain rate. When the temperature approaches the desired final value, the heating rate is reduced to prevent this value from being exceeded. Once the sintering temperature is reached, the temperature is held constant for several minutes. The last stage is cooling step. The current is turned off, the pressure is stopped and the samples are allowed to cool under vacuum in the die (Cavaliere, 2019).

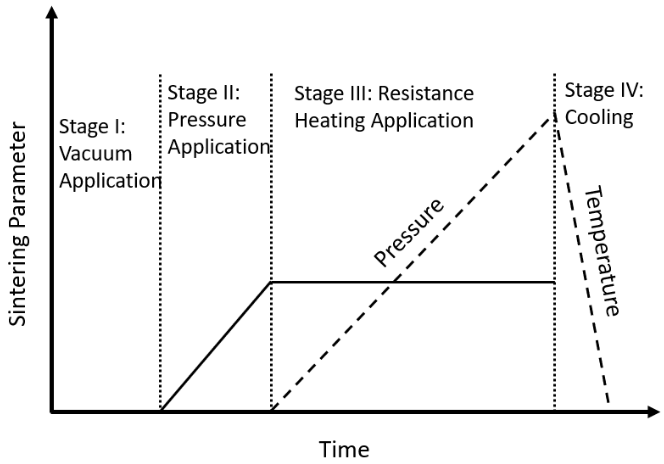

Figure 2.26 : SPS stages, adapted from Cavaliere (2019).

2.9 Literature Review on HEBs

After the discovery of high-entropy boride ceramics, many studies have been published until today. Figure 2.27 shows the graph of the studies published on HEBs. These data are taken from the "Web of Science" database. The term "high-entropy boride" was used in the search to obtain the data.

Gild et al. brought the first publication (2016) to the literature on the production of high-entropy metal diborides. In this publication, equimolar and five-component metal boride ceramics were synthesized using high-energy ball milling and spark plasma sintering methods. Starting powders were mechanically alloyed for 6 h using WC vials and balls in a high-energy ball mill, and green bodies were subjected to cold pressing, and spark plasma sintering (under vacuum, 2000 °C, 5 min, 30 MPa, 100 °C/min heating rate, graphite mold) was applied. High-entropy boride ceramics with single-phase hexagonal structure were obtained after spark plasma sintering, as well as very small amounts of (Zr, Hf)O or $(Ti_{1.6}W_{2.4})B_4$ compounds were detected. It has been reported that sinter bodies have relative density values higher than 92 %. As a result of Vickers hardness measurements (200 kgf/mm^2, 15 sec) made on the sintered bodies, values in the range of 17.5-24 GPa were obtained, and it was found that the hardness values of HEBs were higher than the hardness values of single boride samples.

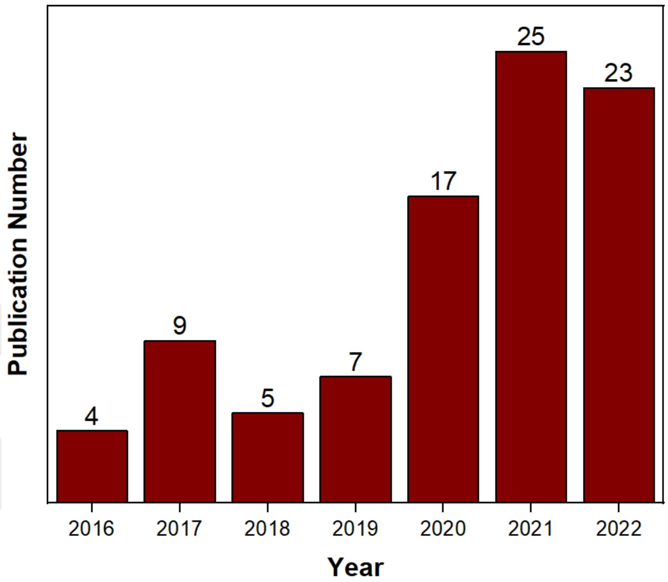

Figure 2.27 : HEB studies published from 2016 to 2022 (Url-7).

Wang et al. (2018) conducted simulation studies to predict the mechanical and electrical properties of $(Hf_{0.2}Zr_{0.2}Ta_{0.2}M_{0.2}Ti_{0.2})B_2$ (M=Nb, Mo, Cr) high-entropy metal borides. As a result of modeling the Vickers hardness values of these materials, it was emphasized that the hardness values of all of them varied in the range of 30-38 GPa, and they should be called superhard materials. $(Hf_{0.2}Zr_{0.2}Ta_{0.2}Nb_{0.2}Ti_{0.2})B_2$ also stated that the interatomic interaction of high-entropy boride is stronger and its electrical conductivity is higher than ceramics with Mo and Cr content.

Zhang et al. (2019) synthesized $(Hf_{0.2}Zr_{0.2}Ta_{0.2}Cr_{0.2}Ti_{0.2})B_2$, $(Hf_{0.2}Zr_{0.2}Mo_{0.2}Nb_{0.2}Ti_{0.2})B_2$ and $(Hf_{0.2}Mo_{0.2}Ta_{0.2}Nb_{0.2}Ti_{0.2})B_2$ high-entropy ceramics as a result of the sintering process with SPS following the borocarbothermal reduction method at 1600 °C. Metal oxides reacted with boron as starting material, and metal diboride synthesis was completed. The relative density values were found between 95 % and 99.2 %. The hardness values measured with $HV_{0.2}$ were calculated as 25.9 ± 1.1 GPa and 28.3 ± 1.6 GPa.

Mayrhofer et al. (2018), single-phase high-entropy $(Zr_{0.23}V_{0.14}Ta_{0.24}Hf_{0.19}Ti_{0.2})B_2$ ceramics onto austenitic stainless steel substrates by magnetron sputtering method (Ar atmosphere, 0.4 MPa, 450 °C) using ZrB_2, TiB_2, HfB_2, TaB_2, VB_2 microplates (99.5 % purity). Boride coatings were deposited and annealed in vacuum at the temperature range of 1100-1500 °C for 10 min. $(Zr_{0.23}V_{0.14}Ta_{0.24}Hf_{0.19}Ti_{0.2})B_2$ high-entropy metal boride coatings were found to have 47 GPa hardness and 540 GPa elastic modulus values.

Tallarita et al. (2020) obtained $(Hf_{0.2}Mo_{0.2}Ta_{0.2}Nb_{0.2}Ti_{0.2})B_2$ high-entropy metal boride ceramics as a result of a two-stage production process. In the first stage, self-propagating high-temperature synthesis (SHS) method (stainless steel cell, Ar atmosphere, W wire) was applied. After short-term milling was applied to the SHS product and the product was pulverized, densified bodies were obtained by using the spark plasma sintering method (1950 °C, 20 min, vacuum, 20 MPa). A very small amount of $(Ta_{0.5}Ti_{0.5})B_2$, $(Hf_{0.5}Ti_{0.5})B_2$, HfB_2 and HfO_2 phases were also detected in the SHS product. It was stated that the HfO_2 phase disappeared after sintering, and the sintered body had a relative density of 92.5 % and a hardness of 23 GPa. It has been emphasized that the single metal borides produced by the same method have an average hardness value of 19 GPa, and $(Hf_{0.2}Mo_{0.2}Ta_{0.2}Nb_{0.2}Ti_{0.2})B_2$ high-entropy metal boride has a significant improvement in its hardness value.

In their study, Qin et al. (2020b) synthesized six different high-entropy boride compounds by spark plasma sintering followed by high-energy ball milling. They found low intensity oxide phases and $(W_x, M_{1-x})B$ phase together with high-entropy boride peaks. They found the hardness values measured at 200 gf and 15 seconds of holding time between 27.5 ± 1.1 and 20.9 ± 1.1 GPa. Finally, they found that high-entropy metal borides containing WB_2 and MoB_2 had unexpectedly higher hardness values.

As can be seen, there are many studies with different production methods for the production and characterization of high-entropy metal borides. In Table 2.4, shows he recent studies reported on HEB ceramics producing by SPS. Here, the method used before SPS, starting raw materials, composition and SPS conditions differ from each other. These differences affect the hardness or relative density values or the phases seen as a result of XRD. In addition, when the literature studies were examined, no study was found with a composition of six or more.

Table 2.4 : Recent studies reported on HEB ceramics produced by SPS.

Composition	Raw Materials	Method & Conditions	SPS Conditions	References
$(Hf_{0.2}Zr_{0.2}Ta_{0.2}Nb_{0.2}Ti_{0.2})B_2$ $(Hf_{0.2}Zr_{0.2}Ta_{0.2}Mo_{0.2}Ti_{0.2})B_2$ $(Hf_{0.2}Zr_{0.2}Mo_{0.2}Nb_{0.2}Ti_{0.2})B_2$ $(Hf_{0.2}Mo_{0.2}Ta_{0.2}Nb_{0.2}Ti_{0.2})B_2$ $(Mo_{0.2}Zr_{0.2}Ta_{0.2}Nb_{0.2}Ti_{0.2})B_2$ $(Hf_{0.2}Zr_{0.2}W_{0.2}Mo_{0.2}Ti_{0.2})B_2$ $(Hf_{0.2}Zr_{0.2}Ta_{0.2}Cr_{0.2}Ti_{0.2})B_2$	Individual Metal Borides	HEBM and SPS	2000°C, 30 MPa	Gild et al. (2016)
$(Hf_{0.2}Zr_{0.2}Ta_{0.2}Cr_{0.2}Ti_{0.2})B_2$ $(Hf_{0.2}Zr_{0.2}Mo_{0.2}Nb_{0.2}Ti_{0.2})B_2$ $(Hf_{0.2}Mo_{0.2}Ta_{0.2}Nb_{0.2}Ti_{0.2})B_2$	Metal oxides and B	Borothermal reduction and SPS	2000°C, 30 MPa	Y. Zhang et al. (2019a)
$(Hf_{0.2}Zr_{0.2}Ta_{0.2}Nb_{0.2}Ti_{0.2})B_2$ $(Hf_{0.2}Zr_{0.2}Mo_{0.2}Nb_{0.2}Ti_{0.2})B_2$ $(Hf_{0.2}Mo_{0.2}Ta_{0.2}Nb_{0.2}Ti_{0.2})B_2$	Metal oxides, B_4C, graphite	Borocarbothermal reduction and SPS	2000°C, 30 MPa	Y. Zhang et al. (2019b)
$(Hf_{0.2}Zr_{0.2}Ta_{0.2}Nb_{0.2}Ti_{0.2})B_2$ $(Hf_{0.2}Zr_{0.2}Mo_{0.2}W_{0.2}Ti_{0.2})B_2$	Metal oxides and B	Borothermal reduction and SPS	2000°C, 30 MPa	Y. Zhang et al. (2020)
$(Hf_{0.2}Zr_{0.2}Ta_{0.2}Cr_{0.2}Ti_{0.2})B_2$	Metal oxides, B_4C, C	Borothermal reduction and SPS	2000°C, 30 MPa	Y. Zhang et al. (2021a)
$(Hf_{0.2}Zr_{0.2}Ta_{0.2}Nb_{0.2}Ti_{0.2})B_2$	Individual metal borides, graphite	HEBM and SPS	2200°C, 80 MPa	Qin et al. (2020a)

Table 2.4 (continued) : Recent studies reported on HEB ceramics produced by SPS,

Composition	Raw Materials	Method & Conditions	SPS Conditions	References
$(Hf_{0.2}Zr_{0.2}Ta_{0.2}Nb_{0.2}Ti_{0.2}) B_2$ $(Hf_{0.2}Zr_{0.2}Ta_{0.2}Mo_{0.2}Ti_{0.2}) B_2$ $(Hf_{0.225}Zr_{0.225}Mo_{0.225}W_{0.225}Ta_{0.225}) B_2$ $(Ti_{0.2}Ta_{0.2}Cr_{0.2}Mo_{0.2}W_{0.2}) B_2$ $(Mo_{0.2}Zr_{0.2}Ta_{0.2}Nb_{0.2}Ti_{0.2}) B_2$ $(Hf_{0.2}Zr_{0.2}W_{0.2}Mo_{0.2}Ti_{0.2}) B_2$	Metal Powders and B	HEBM and SPS	2000°C, 50 MPa	Qin et al. (2020b)
$(Hf_{0.25}Zr_{0.25}Ta_{0.25}Sc_{0.25}) B_2$	Metal oxides and B_4C	Borocarbothermal reduction and SPS	2000°C, 50 MPa	Z. Zhang et al. (2022)
$(Hf_{0.2}Zr_{0.2}Ta_{0.2}V_{0.2}Nb_{0.2}) B_2$	Metal oxides, B_4C and C	HEBM, Borocarbothermal reduction and SPS	1700°C-1800°C, 30 MPa	Y. Yang et al. (2022)
$(Hf_{0.2}Zr_{0.2}Ti_{0.2}Nb_{0.2}Ta_{0.2}) B_2$ $(Hf_{0.2}Zr_{0.2}Ti_{0.2}Ta_{0.2}Mo_{0.2}) B_2$ $(Hf_{0.2}Zr_{0.2}Ti_{0.2}Ta_{0.2}Cr_{0.2}) B_2$ $(Hf_{0.2}Zr_{0.2}Ti_{0.2}W_{0.2}Mo_{0.2}) B_2$	Metal oxides, B_4C and C	Borocarbothermal reduction and SPS	2000°C, 30-80 MPa	Gild et al. (2020)
$(Hf_{0.25}Ti_{0.25}W_{0.25}Zr_{0.25}) B_2$	Metal oxides, B_2O_3, Mg	HEBM, SPS	1800°C-1900°C-2000°C-2050°C, 30 MPa	Kavak et al. (2022b)
$(Hf_{0.2}Mo_{0.2}Ta_{0.2}Nb_{0.2}Ti_{0.2}) B_2$	Metal powders, B	SHS, HEBM and SPS	1950°C, 20 MPa	Tallarita et al. (2020)
$(Hf_{0.2}Nb_{0.2}Ta_{0.2}Ti_{0.2}Zr_{0.2}) B_2$	Metal oxides, B_4C	Borocarbothermal reduction and SPS	1650°C-10 MPa, 2000°C-30 MPa	Qiao et al. (2022)

3. EXPERIMENTAL PROCEDURE

In this study, high-entropy diboride ceramics were synthesized via high-energy ball milling (HEBM) assisted spark plasma sintering (SPS). First of all, each metal boride was synthesized by mechanochemical synthesis (MCS) which is a solid-state synthesis method and purified by HCl leaching. After that, these pure boride powders were hybridized. Detailed characterization studies of both powder samples and sintered bodies were carried out.

3.1 Synthesis of Metal Borides

In this study, HfB_2, TiB_2, ZrB_2, TaB, Mo-B, W-B, Cr-B and Mn-B borides were synthesized by leaching following the mechanochemical synthesis method at room temperature. For these synthesis, related metal oxides (HfO_2, ZrO_2, TiO_2, Ta_2O_5, MoO_3, WO_3, Cr_2O_3, MnO_2; Alfa Aesar^{TM}, in purity > 99 %, particle size < 45 µm), native boron oxide (B_2O_3, ETI Mine, in purity > 98 %, particle size < 470 µm) and magnesium (Mg, MME, in purity > 99 %, particle size < 145 µm) as a reducing agent were used. The theoretical reactions used in the synthesis of metal borides are given in the below equations (3.1)-(3.8).

$$Ta_2O_{5\,(s)} + B_2O_{3\,(s)} + 8\,Mg = 2\,TaB_{(s)} + 8\,MgO_{(s)} \tag{3.1}$$

$$TiO_{2\,(s)} + B_2O_{3\,(s)} + 5\,Mg = TiB_{2\,(s)} + 5\,MgO_{(s)} \tag{3.2}$$

$$HfO_{2\,(s)} + B_2O_{3\,(s)} + 5\,Mg = HfB_{2\,(s)} + 5\,MgO_{(s)} \tag{3.3}$$

$$ZrO_{2\,(s)} + B_2O_{3\,(s)} + 5\,Mg = ZrB_{2\,(s)} + 5\,MgO_{(s)} \tag{3.4}$$

$$MnO_{2\,(s)} + B_2O_{3\,(s)} + 5\,Mg = MnB_{2\,(s)} + 5\,MgO_{(s)} \tag{3.5}$$

$$Cr_2O_{3\,(s)} + 2\,B_2O_{3\,(s)} + 9\,Mg = 2\,CrB_{2\,(s)} + 9\,MgO_{(s)} \tag{3.6}$$

$$WO_{3\,(s)} + B_2O_{3\,(k)} + 6\,Mg = WB_{2\,(s)} + 6\,MgO_{(s)} \tag{3.7}$$

$$MoO_{3\,(s)} + B_2O_{3\,(s)} + 6\,Mg = MoB_{2\,(s)} + 6\,MgO_{(s)} \tag{3.8}$$

First of all, powder mixtures were prepared in stoichiometric or excess amounts over 6 grams according to theoretical reactions. Then, these blends were placed in vials with balls in the MBRAUN™ glovebox under an argon (Ar, Linde™, 99.9 %) atmosphere. The vials and the balls were chosen as hardened steel. The ball-to-powder weight ratio (BPR) was fixed at 10:1. The powder blends were high-energy ball milled in a Spex™ 8000D Mixer/Miller. Two 55 ml vials can be used in the Spex™ 8000D device. Experiments were conducted at different milling times for each boride powder. As a result of the experiments, the milling time was optimized as a process parameter and the optimized results were given. After milling, magnesium oxide (MgO) formed as by-product. For obtaining pure metal borides and removing unwanted by-products, acid leaching was done with 4 or 6 M HCl (Merck™, 37 %) under ultrasonic stirring. During the stirring, pure metal boride powders were obtained by dissolving MgO in the asidic solution. This solution was taken as 10 ml for each 1 g of powder. At the end of stirring, the powders were subjected to repeated washing and centrifugation (Hettich™ Rotofix 32A centrifuge) with distilled water until the pH reached 6-7 in order to obtain pure boride powders. When the pH reached to desired value, it was dried under air in a FN™ 500 stove for 24 h at 120 °C. As a result, the pure metal boride powders were obtained. Besides, in order to obtain pure metal borides in some powder blends, after leaching, annealing was carried out at 1100 °C under an argon and hydrogen (Linde™, 99.9 %) atmosphere in the Protherm™ ASP series in a split quartz tube furnace. The hardened steel balls and vials, Hettich™ Rotofix 32A centrifuge device, GALLENKAMP™ hotbox oven and Protherm™ ASP series of split quartz tube furnaces used in metal boride synthesis are shown in Figure 3.1.

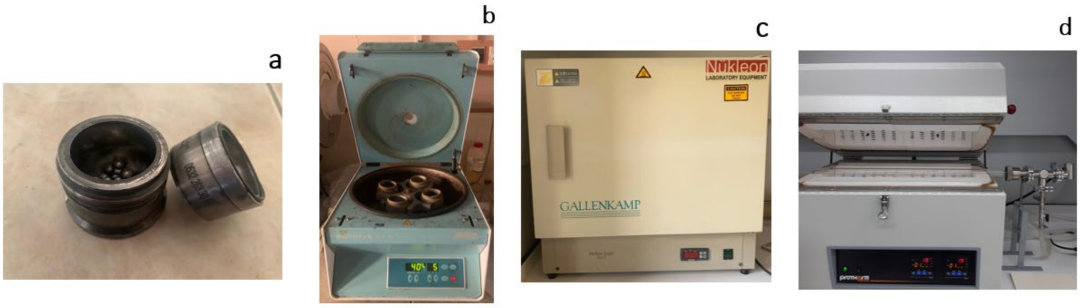

Figure 3.1 : (a) Hardened steel bals and vials, (b) Hettich™ Rotofix 32A centrifuge device, (c) GALLENKAMP™ hotbox oven and (d) Protherm™ ASP series in the split quartz tube furnace.

3.2 Preparation and Hybridization of Powder Blends

Metal borides powders, which are produced in the lab-scale, were hybridized in equimolar ratios with different 3, 4, 5, 6, 7 and 8 constituents. In some boride powders synthesized with different stoichiometry, an amount of amorphous boron powder was added to the mixture during hybridization to form an equimolar composition. After the prepared boride powder blends were using a Schimadzu^{TM} SMK-501 analytical balance (Figure 3.2a), they were blended in a WAB^{TM} T2C Turbula blender for 2 h (Figure 3.2b). Powder blends were prepared for over 10 g. Besides, the powder blends were sealed in vials with balls under an Ar atmosphere in a MBRAUN^{TM} glovebox (Figure 3.2c). The powders in the vials were milled using two different mills: planetary ball milling and high-energy ball milling.

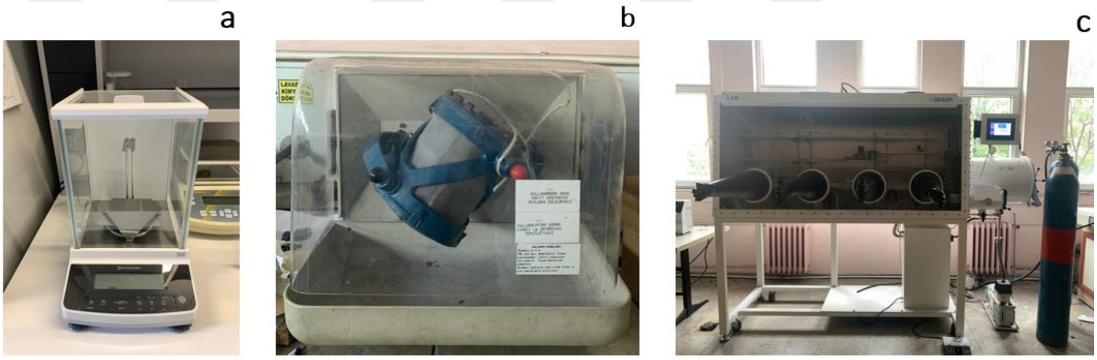

Figure 3.2 : (a) Schimadzu^{TM} SMK-501 analytical balance, (b) WAB^{TM} T2C Turbula blender, (c) MBRAUN^{TM} glovebox.

Table 3.1 : Sample codes and their corresponding compositions.

Sample Code	Composition
HEB 1	$(Ti_{0.33}Zr_{0.33}Hf_{0.33})\ B_2$
HEB 2	$(Ti_{0.25}Zr_{0.25}Hf_{0.25}Mn_{0.2})\ B_2$
HEB 3	$(Ti_{0.2}Zr_{0.2}Hf_{0.2}Cr_{0.2}Mn_{0.2})\ B_2$
HEB 4	$(Ti_{0.2}Zr_{0.2}Hf_{0.2}Ta_{0.2}Mn_{0.2})\ B_2$
HEB 5	$(Zr_{0.25}Hf_{0.25}Cr_{0.25}Mn_{0.25})\ B_2$
HEB 6	$(Ti_{0.25}Hf_{0.25}Mn_{0.25}Cr_{0.25})\ B_2$
HEB 7	$(Ti_{0.25}Zr_{0.25}Mn_{0.25}Cr_{0.25})\ B_2$
HEB 8	$(Ti_{0.167}Zr_{0.167}Hf_{0.167}Mn_{0.167}Mo_{0.167}Cr_{0.167})\ B_2$
HEB 9	$(Ti_{0.167}Zr_{0.167}Hf_{0.167}Mn_{0.167}W_{0.167}Cr_{0.167})\ B_2$
HEB 10	$(Ti_{0.143}Zr_{0.143}Hf_{0.143}Mo_{0.143}W_{0.143}Cr_{0.143}Mn_{0.143})\ B_2$
HEB 11	$(Ti_{0.143}Zr_{0.143}Hf_{0.143}Ta_{0.143}Mo_{0.143}Cr_{0.143}Mn_{0.143})\ B_2$
HEB 12	$(Ti_{0.143}Zr_{0.143}Hf_{0.143}Ta_{0.143}W_{0.143}Cr_{0.143}Mn_{0.143})\ B_2$
HEB 13	$(Ti_{0.125}Zr_{0.125}Hf_{0.125}Ta_{0.125}Mo_{0.125}W_{0.125}Mn_{0.125}Cr_{0.125})\ B_2$

Sample codes for the hybrid powder blends and their corresponding compositions are shown in Table 3.1. Sample codes are named with HEB representing high-entropy boride. To complete the diboride stoichiometry, nano-sized amorphous elemental boron powders (B, Pavtec, in purity > 99 %, particle size < 400 nm) were used. All HEB systems in Table 3.1 have been prepared as equimolar mixtures and will be expressed without specifying their stoichiometric values in the further explanations.

3.2.1 Planetary ball milling

Preliminary experiments were carried out to determine the optimum conditions with the HEB 1 composition, which is the main structure. For the initial hybridization experiments, a Fritsch^{TM} Pulverisette 5 Classic Line planetary ball mill with a 400 rpm rotation speed was used. During experiments, milling container and milling media were chosen as tungsten carbide (WC) vials (500 ml) and balls (Ø 6 mm). Figure 3.3a-b shows the Fritsch^{TM} Pulverisette 5 Classic Line planetary ball mill and WC vials and balls, respectively.

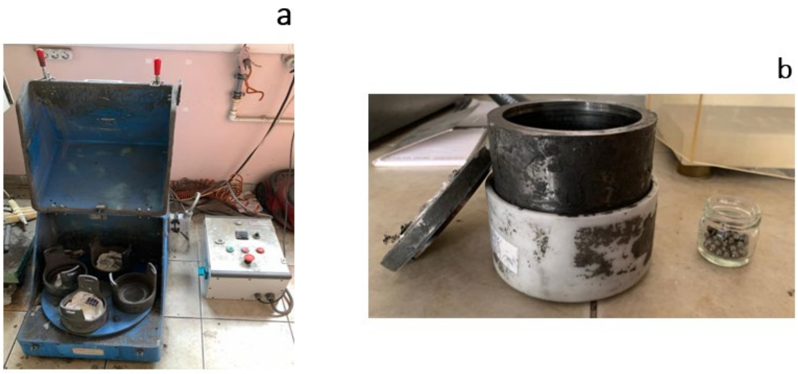

Figure 3.3 : (a) Fritsch^{TM} Pulverisette 5 Classic Line planetary ball mill, (b) WC balls and vials.

During experiments, different milling durations and different BPR have been tried to choose the optimum conditions. These conditions are given at Table 3.2. As a result of these trials, hybridization could not be achieved at the desired level, so high-energy ball milling was tried.

Table 3.2 : Milling durations and different BPRs utilized for the HEB 1 composition milled with planetary ball mill.

BPR	Milling Durations (h)
10:1	30
10:1	60
20:1	60
20:1	100
30:1	60
30:1	100

3.2.2 High-energy ball milling

First of all, HEB 1 compositions were milled for 6 h, 10 h, 15 h and 20 h to determine optimum duration. During the experiment, BPR was chosen as 10:1. In case of carrying out the experiments in the Spex^{TM} 8000D Mixer/Miller, the milling container was a WC vial with a capacity of 50 ml and the milling media were WC balls with a diameter of 6 mm. The Spex device, as well as WC balls and vials, are depicted in Figure 3.4a-b, respectively.

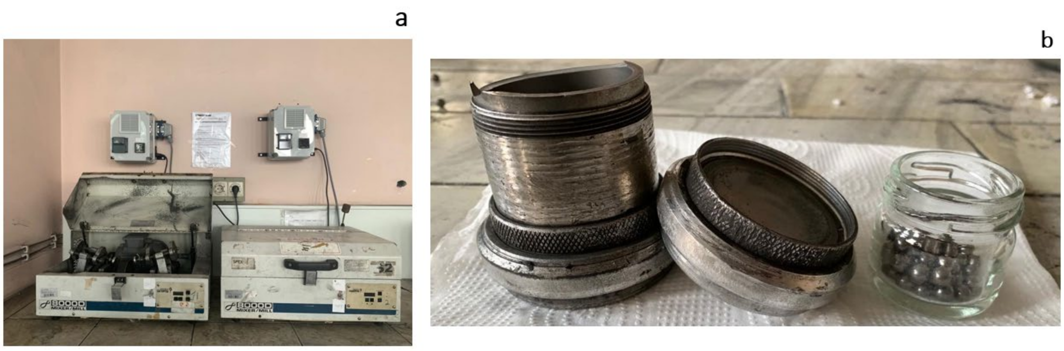

Figure 3.4 : (a) Spex^{TM} 8000D Mixer/Mill, (b) WC vials and balls.

After milling the HEB 1 composition for different durations (6 h, 10 h, 15 h and 20 h), it was determined that the optimum milling time was 6 h. Milling for all other compositions was conducted in the Spex^{TM} 8000D Mixer/Mill device for 6 h with BPR 10:1.

3.3 Powder Characterization

The X-ray diffractometry (XRD) method was used for the characterization of metal boride powders synthesized after MCS and leaching. For this, Bruker^{TM} D8 Advanced Series XRD (Figure 3.5) was used with CuK_{α} (1.5406 Å, 35 kV and 40 mA) radiation in the 2θ range of 10-90° incremented at a rate of 2°/min. Also, XRD investigations of the as-blended and milled hybridized powder blends were performed with the same device and the same conditions. The International Center for Diffraction Data® (ICDD) powder diffraction files were utilized for the identification of phases.

Figure 3.5 : Bruker^{TM} D8 Advanced Series XRD.

Particle size measurements were conducted with Malvern^{TM} Mastersizer 2000 particle size analyzer using distilled water equipped with a Bandelin Sonopuls^{TM} ultrasonic homogenizer, which are shown in Figure 3.6a-b. Before each measurement, distilled water was added to the powders and then agitated with an ultrasonic homogenizer to prevent the formation of agglomerated structures.

a b

Figure 3.6 : (a) Malvern^{TM} Mastersizer 2000 particle size analyzer, (b) Bandelin Sonopuls^{TM} ultrasonic homogenizer.

Density measurements of the powders hybridized for 6 h were made with the Micromeritics^{TM} AccuPyc II 1340 gas pycnometer at room temperature using He gas (Linde^{TM}, in purity of 99.99 %) shown in Figure 3.7. Before the measurement, the sample was weighed andthis value was entered into the program. As a result of repeated measurements nearly 10 times, the average density values and standart deviations were calculated.

Figure 3.7 : Micromeritics™ AccuPycII 1340 Helium-gas pycnometer.

Besides, JEOL™-6000 Neoscope scanning electron microscope (SEM) device shown in Figure 3.8 was used for microstructural characterization of metal borides synthesized under optimum conditions.

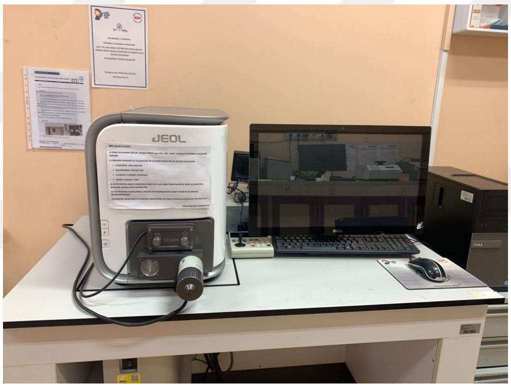

Figure 3.8 : JEOL™-6000 Neoscope SEM device.

3.4 Spark Plasma Sintering

3, 4, 5, 6, 7 and 8 hybrid component powders milled for 6 h were sintered by applying spark plasma sintering (SPS). All of the SPS experiments were performed at Eskişehir Technical University at the Ceramic Research Centre (SAM) Laboratory. For the SPS experiments, the FCT-HP D 25/I SPS system produced by FCT Systeme GMBH™, shown in Figure 3.9a-b, was used. Besides, 20 mm graphite dies lined with graphite foils were selected for the sintering process. First, the lower part of the die was placed and after the powder was filled, the upper part was closed and the powder was compressed with a hydraulic press. After compression, the die was placed inside the SPS system and filled with inert gas before the sintering experiments. SPS specimens were sintered under 30 MPa pressure at 2000 °C. The temperature heating/cooling rate was chosen at 100°C/min. The holding time was 10 min.

a b

Figure 3.9 : FCT-HP D 25/I spark plasma sintering system.

3.5 Sintered Sample Characterization

Phase analyses of the sintered samples were performed with a Bruker^{TM} D8 Advance Series XRD (Figure 3.5). CuK$_\alpha$ (1.5406 Å, 35 kV and 40 mA) radiation in the 2θ range of 20-90° incremented at a rate of 2°/min were used as XRD analysis conditions. Morphological analyses were performed at Boğaziçi University Center for Life Sciences and Technologies using ThermoScientific^{TM} Quattro S SEM shown in Figure 3.10a. Also, the wear tracks of the specimens were examined with a Nikon^{TM} Eclipse L150 optical microscope (OM) using Clemex^{TM} image analysis software. Figure 3.10b shows the Nikon^{TM} Eclipse L150 model OM.

a b

Figure 3.10 : (a) ThermoScientific^{TM} Quattro S, (b) Nikon™ Eclipse L150 optical microscope.

The densities of the sintered samples were measured in distilled water using the Archimedes' method with Schimadzu^{TM} SMK-501 analytical balance and spesific gravity measurement kit (Archimedes' kit) shown in Figure 3.11. Density values were reported as average of three different measurements.

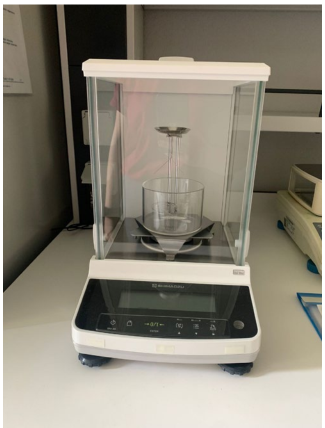

Figure 3.11 : Schimadzu^{TM} SMK-501 spesific gravity measurement kit.

After Archimedes' measurement, sintered samples were hot-mounted with Struers^{TM} LaboPress-1 system. Figure 3.12a shows the hot-mounted device. Hot-mounted samples were grinded and polished in a METKON FORCIPOL^{TM} 2V grinding/polishing instrument and FORMICAT^{TM} specimen holder (Figure 3.12b). Coarse grinding was done with 125 µm mesh triangular diamond discs at 160 rpm for 4 h, and fine grinding was done with 6 µm mesh triangular diamond discs at 180 rpm for 4 h. The polishing process was carried out by using a 3 µm mesh diamond disc with hexagonal cross section, by running the sample holder counterclockwise at 10 rpm and the disc clockwise at 220 rpm for 2 h.

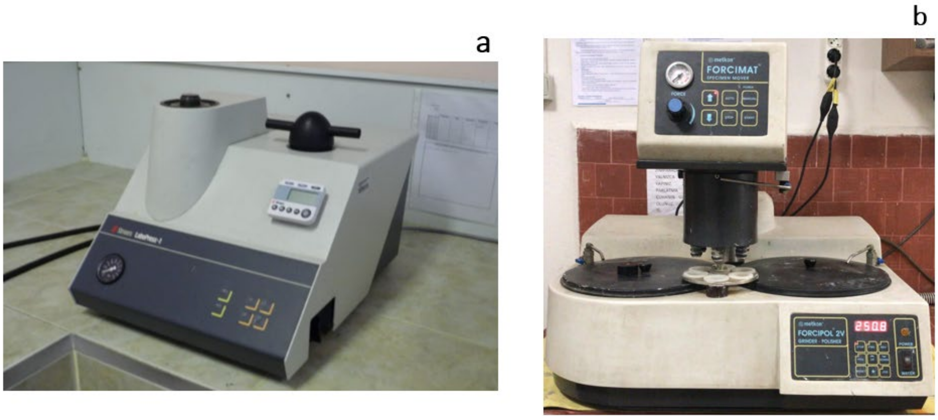

Figure 3.12 : (a) Struers^{TM} LaboPress-1 hot-mounting device, (b) METKON FORCIPOL^{TM} 2V grinding/polishing instrument and FORMICAT^{TM} specimen holder.

The hardness measurements of the grinded and polished samples were carried out with the FutureTech^{TM} Microhardness Tester, shown in Figure 3.13a. Measurement parameters were determined as 0.9807 N load (100 g), 10 sec at room temperature by Vickers method. As a result of 25 different measurements, average hardness values were obtained. Dry sliding wear tests were carried out using WC ball with 5 mm diameter as the wear surface. For the test conditions, 6 mm/s sliding speed, 100 m sliding distance and 2 mm wear track length were employed. The tests were carried out at room temperature with a normal load of 4 N. After carrying out the wear tests, the volumetric wear loss was determined by calculating the arithmetic mean of three different measurements. Besides, relative wear resistance values were calculated by multiplying wear track length and wear track area. The Bruker^{TM} Umt-2 wear instrument is shown in Figure 3.13b and the Veeco^{TM} Dektak 6 M Stylus Profiler is shown in Figure 3.13c.

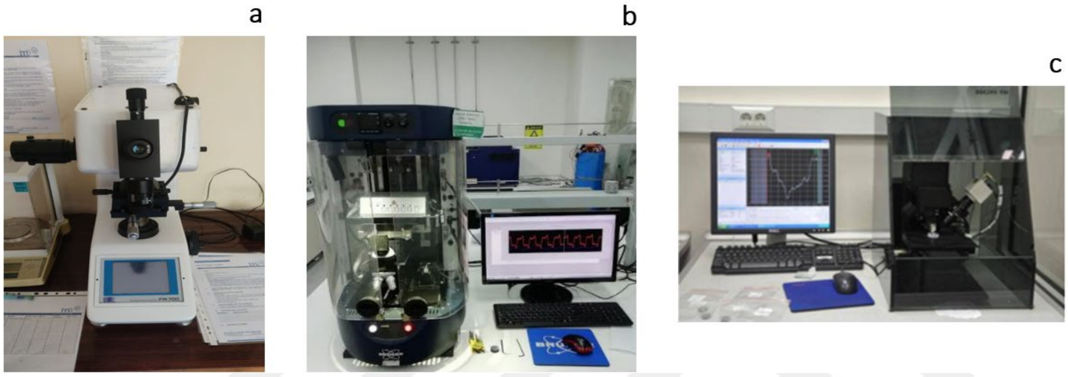

Figure 3.13 : (a) FutureTech^{TM} Microhardness Tester, (b) Bruker^{TM} Umt-2 wear instrument, (c) Veeco^{TM} Dektak 6 M Stylus profiler.

3.6 Thermochemical Calculations

For determining possible phase formations, FactSage^{TM} 7.2 thermodynamic software was used with Calculation of Phase Diagram (CALPHAD) model. This gives the opportunity to compare the designed high-entropy metal boride systems with the limits determined in the literature on whether HEBs will be solid melt and what crystal structure HEBs will have. In this thesis, three different compositions (HEB 1, HEB 3 and HEB 4) were selected and FactSage^{TM} diagrams showing mole fractions versus temperature were drawn and given in represantatively Figure 3.14a-c. On the basis of Figure 3.14a, the solid-solution phase MB_2 is observed in the range of 250-3250 °C. Liquid phase formation is shown after 3250 °C. Whereas, it can be seen from Figure 3.14b that solid melt phases MB_4 up to 750 °C, M_2B up to about 1250 °C, and MB_2 up to about 3250 °C are formed. In addition, liquid phase formation was observed in the range of 1250-3750 °C. Similarly, solid-solution phases MB_2 (up to nearly 3325 °C), MB_2 (up to nearly 1125 °C), MnB_2 (1000 °C-3275 °C) and MnB_4 (up to nearly

1125 °C) were formed according to Figure 3.14c. Again, the liquid phase was formed between about 1775-3750 °C. As can be seen from the graphs, the formation of different metal boride phases is observed at temperatures above 250 °C. The increase in the number of components also increased the diversity of the phases formed. Besides all these, there is liquid phase formation over 3000 °C.

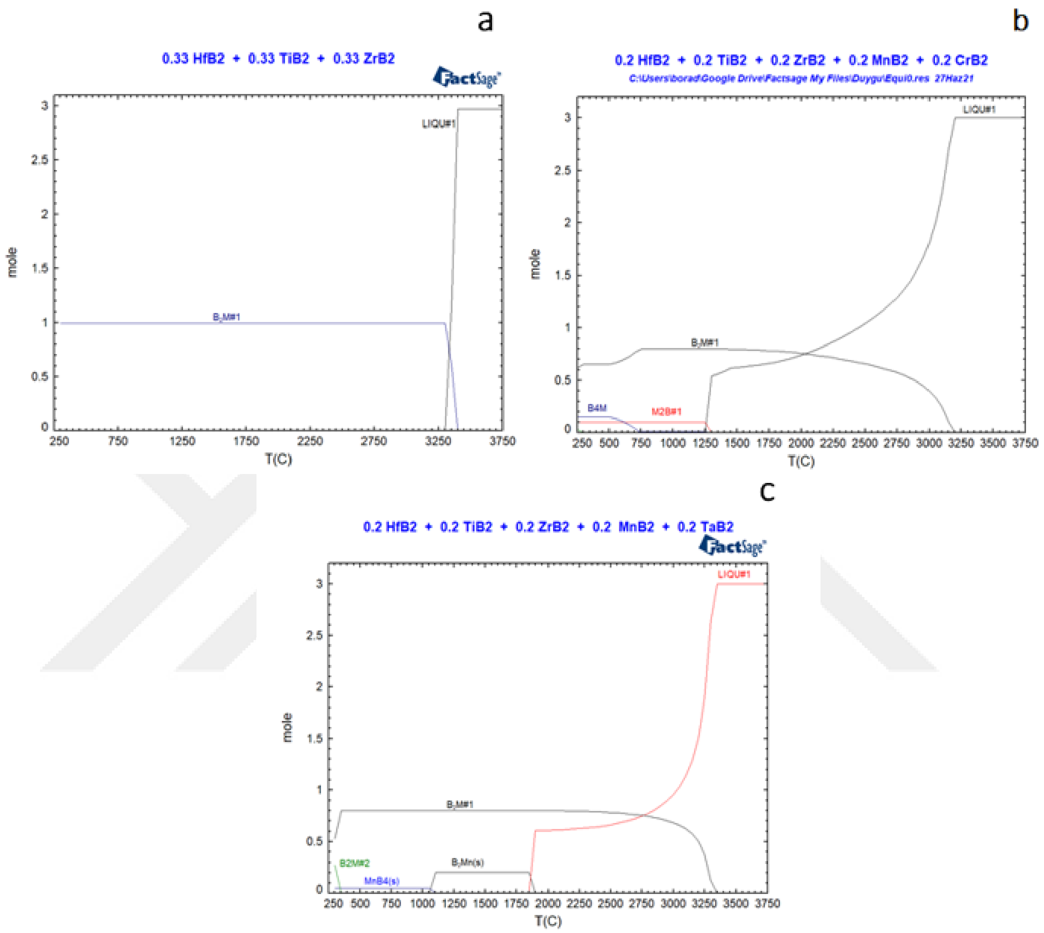

Figure 3.14 : Representative thermochemical calculations of HEB phases: mole fraction of phases determined by FactSage^{TM} (a) HEB 1, (b) HEB 3 and (c) HEB 4.

4. RESULTS AND DISCUSSION

This chapter consists of five sections describing detailed characterization studies. First of all, the production parameters of metal borides synthesized under optimum conditions are explained. The next chapter includes detailed characterization studies of HEB powders after milling. In the last three chapters, detailed phase, microstructural, physical and mechanical characterizations of the SPS sintered sample are explained.

4.1 Optimization of Metal Boride Powders

In this thesis, HfB_2, TiB_2, ZrB_2, TaB, Cr-B, Mo-B, Mn-B and W-B boride powders were synthesized. In the synthesis of boride powders, many different parameters were tried during the leaching process following the mechanochemical synthesis. As a result of these experiments, optimum conditions were obtained. These parameters are explained in Table 4.1.

Table 4.1 : Optimum conditions for the synthesis of metal borides.

Compositions	Optimum Synthesis Conditions
HfB_2	HfO_2-B_2O_3-Mg starting powders prepared in stoichiometric ratio, milling for 12 h and leaching with 6 M HCl
TiB_2	TiO_2-B_2O_3-Mg starting powders prepared in stoichiometric ratio, milling for 5 h and leaching with 6 M HCl
ZrB_2	ZrO_2-B_2O_3-Mg starting powders prepared in stoichiometric ratio, milling for 20 h and leaching with 4 M HCl
TaB	Ta_2O_5-B_2O_3-Mg starting powders prepared in 50 wt.% excess B_2O_3 ratios, milling for 10 h and leaching with 4 M HCl
Mn-B	MnO_2-B_2O_3-Mg starting powders prepared in 100 wt.% excess B_2O_3 and 50 wt.% excess Mg ratios, milling for 10 h, leaching with 4 M HCl, and annealing at 1100°C
Cr-B	Cr_2O_3-B_2O_3-Mg starting powders prepared in 0.8 mole Cr_2O_3 100 wt.% excess B_2O_3 and 25 wt.% excess Mg ratios, milling for 5 h and leaching with 4 M HCl, and annealing at 1100°C
Mo-B	MoO_3-B_2O_3-Mg starting powders prepared in 100 wt.% excess B_2O_3 and 50 wt.% excess Mg ratios, milling for 6 h and leaching with 4 M HCl
W-B	WO_3-B_2O_3-Mg starting powders prepared in 100 wt.% excess B_2O_3 and 50 wt.% excess Mg ratio milling for 20 h and leaching with 4 M HCl

Metal boride powders were synthesized by the mechanochemical synthesis (MCS) method under optimum conditions in the presence of native B_2O_3, Mg and related metal oxides. Figure 4.1a-b shows the XRD patterns of the HfB_2 and TiB_2 powders, respectively. Only HfB_2 (ICDD No: 00-038-1398) and TiB_2 (ICDD No: 01-085-2083) phases were formed without any contamination. Since these phases are stable at high temperature in the binary phase diagram, they are expected to form.

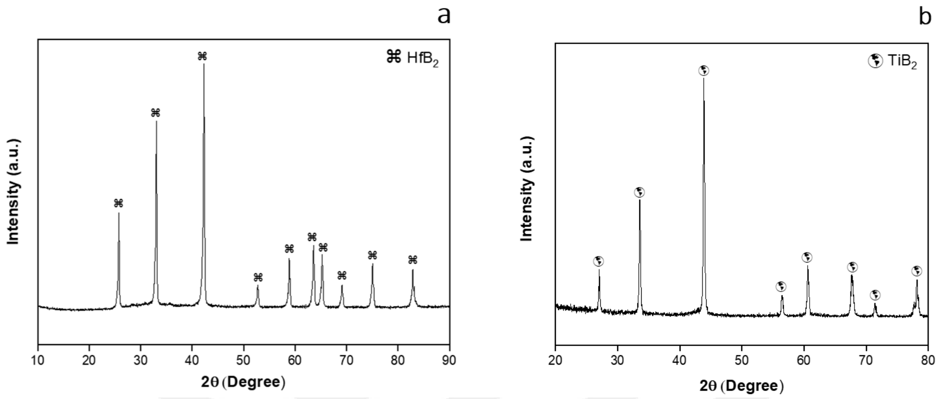

Figure 4.1 : XRD patterns of (a) HfB_2 and (b) TiB_2 powders.

On the basis of Figure 4.2a, only ZrB_2 (ICDD No: 01-089-3826) phase can be observed. Similar to the HfB_2 and TiB_2 phases, the zirconium diboride, is also stable at high temperatures. The Hf, Ti and Zr could be synthesized as diborides without containing multi-phase boride compounds. In previous studies, it was reported that HfB_2 (Akçamlı et al, 2016, 2017; Tekoğlu et al, 2021), TiB_2 (Ağaoğulları et al, 2009a; 2009b; Çelik et al, 2022) and ZrB_2 (Ağaoğulları et al, 2012b; Ağaoğulları et al, 2017) could be produced as diboride with the same synthesis routes starting from different raw materials. Also, the TaB (ICDD No: 01-089-2310) phase occurs without any other boride compounds, as can be seen from Figure 4.2b.

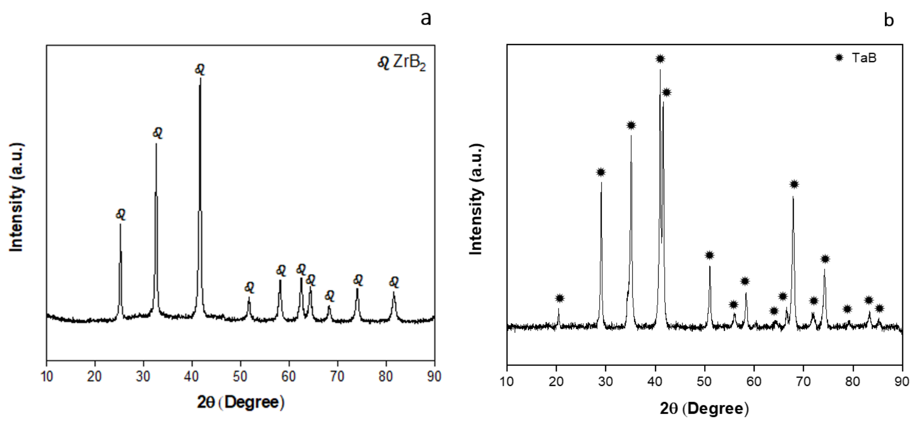

Figure 4.2 : XRD patterns of (a) ZrB_2 and (b) TaB powders.

XRD patterns of Mn boride and Cr boride powders are represented in Figure 4.3a-b, respectively. According to the Mn-B patterns, there are MnB (ICDD: 00-038-1424), Mn_2B (ICDD: 00-025-0335), Mn_3B_4 (ICDD: 01-089-3781), MnB_4 (ICDD: 00-013-0200) and MnB_2 (ICDD No: 01-089-3009) phases (Figure 4.3a). As expected, more than one Mn-B phase are present in the microstructure. Similarly, there are various Cr-B phases (Figure 4.3b) which are Cr_3B_4 (ICDD No: 01-089-3555), CrB_2 (ICDD No: 03-065-1883) and CrB (ICDD No: 01-089-3587).

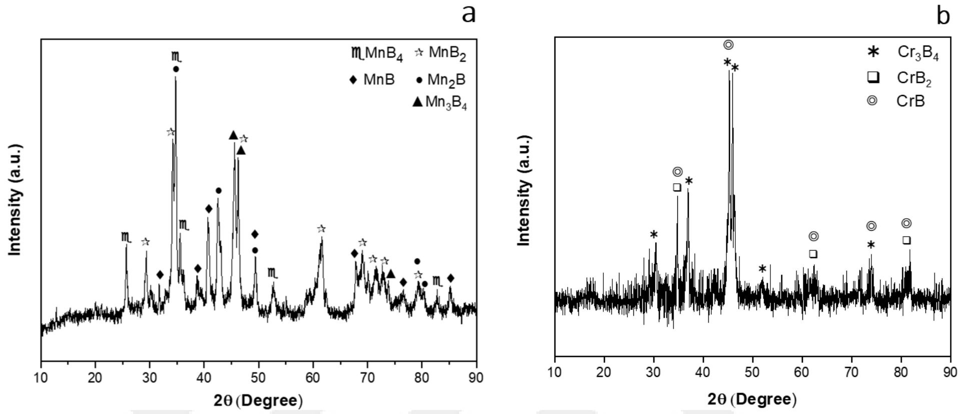

Figure 4.3 : XRD patterns of (a) Mn boride and (b) Cr boride powders.

Figure 4.4a-b consists of XRD patterns of different phases both binary W boride and Mo boride system. WB (ICDD No: 01-073-1769), W (ICDD No: 01-089-2767), W_2B (ICDD No: 00-025-0990) and W_2B_5 (ICDD No: 03-065-3591) peaks are seen from the XRD graph (Figure 4.4a). In a similar way, Mo-B exhibits (Figure 4.4b) Mo (ICDD No: 01-089-5023) and multi-phase boride compounds like α-MoB (ICDD No: 00-051-0940), β-MoB (ICDD No: 00-006-0644), Mo_2B (ICDD No: 01-089-1990), MoB_2 (ICDD No: 01-089-3785), MoB_4 (ICDD No: 00-020-1235) and Mo_2B_5 (ICDD No: 00-038-1460).

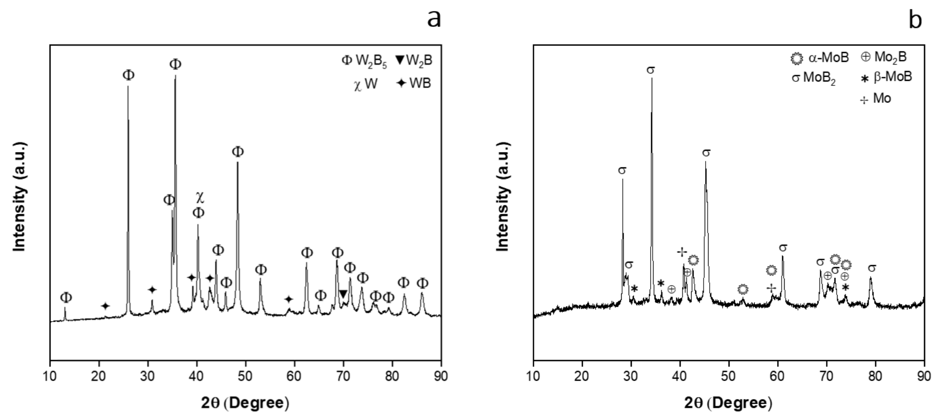

Figure 4.4 : XRD patterns of (a) W boride and (b) Mo boride powders.

The Cr (Iizumi et al, 2011), Mn (Şimşek et al, 2019), W (Coşkun & Öveçoğlu, 2013; Şenyurt et al, 2021) and Mo (Kudaka et al, 2001; Yamauchi et al, 2007) borides contain multi-phases as described in this thesis. Similarly, in several other investigations, it has been reported that the variety in the stoichiometry of borides can occur instead of a diboride. These phases may not be thermodynamically stable and are certainly affected by some kinetic factors. The stoichiometry of boride phases is affected under non-equilibrium conditions during MCS (Balcı et al, 2016, 2019).

SEM images of metal boride powders synthesized under optimimum conditions at different magnifications (500X, 1500X) are shown in Figure 4.5a-h. According to these images, it is understood that all metal boride powders are synthesized in submicron sizes. Also, all metal boride powders appear to be agglomerated and all of the metal boride powders are irregular in shape because of repeated collisions at prolonged milling durations.

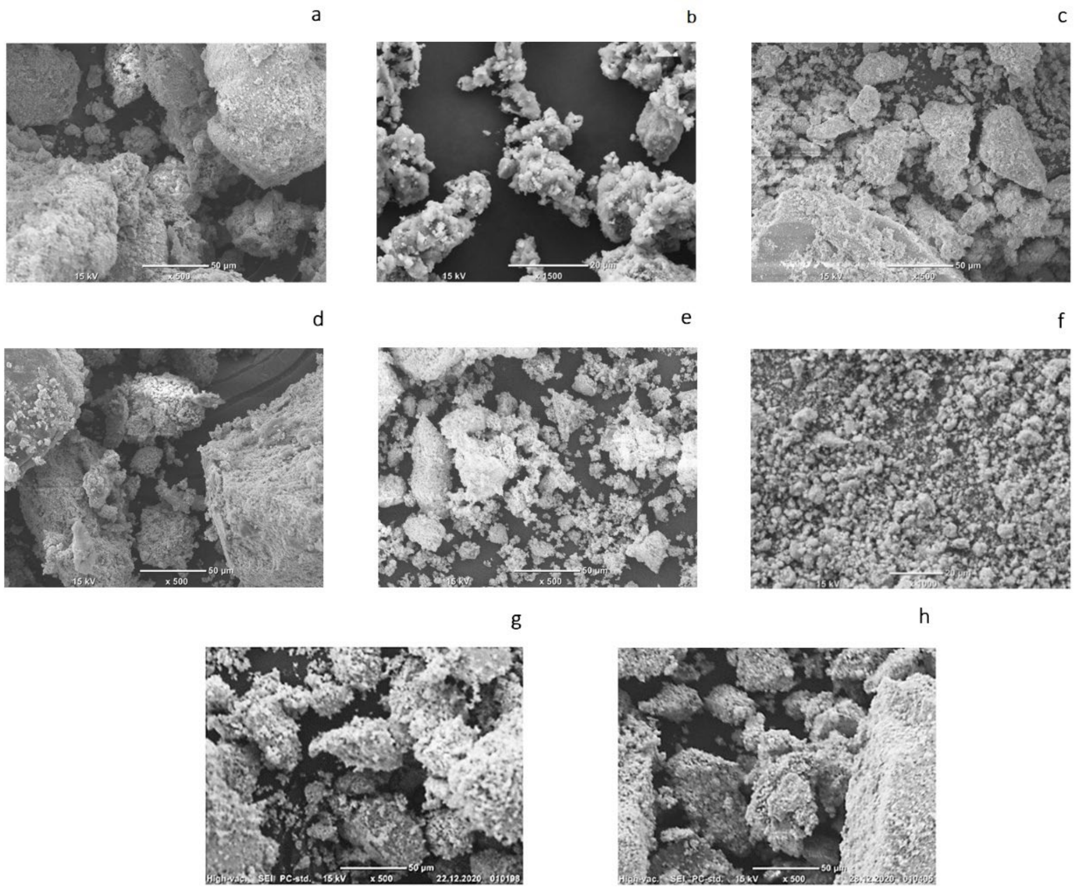

Figure 4.5 : SEM images of metal boride powders synthesized under optimimum conditions at different magnifications (500X, 1500X): (a) HfB_2, (b) TiB_2, (c) ZrB_2, (d) Mo-B, (e) W-B, (f) TaB, (g) Cr-B, (h) Mn-B.

Metal boride powders were synthesized using the optimum conditions determined as a result of the experiments in the lab-scale. These boride powders were synthesized repeatedly in large amounts for hybridization studies.

4.2 Powder Characterization

Phase analysis and particle size measurement results of metal boride powders produced at lab-scale, reproduced and hybridized are explained. At the end of the chapter, the density values of the hybridized powders measured by a pycnometer are given comparatively.

4.2.1 (Hf-Ti-Zr)B_2 composition

The first aim for this ternary composition is to determine the optimum milling method and optimum duration. For this reason, the HEB 1 composition was synthesized using both planetary ball milling and high-energy ball milling (HEBM) systems. In order to compare with the milled powders, the as-blended (non-milled) ones were examined. XRD pattern of the as-blended HEB 1 composition is given in Figure 4.6. The dominant peaks belong to the HfB_2, TiB_2 and ZrB_2 phases found in the starting powder blends. In addition, low-intensity peaks of the HfO_2 (ICDD No: 00-006-0318) phase are also seen at 2θ values of nearly 29° and 32°, respectively. The reason for this could be the surface oxidation of the powders during production under laboratory conditions.

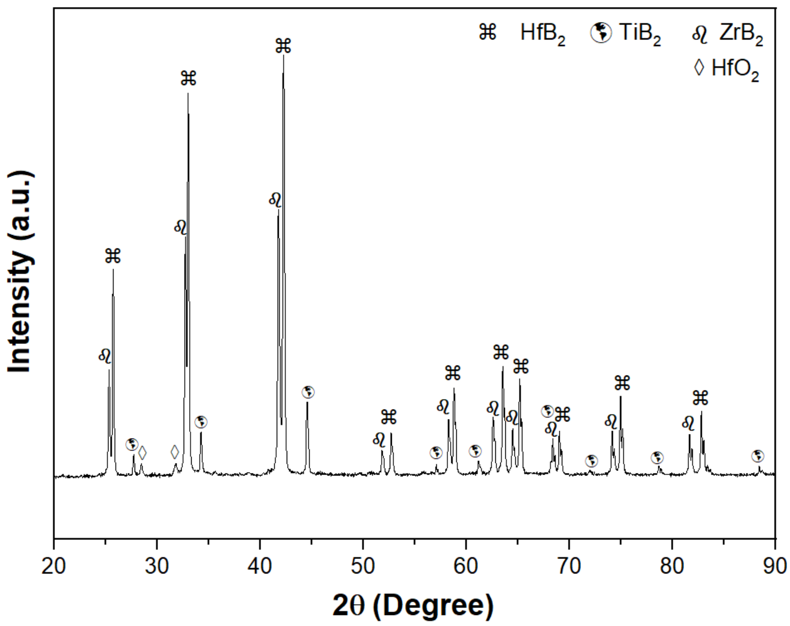

Figure 4.6 : XRD pattern of the as-blended HEB 1 composition.

4.2.1.1 Planetary ball milling

As mentioned before, high-entropy alloys contain four or five components in the composition. However, our HEB 1 composition contains three main components, which are HfB_2, TiB_2 and ZrB_2. The composition containing three elements is defined as "medium-entropy alloys/borides (MEB)". Demirskyi et al. (2020) synthesized another three-component system, which is a equimolar $(Zr_{1/3}Hf_{1/3}Ta_{1/3})B_2$, and defined as medium-entropy diboride. On the other hand, Monteverde and Saraga (2020) calculated some parameters required to form ideal equimolar solid-solutions of metal diborides. Accordingly, in the three metals Hf-Ti-Zr system, the ratio of a and c lattice parameters were found to be 1.82 % ($\delta_{c/a}$ = 1.82 %), lattice volume 7.45 % (δ_{V} = 7.45 %), atomic radius 4.62 % (δ_{r} = 4.62 %) and electronegativity value 7.68 % ($\delta_{e\text{-}neg}$ = 7.68 %). In addition, it was recommended in that the various diboride powders varying in particle shapes and sizes can be utilized for a successful synthesis of medium-entropy ceramics (Castle et al, 2018). As a result, HEB 1 composition is a medium-entropy alloy and it is the main composition. HEB 1 composition was synthesized in order to be a base alloy for other samples and to be able to compare. The HEB 1 composition, blended in an equimolar ratio, was milled for 30, 60 or 100 h. The BPRs were varied as 10:1, 20:1 and 30:1 for these milling durations. The XRD patterns of the samples milled at both different durations and different BPRs are given in Figure 4.7. When Figure 4.7(c-f) is examined, it can be seen that the medium-entropy boride phases started to form their formations were not completed for the conditions of BPR 20:1 and 30:1. The XRD patterns of the milled samples of the BPR of 10:1 (Figure 4.7a-b) are similar to those of the as-blended ones (Figure 4.6). There are HfB_2, TiB_2 and ZrB_2 phases in the structure. When the milling duration is increased to 60 h, a slight decrease in peak intensity is observed, but there are no MEB phases. This proves that the 10:1 BPR condition in the planetary ball mill is not sufficient for the formation of the MEB phase after 30 and 60 h of milling. Figure 4.7c-d displays the XRD patterns of the 20:1 BPR condition at milling durations of 60 h and 100 h. Here, MEB phases are formed, but there is a TiB_2-rich phase that does not participate in the structure. The XRD patterns after 60 h and 100 h of milling are quite similar. Figure 4.7e-f includes XRD patterns for the 30:1 BPR condition. Similar to Figure 4.7c-d, medium-entropy boride phases are formed with the occurence of a TiB_2-rich phase. When all conditions are considered together, the condition with a BPR of 30:1 and milling duration of

100 h has the lowest peak intensity and largest peak broadening. The TiB_2 phase or the TiB_2-rich phase is present for all conditions. In addition, counts of XRD patterns in Figure 4.7 are almost the same. Despite all, the peak intensities and broadenings are still close to the as-blended powders. Similarly, in a study conducted in the literature, it was stated that the mechanical alloying procedure extended up to 60 h did not result in a significant change in the XRD pattern (C. Wang et al, 2014).

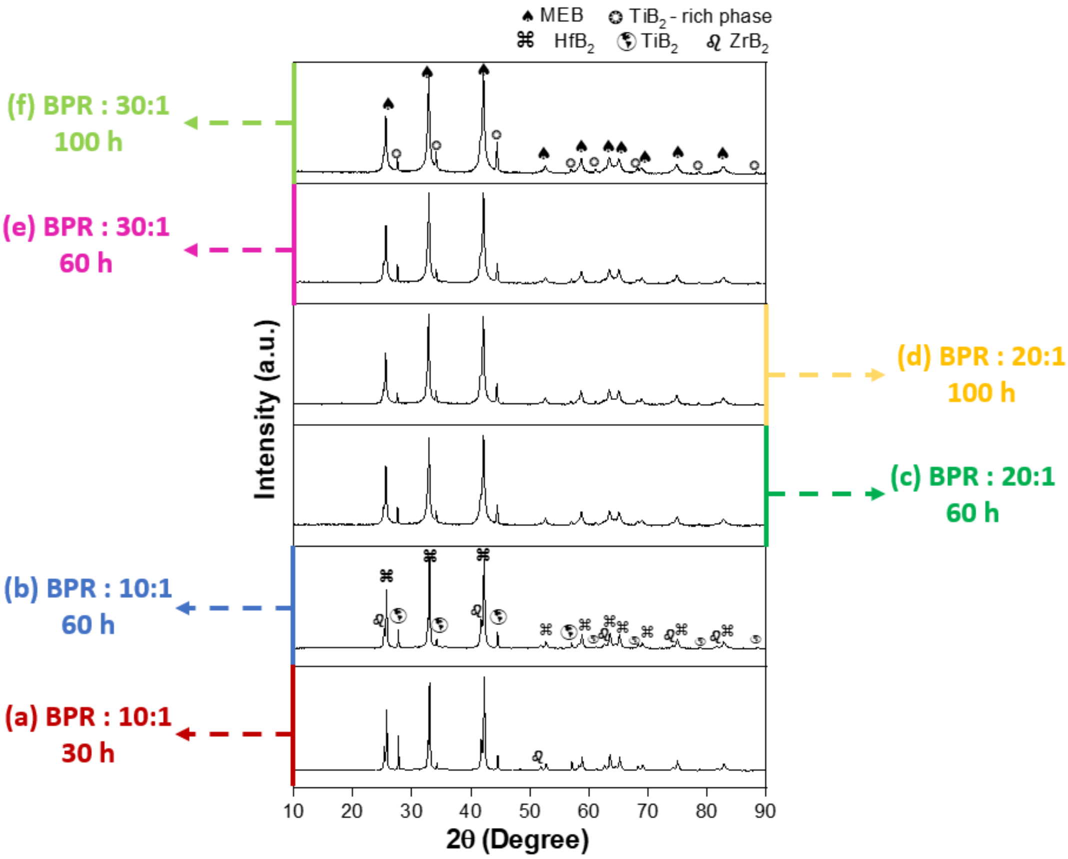

Figure 4.7 : XRD patterns of the HEB 1 composition mechanical alloyed in a planetary ball mill at different durations and ball-to-powder weight ratios.

Figure 4.8 exhibits the average density measurement values of the powders milled in a planetary ball mill. For the milled samples having BPR of 10:1, the average densities are found as 6.7151 ± 0.0154 and 6.48 ± 0.0165 g/cm^3 for 30 h and 60 h, respectively. Also, when BPR is 20:1, the average density values are measured as 6.6649 ± 0.0134 and 6.713 ± 0.0055 g/cm^3 for 60 h and 100 h, respectively. And when BPR is 30:1, the average densities are determined as 6.7539 ± 0.0053 and 6.4466 ± 0 .0017 g/cm^3 for 60 h and 100 h, respectively. When the BPR condition is 10:1 and 30:1, it is seen that the average density value decreases as the milling time increases. However, when the BPR condition is 20:1, the average density value increases with the increase in milling duration. While the highest density value is obtained with BPR 30:1 milling for 60 h, the lowest density value is obtained after 100 h of milling under BPR 30:1 condition. With average density values, there is no significant difference between milling times and BPR conditions. Therefore, there exists no correlation between BPR and milling durations.

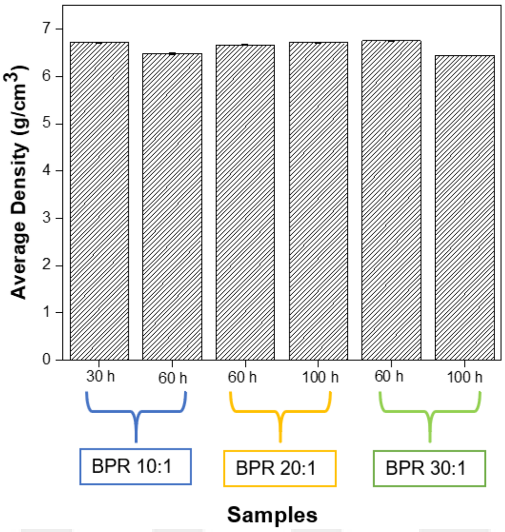

Figure 4.8 : Average density measurement values of HEB 1 powders mechanical alloyed in a planetary ball mill.

4.2.1.2 High-energy ball milling

Since significant differences could not be obtained for different BPRs, the BPR was chosen only as 10:1 during high-energy ball milling process in the Spex^{TM} Mixer/Miller. The XRD patterns of the powders milled using Spex^{TM} mill at different durations (6 h, 10 h, 15 h and 20 h) and BPR of 10:1 are given in Figure 4.9.

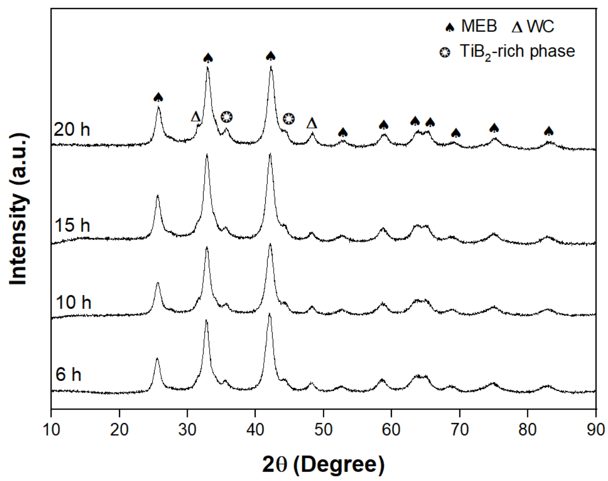

Figure 4.9 : The XRD patterns of the mehanical alloyed HEB 1 powders using Spex^{TM} at different durations (6 h, 10 h, 15 h, 20 h) and BPR: 10:1.

According to the XRD patterns, it is seen that medium-entropy boride phases begin to form even after 6 h of milling. There are also low-intensity peaks of the TiB_2-rich phase at 2θ value of ~35° and ~44°. In addition, WC phase (ICDD No: 00-002-1055) peaks (~31°, 35°, 47°) are seen as contamination from the milling balls and vials. The amount of WC contamination increases as the milling time approaches 20 h. When all XRD patterns are compared with the XRD pattern of the as-blended powders (Figure 4.6, an intensity decrease and a peak broadening are observed. The broadening of the peaks, the decrease in peak intensity and the overlapping of individual peaks are simply attributed to the formation of solid-solutions. Furthermore, the broadening of the peaks and/or the reduction of the peak intensity are dependent on three factors during the high-energy ball milling: grain size reduction, high lattice strain and decreased crystallinity (Duan et al, 2020; Long et al, 2021; C. Wang et al, 2014). Since such hybridization was not observed when planetary ball milling was used, further studies were continued using HEBM.

The particle size measurement for the HEB 1 composition milled for 6 h [d(0.1)=0.94 µm, d(0.5)=4.6 µm, d(0.9)=23.22 µm], 10 h [d(0.1)=1.58 µm, d(0.5)=6.52 µm, d(0.9)=24.32 µm], 15 h [d(0.1)=1.49 µm, d(0.5)=5.8 µm, d(0.9)=23.6 µm] and 20 h [d(0.1)=0.79 µm, d(0.5)=1.87 µm, d(0.9)=3.26 µm] is seen in Figure 4.10a-d, respectively. Generally, as the milling time increases, the particle size of the powders is expected to decrease (Ağaoğulları et al, 2012a; Suryanarayana, 2001). However, under these conditions, it is observed that the average particle size decreases after only 20 h of milling compared to that of 6 h milling. It is notable that the agglomeration of the particles prevents the observation of smaller ones.

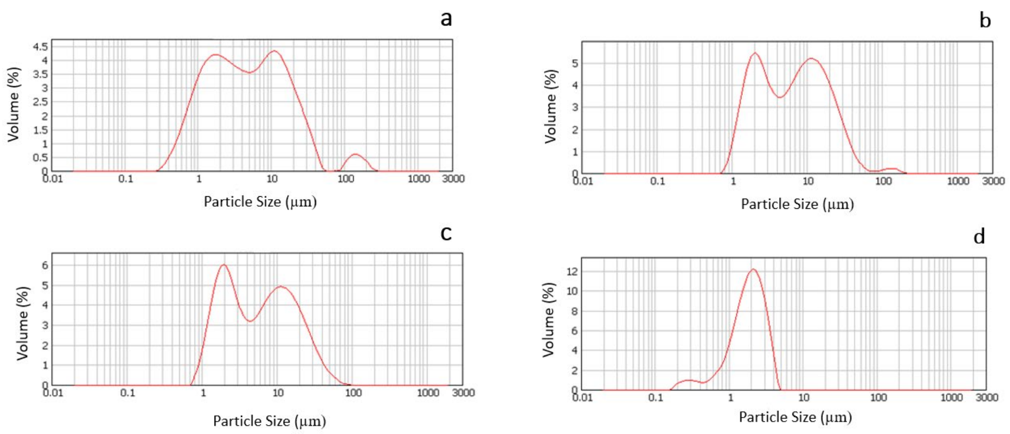

Figure 4.10 : Particle size distrubution of the HEB 1 composition milled at: (a) 6 h, (b) 10 h, (c) 15 h and (d) 20 h.

Figure 4.11 shows the average density values of powders milled in a Spex^{TM} device with different durations. The average density values are 6.5912 ± 0.002, 6.4014±0.0075 g/cm^3, 6.3228±0.0068 and 6.1041±0.00065 g/cm^3 for 6, 10, 15 and 20 h, respectively. It is clearly seen that the density values decrease as the milling duration increases. However, this is not a proof of a proper correlation.

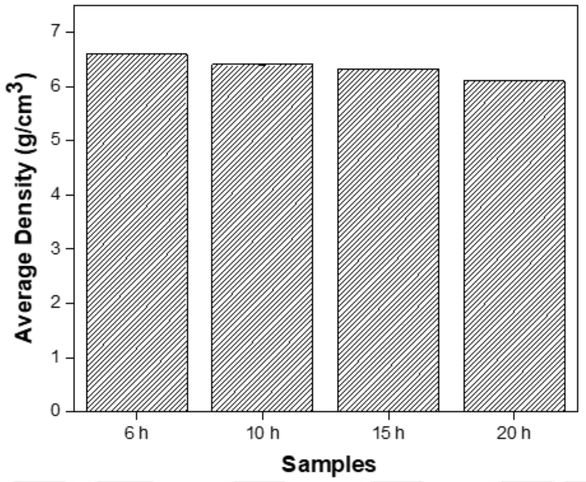

Figure 4.11 : Average density measurement values of HEB 1 powders high-energy ball milled at different durations.

The milling time of 6 h is chosen as optimum in the condition of BPR: 10:1 using a Spex^{TM} due to the fact that increased contamination and decreased density as the milling time increases according to the XRD patterns. In this thesis, high-entropy boride ceramics were synthesized above-mentioned condition.

4.2.2 (Hf-Ti-Zr-Mn)B_2 composition

Mn boride powders were investigated its effect to the main composition. Figure 4.12a-b represents the XRD patterns of as-blended and milled HEB 2 composition. The as-blended XRD pattern (Figure 4.12a) includes the HfB_2, TiB_2, ZrB_2, MnB, MnB_2, Mn_2B, Mn_3B_4 and HfO_2 phases. Table A.1 shows the approximate 2θ values corresponding to the Mn_aB_b peaks. The HfB_2 phase has the strongest peak at nearly 2θ value of 42°. Peak shifting and overlapping are observed after 6 h of milling (Figure 4.12b) when compared to the as-blended powders, like HEB 1 composition. High-entropy boride phases started to form, but this formation was not fully completed. There is TiB_2-rich phase (2θ ≅ 44.3°) in the structure. It is also thought that the MnB is formed around 2θ value of 44.6°. This peak is interpreted as TiB_2-rich because of the exact overlapping with the peak position. There are boride peaks that do not participate into the hexagonal lattice structure.

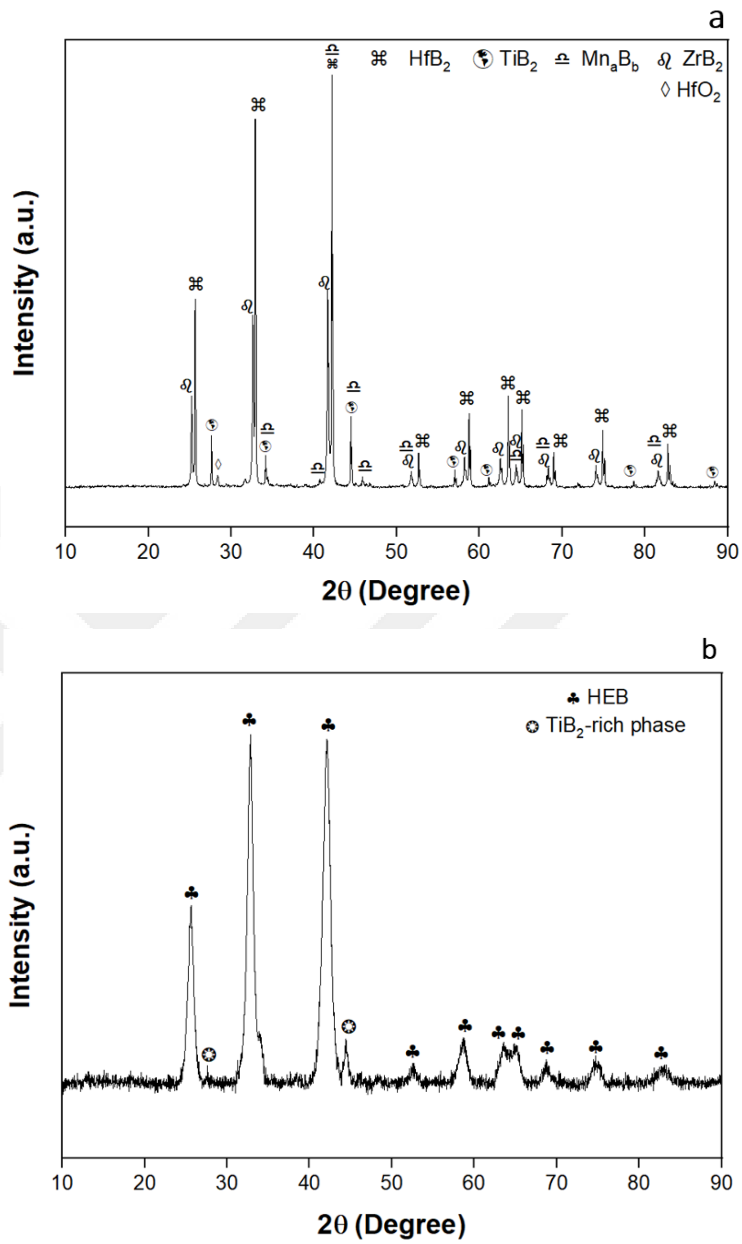

Figure 4.12 : XRD patterns of the (a) as-blended and (b) milled HEB 2 composition.

Figure 4.13 is the particle size distribution graph of the HEB 2 composition [d(0.1)=1.43 μm, d(0.5)=4.53 μm, d(0.9)=20.68 μm]. Particle size shows a bimodal distribution. The average particle size is approximately 4.5 μm. Most of the powder particles have sizes below 20 μm. According to the three-component HEB 1 system, the addition of Mn boride as the fourth component did not cause a significant change in the particle size.

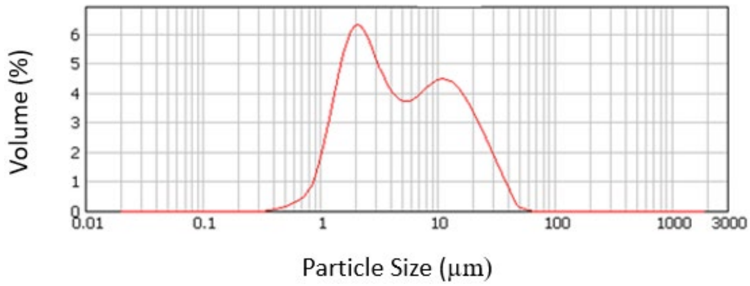

Figure 4.13 : Particle size distribution of the HEB 2 composition.

4.2.3 (Hf-Ti-Zr-Mn-Cr)B_2 composition

By adding Cr-B to the four-component system, a new five-component composition was obtained and properties of this new system were investigated. Figure 4.14a-b shows the XRD patterns of the as-blended and milled HEB 3 composition, respectively. There are HfB_2, TiB_2, ZrB_2, MnB, MnB_2, Mn_2B, Mn_3B_4, CrB, CrB_2, Cr_2B, Cr_3B_4 phases in the as-blended XRD pattern. Table A.1 exhibits approximate 2θ values corresponding to the Mn_aB_b and Cr_xB_y peaks. As mentioned before, the reason for the presence of different phase stoichiometries is due to the purity of the powders synthesized in the lab-scale. The strongest peaks are detected at about 2θ value of 41° for ZrB_2 and Cr-B phases.

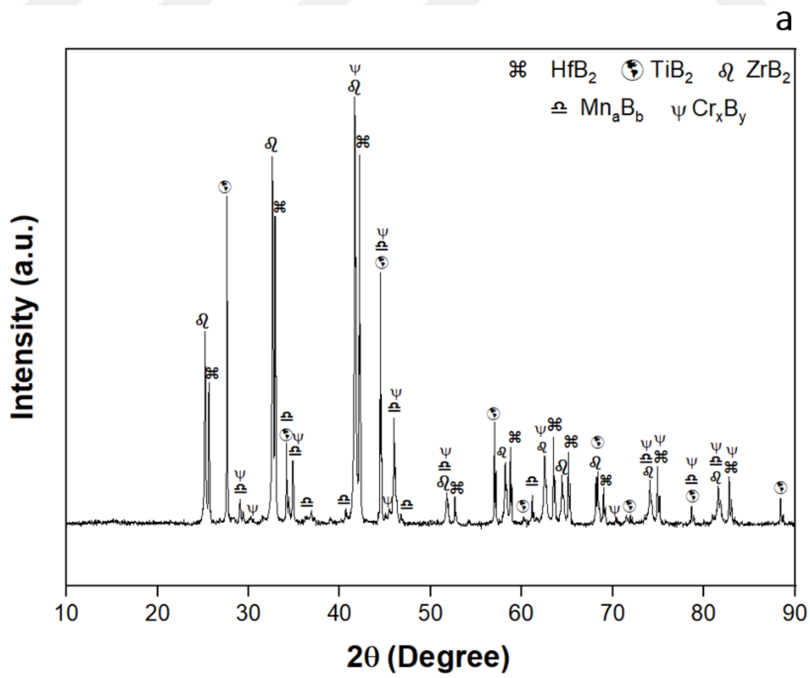

Figure 4.14 : XRD patterns of the (a) as-blended and (b) milled HEB 3 composition.

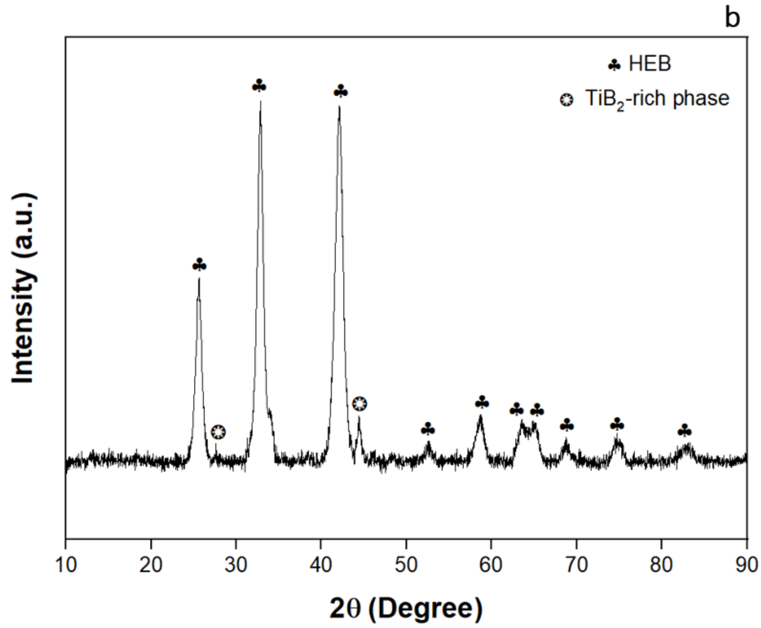

Figure 4.14 (continued) : XRD patterns of the (a) as-blended and (b) milled HEB 3 composition.

When the XRD patterns are examined after milling (Figure 4.14b), it is seen that high-entropy boride phases begin to form. As seen in other examples, TiB_2-rich phase occurs in two peak positions ($2\theta \cong 27.5^{o}$ and 44.3^{o}). Besides, it is also thought that MnB ($2\theta \cong 44.6^{o}$) and Cr_2B ($2\theta \cong 44.1^{o}$) phases are formed, but TiB_2 was considered to be more dominant and overlapped phase. Therefore, it has been referred to that the phase is TiB_2-rich. Also, Cr_2B and MnB phases do not participate in the high-entropy lattice structure.

Figure 4.15 represents the particle size distribution graph, which shows a bimodal distribution for the HEB 3 composition [d(0.1)=1.4 µm, d(0.5)=3.70 µm, d(0.9)=20.40 µm]. 50 % of the powder particles have a distribution below than 3.7 µm and 90 % have a distribution below than 20.4 µm. It is clearly seen that the particle size decreases in comparison with both three and four-component systems.

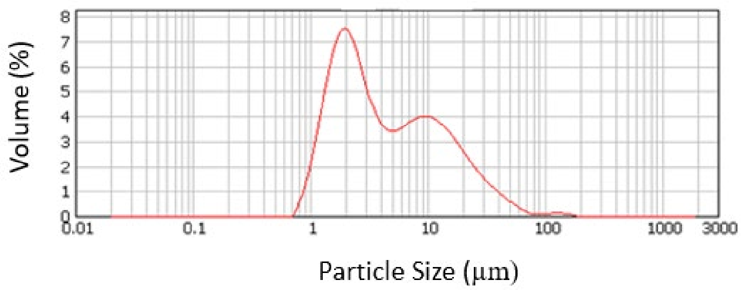

Figure 4.15 : Particle size distribution of the HEB 3 composition.

4.2.4 (Hf-Ti-Zr-Mn-Ta)B_2 composition

Firstly, the Mn-B phase constituted powders was added to the three-component basic system. In order to examine the addition of different elements in quinary systems, the TaB phase was added instead of Cr-B. The production of the five-component system containing the TaB was carried out using optimum conditions, as in all other samples. The XRD patterns of the as-blended and high-energy ball milled HEB 4 composition are shown in Figure 4.16a-b. The as-blended peaks are sharp and most of the peaks have high intensities. Besides, the most intense peaks are the ZrB_2 and TaB phases. The XRD pattern consists of HfB_2, TiB_2, ZrB_2, MnB, MnB_2, Mn_2B, Mn_3B_4 and TaB phases. On the basis of Table A.1, the approximate peak positions versus 2θ in the Mn boride phases are shown in detail. According to the Figure 4.16b, almost all of the peaks appearing in the as-blended powders formed high-entropy boride phases after milling. In addition, it is seen that TiB_2-rich and TaB phases also exist. Besides, the TiB_2-rich peak at 2θ value of nearly 44.3° is thought to also contain the MnB phase (2θ ≅ 44.6°). This indicates that solid-solution formation has started but not been completed yet.

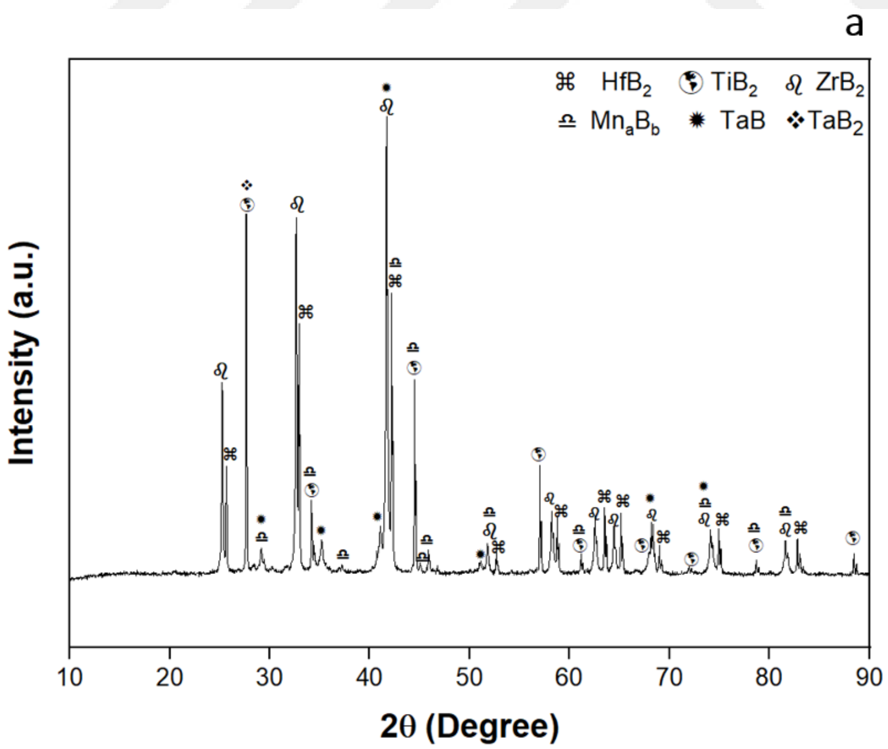

Figure 4.16 : XRD patterns of the (a) as-blended and (b) milled HEB 4 composition.

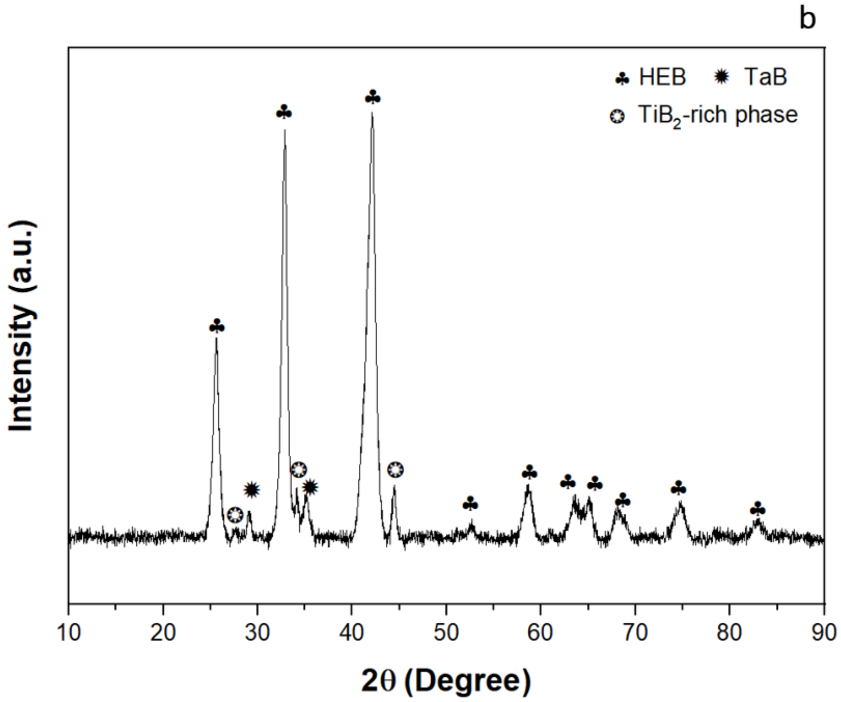

Figure 4.16 (continued) : XRD patterns of the (a) as-blended and (b) milled HEB 4 composition.

The particle size distribution of the HEB 4 composition is illustrated [d(0.1)=1.57 µm, d(0.5)=6.35 µm, d(0.9)=44.52 µm] in Figure 4.17. Particle size graph illustrates an inhomogenous distribution. The average particle size is approximately 6 µm. Almost all of the powder particles have a size distribution below than 44 µm. In comparison with the five-component HEB 3 composition, it is seen that the average particle size increases.

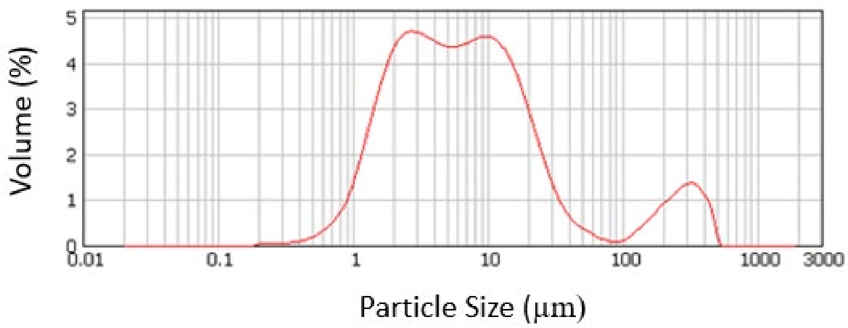

Figure 4.17 : Particle size distribution of the HEB 4 composition.

4.2.5 (Hf-Zr-Mn-Cr)B_2 composition

In this thesis, the (Hf-Ti-Zr)B_2 system was first chosen as the base ternary system. Then, the second base structure was obtained by adding Mn boride powders to this ternary system. Five-component compositions were obtained by adding Cr boride and

TaB phases to the quartet system. It was decided to proceed these studies by adding the Mn boride and Cr boride powders and enhancing the five-component systems up to eight.

In order to determine the main boride compound constituting the three-component system, Mn boride and Cr boride powders were added to the composition of the HEB 1 and four-component compositions such as (Hf-Ti-Mn-Cr)B_2, (Hf-Zr-Mn-Cr)B_2 and (Ti-Zr-Mn-Cr)B_2 were synthesized. First, the effect of the TiB_2 phase was investigated. The XRD patterns of the as-blended and milled powders without TiB_2 phase are shown in Figure 4.18a-b. There are HfB_2, ZrB_2 and multi Mn boride and Cr boride compounds in the structure. Table A.1 includes the detailed peak positions of the Mn_aB_b and Cr_xB_y phases. The as-blended powders consist of starting powders; they do not contain any oxide phase. The most intense peaks belong to the HfB_2 phase. On the other hand, the other boride compounds have low intensities. It is observed that high-entropy boride peaks begin to occur after milling in the absence of TiB_2 phase. In the nearly 2θ value of 44°, TiB_2-rich phase is not formed; besides, Mn or Cr borides are not observed, unlike other compositions. Some of the formed high-entropy boride phases (2θ ≅ 52°, 69°, 82°) do not have the expected high intensity. Furthermore, a proper phase determination cannot be done at 2θ values between 60° and 70° because of broadening. Therefore, solid-solution formation is incomplete. A sintering method is needed to obtain high-entropy boride phases.

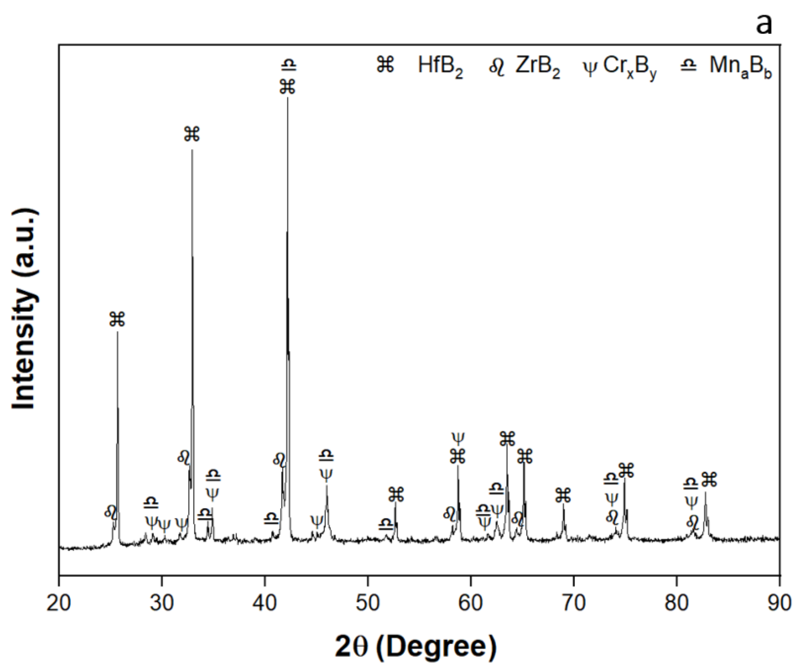

Figure 4.18 : XRD patterns of the (a) as-blended and (b) milled HEB 5 composition.

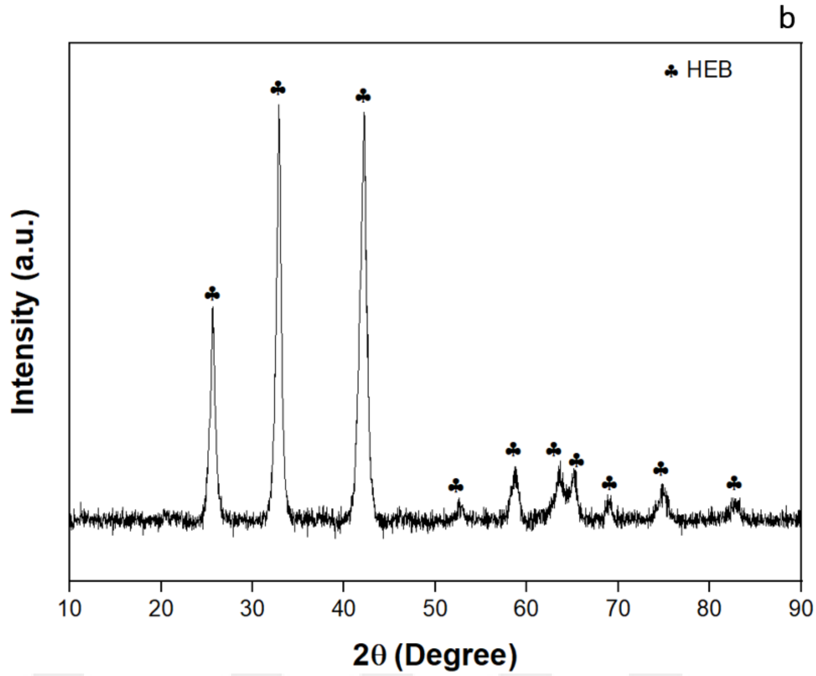

Figure 4.18 (continued) : XRD patterns of the (a) as-blended and (b) milled HEB 5 composition.

Figure 4.19 shows the particle size distribution of the HEB 5 composition [d(0.1)=1.52 µm, d(0.5)=5.03 µm, d(0.9)=26.38 µm]. The average particle size is around 5 µm. 90 % of the powders have a particle size below than 26.3 µm. It is seen that the particle size increased in contrast to the five-component HEB 3 composition. A similar increase occurs when compared to the HEB 1 composition. However, there is an insignificant increase in the particle size of the powders.

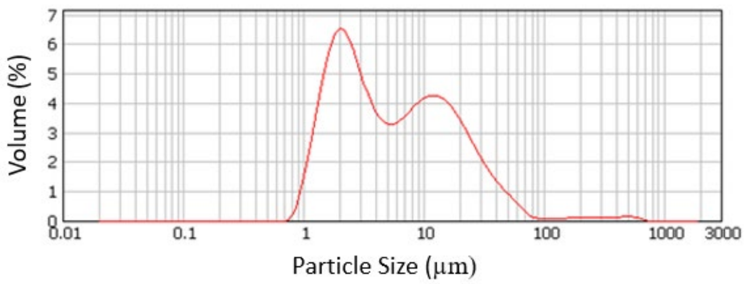

Figure 4.19 : Particle size distribution of the HEB 5 composition.

4.2.6 (Hf-Ti-Mn-Cr)B_2 composition

In the HEB 6 composition, the ZrB_2 phase vanished from the structure. Figure 4.20a includes the as-blended XRD pattern. This consists of HfB_2, TiB_2, MnB, MnB_2, Mn_2B, Mn_3B_4, CrB, CrB_2, Cr_2B and Cr_3B_4 phases. The peak positions of Mn boride and Cr boride phases are detailed in Table A.1. Figure 4.20b exhibits the XRD pattern of the milling HEB 6 composition. There are high-entropy boride phases with high intensities. Also, there are three different peaks belonging to the TiB_2-rich phase in the 2θ values of nearly 27°, 34° and 44°. As seen in other samples, it is thought that there are MnB and Cr_2B phases along with the TiB_2-rich phase at about 2θ = 44°. The peak intensities of the binary boride phases are low. In addition, a single-phase high-entropy boride structure could not be obtained, and hence sintering is needed after milling.

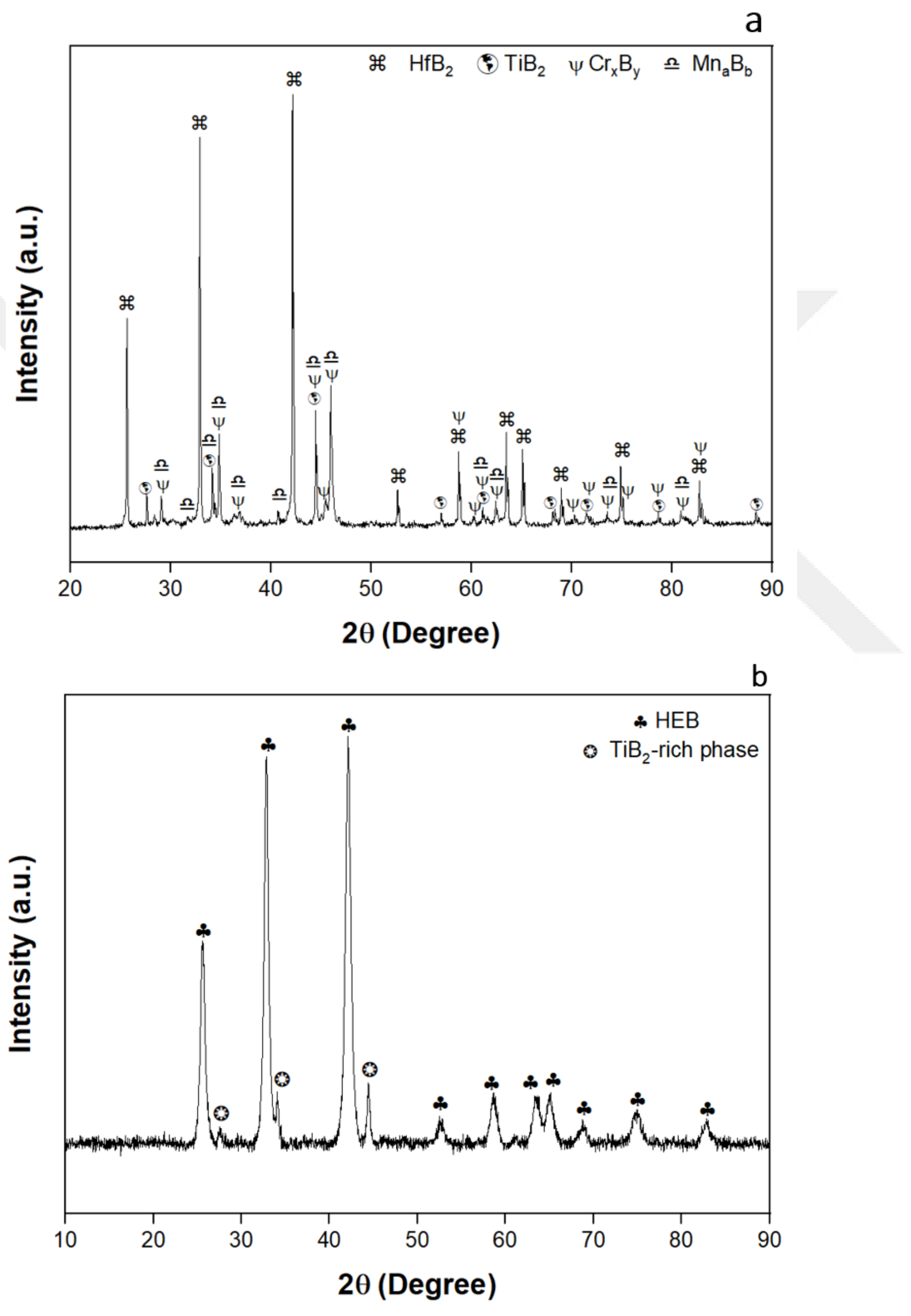

Figure 4.20 : XRD patterns of the (a) as-blended and (b) milled HEB 6 composition.

The particle size distribution of HEB 6 composition [d(0.1)=1.21 µm, d(0.5)=4.57 µm, d(0.9)=25.26 µm] is given in Figure 4.21. The histogram showing a bimodal like distribution is evident for this composition. The average particle size is approximately 4.5 µm. Furthermore, the majority of the powder particles are less than 25 µm in size. The decrease is not sharp in particle size when compared with the HEB 5 composition. It is also seen that the particle distribution graphs are similar with each other. According to the three-component HEB 1 system, the particle size is less than 0.1 µm.

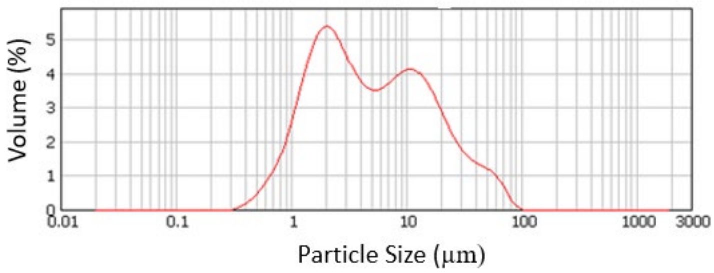

Figure 4.21 : Particle size distribution of the HEB 6 composition.

4.2.7 (Ti-Zr-Mn-Cr)B_2 composition

The synthesis was completed without the HfB_2 phase using the optimum condition in order to examine the effect of the elements in the main structure. The as-blended XRD pattern is given in Figure 4.22a. This pattern includes ZrB_2, TiB_2, Mn boride and Cr boride powders in the composition. Table A.1 includes the peak positions of the different Mn and Cr boride phases in the as-blended powders. The peaks are sharp; also, the most intense peaks belong to the TiB_2, MnB and Cr_2B phases. The as-blended XRD pattern does not contain any oxide phase. Figure 4.22b represents the after milling XRD pattern. There are high-entropy boride phases. However, the counts of high-entropy boride peaks formed after about $2\theta \cong 50^o$ are not so intense. In addition, the broadening of the peaks is not as expected. The peak at $2\theta \cong 47^o$ includes many Cr and Mn boride (Mn_3B_4, MnB_2, Cr_3B_4, CrB_2 and CrB) phases. Most high-entropy boride phases occur at lower intensities. Moreover, as in other compositions, the MnB ($2\theta \cong 44.7^o$) and Cr_2B ($2\theta \cong 44^o$) phases could be formed together with the TiB_2-rich phase ($2\theta \cong 44.3^o$). As a result, it is evaluated that it is rich in TiB_2 due to the overlapping. In the HEB 7 composition, the TiB_2-rich phase, which form at low intensity in other compositions at about 2θ value of 27°, occurs at high intensity. The Mn_3B_4 and Cr_3B_4 phase were observed at nearly about 61°. The XRD pattern of the milled HEB 7 composition contains metal boride powders that have a higher intensity but do not significantly participate in hexagonal structure as compared with those of HEB 5 and HEB 6 compositions. This shows that the HfB_2 phase forms the basis of the main structure and suppresses the different metal boride compounds that may occur. For the HEB 7 composition, it is not sufficient to obtain a single-phase high-entropy boride with mechanical alloying; a subsequent method is also needed.

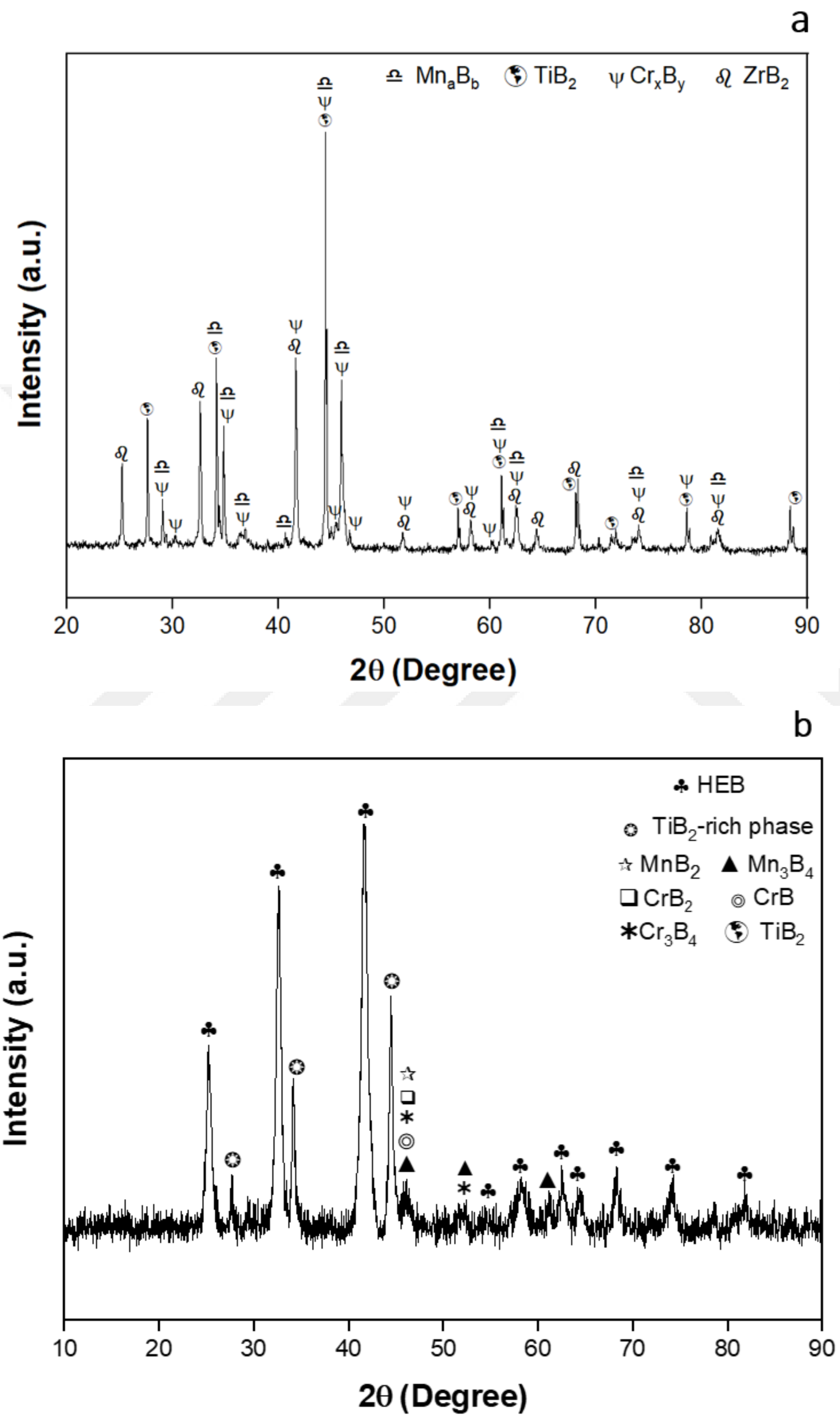

Figure 4.22 : XRD patterns of the (a) as-blended and (b) milled HEB 7 composition.

For the HEB 7 composition, particle sizes have multi-modal distribution [d(0.1)=1.65 μm, d(0.5)=9.16 μm, d(0.9)=41.75 μm] in the Figure 4.23. The average particle size is nearly 9 μm. It is also seen that 90 % of the powder particles are synthesized below than 41 μm. However, the increase in particle size of the HEB 7 composition is evident in contrast to the HEB 5 and HEB 6 compositions. Also, there is a significant increase as compared to the three-component system, which is HEB 1 composition. It is understood that the HfB_2 phase has a higher effect on the main composition than other elements.

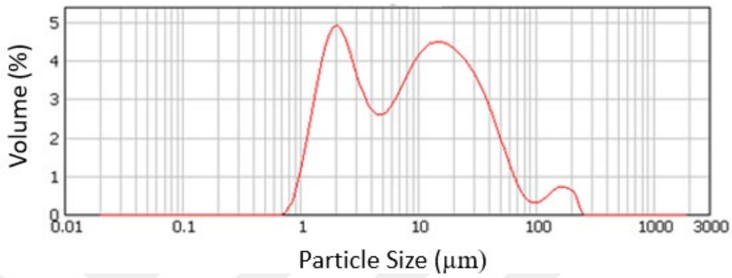

Figure 4.23 : Particle size distribution of the HEB 7 composition.

4.2.8 (Hf-Ti-Zr-Mn-Cr-Mo)B_2 composition

Synthesizing experiments were carried out by adding different boride compounds to the HEB 3 composition, which was chosen as the basic structure, until a six and/or eight-component structure was obtained.

First, the Mo boride powders were added to the HEB 3 composition. The XRD graph of the as-blended HEB 8 composition is seen in Figure 4.24a. This graph does not exhibit any oxide phase or by-product; it only includes starting powders. There are multi Mn boride, Cr boride and Mo boride compounds. These compounds are located at different peak positions, as shown in Table A.1. According to the XRD pattern of Figure 4.24b, there are high-entropy boride and TiB_2-rich phases at about 2θ values of 27 °, 33.9 ° and 44.3°. With TiB_2-rich phases, MnB (≌ 44.7°) and Cr_2B (≌ 44.1°) are more likely to occur. Besides, MoB_2 (≌ 34.7°) and MoB_4 (≌ 34.3°) phases can take place in the structure. As the number of components increased, the multi-boride compounds that did not participate in the structure increased with low peak intensities. The strongest peaks still belong to the high-entropy boride phases. Nonetheless, a single-phase high-entropy boride structure could not be obtained yet.

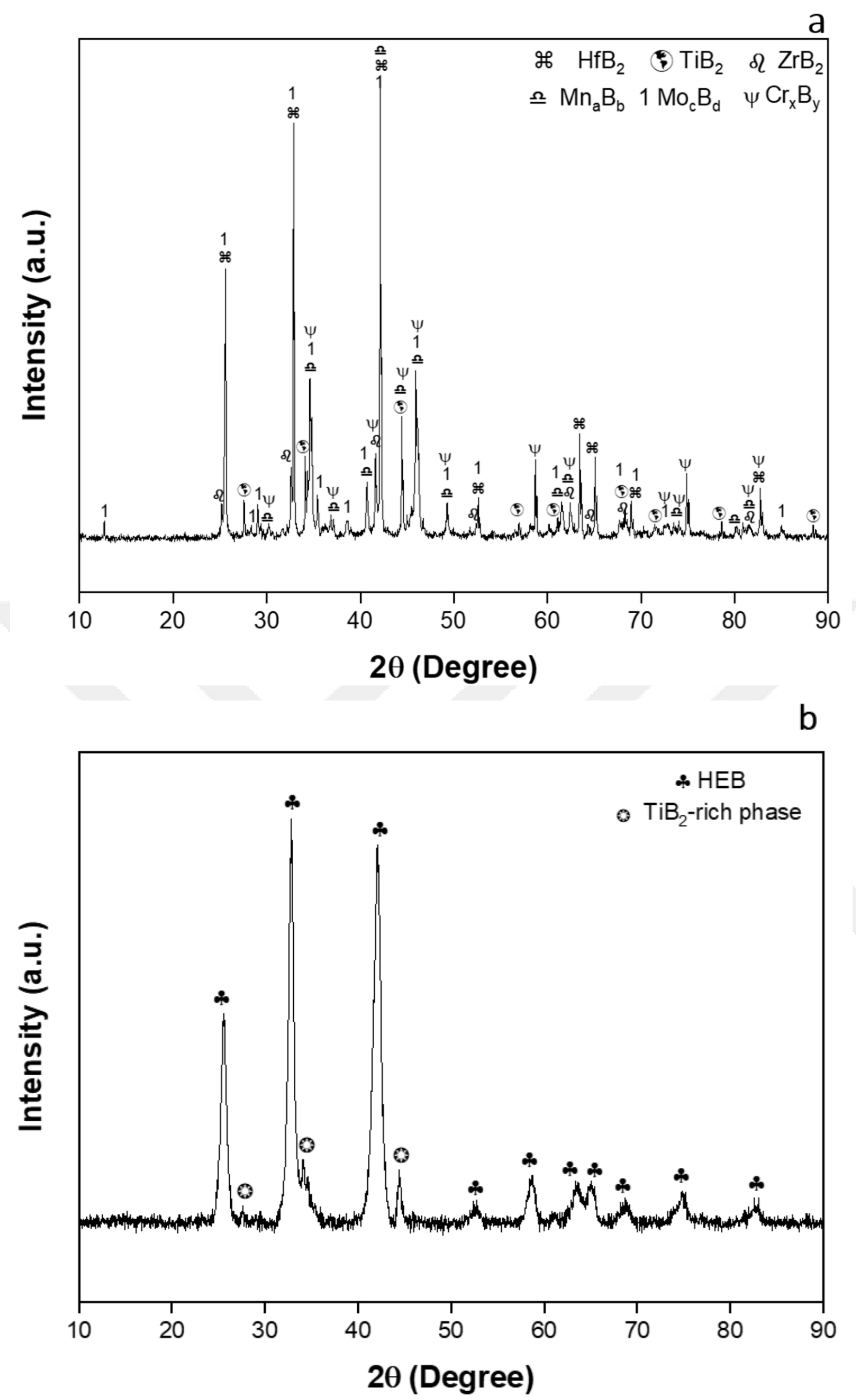

Figure 4.24 : XRD patterns of the (a) as-blended and (b) milled HEB 8 composition.

Figure 4.25 illustrates the multi-modal particle size distribution of HEB 8 composition [d(0.1)=1.44 µm, d(0.5)=3.45 µm, d(0.9)=15.29 µm]. The most of powder particles were synthesized below than 15.2 µm and the average particle size is about 3 µm, indicating that the addition of Mo boride phase reduces the particle size when compared to the HEB 3 composition.

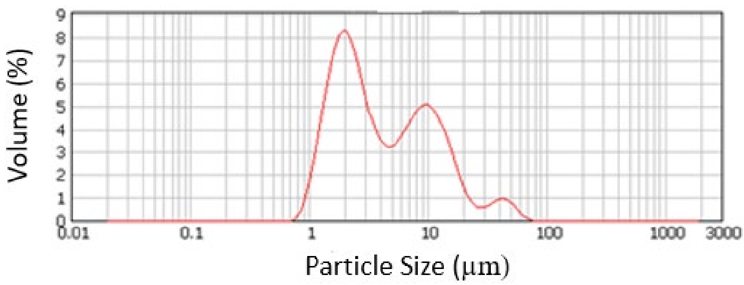

Figure 4.25 : Particle size distribution of the HEB 8 composition.

4.2.9 (Hf-Ti-Zr-Mn-Cr-W)B_2 composition

On the basis of Figure 4.26a, it is seen that the HfO_2 phase (≅ 27°) occured with the starting powders. Descriptions and detailed positions of Mn-B, Cr-B, W-B phases are given in Table A.1. There are a lot of sharp peaks in the as-blended powders. In Figure 4.26b, high-entropy boride phases with low and high intensities were formed. TiB_2-rich phases observed at nearly 44.3° in all compositions were formed at low intensity. This TiB_2-rich phase is thought to be accompanied by MnB (≅ 44.7°) and Cr_2B (≅ 44.1°). In addition, it is seen that a high intensity W_2B (≅ 40°) phase is formed. Also, Mn_3B_4 and CrB phases are emerged at different peak positions and with many W_2B phases. A second method is needed due to the high-entropy boride phases that cannot be obtained in a single-phase and the different boride compounds are seen.

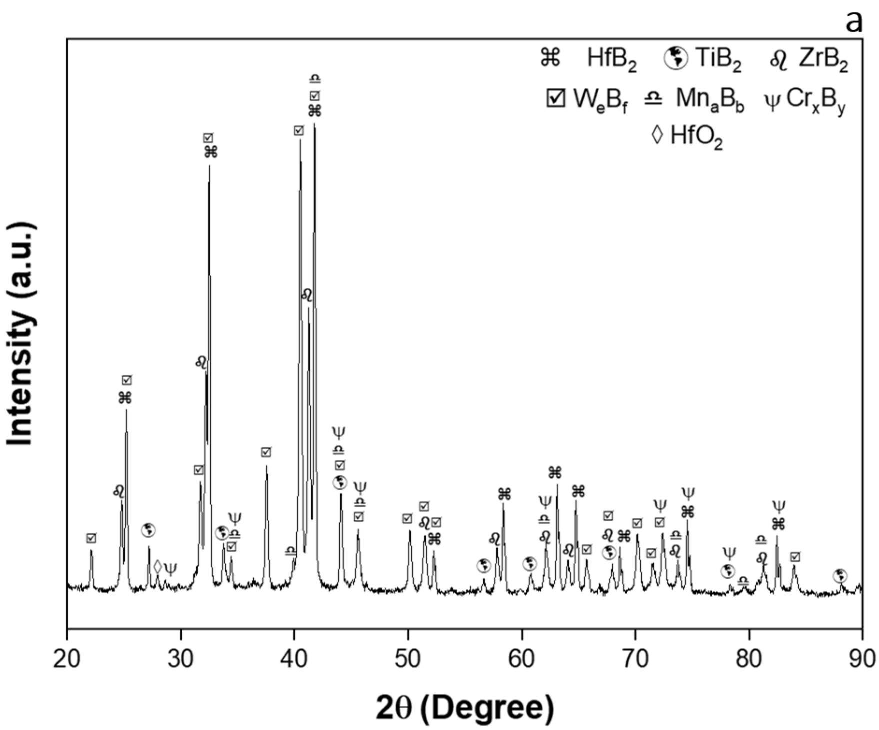

Figure 4.26 : XRD patterns of the (a) as-blended and (b) milled HEB 9 composition.

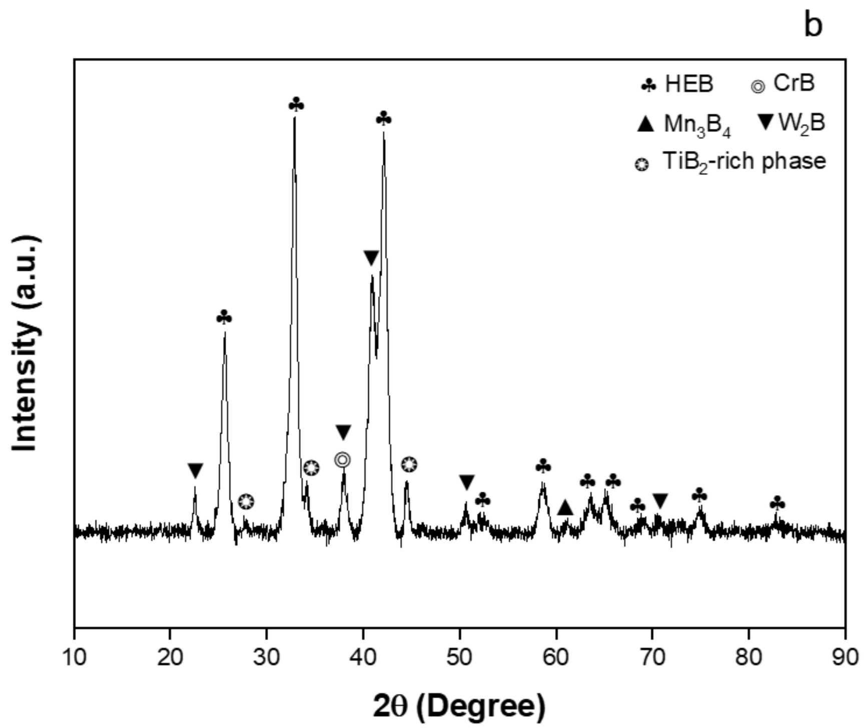

Figure 4.26 (continued) XRD patterns of the (a) as-blended and (b) milled HEB 9 composition.

A multi-modal particle size distribution are in Figure 4.27 for the HEB 9 composition [d(0.1)=1.39 μm, d(0.5)=3.02 μm, d(0.9)=14.06 μm]. The low reductions in the particle sizes can be observed in comparison with the HEB 8 composition. The average particle size is nearly 3 μm and most of the powder particle sizes are lower than 14 μm.

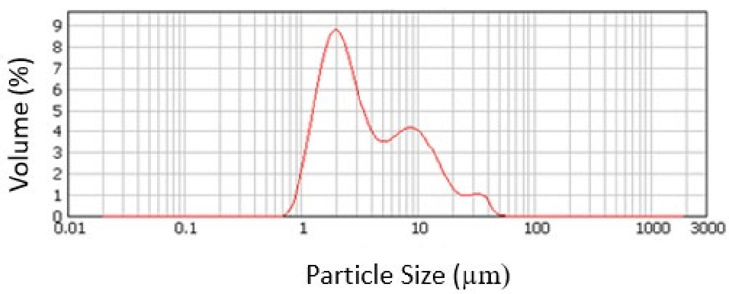

Figure 4.27 : Particle size distribution of the HEB 9 composition.

4.2.10 (Hf-Ti-Zr-Mn-Cr-Mo-W)B_2 composition

As a result of the six-component systems, a single-phase structure could not be obtained and no significant change in particle sizes was observed. Therefore, a seven-component structure was obtained by adding the Mo boride and W boride phases together. Figure 4.28a-b represents XRD patterns of the HEB 10 composition both as-blended and milled powders. According to the as-blended powders (Figure 4.28a), there are only starting constituent and they do not contain any oxide phases. The HfB_2, TiB_2 and ZrB_2 phases are present as diborides, whereas the Mn boride, Cr boride, W boride and Mo boride powders are present as different boride compounds. The descriptions of these multi-phase boride compounds are given in detail in Table A.1. After milling, low and high intensity, high-entropy boride peaks are observed together, as in other compositions (Figure 4.28b). Along with all these, there are CrB, Mn_3B_4, Mo_2B, W_2B and TiB_2-rich phases with different intensities and peak positions. The most intense peaks belong to two different high-entropy boride phases, W_2B (≅ 40°) and Mo_2B (≅ 40°). As with other compositions, an additional method is needed to obtain a single-phase structure.

There is a bimodal particle size distribution of the HEB 10 composition [d(0.1)=1.44 µm, d(0.5)=3.07 µm, d(0.9)=11.56 µm], in Figure 4.29. According to the HEB 9 composition, there is no significant reduction in average particle size after milling (~ 3 µm), since all the constituent powders are below than 11.5 µm.

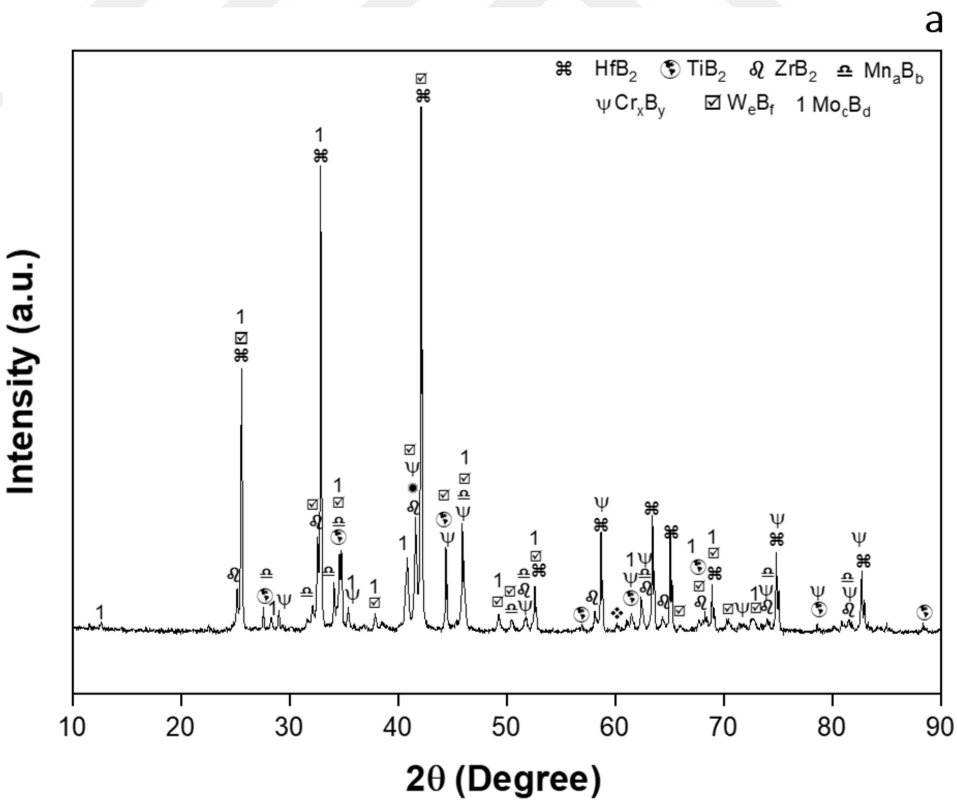

Figure 4.28 : XRD patterns of the (a) as-blended and (b) milled HEB 10 composition.

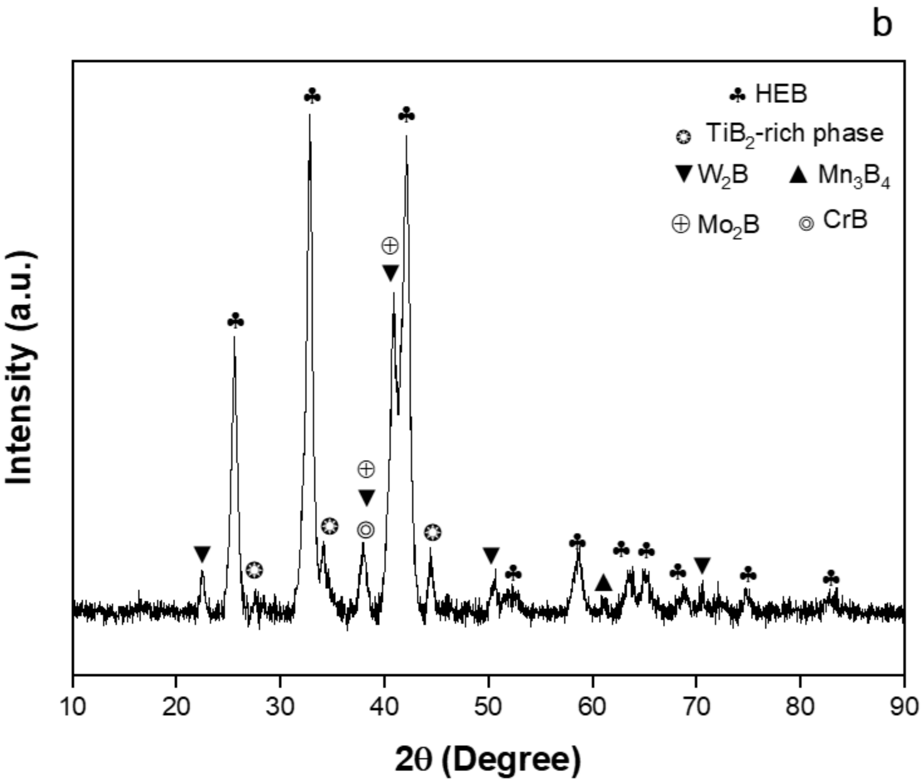

Figure 4.28 (continued) : XRD patterns of (a) as-blended and (b) milled HEB 10 composition.

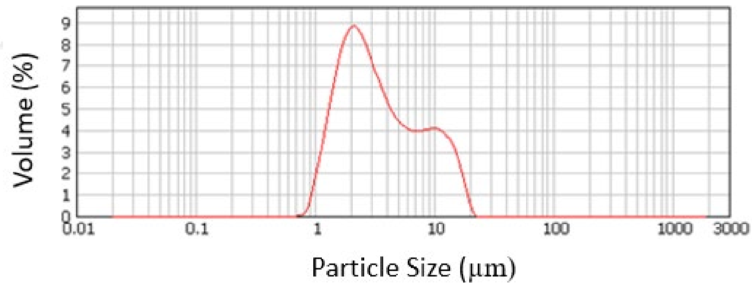

Figure 4.29 : Particle size distribution of the HEB 10 composition.

4.2.11 (Hf-Ti-Zr-Mn-Cr-Mo-Ta)B_2 composition

In order to examine the effect of Mo boride and W boride powders with TaB powder, seven-component compositions were created separately. Figure 4.30a-b shows the XRD patterns of the as-blended and milled seven-component structure containing Mo-B and TaB phases. The XRD pattern of the as-blended composition consists of the HfB_2, TiB_2, ZrB_2, TaB, TaB_2 and different Mn-B, Cr-B, Mo-B boride compounds as shown in Table A.1. Moreover, there exists no oxide phase or by-product. After milling (Figure 4.30b), high-entropy boride phases at different peak positions like TiB_2-rich phases (≅ 33.9° and 44.3°) and TaB (≅ 29° and 34°) are present. It is quite evident that a single-phase structure could not be obtained. It is also thought that Cr_2B

($\cong$ 44.1°), MnB ($\cong$ 44.7°) and MoB_4 ($\cong$ 34.3°) can be formed in the TiB_2-rich phases. These peaks have low intensities.

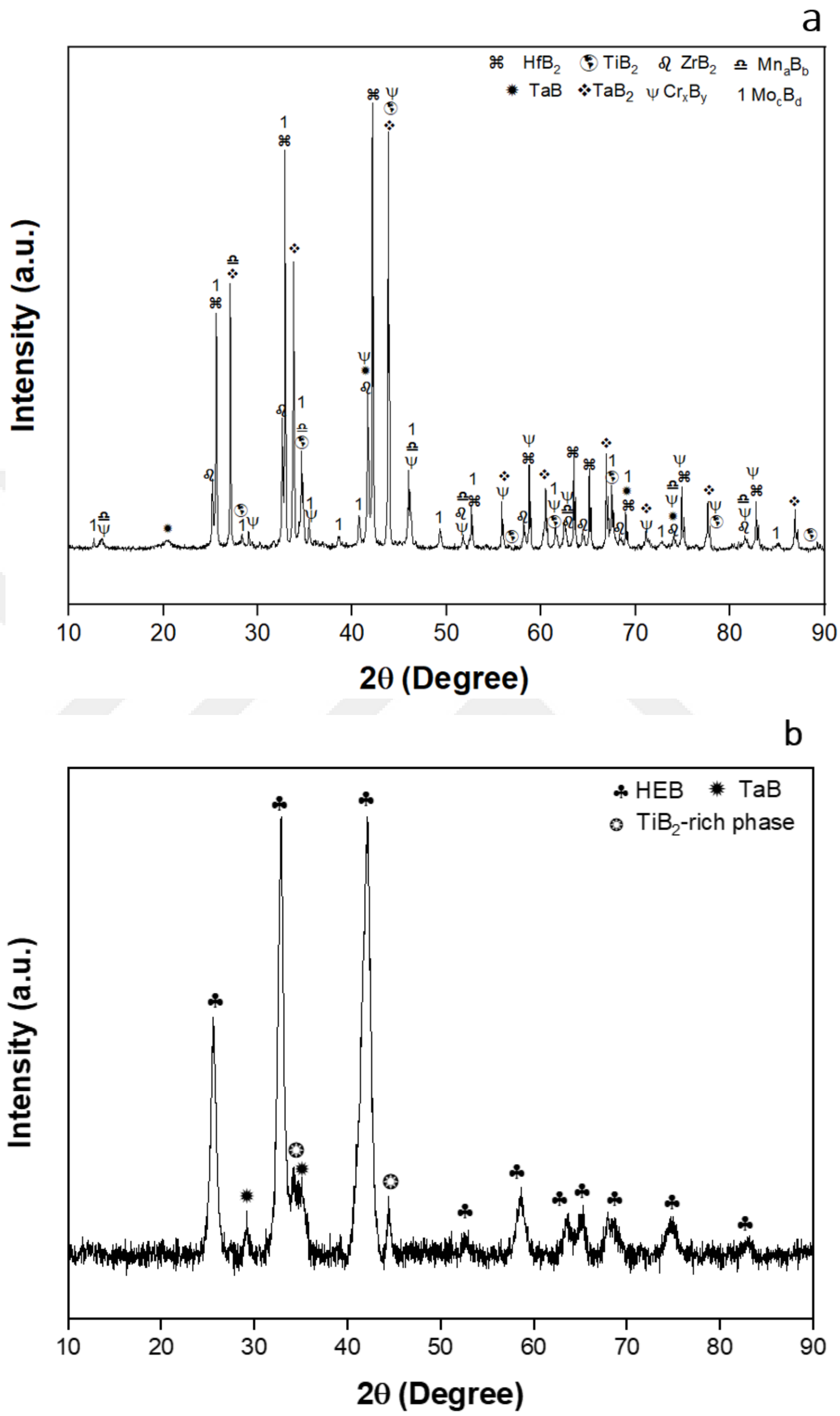

Figure 4.30 : XRD patterns of the (a) as-blended and (b) milled HEB 11 composition.

The average particle size of the HEB 11 composition [d(0.1)=1.27 μm, d(0.5)=2.24 μm, d(0.9)=5.42 μm] is about 2 μm. The particle size distribution graph can be seen in Figure 4.31. Most of the particles are below than 5.4 µm. A more homogenous particle size distribution was obtained in the seven-component composition.

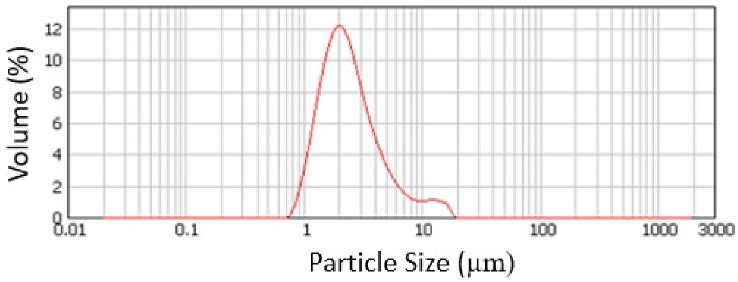

Figure 4.31 : Particle size distribution of the HEB 11 composition.

4.2.12 (Hf-Ti-Zr-Mn-Cr-W-Ta)B_2 composition

A seven-component system was obtained by adding W boride structure instead of Mo boride and its properties were compared with those of other compositions. According to the XRD pattern of Figure 4.32a, there are HfB_2, TiB_2, ZrB_2, TaB, TaB_2 boride phases at different positions. Also, there are Mn boride, Cr boride and W boride phases that occur in different peaks and their explanations are given in Table A.1. In addition to all these, it is seen in Figure 4.32b that high-entropy boride phases begin to form after milling, but these HEB phases are together with different boride phases with high peak intensities and different positions. These peaks are TiB_2-rich phases (≅ 27.2°, 33.9° and 44.3°), CrB (≅ 37.9°), TaB (≅ 40.7°) and W_2B (≅ 22.5°, 37.9° and 40.7°) at various 2θ positions. On the other hand, it can be stated that MnB, Cr_2B and TaB_2 phases also take place in the peak position at 44.9°. However, due to overlapping peaks, this peak was interpreted as TiB_2 dominant. For this reason, it was named as TiB_2-rich phase. Besides, there is a WC phase contamination located at 2θ value of ≅ 78°. In this case, a second method should be used to obtain the single-phase structure.

The bimodal particle size distribution graph with an average particle size of 2 µm is shown in Figure 4.33. As in the HEB 12 composition [d(0.1)=1.24 µm, d(0.5)=2.08 µm, d(0.9)=9.37 µm], it is observed that the average particle size decreased in contrast to the other components.

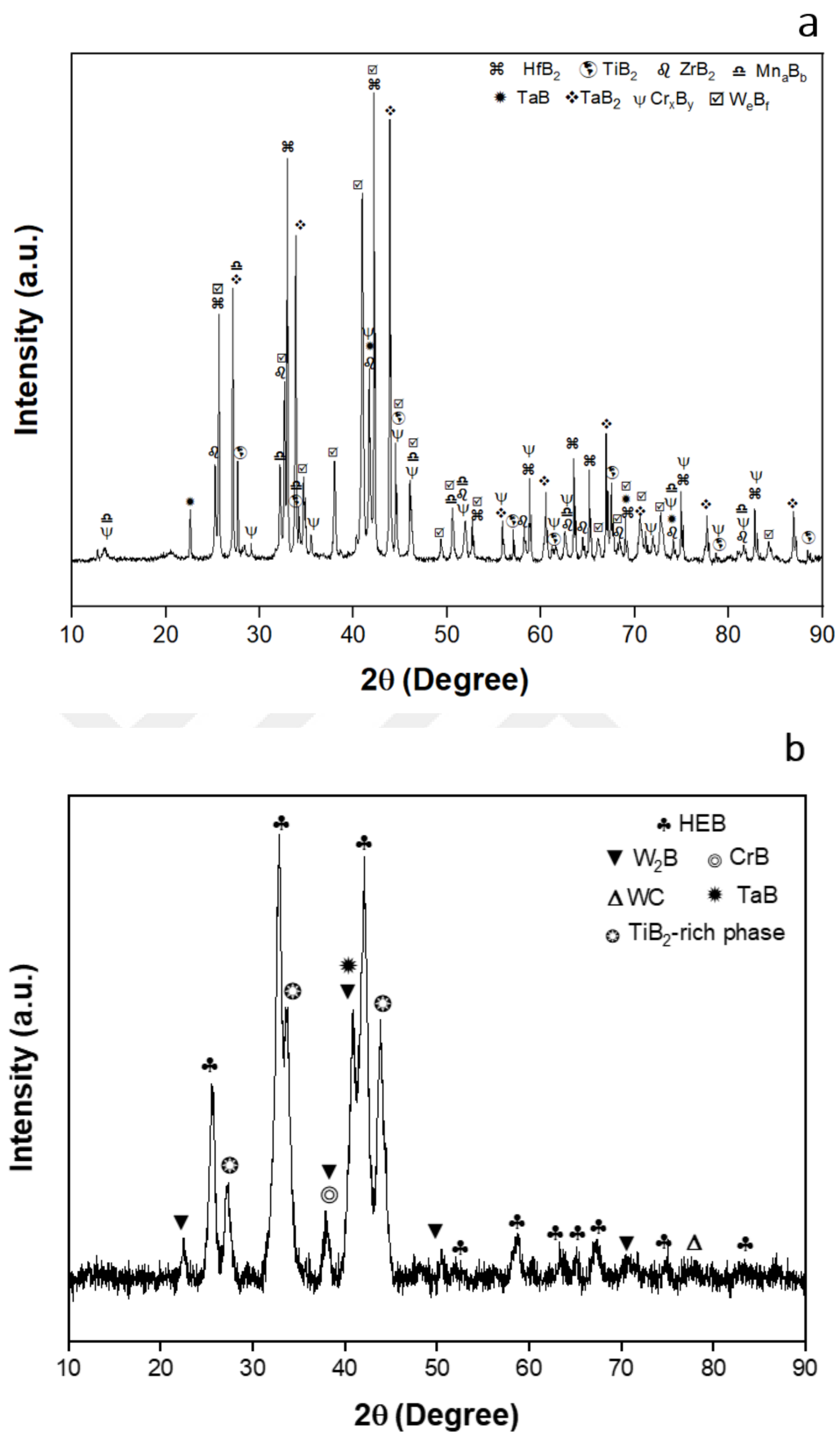

Figure 4.32 : XRD patterns of the (a) as-blended and (b) milled HEB 12 composition.

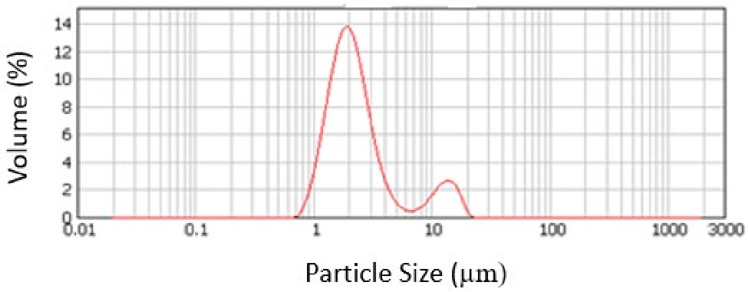

Figure 4.33 : Particle size distribution of the HEB 12 composition.

4.2.13 (Hf-Ti-Zr-Mn-Cr-Mo-W-Ta)B_2 composition

Finally, an eight-component sample containing all synthesized borides at lab-scale was produced. Figure 4.34a exhibits the XRD pattern of the as-blended, consisting of only the starting phases without any contamination. Detailed peak positions and explanations of the initial phases are given in Table A.1. On the other hand, Figure 4.34b shows the XRD pattern of milled HEB 13 composition. It contains different compounds high-entropy boride phase in addition to different compounds belonging to the initial boride phases (TiB_2-rich phases, TaB, W_2B, CrB and Mo_2B). It is clearly seen that a single-phase high-entropy boride structure could not be obtained.

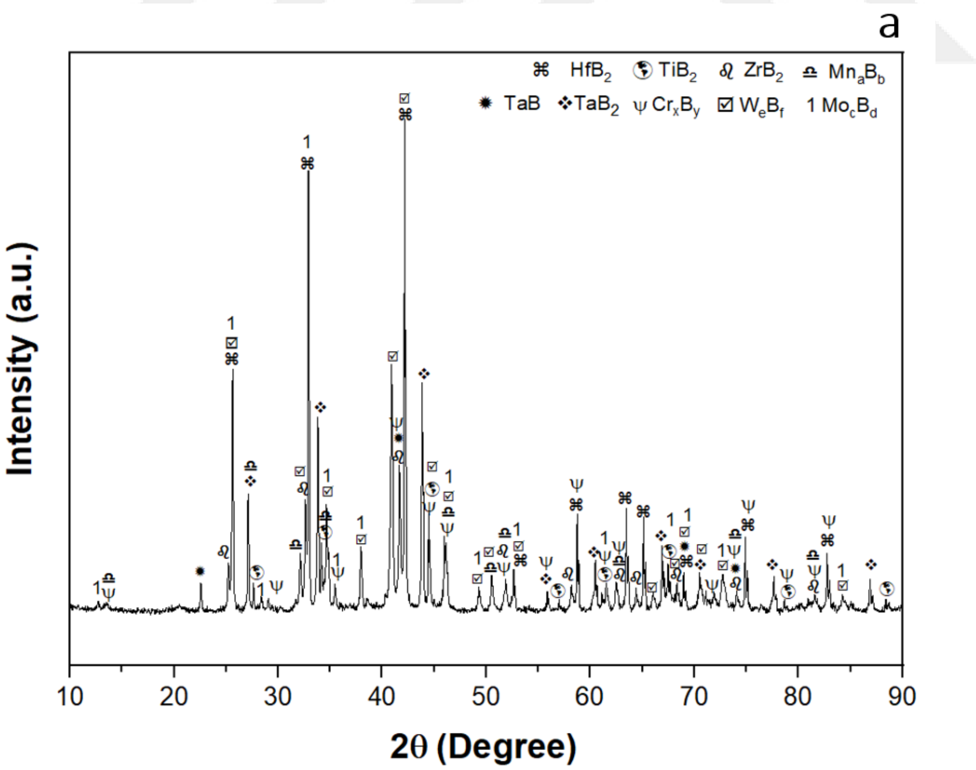

Figure 4.34 : XRD patterns of the (a) as-blended and (b) milled HEB 13 composition.

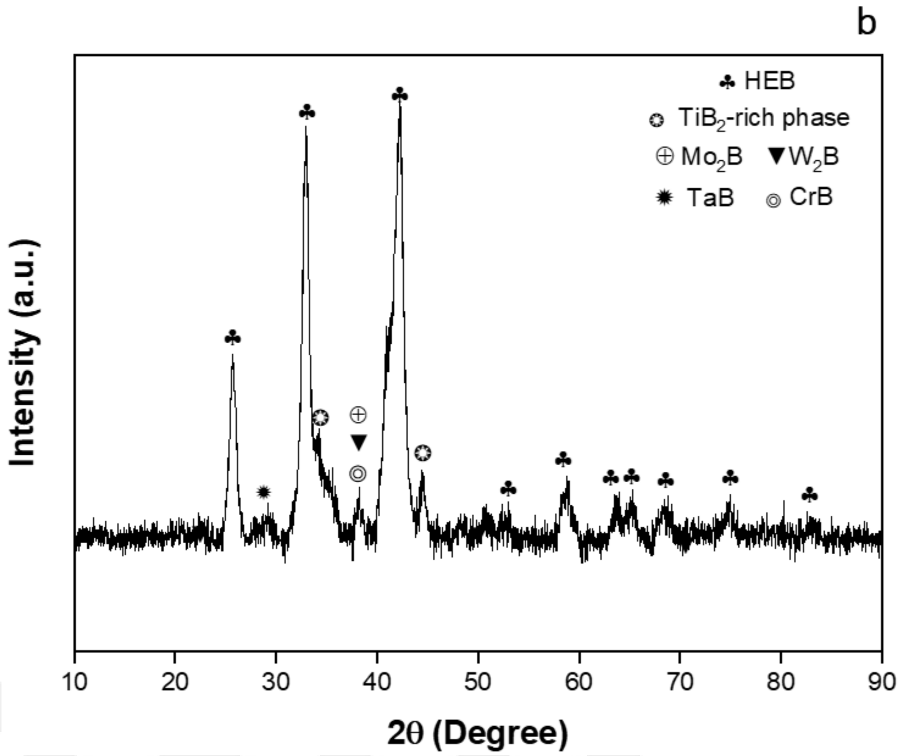

Figure 4.34 (continued) : XRD patterns of the (a) as-blended and (b) milled HEB 13 composition.

The last particle size distribution graph is given at Figure 4.35 for the HEB 13 composition [d(0.1)=1.31 μm, d(0.5)=2.2 μm, d(0.9)=5.6 μm]. Average particle size is around 2 μm. The particle size increased insignificantly (about 0.1 μm) over the seven-component systems. However, almost all of the synthesized powder particles are below than 5.6 μm. It can be said that eight-component sytsem have the lowest particle size in all of the compositions.

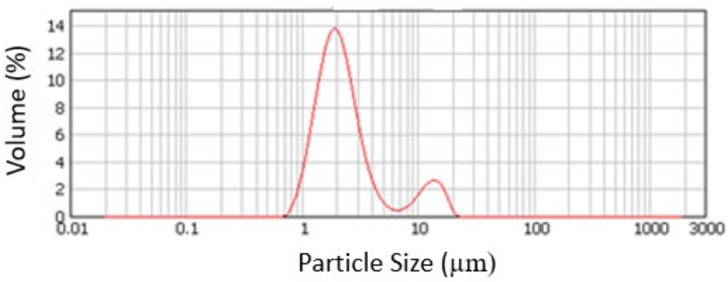

Figure 4.35 : Particle size distribution of the HEB 13 composition.

Considering all compositions, it was understood that a single-phase high-entropy boride structure could not be synthesized after high-energy ball milling and and hence subsequent method was needed. In the literature studies, multi-phases with very different crystal structures were detected after high-energy ball milling (Gild et al, 2016; Qin et al, 2020a; Storr et al, 2021). This indicates that temperature and mechanical impact are not sufficient for the formation of a single-phase high-entropy boride structure (Gild et al, 2020; Y. Zhang et al, 2020). Single-phase high-entropy boride synthesis can be completed using different sintering methods. In this thesis, the spark plasma sintering (SPS) method was used after milling to obtain a single-phase structure.

4.2.14 Density measurement of hybridized powders

Table 4.2 and Figure 4.36 show the average density values of the hybridized powders. The highest density value is seen in the HEB 12 composition consisting of (Hf-Ti-Zr-Mn-Cr-W-Ta)B_2, and the lowest density value is seen in the HEB 7 composition consisting of (Ti-Zr-Mn-Cr)B_2. Since the density of the HfB_2 phase is higher than that of other binary boride compounds, the composition without this phase is expected to have the lowest density value.

Table 4.2 : Average density values of hybridized powders.

Sample Code	Average Density (g/cm^3)
HEB 1	6.5912 ± 0.002
HEB 2	6.365 ± 0.004
HEB 3	6.1728 ± 0.0047
HEB 4	6.6487 ± 0.0054
HEB 5	6.4485 ± 0.0065
HEB 6	6.2225 ± 0.0077
HEB 7	4.9708 ± 0.005
HEB 8	6.1034 ± 0.0044
HEB 9	6.7467 ± 0.0035
HEB 10	6.8445 ± 0.0083
HEB 11	6.5268 ± 0.0067
HEB 12	7.1379 ± 0.0057
HEB 13	6.842 ± 0.006

In five-component systems, it is seen that the addition of TaB increases the powder density in contrast to the addition of Cr boride. The densities of all four-component systems are lower than that of the HEB 1, which is the main structure. In quaternary systems, the HEB 5 composition, which does not contain the TiB_2 phase, has the highest density value. In systems with six-components, it is evident that the addition of the W boride powder significantly increases the density value in contrast to the Mo boride phase. When the W boride and TaB phases were combined in the seventh system, the powder density was at its highest. With the addition of the Mo boride phase, the density value decreased under all conditions. There is no direct relationship between the number of components and the density value. It has been observed that HfB_2, TaB and W boride phases cause an increase in the powder density under their composition conditions. HfB_2, TaB and W boride densities are shown in Table 2.2.

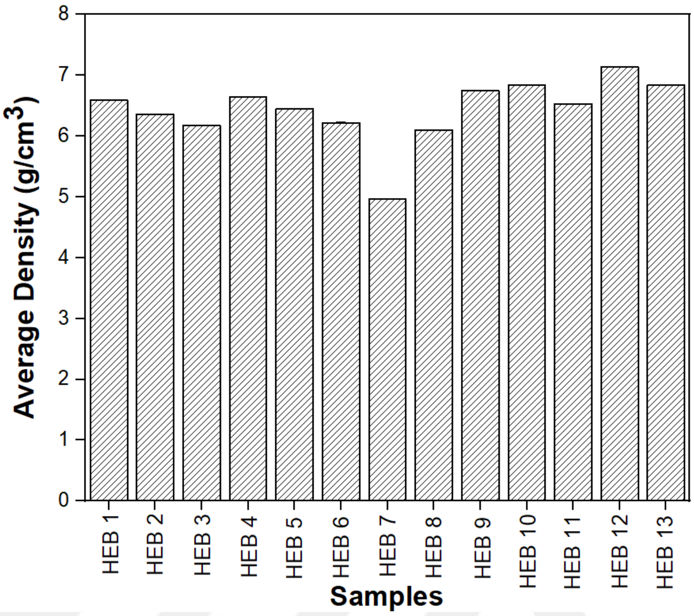

Figure 4.36 : Average density values of hybridized powders.

4.3 Phase and Microstructural Analysis of Sintered Samples

The characterization of the sintered samples using spark plasma sintering (SPS) will be explained in this section. First of all, the phase analysis performed with XRD will be mentioned. Then, microstructural characterization will be explained with the EDS analysis results.

4.3.1 (Hf-Ti-Zr)B_2 composition

Figure 4.37 shows the XRD pattern of the HEB 1 composition after SPS. Compared to Figure 4.9, it can be observed that the peak positions shifted and the peaks became more intense. This indicates that the crystal structure is still stable and the crystallinity is high. Small intensity peaks in the TiB_2-rich phase disappeared. Also, the WC phase, which occurs as a contamination, is not detected. This indicates that these phases react under the influence of high temperature and pressure. In addition, there are small amount of (Hf, Zr)O_2 phase formed. It is due to the stability of the HfO_2 and ZrO_2 (ICDD No: 01-083-0810) structures. As previously stated, three element compositions are defined as "middle-entropy alloys". So this base alloy is a “medium-entropy boride” and these peaks belong to the medium-entropy phase. In addition, Demirskyi et al. (2020) synthesized medium-entropy $(Zr_{1/3}Hf_{1/3}Ta_{1/3})B_2$ using the spark plasma sintering route from diboride powders. Using a sintering temperature of 1927 ℃ and dwell time of 20 min, AlB_2 type single-phase structure was obtained. Also, they synthesized another medium-entropy $(Zr_{1/3}Nb_{1/3}Ta_{1/3})B_2$ diboride ceramics with the same route (Demirskyi et al, 2020).

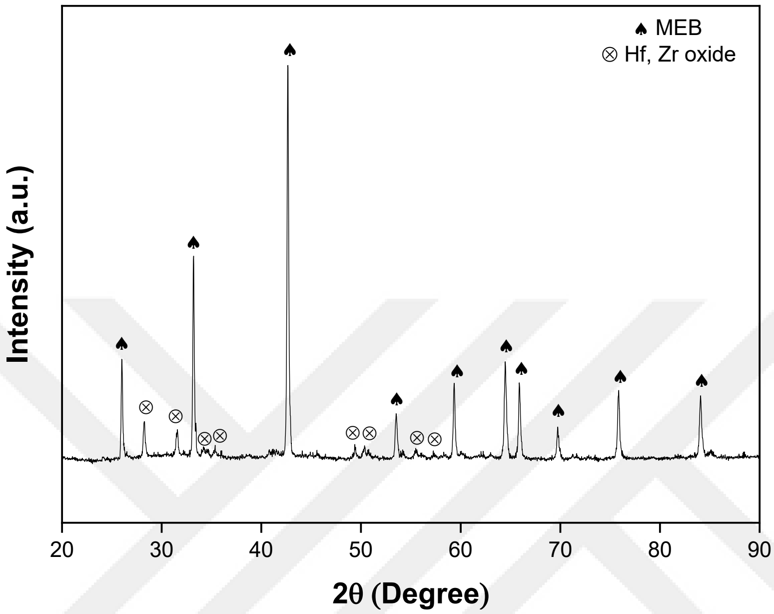

Figure 4.37 : XRD pattern of the HEB 1 composition after SPS.

Figure 4.38a-b shows the SEM and color EDS images of the HEB 1 composition at a magnification of 2500X. The matrix exhibits an inhomogenous microstructure, like "stony" appearance. With light and dark colored regions. It is seen that eutectic zones are formed between grains, albeit partially. According to the color analysis (Figure 4.38b), it is clearly evident that the Hf element, which appears as yellow color in the structure, is dominant. The mixture of Zr, which is blue, and Hf, which is yellow, gives the green color. The green color in the color EDS image represents the Zr elements distributed over Hf. In addition to all these, the purple-colored Ti element has a partical dispersion in the microstructure. Boron element could not be properly detected due to the probable peak overlapping and limited detection capability. The results of general EDS analysis (Table 4.3) also confirmed that the Hf element is dominant in the structure, followed by Zr and Ti elements. When the first point is examined, it is seen that there is a high amount of Hf element in weight, and the Ti structure is almost non-existent. In this case, it can be said that light-colored, white regions are Hf-rich regions. As the second point distribution is closer to the general distribution; it is the richest Zr region. It is understood that while Hf decreases in weight, Ti and Zr increase in weight. The third point may represent the matrix and gives a closer result to the general distribution. The fourth point is the richest Ti region. Dark colors dominate here. At the fifth point, it is seen that Ti and Zr increase according to the general distribution. Also, dark areas might be porous regions.

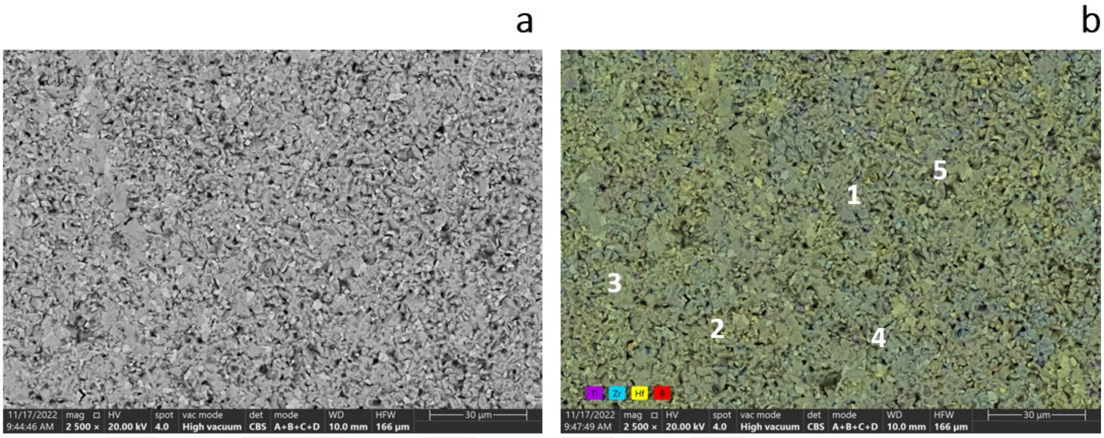

Figure 4.38 : (a) SEM and (b) color EDS images of the HEB 1 composition at 2500X.

Table 4.3 : EDS spectral analyses of the HEB 1 composition.

Weight (%)	General	Point 1	Point 2	Point 3	Point 4	Point 5
Ti	14.5	0.8	16.5	16.3	19.5	16.5
Zr	26.0	22.4	35.2	27.9	27.0	30.7
Hf	59.5	76.8	48.3	55.8	53.5	52.8

4.3.2 (Hf-Ti-Zr-Mn)B_2 composition

Figure 4.39 displays the XRD pattern of the SPS'd HEB 2. In comparison with Figure 4.12, there are no TiB_2, MnB and Mn_2B phases. All of the secondary boride phases completed the solid-solution formation, incorporated into the matrix by diffusion and a single-phase high-entropy boride structure was obtained. In addition, as described in the HEB 1 composition, low intensity and few oxide phases are also detected in very small incubations.

Figure 4.40a-b shows SEM and color EDS images of the HEB 2 composition at 2500X magnification. Compared to the HEB 1 composition, it is seen that the discrete regions on the matrix disappeared. Instead, there are irregular and almost dendritic structures on the light and dark gray matrix. Also, there is a non-homogenous distribution in the structure. Table 4.4 represents the point and region values of the color EDS analysis. According to the values, Hf is the most dominant element not only in the general but also in all of the point distributions, as can be seen from the color EDS images, which is blue (Figure 4.40b). The Hf is followed by the Zr and Ti elements. Mostly Zr, Ti and Mn elements in different colors (orange, red and purple, respectively) are also seen in the structure. Boron element was not found again. It is seen that the Mn remains below 3 wt.%. The distributions at the first, third, fourth and fifth points are similar to the general by weight, but at the second point, Mn increased in weight, and accordingly a decrease in other elements occurred. It is seen that Hf, Ti and Zr have internally consistent weight percentages in all points and general distributions. But at point 2, Mn showed a very high increase. The fifth point, which gives almost the same results as the distribution by region, may represent the matrix. As a result, the elements constituting the main structure, particularly Hf, suppress the Mn. The reason for this situation may be due to the lower melting point and molecular weight of Mn compared to other elements. In addition, dark areas could be considered as porosity.

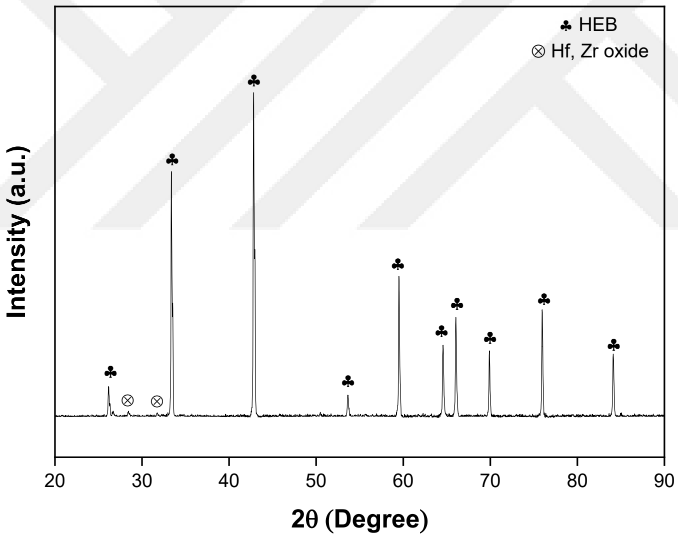

Figure 4.39 : XRD pattern of the HEB 2 composition after SPS.

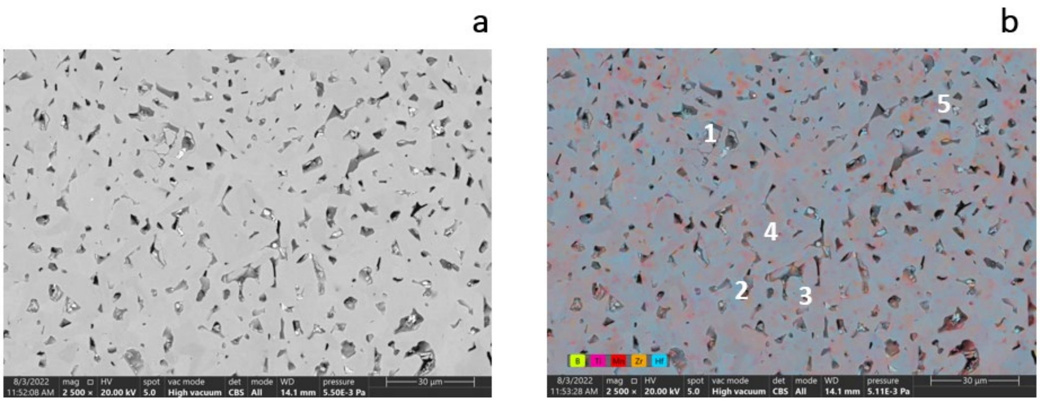

Figure 4.40 : (a) SEM and (b) color EDS images of the HEB 2 composition at 2500X.

Table 4.4 : EDS spectral analyses of the HEB 2 composition.

Weight (%)	General	Point 1	Point 2	Point 3	Point 4	Point 5
Ti	14.3	14.8	12.8	14.6	14.6	15.2
Mn	2.4	2.1	6.9	3.8	2.2	2.8
Zr	26.1	26.4	24.8	24.2	26.1	24.8
Hf	57.2	56.7	55.5	57.4	57.1	57.2

4.3.3 (Hf-Ti-Zr-Mn-Cr)B_2 composition

The XRD pattern of the SPS'd HEB 3 composition is seen in Figure 4.41, exhibiting a single-phase high-entropy boride structure without any detectable secondary boride phases. Otherwise, this composition includes oxide phases like the other ones. The absence of the secondary boride phase indicates that the production has been completed successfully.

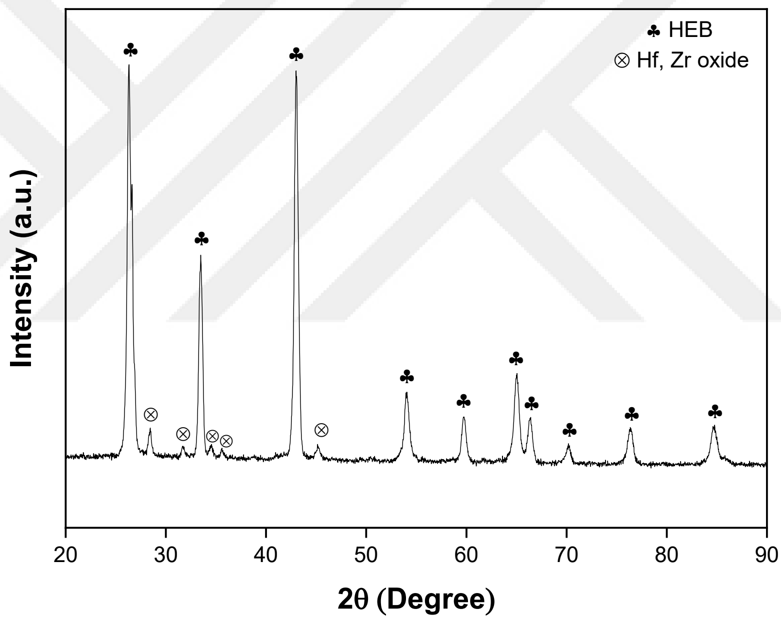

Figure 4.41 : XRD pattern of the HEB 3 composition after SPS.

According to the SEM image (Figure 4.42a), color EDS (Figure 4.42b), and EDS analysis value (Table 4.5) of the HEB 3 composition, there is a non-dendritic distribution. The color EDS image shows the green and yellow Zr and Ti elements above the purple Hf. Hf is the most dominant element in the HEB 3 composition. It is seen that Zr and Ti dominate Mn and Cr elements. Mn and Cr remained below and equal to 5 wt.% at all points and in the general analysis. Besides, Mn and Cr are thought to form a binary eutectic region. Compared to the HEB 1 composition, the discrete regions are disappeared, and the eutectic regions of Mn and Cr became evident. Points 1, 2, 4 and 5 give similar results with the general analysis. However, in point 3, Mn and Cr are less than 1 wt.% and Hf is more than 75 wt.%. Ti and Zr have lower weights than detected in the general analysis. Hf predominates in light colored areas. It is obvious that the five elements are not homogenously distributed in the composition. Besides, dark areas could contain porosity.

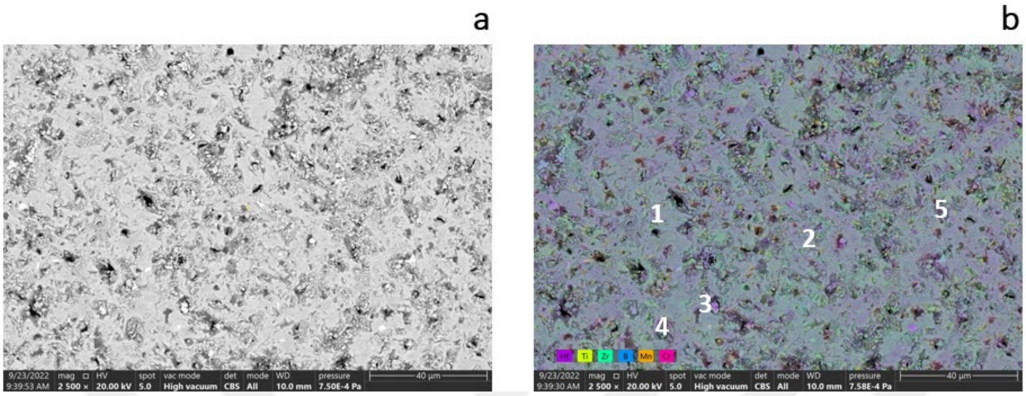

Figure 4.42 : (a) SEM and (b) color EDS images of the HEB 3 composition at 2500X.

Table 4.5 : EDS spectral analyses of the HEB 3 composition.

Weight (%)	General	Point 1	Point 2	Point 3	Point 4	Point 5
Ti	14.6	13.7	15.5	0.9	12.7	13.7
Cr	5.0	4.1	4.8	0.2	3.5	4.5
Mn	2.7	1.6	2.5	0.4	2.2	2.9
Zr	23.2	24.9	22.5	19.7	22.5	22.2
Hf	54.5	55.7	54.7	78.8	59.1	56.7

Figure 4.43 shows the EDS spectral analyses of the HEB 3 composition until 10 keV. When the figure is examined, it is seen that Ti, Mn and Cr peaks overlapped in the range of 0 eV and 5 keV, and the peaks of Mn and Cr are overlapped in the range of 5 keV and 10 keV. It should be evaluated that this situation also affects the weight percentage, especially when detecting Mn and Cr elements.

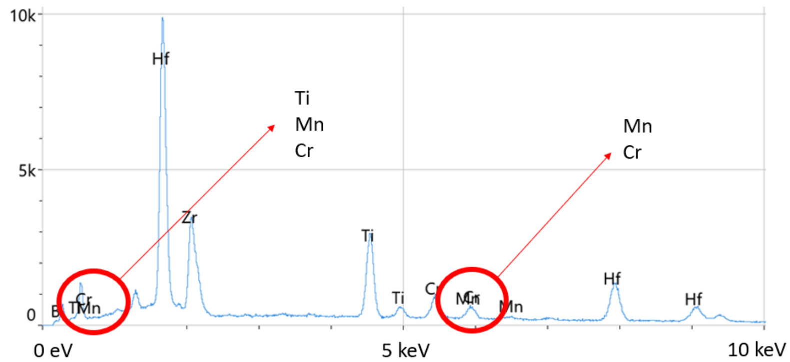

Figure 4.43 : EDS spectral analyses of the HEB 3 composition. The overlapping peaks were mentioned at the graph.

4.3.4 (Hf-Ti-Zr-Mn-Ta)B_2 composition

Figure 4.44 indicates the XRD graph of the HEB 4 composition SPS'd at 2000 °C. XRD shows that all of the secondary boride phases (shown in Figure 4.16) have taken place in the reaction by forming a solid-solution and the single-phase high-entropy boride synthesis is completed. On the other hand, it can also be observed that several hafnium and zirconium oxide phases are formed. The synthesis of high-entropy boride ceramics in five-component systems has been completed.

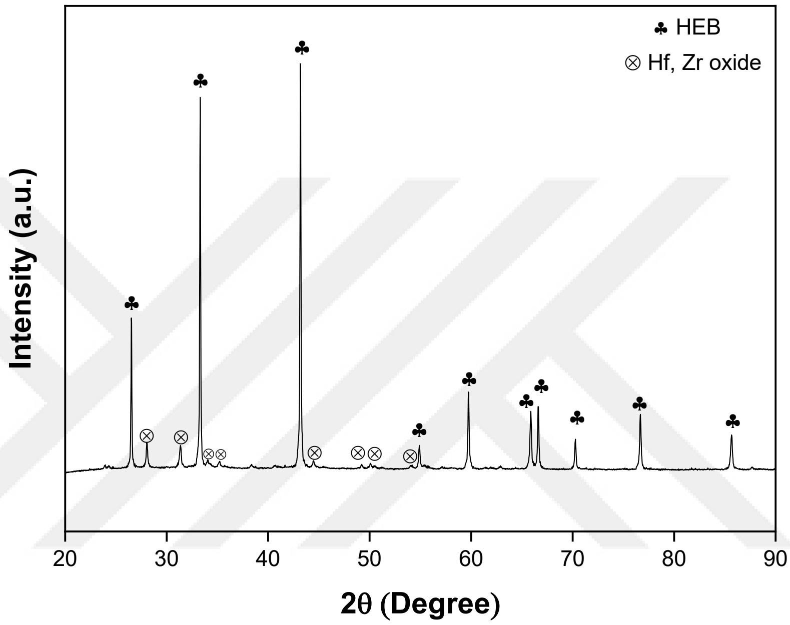

Figure 4.44 : XRD pattern of the HEB 4 composition after SPS.

Figure 4.45a shows the SEM image of the HEB 4 composition taken at 2500X. In the light and dark colored regions, irregular shapes and dispersions of the elements in different colors can be seen. A color EDS image is given in Figure 4.45b. It is seen that Hf and Ta elements in orange and yellow are predominantly distributed. The distribution of Zr in green and Ti in purple is in small amounts. The dark-colored distribution points contain blue-colored Mn. The EDS analysis results in Table 4.6 confirm that Hf and Ta are dominant. Then there are Zr and Ti elements, while Mn is below 3 wt.%. Elements (Mn, Ti) that overlap each other and their effects on overall weight percentages are given in Figure 4.43. The distribution of elements in point analyses is almost the same as in the general analysis. It can be seen from the first and second points that the light gray and dark gray regions in the matrix contain almost the same elemental amounts. At the fourth point, Mn showed a significant increase in weight. At the fifth point, it is understood that while the amount of Hf and Zr by weight increases, Ta and Ti decrease. Therefore, there is a non-homogenous distribution in the structure. Furthermore, dark areas are evalpertain to porous regions.

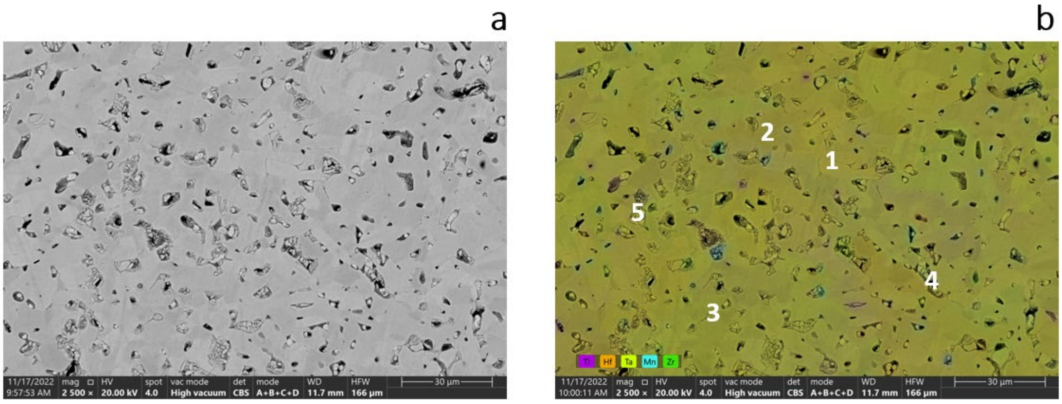

Figure 4.45 : (a) SEM and (b) color EDS images of the HEB 4 composition at 2500X.

Table 4.6 : EDS spectral analyses of the HEB 4 composition.

Weight (%)	General	Point 1	Point 2	Point 3	Point 4	Point 5
Ti	11.4	11.8	11.3	11.5	10.8	10.1
Mn	2.8	2.6	2.7	2.4	4.3	2.9
Zr	16.2	16.4	15.6	17.0	17.5	18.2
Hf	37.0	36.1	35.9	36.7	35.5	38.6
Ta	32.6	33.1	34.5	32.4	31.9	30.2

4.3.5 (Hf-Zr-Mn-Cr)B_2 composition

In the XRD pattern in Figure 4.46, it is observed that single-phase high-entropy boride phases were formed after spark plasma sintering. At the same time, small peaks belong to the hafnium and zirconium oxide phases. In comparison with Figure 4.18, high-entropy boride peaks are sharp with high intensities.

On the basis of the SEM image of HEB 5 composition at 2500X (Figure 4.47a), there is an irregular elemental distribution dispersed over the light and dark gray regions. Also, some small white dots are observed at the microstructure. On the basis of Figure 4.47b and Table 4.7, Hf is the most dominant element in the structure. The Mn and Cr elements are almost 1 wt.%. As it can be seen from Figure 4.43, Mn and Cr are overlapped. As a result of this situation, their weight percents are affected. Yellow Hf and blue Zr give a color close to green at these points. Boron was not found in the structure and a small amount of Mn and Cr are seen. The first point is white in color and consists almost entirely of the Hf element. Cr and Zr elements were not found. The second and third points represent the dark and light gray microstructure and give a result close to the general distribution. At the fourth point, Mn showed a significant increase in weight. While Cr is not included in weight, Zr decreases. The fourth point is the Mn-rich section. At the fifth point, there is a distribution close to the general. Eutectic regions in the HEB 3 composition are not seen here. It is thought that the absence of Ti in the composition causes this situation. In the absence of Ti, it is evident that contrast regions has larger areas, which can be attributed to grain size. According to all results, every point in the microstructure does not show a homogenous distribution.

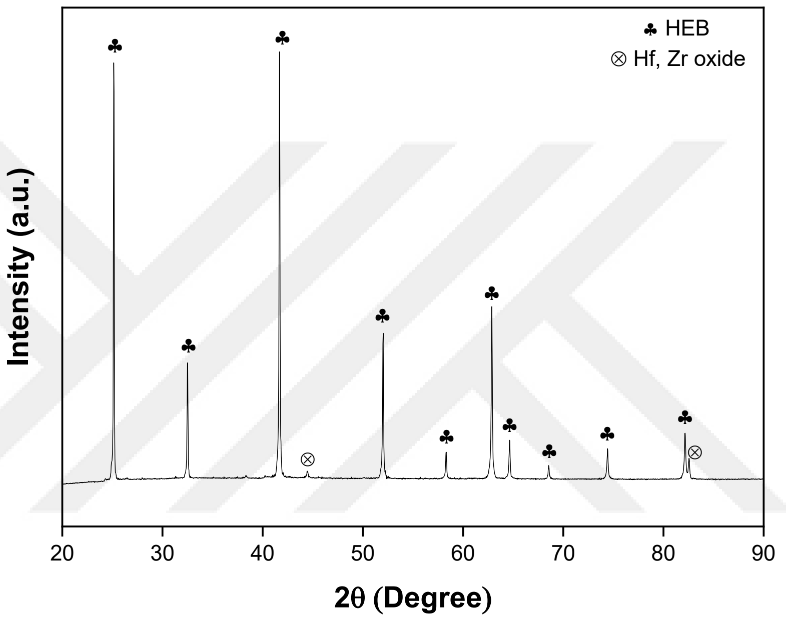

Figure 4.46 : XRD pattern of the HEB 5 composition after SPS.

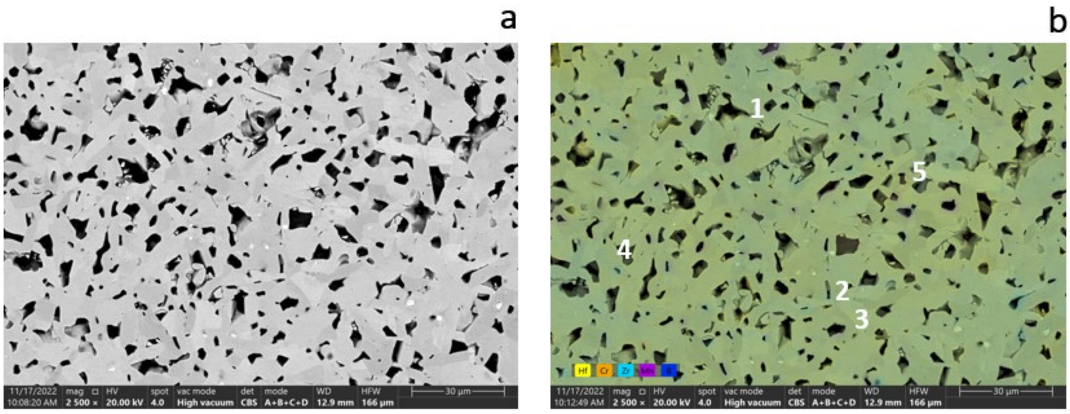

Figure 4.47 : (a) SEM and (b) color EDS images of the HEB 5 composition at 2500X.

Table 4.7 : EDS spectral analyses of the HEB 5 composition.

Weight (%)	General	Point 1	Point 2	Point 3	Point 4	Point 5
Cr	1.3	0.0	1.0	1.2	0.0	1.1
Mn	1.2	0.2	0.6	0.7	11.1	0.7
Zr	30.8	0.0	31.5	31.8	21.4	31.6
Hf	66.7	99.8	66.9	66.3	67.5	66.6

4.3.6 (Hf-Ti-Mn-Cr)B_2 composition

As seen in Figure 4.48, the high-entropy boride peaks are observed after spark plasma sintering at high intensities. Approximately 2θ positions at 28°, 34°, 38°, and 88°, a very weak HfO_2 phase is formed. At 2θ value of 45°, the secondary phase is formed. When searching for secondary phases, two intermetallics are found: MnTi (ICDD: 00-007-0132) and/or $Mn_{0.56}Ti_{0.44}$ (ICDD: 00-015-0338). When the peak positions of these phases are examined, it is predicted that the secondary phases may be Mn-Ti rich. Also, it is expected that the fourth point (Table 4.8) in the EDS analysis will also confirm this result. It is considered that the absence of the ZrB_2 phase in the main structure can cause the formation of the secondary phase.

As represented in Figure 4.49a, elemental distribution with irregular shape, size and colors was formed in HEB 6 composition, just as it was in other compositions. As it can be seen from Figure 4.49b and Table 4.8, the dominant Hf distribution is clearly evident in yellow. Ti, which is the second most abundant element in the structure after Hf, is collected in certain regions as pink. Mn and Cr are below 10 wt.%, as expected. This situation was showed in Figure 4.43. When the point EDS results are examined, it is clear that the first and second points (light and dark regions) are almost the same as the general distribution. The white colored part at the third point is entirely Hf by wt and contains only 1 wt.% Ti. At the fourth point, while Hf was found to be rich, Ti decreased significantly and Mn increased significantly in weight. The fourth point is the region where Mn is richest. The fifth point is the region where Ti and Cr are at highest amounts. In contrast to other compositions, despite its small amounts (less than 1 wt.%), low molecular weight element B was detected here. At the first, second and fifth points, the amount of B increased by more than 1 wt.%. While the Zr element was not found in the composition, the detection of boron as a result of EDS analyses indicates that the Zr and B peaks may have overlapped. There is no homogenous distribution as in other compositions.

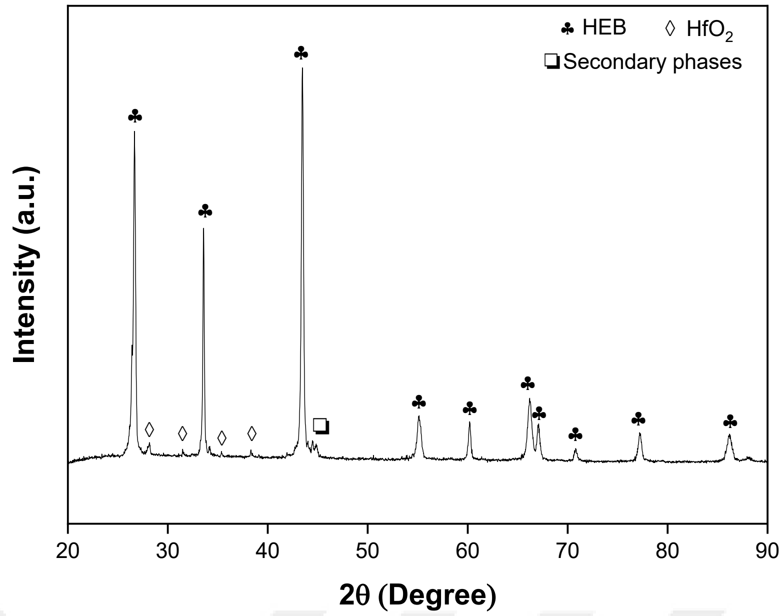

Figure 4.48 : XRD pattern of the HEB 6 composition after SPS.

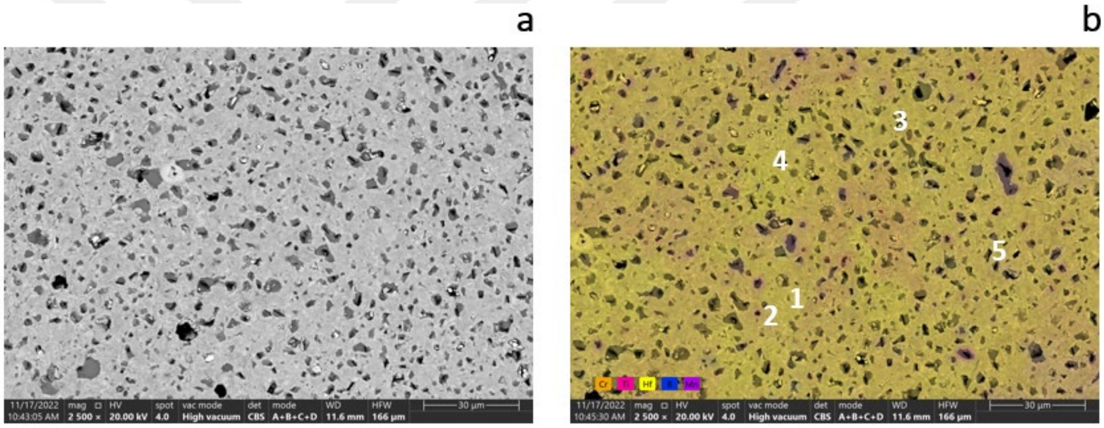

Figure 4.49 : (a) SEM and (b) color EDS images of the HEB 6 composition at 2500X.

Table 4.8 : EDS spectral analyses of the HEB 6 composition.

Weight (%)	General	Point 1	Point 2	Point 3	Point 4	Point 5
B	0.9	1.3	1.3	0.0	0.4	1.2
Ti	18.2	19.3	19.7	1.0	11.9	20.4
Cr	8.7	8.4	8.6	0.0	5.9	9.5
Mn	4.7	3.3	3.6	0.0	8.6	3.7
Hf	67.5	67.7	66.7	99.0	73.2	65.2

4.3.7 (Ti-Zr-Mn-Cr)B_2 composition

XRD patterns of HEB 7 composition sintered without HfB_2 phase are given in Figure 4.50. High-entropy boride phases are seen; however, peaks are not sharp and have low intensities. Furthermore, many ZrO_2 phases and one TiO_2 phase are formed. In addition to HEB and oxide phases, secondary ones occur at three different 2θ positions

(~ 27°, 33° and 44°). The reason for the formation of secondary phases at high intensity could be due to the absence of HfB_2, which may act as a main structure in the high-entropy composition. It is predicted that the boride compounds enter the HfB_2 lattice. In the study examining the interdiffusion between HfC-TiC, it was observed that TiC diffused faster, while HfC acted as the main material (Heiligers et al, 2012). In another study reported on the diffusion between HfC-ZrC, it was explained that Hf and Zr had similar inter-diffusion rates (Ghaffari et al, 2013). According to these studies, it is understood that the phases containing Hf or Zr act as the base structure, while other elements diffuse into this structure. Similarly, Kavak et al. (2020a) were suggested this situation. They found that HfC and ZrC are host materials. Generally, in the (Hf-Ti-Zr)B_2 system, the high diffusion rate of the Hf element suppresses the formation of the secondary phases. When the microstructure was examined, it was evaluated that intermetallic phases could form between Zr-Cr or Zr-Mn, which would also result in dendritic structures. Kanazawa et al. (2022) were observed that the dendritic $ZrCr_2$ Laves phase is surrounded by two different eutectic regions. It was also revealed that this phase was embedded in the Cr solid-solution. Based on this study, it was interpreted that the secondary phases could be $ZrCr_2$ Laves phase; on the other hand, this cannot be confirmed because there is no match in the ICDD cards.

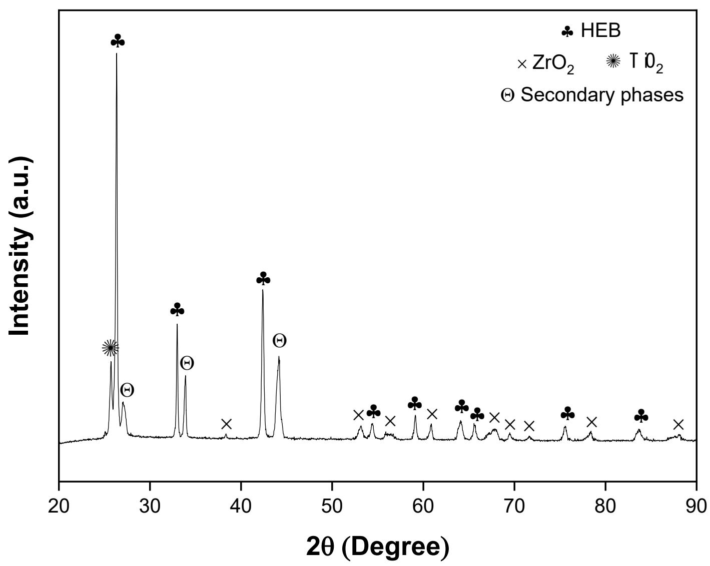

Figure 4.50 : XRD pattern of the HEB 7 composition after SPS.

SEM image of HEB 7 composition at 2500X is in Figure 4.51a. It is clearly seen that the HEB 7 composition has a different microstructure from all other compositions. There is an inhomogeneous distribution. Dendritic-like complex microstructure was formed. The absence of Hf is predicted to cause this microstructure. In the color EDS analyses (Figure 4.51b, Table 4.9), the dominant Zr is blue, and the secondary element Ti is visible in the areas surrounded by pink. Boron was not detected. Cr is present at amount of 15 wt.%. Mn was still less than 10 wt.%. The reason for the high amount of Mn and Cr elements by weight shows that Hf dominates these elements. However, the overlapping peaks described in Figure 4.43 should be considered when evaluating results weight percents. At the first point, Zr is about 75 wt.%. According to the general distribution, Ti, Cr and Mn decreased significantly. At the second point, while Zr decreased, Cr and Ti elements by weight increased greatly. At the third point Zr is over 70 wt.%. Mn has the highest weight percents, the third point is the Mn-rich region. The fourth point is the richest Cr region. While Ti is increasing, there is a significant decrease in Mn and especially Zr. The fifth point has high fractions of Mn and Cr at the same time. This indicates that the dark distribution is rich in Mn and Cr. Zr is present in almost the same ratio as Cr, the highest fraction is seen in Ti element.

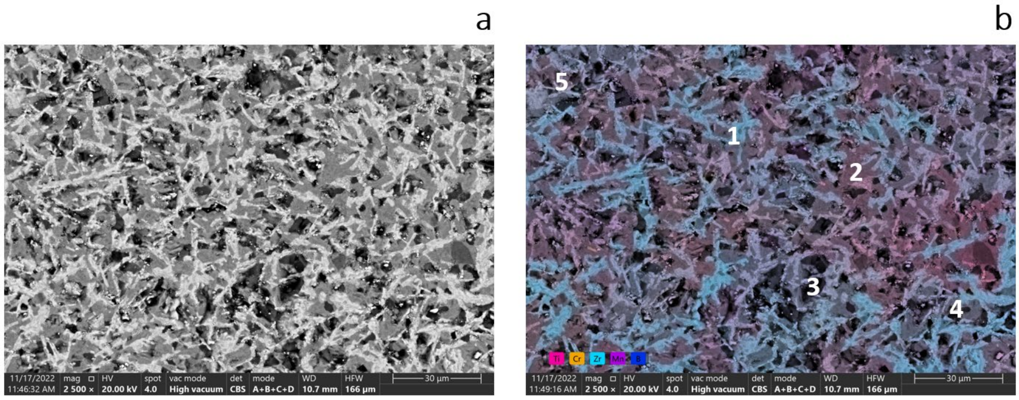

Figure 4.51 : (a) SEM and (b) color EDS images at 2500X of the HEB 7 composition.

Table 4.9 : EDS spectral analyses of the HEB 7 composition.

Weight (%)	General	Point 1	Point 2	Point 3	Point 4	Point 5
Ti	27.0	17.3	35.7	11.5	33.7	33.2
Cr	15.2	4.2	21.5	2.9	26.3	27.8
Mn	7.4	3.3	8.5	13.8	3.8	10.1
Zr	50.4	75.2	34.3	71.8	36.2	28.9

When the three elements constituting the main structure are compared with each other, it is interpreted that secondary phases are formed in the absence of ZrB_2 and HfB_2, and that the secondary ones have both low peak intensities and do not form sharply without HfB_2. In addition, according to the SEM images, it has been understood that a different microstructure occurs in HfB_2 deficiency. Therefore, the HfB_2 phase is interpreted to have the most significant effect on the formation of high-entropy boride peaks.

4.3.8 (Hf-Ti-Zr-Mn-Cr-Mo)B_2 composition

On the basis of Figure 4.52, the HEB 8 composition contains high intensity and sharp high-entropy boride peaks. With all this, there are also some impurities like hafnium oxide and zirconium oxide. The boride phases, which are TiB_2, MnB, Mn_2B, Cr_2B and MoB_4, in the XRD pattern after milling (Figure 4.24) formed a completely solid-solution.

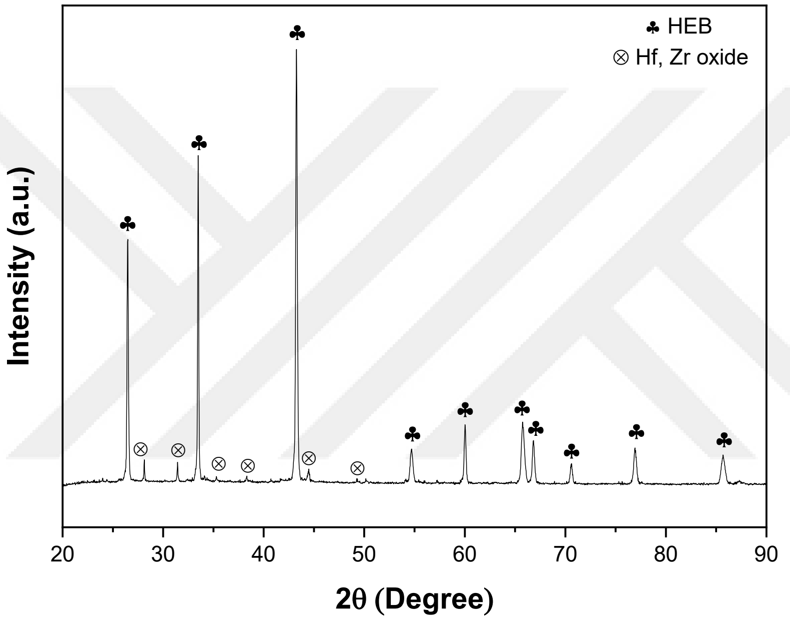

Figure 4.52 : XRD pattern of the HEB 8 composition after SPS.

When the SEM image of the HEB 8 composition is examined (Figure 4.53a), as expected, a light and dark colored elemental distribution with irregular shape and size is formed over the gray regions. When Table 4.10 and Figure 4.53b are examined together, the dominant yellow Hf element is seen. Furthermore, green color is thought to occur because blue color Zr is distributed over Hf. In addition, the element Mo, which is almost as much as Zr, is also shown in green. When the general distribution is examined, Mn and Cr are below 10 wt.%. The reason for this situation can be interpreted as the peak overlapping shown in Figure 4.43. The first, third and fifth points gave almost the same amounts at the general distribution. When the second point is examined, it is seen that Hf is over 70 wt.% and Zr is around 23 wt.%. Ti, Mn and Cr elements are below 1 wt.%. This indicates that the light colored dots scattered on the matrix are Hf-rich regions. Looking at the fourth point, the amounts of Mn and Cr are at their highest value. Mn, in particular, increased significantly. The fact that the fourth point includes the Mn-Cr-rich region, in addition to the major Hf element. There is an inhomogeneous distribution.

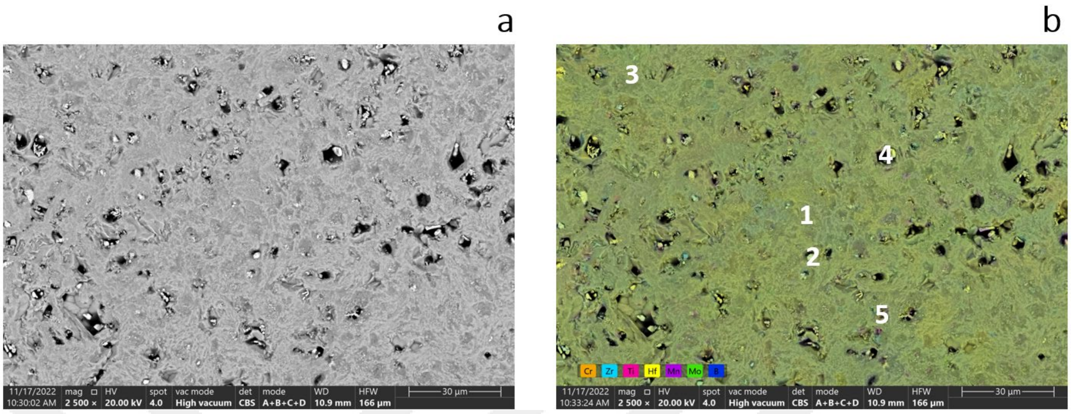

Figure 4.53 : (a) SEM and (b) color EDS images of the HEB 8 composition at 2500X.

Table 4.10 : EDS spectral analyses of the HEB 8 composition.

Weight (%)	General	Point 1	Point 2	Point 3	Point 4	Point 5
Ti	11.0	11.1	0.7	11.2	9.9	11.7
Cr	7.3	7.2	0.7	6.9	8.1	7.8
Mn	4.2	5.2	0.8	4.6	18.2	5.1
Zr	17.3	17.5	23.4	17.3	4.2	15.3
Mo	19.7	19.6	1.9	19.4	3.3	18.3
Hf	40.5	39.4	72.5	40.6	56.3	41.8

4.3.9 (Hf-Ti-Zr-Mn-Cr-W)B_2 composition

The XRD pattern of HEB 9 composition obtained by SPS is displayed in Figure 4.54. Only high-entropy boride phases are obtained, as expected. In spite of these phases, there are very small oxide peaks. The addition of the W boride phase clearly does not prevent the formation of high-entropy boride peaks. All of the secondary boride phases (Figure 4.26b) were incorporated into the matrix. It has been understood that high-entropy boride synthesis has been successfully completed in the six-component systems. According to the SEM (Figure 4.55a) color EDS (Figure 4.55b) and EDS analysis results (Table 4.11), there are nearly dendritic and irregular phase distributions on the matrix, consisting of light and dark gray regions. Dissimilar to the other compositions, in the addition of W boride has an irregular distribution within each region. The most dominant element is Hf and followed by W in dark orange. It is thought that the Zr distribution is above Hf. Ti, Mn and Cr are found in small regions.

Mn and Cr elements are below 5 wt.%. Figure 4.43 shows the possible cause of this situation. There is no boron element detected. EDS analyses (points 1 and 2) made from light and dark colored regions show that they give almost the same result for the general distribution. Similarly, in the fourth point, there is a similar result compared with the general distribution. It is seen that the third point is the Hf-rich region. While W, Ti, Mn and Cr decreased significantly, Zr increased slightly. The fifth point is the Mn-rich region. As seen in other compositions, dark areas mostly contain Mn. The amount of Hf increased at a high rate, while the amount of W decreased at a high rate. In this case, like the other ones, there is no homogenous distribution.

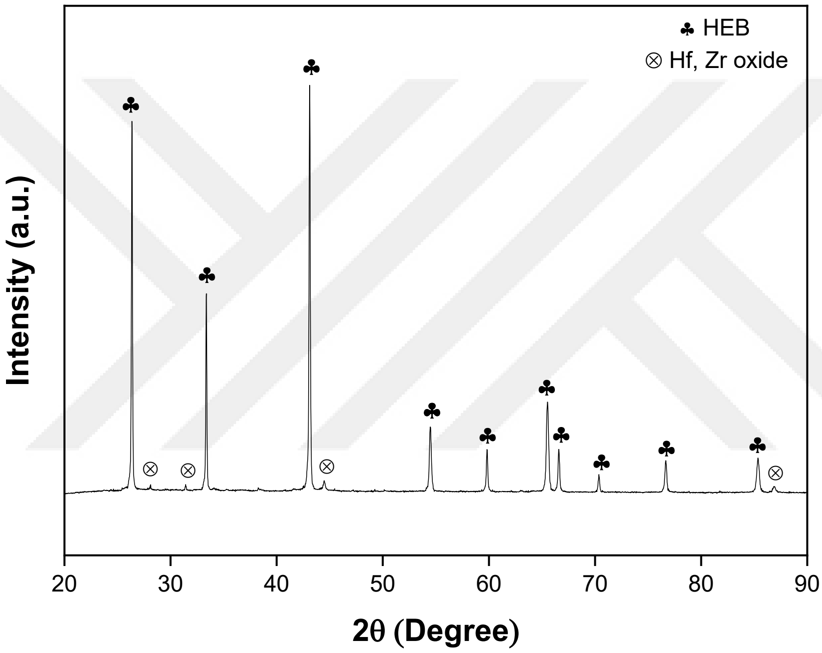

Figure 4.54 : XRD pattern of the HEB 9 composition after SPS.

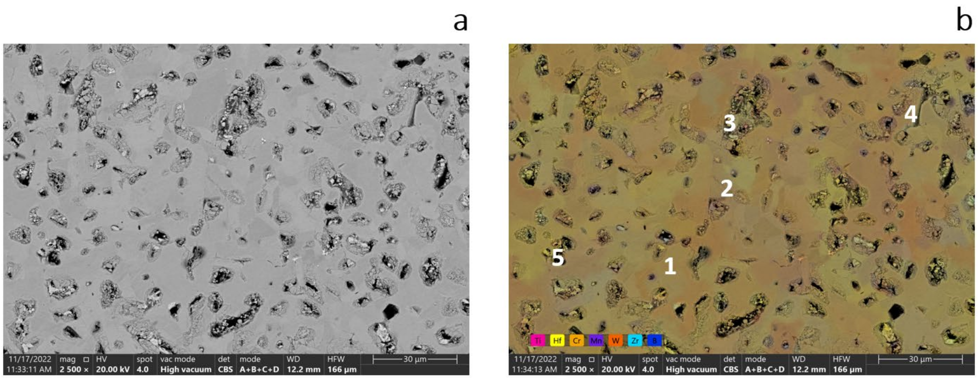

Figure 4.55 : (a) SEM and (b) color EDS images of the HEB 9 composition at 2500X.

Table 4.11 : EDS spectral analyses of the HEB 9 composition.

Weight (%)	General	Point 1	Point 2	Point 3	Point 4	Point 5
Ti	10.8	11.7	11.1	1.6	11.4	8.1
Cr	4.0	4.2	4.6	0.5	4.2	3.0
Mn	2.5	2.4	2.4	0.6	2.2	11.3
Zr	16.9	16.4	16.5	18.7	16.5	17.2
Hf	39.1	39.1	38.4	75.3	40.3	50.3
W	26.7	26.2	27.0	3.3	25.4	10.1

4.3.10 (Hf-Ti-Zr-Mn-Cr-Mo-W)B_2 composition

As can be seen from the XRD pattern of the seven-component HEB 10 system after SPS (Figure 4.56), the high-entropy boride phases were formed with sharp and high peaks. Again, oxide phases are observed at four different peak positions like the HEB 9 composition. All of the binary boride phases that formed after milling turned into the high-entropy phase.

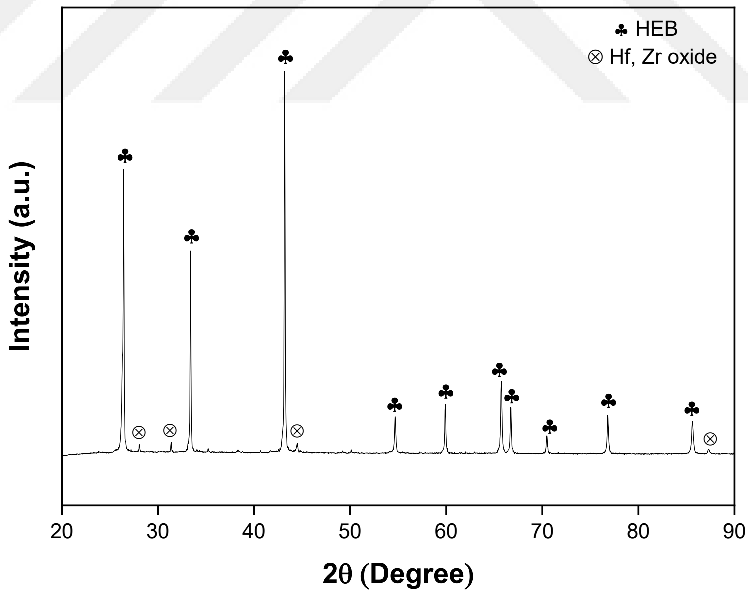

Figure 4.56 : XRD pattern of the HEB 10 composition after SPS.

According to the SEM image given at 2500X in Figure 4.57a for the HEB 10 composition, irregular and large shaped particles were distributed on the matrix consisting of gray areas. Particles containing W have a discrete appearance in themselves. According to the colored EDS in Figure 4.57b and the analysis results in Table 4.12, the dominantly yellow Hf element is seen. W, Zr and Mo have almost the same weight percentages. Ti is less than 10 wt.%, Mn and Cr are less than 5 wt.%. The overlap of the peaks are thought to cause this situation which is expressed in Figure 4.43. According to these results, it can be said that there is no homogenous distribution. The first and second points, representing the light and dark gray regions, show almost the same general distribution. As expected, the Mn content increased at the third point in the dark region. With Mn, Ti increased while Hf and W decreased. It also exhibits a small increase in Cr. At the fifth point, which consists of the light-colored region, there is a high percentage of Hf and partially Zr, as expected, and approximately 1 wt.% of Mn and Mo. At the fifth point it has amounts close to the general distribution. W increased while Hf decreased.

a b

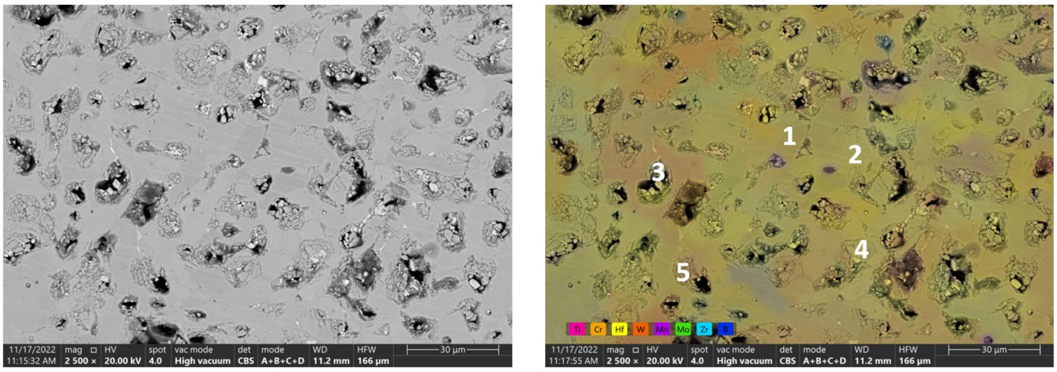

Figure 4.57 : (a) SEM and (b) color EDS images of the HEB 10 composition at 2500X.

Table 4.12 : EDS spectral analyses of the HEB 10 composition.

Weight (%)	General	Point 1	Point 2	Point 3	Point 4	Point 5
Ti	8.6	8.5	8.6	11.4	0.0	8.5
Cr	4.8	4.7	4.8	6.4	0.0	4.5
Mn	3.5	2.8	2.4	11.1	1.2	2.6
Zr	15.0	14.6	14.9	19.2	21.3	15.0
Mo	12.1	12.7	12.9	10.5	0.7	13.1
Hf	36.6	35.6	34.8	24.6	76.8	33.9
W	19.4	21.1	21.6	16.8	0.0	22.4

4.3.11 (Hf-Ti-Zr-Mn-Cr-Mo-Ta)B_2 composition

On the basis of Figure 4.58, for the HEB 11 system, it is seen that the high-entropy phases are formed with the secondary phase. It is evaluated that the secondary phases are Hf-Ta-rich phases when the EDS results are examined (Table 4.13). However, a large number of weak oxide phases were also formed. It is seen that the addition of TaB instead of the W boride phase causes the formation of the secondary phase. The addition of TaB to HEB 4 composition did not cause secondary phase formation in five-component systems. It is thought that the increase in the number of components may also cause the formation of the secondary phase.

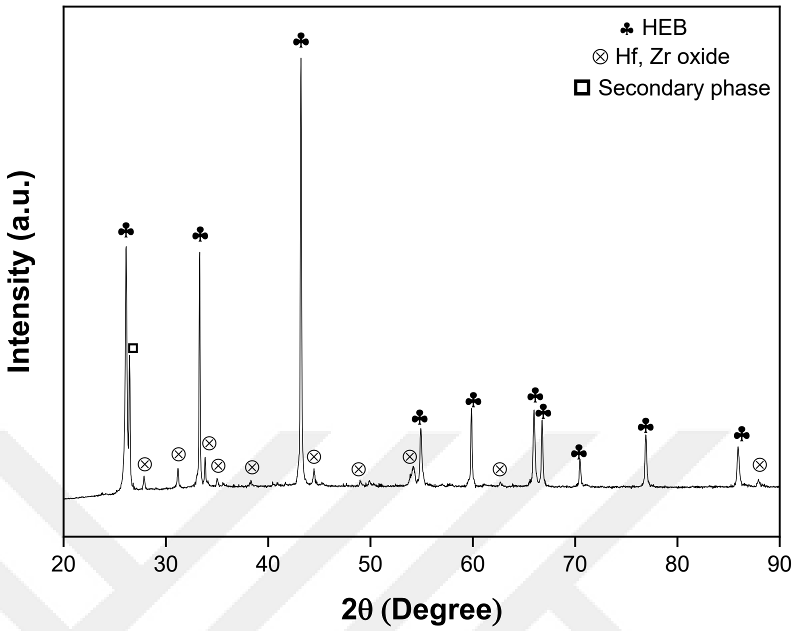

Figure 4.58 : XRD pattern of the HEB 11 composition after SPS.

There is a SEM image of HEB 11 composition in Figure 4.59a. On the light and dark gray matrix layer, rounded particles at different sizes, most of the in white and some in dark color, stand out. In addition, cracks are seen in these particles. There are color EDS image and EDS results of HEB 11 composition in Figure 4.59b and Table 4.13, respectively. According to the general distribution results, Hf and Ta are almost in the same fractions, and the yellow and blue distributions confirm these ones. Zr and Mo also have similar ratios. This situation is also evident with the light blue and green colored distribution in places. Ti and Cr are below 10 wt.%, Mn is below 3 wt.%, the least common element in the structure is Mn. As seen in other compositions, the percentages of Mn and Cr are the lowest, as expected from Figure 4.43. When the first point is examined, as expected, Hf is over 70 wt.% and Zr is around 24 wt.%. Light colored white dots are Hf-rich regions. The second and third points, light and dark gray matrix regions gave almost the same results as the general distribution. This situation is similar to other combinations as well. The second point is the highest concentration of Cr. At the fourth point, Mn has its highest value. The analysis results are close to the general distribution. The fifth point is similar to the first point, Hf is the rich region. There is no homogeneity in this composition like the others and there are some porosites.

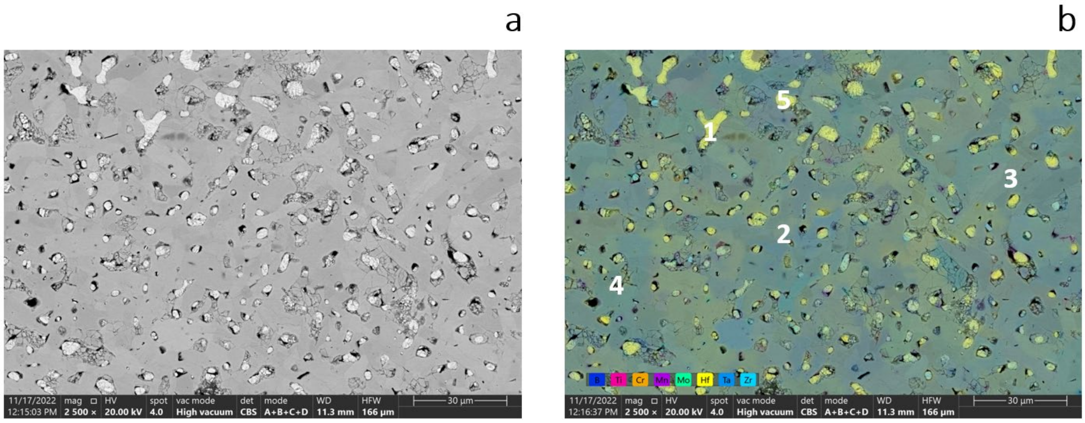

Figure 4.59 : (a) SEM and (b) color EDS images of the HEB 11 composition at 2500X.

Table 4.13 : EDS spectral analyses of the HEB 11 composition.

Weight (%)	General	Point 1	Point 2	Point 3	Point 4	Point 5
Ti	8.4	0.1	9.3	8.8	6.9	0.2
Cr	7.6	0.4	8.3	7.7	6.4	0.2
Mn	2.8	0.2	2.7	2.8	5.7	0.2
Zr	13.8	24.1	12.6	12.8	13.6	22.6
Mo	15.5	0.0	16.5	15.9	11.4	0.3
Hf	27.8	73.1	23.9	24.7	32.1	73.9
Ta	24.1	2.1	26.7	27.3	23.9	2.6

4.3.12 (Hf-Ti-Zr-Mn-Cr-W-Ta)B_2 composition

The XRD pattern of HEB 12 composition sintered with SPS at 2000°C is displayed in Figure 4.60. Similar to the HEB 11 composition, besides the high-entropy boride peaks formed as the severe and main phase, secondary phase formation was also observed. When the EDS analyses and Table 4.14 results are examined, it is predicted that the secondary phases could contain Hf-Ta-W. However, verification could not be made with ICDD cards. In addition, the oxide phase appeared at low intensity and at three different peak positions. Although secondary phases are also formed in seven-component systems, sharp high-entropy boride phases could be obtained as the main component.

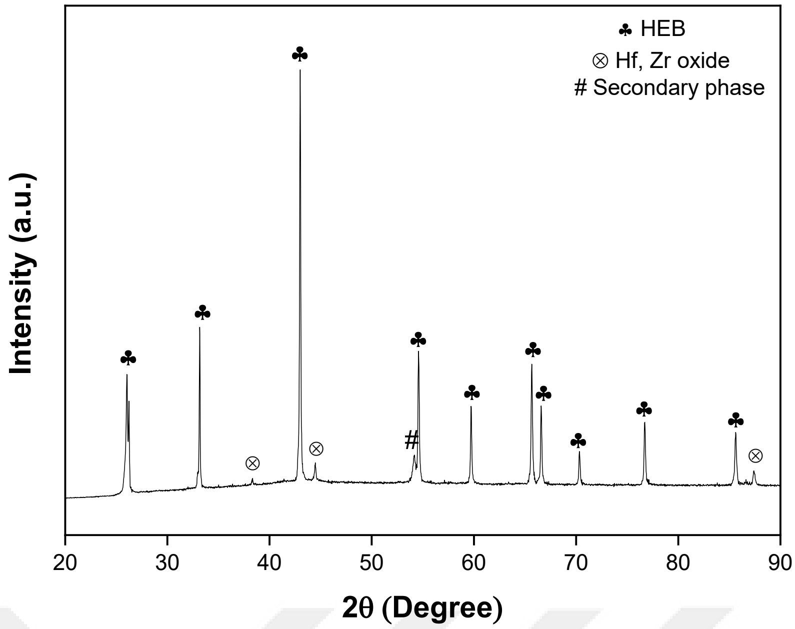

Figure 4.60 : XRD pattern of the HEB 12 composition after SPS.

The SEM image in Figure 4.61a shows particles dispersed on the light and dark gray matrix. These particles are irregularly shaped and have different sizes from each other. In the colored EDS images in Figure 4.61b, predominantly yellow, blue and orange colors are evident. In places, pink, purple or orange colors are also seen. The EDS results in Table 4.14 confirm the color SEM images. There are almost the same fractions of Hf, Ta and W elements in the composition of the general distribution (approximately 24-25 wt.%). The zircon element is about 11 wt.%. Ti, Mn and Cr are all below than 10 wt.%. The possible explanation which cause this situation is given in Figure 4.43. At the first point, Ti decreased while W significantly increased in weight. This region is the W-rich region. A high amount of decrease is also seen in the Zr element. Boron element was detected when Zr decreased below 10 wt.%. Boron element was also detected in another composition (HEB 6) which did not contain ZrB_2 phase. The second point gave close results with the general distribution. When the third point is examined, it is seen that Hf and Mn increase in large amounts. The third point is the Mn-rich region. At the same point, it should be noted that the Ta and W elements are greatly reduced. At the fourth and fifth points, it gives close results with the general distribution. The fourth point is the region with the highest Cr content.

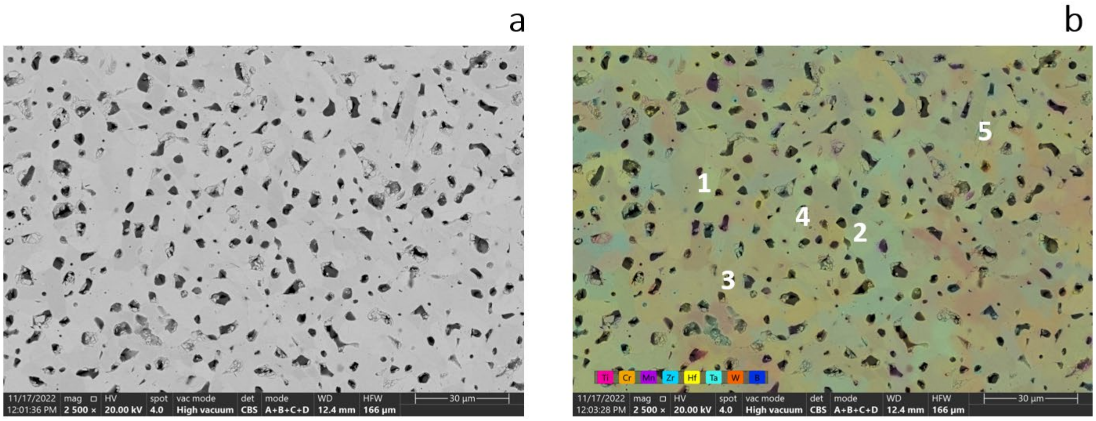

Figure 4.61 : (a) SEM and (b) color EDS images of the HEB 12 composition at 2500X.

Table 4.14 : EDS spectral analyses of the HEB 12 composition.

Weight (%)	General	Point 1	Point 2	Point 3	Point 4	Point 5
Ti	6.1	1.6	6.7	2.8	6.1	6.1
Cr	5.3	5.2	5.7	3.1	6.2	4.9
Mn	4.5	3.9	4.5	14.7	5.3	5.5
Zr	11.4	9.7	12.3	17.2	12.0	13.0
Hf	24.6	24.4	24.6	44.6	25.3	26.5
Ta	23.7	22.2	22.4	9.0	22.5	21.3
W	24.4	32.6	23.8	8.6	22.6	22.7
B	0.0	0.4	0.0	0.0	0.0	0.0

4.3.13 (Hf-Ti-Zr-Mn-Cr-Mo-W-Ta)B_2 composition

For the last composition, the XRD pattern after SPS is shown in Figure 4.62. Even when all boride phases are combined, the formation of high-entropy boride phases is complete without a secondary peak. The peaks, which belong to hafnium and zirconium oxide, are sharp with very low intensities. According to the SEM/EDS analysis, secondary phase may be considered with Hf-Ta-rich phase. However, this cannot be verified with ICDD cards.

SEM and color EDS analysis images of the HEB 13 composition sintered with SPS and values of these images are given in Figure 4.63a-b and Table 4.15, respectively. The eight-component system has a microstructure similar to the five-component HEB 3 system. The darker regions draw attention. It is seen that the darkly colored regions are distributed on the matrix. These regions have different shapes and sizes. There is an inhomogeneous system.

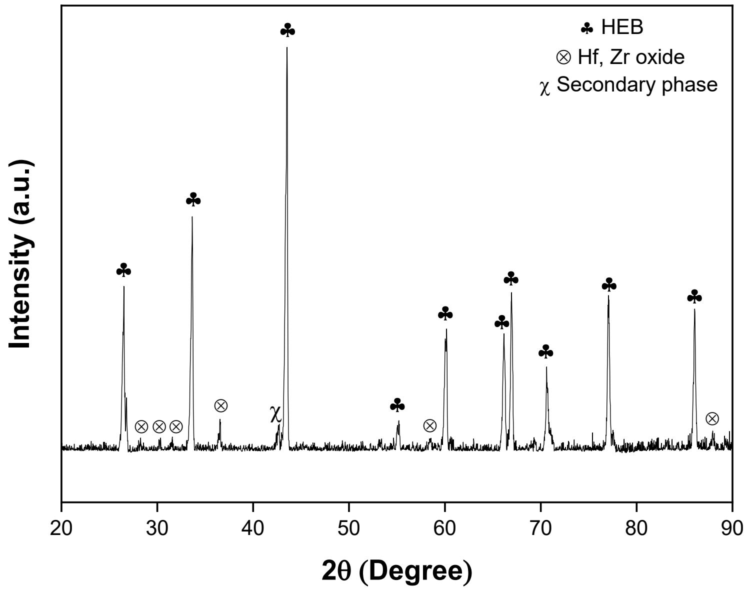

Figure 4.62 : XRD pattern of the HEB 13 composition after SPS.

When the results of the general analysis are examined, it is seen that Hf and Ta elements are dominant. Zr, Mn and Mo are in the range of 10 to 15 wt.%. Ti is below than 10 wt.%, Mn and Cr below 5 wt.%. This is expected, as summarized in Figure 4.43. The blue distribution confirms the predominance of Hf and Ta. The first, third, fourth and fifth points have almost the same fractions as measured the general distribution. The third point is the region with the most intense W. At the second point, as observed in other compositions, Hf is about 75 wt.%, while Zr is about 23 wt.%. This region is the Hf-rich region. A sharp decrease is observed in other elements.

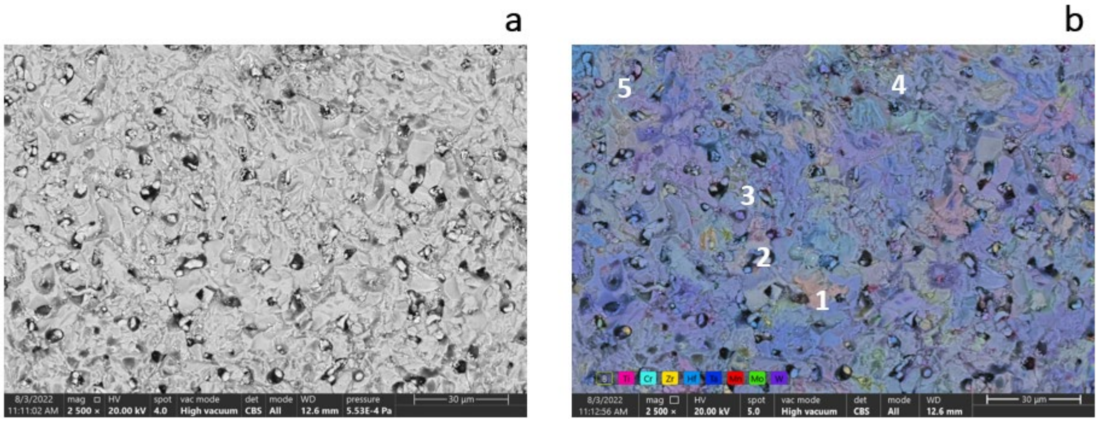

Figure 4.63 : (a) SEM and (b) color EDS image at 2500X of the HEB 13 composition.

Table 4.15 : EDS spectral analyses of the HEB 13 composition.

Weight (%)	General	Point 1	Point 2	Point 3	Point 4	Point 5
Ti	7.5	8.1	0.2	7.8	8.6	8.1
Cr	4.7	4.8	0.3	4.6	4.6	4.7
Mn	3.3	2.7	0.2	2.9	3.3	3.1
Zr	12.0	12.2	23.3	9.9	12.6	11.3
Mo	10.6	11.7	0.2	9.3	11.6	10.5
Hf	27.8	24.3	74.4	26.9	24.4	24.6
Ta	21.1	22.4	1.3	23.2	20.7	23.3
W	13.0	13.8	0.1	15.4	14.2	14.4

Depending on the composition, the diffusion rates of the elements and their dissolution in each other, the microstructures contain differences in terms of shape, irregularity and size of the dispersed particles. According to the EDS results, when all samples are examined, Hf is the most dominant element. Mn and Cr are below 10 wt.%. in all compositions except the HEB 7 composition, which does not contain HfB_2. The heavier elements could suppress the lighter ones. There is an inhomogeneous distribution in all compositions according to the both SEM and EDS images. In the SEM images of all compounds, it is seen that the elements exhibit semi-homogeneous distribution even in micron scale. This indicates that the solid-solution has been completed (Chen et al, 2019). There are some porosities throughout the structure as well. Qin et al. (2021) also determined the porosities in their samples' microstructure. In addition, while most elements are homogeneously distributed, there are also elements that do not exhibit homogeneous distribution. Barbarossa et al. (2021b) similarly emphasized that the elements are not homogeneously distributed at every point of the surfaces they examined. In another study they carried out, they stated that they encountered porosity as a result of the synthesis and they calculated the amount of porosity as 2.2 ± 0.2 vol.% (Barbarossa et al, 2021a). Besides, Chen et al. (2019) stated that necking between grains causes porosity.

In all samples, high-entropy boride structure was obtained after SPS. On the other hand, as mentioned in earlier studies, the solid solubility of CrB_2 in HfB_2 and ZrB_2 is limited (Post et al, 1954). But similarly, Gild et al. (2016) showed that single-phase high-entropy structure can be formed by the SPS method in compositions containing CrB_2. Several studies with different compositions have shown that single-phase high-entropy boride ceramics are synthesized similarly after spark plasma sintering (Barbarossa et al, 2021b; Gild et al, 2016, 2020; Murchie et al, 2022; Qin et al, 2020a, 2020b, 2021; Y. Wang et al, 2018; Y. Zhang et al, 2019a, 2019b, 2021a, 2021b). As mentioned in previous studies in the literature, single-phase high-entropy boride has AlB_2 type hexagonal close-packed (HCP) crystal structure with *P6/mmm* space group (D. Liu et al, 2019; Mayrhofer et al, 2018; Y. Wang et al, 2018). With high-entropy boride phases, there are weak oxide peaks in the XRD pattern. In different studies, in which high-entropy boride phases were produced by different or the same routes, low amounts and weak (Hf, Zr)O_2 phases in low amounts were observed (Gild et al, 2019b; Gu et al, 2019; Tallarita et al, 2020; Y. Zhang et al, 2019a, 2019b). Qin et al. (2021), in their study, predicted that oxide phases can be removed if extra boron is added to the composition. However, this situation disrupts the stoichiometric diboride structure.

4.4 Physical Characterization of Sintered Samples

Table 4.16 and Figure 4.64 show the average Archimedes' densities values of the sintered specimens. The highest density value is seen in the HEB 13 composition consisting of (Hf-Ti-Zr-Mn-Cr-Mo-W-Ta)B_2, and the lowest density value is seen in the HEB 7 composition consisting of (Ti-Zr-Mn-Cr)B_2. It was observed that the average density values increased after SPS in all samples, except for the HEB 7 composition, which did not contain the HfB_2 phase. When the four-component systems are compared with each other, it is seen that the HEB 5 composition, which does not contain the TiB_2 phase, has the highest density value. Except for the HEB 5 composition, the average density values of all four component systems are lower than that of the HEB 1 composition. In the five-component ones, it is understood that the addition of TaB gradually increased the density compared to the addition of Cr boride. In six-component systems, the addition of W boride changed the density positively in comparison with the addition of Mo boride. When we look at the seven and eight components, it is seen that the addition of Mo boride decreases the density, while the additions of W boride and TaB increase the density. The eight-component composition, on the other hand, has a higher density value than densities of the seven-components. As a result, there is no correlation between the number of components and the measured average density values. In the compositions HEB 6, HEB 7, HEB 11, HEB 12 and HEB 13 where secondary phases are present, it should be considered that the secondary phases also affect the density values. In addition, low amounts of porosity are present in the compositions, as can be seen from the SEM images. It is predicted that the porosity may affect the density values. It is difficult to produce a fully dense sample, as evidenced by the porous structures. First, strong chemical bonds cause slow diffusion, and second, oxygen contamination causes coarsening (Gild et al, 2020).

Tallarita et al. (2020) synthesized a $(Hf_{0.2}Mo_{0.2}Ta_{0.2}Nb_{0.2}Ti_{0.2})B_2$ composition with a density of 8.07 ± 0.01 g/cm^3. Also, Zhang et al. (2022) synthesized $(Hf_{0.25}Zr_{0.25}Ta_{0.25}Sc_{0.25})B_2$ ceramics with 7.97 g/cm^3. Yang et al. (2022), on the other hand, found the densities to be between 6.86 g/cm^3 and 7.36 g/cm^3 in their study. The measured density values are seen as average when compared with those of the literature.

Table 4.16 : Average density Archimedes' values of the sintered samples.

Sample Code	Average Density (g/cm^3)
HEB 1	6.7289 ± 0.0016
HEB 2	6.5427 ± 0.0048
HEB 3	6.2544 ± 0.0118
HEB 4	7.4347 ± 0.0025
HEB 5	7.2559 ± 0.0022
HEB 6	6.4691 ± 0.0067
HEB 7	4.7517 ± 0.0015
HEB 8	6.3631 ± 0.0044
HEB 9	7.0504 ± 0.0034
HEB 10	7.0766 ± 0.0019
HEB 11	6.9134 ± 0.0032
HEB 12	7.3325 ± 0.0067
HEB 13	7.4794 ± 0.0065

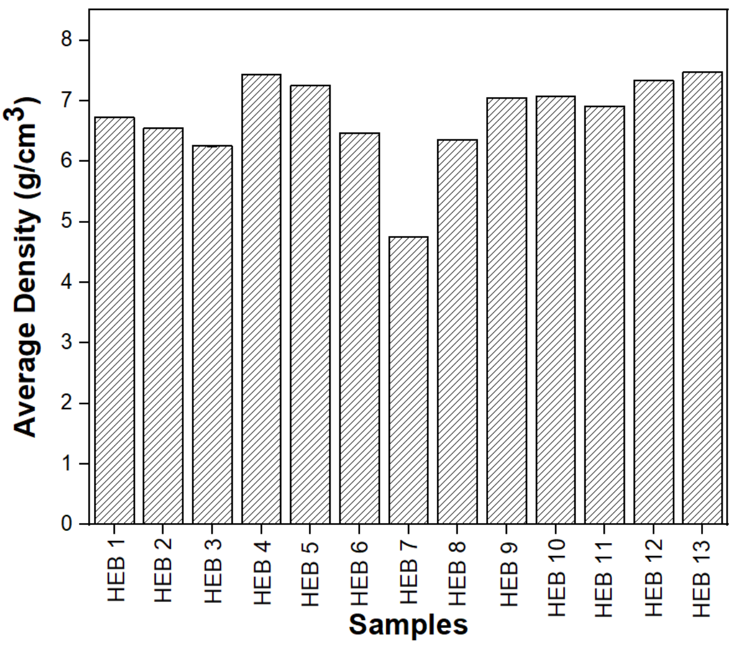

Figure 4.64 : Average Archimedes' density values of the sintered samples.

4.5 Mechanical Characterization of Sintered Samples

4.5.1 Hardness measurement

The hardness measurement results of the samples sintered with SPS can be found in Table 4.17 and Figure 4.65. The lowest hardness value was measured in the eight-component HEB 13 composition, and the highest hardness value was measured in the HEB 6 composition, which does not contain the ZrB_2 phase. The hardness value of HEB 1 composition, which is the main composition, is higher than the HEB 2, HEB 5, HEB 8, HEB 9, HEB 12 and HEB 13. When the four-components are compared with each other, the highest value is seen in the HEB 6 composition, and the lowest value is seen in the HEB 7 in the absence of the HfB_2. It is understood that the addition of Mn boride reduces the hardness. When the five-components were compared, it was observed that the TaB phase (HEB 4) significantly reduced the values compared to the Cr-B one (HEB 3). Looking at the HEB 2 and the HEB 3 compositions, the addition of the Cr-B phase increased the hardness again (HEB 2). When we look at the HEB 8 and the HEB 9 in six-component systems, it is understood from the HEB 9 composition that the addition of W boride significantly reduces the hardness. However, it is seen that the addition of both Mo boride and W boride reduces the hardness according to the composition of HEB 3, which is the base alloy. The addition of TaB reduced the hardness of seven-components. The W boride phase in the HEB 12 composition provided an insignificant increase in hardness compared to presence of the Mo boride in the HEB 11 composition. Since the HEB 6 composition contains a secondary phase, this secondary phase can be considered to increased the hardness value. Similarly, HEB 7, HEB 11, HEB 12 and HEB 13 compositions also contain secondary phases, which are predicted to affect the hardness values. As a result, it was observed that the addition of TaB significantly reduced the hardness in all compositions.

The order of hardness calculated in the study of Zhou et al. (2015) is as follows: $TiB_2 > ZrB_2 > HfB_2 > TaB_2 > CrB_2 > MoB_2 > WB_2$. According to this calculation, the composition without the ZrB_2 phase is not expected to have high hardness. In general, it is predicted that the MoB_2 and CrB_2 phases have lower hardness than the whole Group IV diborides (Mahesh et al, 2015; Y. Zhou et al, 2015). This means that in HEB ceramics containing MoB_2 and CrB_2 phases is expected to have lower hardness. Also, MoB_2 does not have a stable phase at room temperature, so there is no hardness value obtained as a result of experimental calculations, but it is estimated as a result of discrete fourier transform (DFT) studies that the hardness value is low (Y. Zhou et al, 2015). However, in this study, Mo-B and especially Cr-B systems increased the values. Similarly, in the study of Gild et al. (2020), additions to MoB_2 and CrB_2 seem to increase hardness (parameters: 200 gf, 15 sec). Similarly, in another study, compositions containing MoB_2, CrB_2 and WB_2 were found to have higher hardness (Qin et al, 2020b). In a study by Zhang et al. (2019), the hardness values of $(TiZrNbHfTa)B_2$, $(TiZrNbHfMo)B_2$ and $(TiNbMoHfTa)B_2$ compounds were measured at 21.7 ± 1.1 GPa, 26.3 ± 1.8 GPa, 27 ± 0.4 GPa, respectively. Again, the system containing Mo-B has a higher hardness value. In a study conducted in the literature, they calculated hardness of $(TiZrNbHfTa)B_2$ and $(TiZrWHfMo)B_2$, which resulting in values of 20.5 ± 1 GPa, 29.4 ± 1.7 GPa, respectively. It was determined that the secondary phases changed the hardness values and higher hardness values were obtained after densification (Y. Zhang et al, 2020). Feng et al. (2021) observed that the secondary phases affect the hardness values. Failla et al. (2020) synthesized compositions $(TiZrCrHfTa)B_2$, $(TiZrHfTa)B_2$, $(TiZrHfCr)B_2$, $(TiCrHfTa)B_2$, $(ZrCrHfTa)B_2$ and $(TiZrCrTa)B_2$. They measured the hardness values of these compositions at three different loads (1 kgf, 500 kgf and 200 kgf, 15 sec). The composition that does not contain the TiB_2 phase has the lowest hardness value under all conditions. However, similar to this study, the composition without the TaB_2 phase had the highest hardness values. It was observed that the hardness decreased when TaB_2 was added. Another study of Qin et al. (2020a), in their study, measured the hardness values of the $(TiZrNbHfTa)B_2$ ceramic with a loading force of 1 kgf and 200 gf, and a holding time of 15 sec. The results were 19.4 ± 1.3 GPa and 20.2 ± 1 GPa, respectively. It is observed that the hardness value increases as the load force decreases.

Solid-solution hardening has improved hardness. Furthermore, the composition and elements contained in the solid-solution have a significant impact on hardness values. The lattice parameter of each metal boride in the composition is different, it states that it forms solid-solution in different ways and changes the properties of chemical bonds. As a result, hardness values are affected (Feng et al, 2021; Z. Zhang et al, 2022).

Table 4.17 : Hardness values of the sintered samples.

Sample Code	Hardness (GPa)
HEB 1	24.61 ± 2.61
HEB 2	23.58 ± 2.10
HEB 3	26.55 ± 1.42
HEB 4	24.68 ± 1.41
HEB 5	23.24 ± 1.84
HEB 6	26.74 ± 1.85
HEB 7	24.72 ± 2.30
HEB 8	24.57 ± 2.55
HEB 9	22.26 ± 3.76
HEB 10	25.13 ± 2.97
HEB 11	23 ± 2.31
HEB 12	23.90 ± 2.81
HEB 13	17.08 ± 2.32

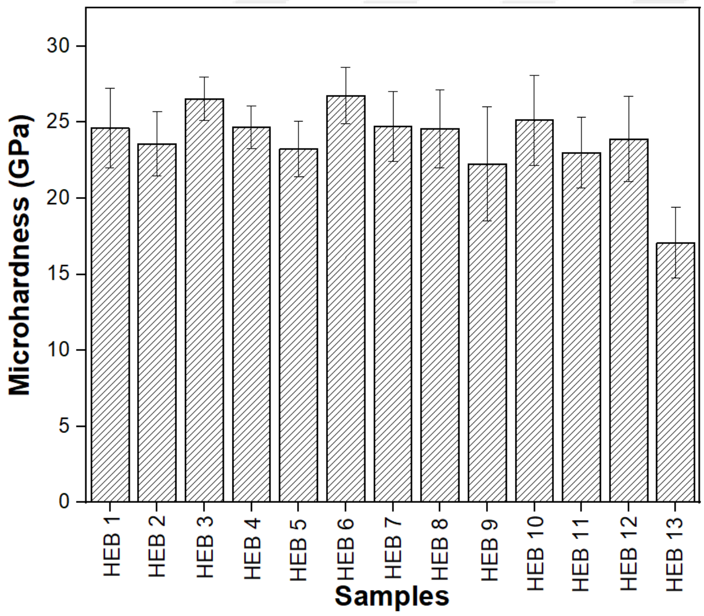

Figure 4.65 : Hardness values of the sintered samples.

4.5.2 Wear volume loss

Relative wear resistance and wear volume loss values of the sintered samples are given in 0 and Figure 4.66, respectively. The most wearing composition belongs to the eight-component system. The composition with the lowest hardness is HEB 13. The highest wear resistance belongs to the $(HfTiZrMnCrMo)B_2$ composition. When the third and four-component systems are examined, it is seen that their wear resistance can be characterized as low and similar to each other. The addition of Mn boride (HEB 2) has higher resistance than that of the base alloy (HEB 1). The absence of the TiB_2 phase (HEB 5) increased the wear resistance compared to the absence of the HfB_2 (HEB 7) and ZrB_2 (HEB 6) phases. The HEB 6 composition has almost the lowest one. Wear volume losses and relative wear resistances of the sintered samples.

Sample Code	Wear Volume Loss (mm^3)	Relative Wear Resistance
HEB 1	$0.00077 \pm 9.4x10^{-5}$	3.81
HEB 2	0.00067 ± 0.00019	4.36
HEB 3	0.00084 ± 0.00011	3.47
HEB 4	0.00081 ± 0.00011	3.61
HEB 5	0.00068 ± 0.00061	4.33
HEB 6	0.00272 ± 0.00064	1.08
HEB 7	0.00146 ± 0.00065	2.00
HEB 8	$0.00023 \pm 8x10^{-5}$	12.52
HEB 9	$0.00036 \pm 1.8x10^{-5}$	8.17
HEB 10	$0.00024 \pm 1.5x10^{-5}$	11.95
HEB 11	$0.00024 \pm 3.4x10^{-5}$	12.10
HEB 12	0.00056 ± 0.00019	5.19
HEB 13	0.00293 ± 0.00188	1

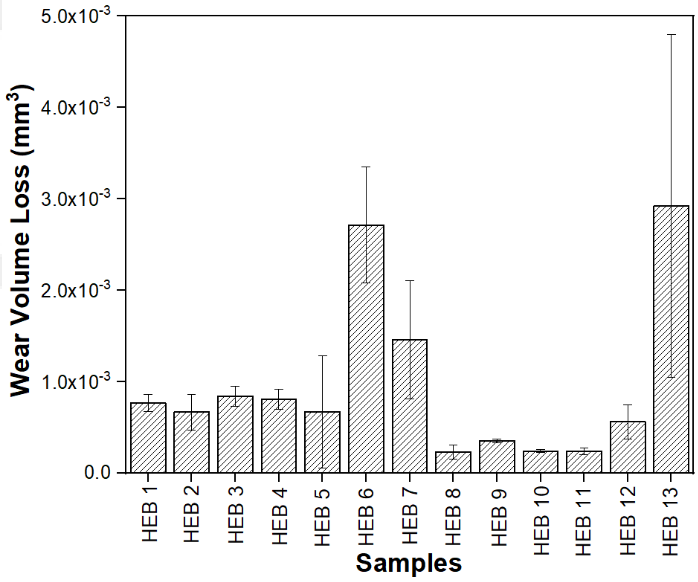

Figure 4.66 : Wear volume loss values of the sintered samples.

Although the addition of TaB (HEB 4) decreased the hardness, it increased the wear resistance compared to the HEB 3 composition. It is also seen that the addition of Cr boride did not improve the wear resistance in compared with the HEB 2 composition. When W boride was added, the resistance of the six-component systems decreased significantly. When the seven-component systems are compared with each other, the highest one is seen in the HEB 12 composition, where Mo boride and TaB additions are made together. A high decrease is observed in the composition (HEB 12), which includes the W boride and TaB phases together. Looking at all the results, it is seen that the additions of Mo boride and/or TaB increase the wear resistance.

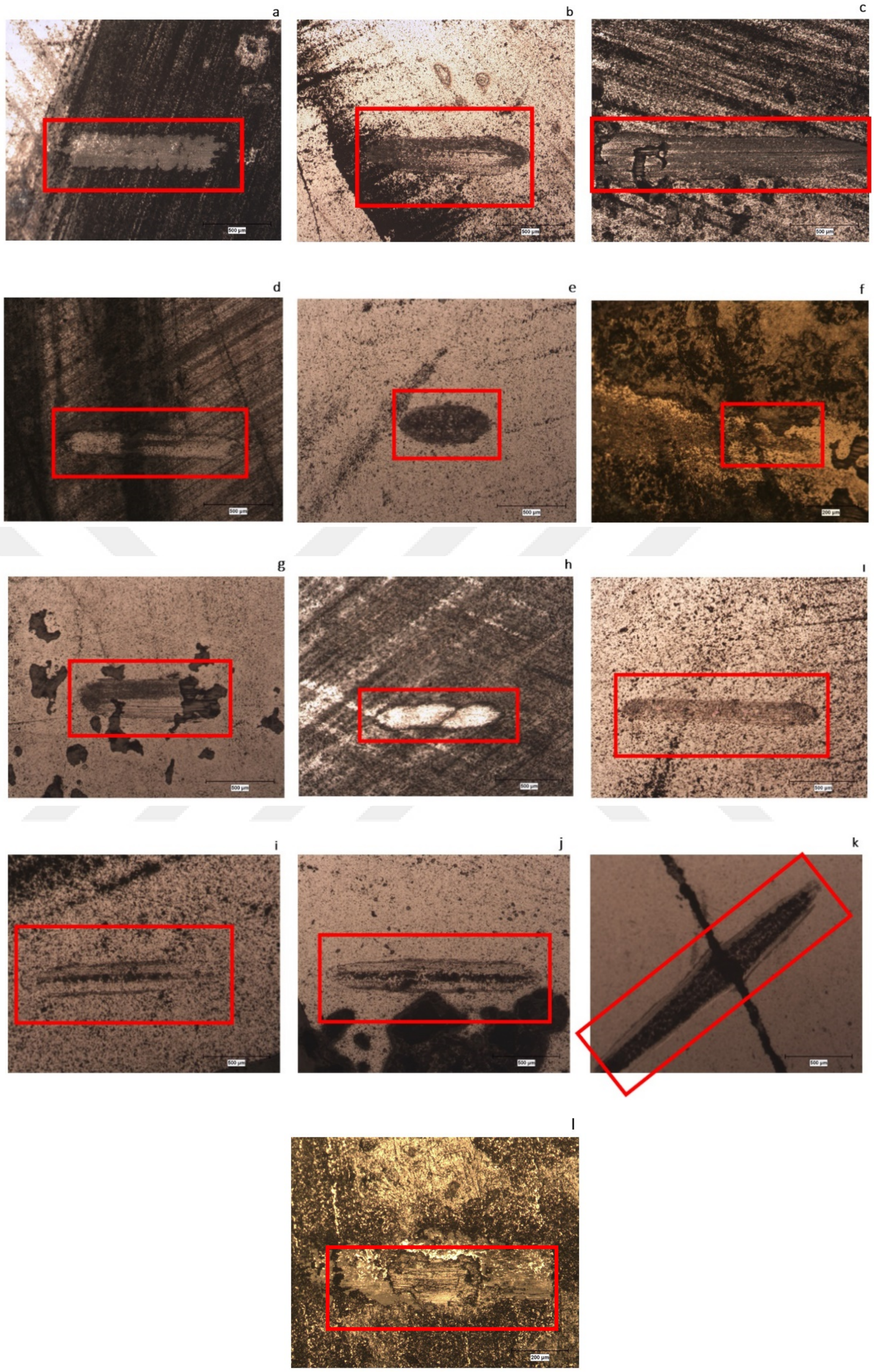

Figure 4.67 : Optical microscope images of wear tracks at 50X : (a) HEB 1, (b) HEB 2, (c) HEB 3, (d) HEB 4, (e) HEB 5, (f) HEB 6, (g) HEB 7, (h) HEB 8, (ı) HEB 9, (i) HEB 10, (j) HEB 11, (k) HEB 12, (l) HEB 13.

The images of the wear tracks taken with an optical microscope at 50X magnification are shown in Figure 4.67a-l. Each wear track having different widths and lengths confirms that the results are different from each other. Also, some tracks are are insignificantly visible. This is an indication that the wear marks remain on the surface and enhanced they cannot deptly abrade the surface. The high hardness of the samples makes it difficult to wear. High-entropy boride ceramics are wear resistant materials as expected.

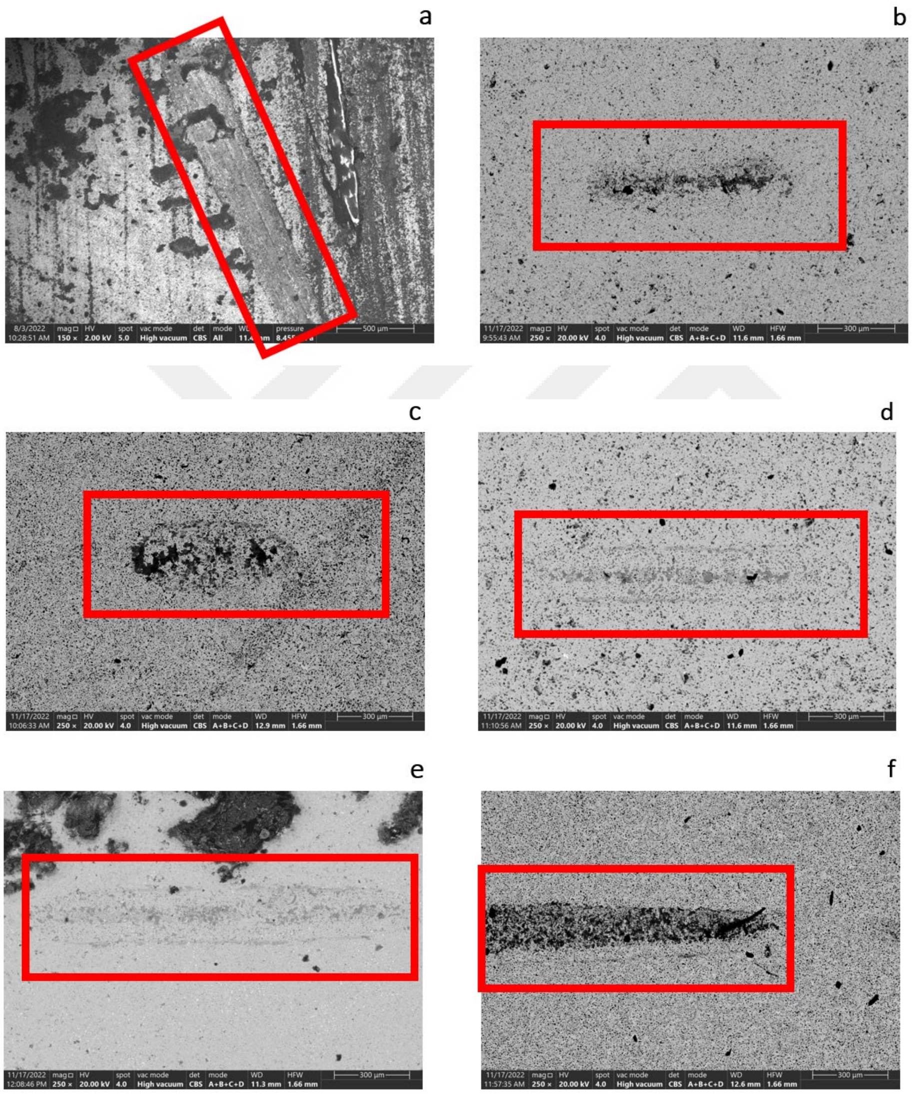

Figure 4.68 : SEM images of wear tracks at 150X (a) and 250X (b-f) of the representative samples : (a) HEB 3, (b) HEB 4, (c) HEB 5, (d) HEB 10, (e) HEB 11, (f) HEB 12.

SEM images of some representative samples (HEB 3, HEB 4, HEB 5, HEB 10, HEB 11, HEB 12, respectively) taken at different magnifications (150X and 250X) of the wear tracks are given in Figure 4.68. Wear tracks are clearly visible in the HEB 3, HEB 5 and HEB 12 compositions. However, these are not evident in HEB 4, HEB 10 and HEB 11 compositions. The correlation between the relative wear resistance and the apparent wear marks in the SEM images is not so accurate due to the high standard deviations.

2-D profiles taken from the surface of the wear tracks are shown in Figure 4.69a-h. It is understood that the wear tracks have different depths and widths. Elemental differences of compositions is the main factor of the wear resistances. Also, pore size, grain size, phase fractions and porosity are effect the resistance (Kavak et al, 2022b). Kavak et al. (2022b) synthesized $(HfTiZrW)B_2$ ceramics at different temperatures in their study. They observed that as the amount of porosity increases, the relative wear resistances decreases and the HEB ceramics wear more easily. When the literature studies are examined, there are a limited number of studies on the calculation of the relative wear value and öicrostructural analysis of wear trace in high-entropy borides.

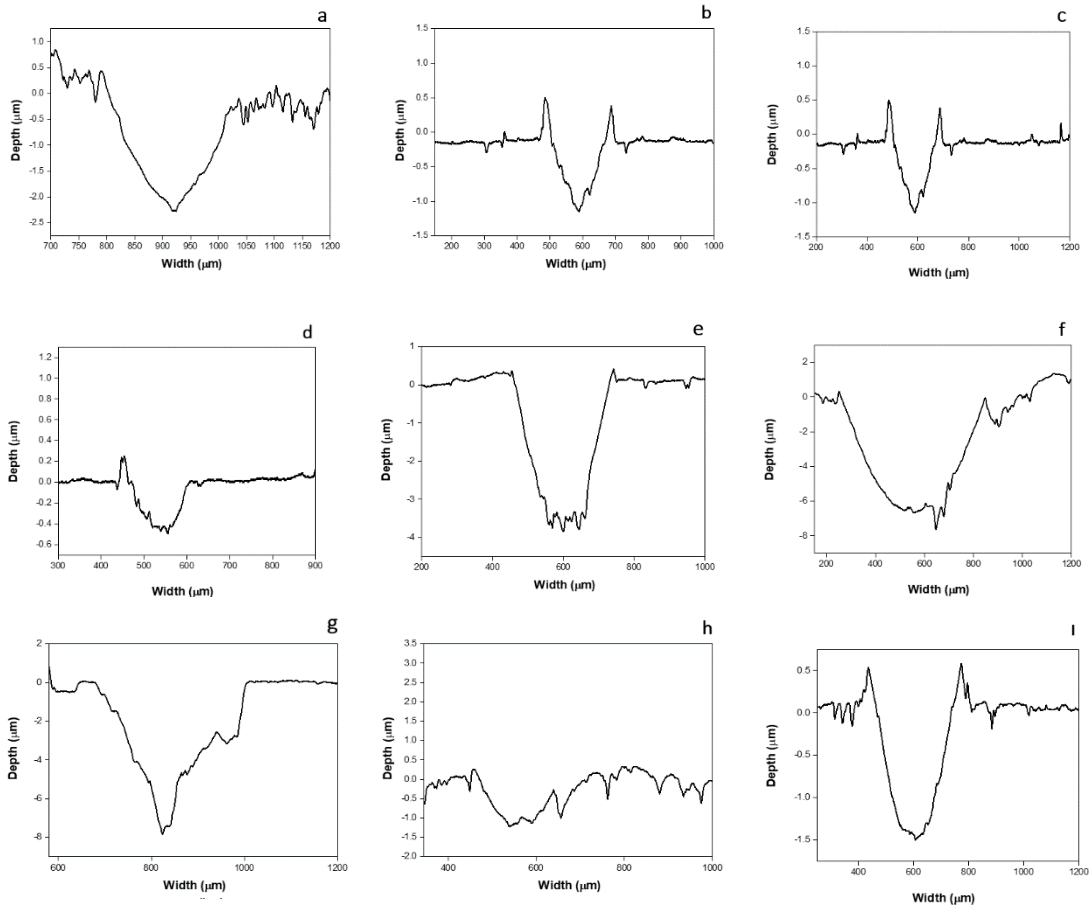

Figure 4.69 : 2-D profiles of the sintered samples: (a) HEB 1, (b) HEB 2, (c) HEB 3, (d) HEB 4, (e) HEB 5, (f) HEB 6, (g) HEB 7, (h) HEB 8, (ı) HEB 9, (i) HEB 10, (j) HEB 11, (k) HEB 12, (l) HEB 13.

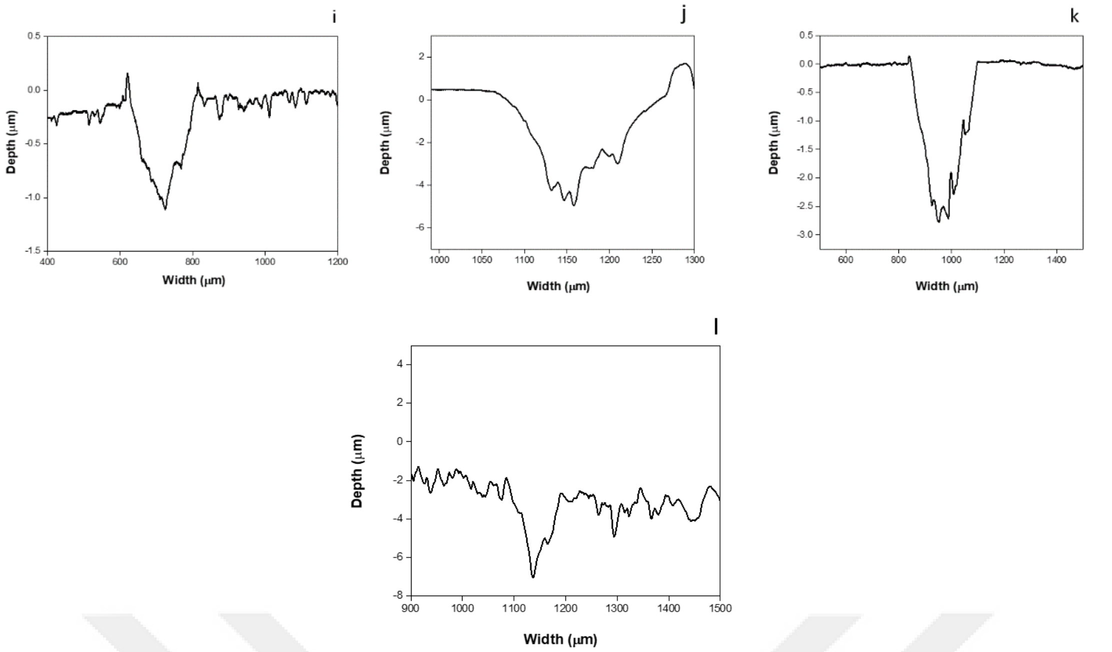

Figure 4.69 (continued) : 2-D profiles of the sintered samples: (a) HEB 1, (b) HEB 2, (c) HEB 3, (d) HEB 4, (e) HEB 5, (f) HEB 6, (g) HEB 7, (h) HEB 8, (ı) HEB 9, (i) HEB 10, (j) HEB 11, (k) HEB 12, (l) HEB 13.

5. CONCLUSIONS

Experimental studies and their literature comparison are given extensively in the results and discussion chapter. In this section, the general experimental results are summarized as follows:

- The synthesis of metal boride powders was completed in the lab-scale by mechanochemical synthesis using related metal oxides, native boron oxide and magnesium reductant and by purification. The optimum conditions for the production of metal boride powders are given below. The powders were synthesized in large amounts from the optimum conditions.
  - TiB_2 phase was synthesized from the starting powders of TiO_2–B_2O_3–Mg prepared in stoichiometric ratio, which were milled for 5 h and 6 M leached.
  - HfB_2 phase was synthesized from the starting powders of HfO_2–B_2O_3–Mg prepared in stoichiometric ratio, which were milled for 12 h and 6 M leached.
  - ZrB_2 phase was synthesized from the starting powders of ZrO_2–B_2O_3–Mg prepared in stoichiometric ratio, which were milled for 20 h and 4 M leached.
  - TaB phase was synthesized from the starting powders of Ta_2O_5–B_2O_3–Mg prepared in 50 wt.% excess B_2O_3, which were milled for 10 h and 4 M leached.
  - Mn-B phase were synthesized from the starting powders of MnO_2–B_2O_3–Mg prepared in 100 wt.% excess B_2O_3 and 50 wt.% excess Mg, which were milled for 10 h, 4 M leached and annealed at 1100°C.
  - Cr-B phase were synthesized from the starting powders of Cr_2O_3–B_2O_3–Mg prepared in 100 wt.% excess B_2O_3 and 25 wt.% excess Mg, which were milled for 5 h, 4 M leached and annealed at 1100°C,

- Mo-B phase was synthesized from the starting powders of MoO_3–B_2O_3–Mg prepared in 100 wt.% excess B_2O_3 and 50 wt.% excess Mg, which were milled for 6 h and 4 M leached.
- W-B phase was synthesized from the starting powders of WO_3–B_2O_3–Mg prepared in 100 wt.% excess B_2O_3 and 50 wt.% excess Mg, which were milled for 20 h and 4 M leached.

- The synthesized metal boride powders were converted into systems with 3, 4, 5, 6, 7 and 8 components and were mechanically alloyed. (Hf-Ti-Zr)B_2 system (HEB 1) was choosen as a main system. Only this system was planetary ball milled in various hours (30 h, 60 h, 100 h) and ball-to-powder weight ratios (10:1, 20:1, 30:1). As a result the expected peak formation which corresponds to single-phase was not observed.
- After that, the HEB 1 composition were high-energy ball milled at 6 h, 10 h, 15 h and 20 h. After mechanical alloying, hybrid phases began to form, but were not completed. As a result of mechanical alloying, besides hybrid phases, binary boride compounds and very slight contamination (WC) from vials were formed. Acoording to the peak intensities and broadenings, 6 h was choosen as an optimum duration.
- Particle size analyses shows bimodal or multi-modal distributions. It is seen that all powders are synthesized at the micron level.
- According to the density measurement results of the powders conducted using pycnometer, the highest density value is measured in the composition HEB 12 as 7.1379 ± 0.0057 g/cm^3, and the lowest density is seen in the composition HEB 7 as 4.9708 ± 0.005 g/cm^3. When all compositions are examined, it is seen that the Mo-B phase decreases the density value, while the HfB_2, TaB and W-B phases increase the density value.
- After SPS, high-entropy boride phases were formed as the major phase in all systems. However, there are also peaks of low intensity (Hf, Zr) oxide phases in the all compositions. Besides, secondary phases were formed in HEB 6, HEB 7, HEB 11, HEB 12 and HEB 13 compositions.

- Density values of the samples sintered with SPS were measured by Archimedes' method. While the highest density value was observed in the composition HEB 13 as 7.4794 ± 0.0065 g/cm^3, the lowest density value was observed in the composition HEB 7 as 4.7517 ± 0.0015 g/cm^3. Density value increased after sintering in all samples except HEB 7 composition. It is thought that the density value of HEB 6, HEB 7, HEB 11, HEB 12 and HEB 13 are affected by the secondary phases.
- When the SEM and EDS analyses are examined, it is seen that there is an inhomogeneous distribution in all microstructures. Hf is the most dominant element in all compositions except HEB 7 which does not contain Hf. Compositions containing Ta (HEB 4, HEB 11, HEB 12, HEB 13), it evaluated that Ta dominates the system after Hf element. Mn and Cr elements are below 10 wt.% in all compositions except HEB 7. The microstructure of the samples is similar to each other except the HEB 1, which is the main structure, and HEB 7 composition, which does not contain the HfB_2 phase.
- The highest hardness value of the samples sintered with SPS belongs to the HEB 6 composition with 26.74 ± 1.85 GPa and the lowest hardness value belongs to the HEB 13 composition with 17.08 ± 2.32 GPa. The average hardness value is about 24 GPa. The addition of Cr-B increased the value, while the addition of TaB decreased the value.
- The lowest wear resistance composition is HEB 13, while the highest composition is HEB 8. Among all compositions, additions of Mo-B or TaB appear to increase wear resistance.
- The contribution of the eight-component sample to the mechanical values is negative. However, when all compositions are examined, there is no correlation between the number of components and values.

As a result of all the experimental studies carried out until the completion of the project, some points as suggestions are summarized below:

- Since the mechanochemical synthesis method for the synthesis of metal boride powders from metal oxides is carried out at room temperature and has a low investment cost, it can be scaled up for the further large volume experiments.

- As a result of sintering studies with SPS, high hardness values and high density results were found together with high-entropy peaks. The use of the SPS method is suitable for the production of high-entropy boride ceramics. It would be appropriate to design dies for larger material productions.

REFERENCES

Ağaoğulları D., Aynıbal F., Demirhan O. C. & Duman İ. (2009a). Synthesis of titanium diboride by solid-state reaction between TiO_2-B_2O_3 and Mg, *1st Internation Ceramic Glass, Porselain Enamel, Glaze and Pigment Congress*, Eskişehir, Turkey, October 12-14.

Ağaoğulları D., Aynıbal F., Demirhan O. C. & Duman İ. (2009b). An optimization study for seperation of TiB_2 from a solid-state reaction product by HCl leaching, *1st Internation Ceramic Glass, Porselain Enamel, Glaze and Pigment Congress*, Eskişehir, Turkey, October 12-14.

Ağaoğulları, D., Duman, İ., & Öveçoğlu, M. L. (2012a). Synthesis of LaB_6 powders from La_2O_3, B_2O_3 and Mg blends via a mechanochemical route. *Ceramics International*, *38*(8), 6203–6214.

Ağaoğulları, D., Gökçe, H., Duman, İ., & Öveçoğlu, M. L. (2012b). Characterization investigations of ZrB_2/ZrC ceramic powders synthesized by mechanical alloying of elemental Zr, B and C blends. *Journal of the European Ceramic Society*, *32*(7), 1447–1455.

Ağaoğulları, D., Balcı, Ö., Öveçoğlu, M. L., Suryanarayana, C., & Duman, İ. (2015). Synthesis of bulk nanocrystalline samarium hexaboride. *Journal of the European Ceramic Society*, *35*(15), 4121–4136.

Ağaoğulları, D., Balcı, Ö., Öveçoğlu, M. L., & Duman, İ. (2017). Microstructural Evaluation of ZrB_2/ZrO_2 Ceramic Powders Prepared by Milling-Assisted Magnesiothermic Reduction of Oxide Raw Materials. *KONA Powder andParticleJournal*, *34*(0),183–196.

Ağaoğulları, D., Balcı, Ö., Akçamlı, N., Suryanarayana, C., Duman, İ., & Öveçoğlu, M. (2019). Mechanochemical synthesis and consolidation of nanostructured cerium hexaboride. *Processing and Application of Ceramics*, *13*(1), 32–43.

Akçamlı, N., Ağaoğulları, D., Balcı, Ö., Öveçoğlu, M. L., & Duman, İ. (2016). Synthesis of HfB powders by mechanically activated borothermal reduction of $HfCl_4$. *Ceramics International*, *42*(3), 3797–3807.

Akçamlı, N., Ağaoğulları, D., Balcı, Ö., Öveçoğlu, M. L., & Duman, İ. (2017). Synthesis of bulk nanocrystalline HfB_2 from $HfCl_4$–$NaBH_4$–Mg ternary system. *Journal of Materials Science*, *52*(21), 12689–12705.

Akgün, B., Çamurlu, H. E., Topkaya, Y., & Sevinç, N. (2011). Mechanochemical and volume combustion synthesis of ZrB_2. *International Journal of Refractory Metals and Hard Materials, 29*(5), 601–607.

Akopov, G., Yeung, M. T., & Kaner, R. B. (2017). Rediscovering the Crystal Chemistry of Borides. *Advanced Materials*, *29*(21), 1604506.

Akrami, S., Edalati, P., Fuji, M., & Edalati, K. (2021). High-entropy ceramics: Review of principles, production and applications. *Materials Science and Engineering:R:Reports*,*146*,100644.

Albert, B., & Hillebrecht, H. (2009). Boron: Elementary Challenge for Experimenters and Theoreticians. *Angewandte Chemie International Edition*, *48*(46), 8640–8668.

Altıntaş, Z., Khoshsima, S., Schmidt, M., Bobnar, M., Burkhardt, U., Somer, M., & Balcı, Ö. (2021). Evolution of magnetic properties of crystalline cobalt-iron boride nanoparticles via optimization of synthesis conditions using hydrous metal chlorides. *Journal of Magnetism and Magnetic Materials*, *523*, 167634.

Balaz, P. (2008). *Mechanochemistry in Nanoscience and Minerals Engineering*. Springer, Kosice, Slovakia.

Baláž, P., Achimovičová, M., Baláž, et al. & Wieczorek-Ciurowa, K. (2013). Hallmarks of mechanochemistry: From nanoparticles to technology. *Chemical Society Reviews*, *42*(18), 7571.

Balcı, Ö., Ağaoğulları, D., Duman, İ., & Öveçoğlu, M. L. (2012). Synthesis of CaB_6 powders via mechanochemical reaction of Ca/B_2O_3 blends. *Powder Technology*,*225*, 136–142.

Balcı, Ö., Ağaoğulları, D., Öveçoğlu, M. L., & Duman, İ. (2016). Synthesis of niobium borides by powder metallurgy methods using Nb_2O_5, B_2O_3 and Mg blends. *Transactions of Nonferrous Metals Society of China*, *26*(3), 747–758.

Balcı, Ö., Ağaoğulları, D., Suryanarayana, C., Duman, İ., & Öveçoğlu, M. L. (2019). Synthesis and characterization of vanadium boride powders and their sintered bodies. *Materials Research Express*, *6*(9), 096542.

Barbarossa, S., Orrù, R., Garroni, S., Licheri, R., & Cao, G. (2021a). Ultra high temperature high-entropy borides: Effect of graphite addition on oxides removal and densification behaviour. *Ceramics International*, *47*(5), 6220–6231.

Barbarossa, S., Orrù, R., Cannillo, V., Iacomini, A., Garroni, S., Murgia, M., & Cao, G. (2021b). Fabrication and Characterization of Quinary High Entropy-Ultra-High Temperature Diborides. *Ceramics*, *4*(2), 108–120.

Battezzati, L. (2019). *Solid Solutions in Metals: From Hume-Rothery's Rules to High Entropy Alloys*. 16.

Benjamin, J. S., & Volin, T. E. (1974). The mechanism of mechanical alloying. *Metallurgical Transactions*, *5*(8), 1929–1934.

Bilgi, E., Çamurlu, H. E., Akgün, B., Topkaya, Y., & Sevinç, N. (2008). Formation of TiB_2 by volume combustion and mechanochemical process. *Materials Research Bulletin, 43*(4), 873–881.

Cantor, B., Chang I.T.H., Knight, P. & Vincent, A.J.B. (2004). Microstructural development in equiatomic multicomponent alloys. *Material Science and Engineering, A*(375-377), 213-218.

Cantor, B. (2014). Multicomponent and High Entropy Alloys. *Entropy*, *16*(9), 4749–4768.

Cantor, B. (2021). Multicomponent high-entropy Cantor alloys. *Progress in Materials Science*, *120*, 100754.

Castle, E., Csanádi, T., Grasso, S., Dusza, J., & Reece, M. (2018). Processing and Properties of High-Entropy Ultra-High Temperature Carbides. *Scientific Reports*, *8*(1), 8609.

Cavaliere, P. (Ed.). (2019). *Spark Plasma Sintering of Materials: Advances in Processing and Applications*. Springer International Publishing.

Chen, C.-J., & Chen, D.-H. (2012). Preparation of LaB_6 nanoparticles as a novel and effective near-infrared photothermal conversion material. *Chemical Engineering Journal*, *180*, 337–342.

Chen, H., Xiang, H., Dai, F.-Z., Liu, J., & Zhou, Y. (2019). Porous high entropy $(Zr_{0.2}Hf_{0.2}Ti_{0.2}Nb_{0.2}Ta_{0.2})B_2$: A novel strategy towards making ultrahigh temperature ceramics thermal insulating. *Journal of Materials Science & Technology*, *35*(10), 2404–2408.

Chen, T. K., Shun, T. T., Yeh, J. W., & Wong, M. S. (2004). Nanostructured nitride films of multi-element high-entropy alloys by reactive DC sputtering. *Surface and Coatings Technology*, *188–189*, 193–200.

Chen, W., Anselmi-Tamburini, U., Garay, J. E., Groza, J. R., & Munir, Z. A. (2005). Fundamental investigations on the spark plasma sintering/synthesis process. *Materials Science and Engineering: A*, *394*(1–2), 132–138.

Chen, Y., Hwang, T., Marsh, M., & Williams, J. S. (1997). Study on mechanism of mechanical activation. *Materials Science and Engineering: A*, *226–228*, 95–98.

Cho, F.-Y., Tung, S.-W., & Ouyang, F.-Y. (2022). High temperature oxidation behavior of high entropy alloy $Al_4Co_3Cr_{25}Cu_{10}Fe_{25}Ni_{33}$ in oxygen-containing atmospheres. *Materials Chemistry and Physics*, *278*, 125678.

Coşkun, S., & Öveçoğlu, M. L. (2013). Room-Temperature Mechanochemical Synthesis of W2B5 Powders. *Metallurgical and Materials Transactions A*, *44*(4), 1805–1813.

Çelik, F. N., Tekoğlu, E., Mertdinç, S., Gökçe, H., Öveçoğlu, M. L., & Ağaoğulları, D. (2022). Mechanochemical synthesis investigations on the ternary and quaternary $B_2O_3/TiO_2/Mg/C$ systems. *Solid State Sciences*, *128*, 106897.

Dai, J., Zhu, J., Chen, C., & Weng, F. (2016). High temperature oxidation behavior and research status of modifications on improving high temperature oxidation resistance of titanium alloys and titanium aluminides: A review. *Journal of Alloys and Compounds*, *685*, 784–798.

Delogu, F. and Mulas, G. (2010). Kinetic processes and mechanism of mechanical alloying, in *High-energy ball milling: mechanochemical processing of nanopowders,* Italy, p. 92-100, Ed. Sopicka-Lizer, M., Woodhead Publishing Limited, CRC, Cambridge, UK.

Demirskyi, D., Suzuki, T.S., Yoshimi, K. & Vasylkiv, O. (2020). Synthesis of medium-entropy $(Zr_{1/3}Hf_{1/3}Ta_{1/3})B_2$ using the spark plasma consolidation of diboride powders. *Journal of Ceramic Society of Japan, 128*(11), 977-980.

Demirskyi, D., Nishimura, T., Yoshimi, K. & Vasylkiv, O. (2023). High-strength, medium entropy Zr-Ta-Nb diboride ceramics. *Scripta Materialia, 225.*

Dobodoe, R.S., West, G.D. & Lewi, M.H. (2013). Spark plasma sintering of ceramics: understanding temperature distribution enables more realistic comparison with conventional processing. *Advances in Applied Ceramics, 104*(3), 110-116.

Duan, B., Yu, Y., Liu, X., Wang, D., & Wu, Z. (2020). A Novel Non-Equiatomic $(W_{35}Ta_{35}Mo_{15}Nb_{15})_{95}Ni_5$ Refractory High Entropy Alloy with High Density Fabricated by Powder Metallurgical Process. *Metals*, *10*(11), 1436.

El-Eskandarany, M. (2015). Mechanical alloying : nanotechnology, materials science and powder metallurgy, *Elsevier Inc*. 2,13–35.

Euh, K., Lee, J., & Lee, S. (2001). Microstructural Modification and property improvement of boride/Ti-6Al-4V surface-alloyed materials fabricated by high-energy electron-beam irradiation. *Metallurgical and Materials Transactions A*, *32*(10), 2499–2508.

Fahrenholtz, W. G., Hilmas, G. E., Talmy, I. G., & Zaykoski, J. A. (2007). Refractory Diborides of Zirconium and Hafnium. *Journal of the American Ceramic Society*, *90*(5), 1347–1364.

Fang, S., Xiao, X., Xia, L., Li, W., & Dong, Y. (2003). Relationship between the widths of supercooled liquid regions and bond parameters of Mg-based bulk metallic glasses. *Journal of Non-Crystalline Solids*, *321*(1–2), 120–125.

Feltrin, A. C., Hedman, D., & Akhtar, F. (2021). Transformation of metastable dual-phase $(Ti_{0.25}V_{0.25}Zr_{0.25}Hf_{0.25})B_2$ to stable high-entropy single-phase boride by thermal annealing. *Applied Physics Letters*, *119*(16), 161905.

Feng, L., Monteverde, F., Fahrenholtz, W. G., & Hilmas, G. E. (2021). Superhard high-entropy AlB_2-type diboride ceramics. *Scripta Materialia*, *199*, 113855.

Feuerbacher, M., Heidelmann, M., & Thomas, C. (2015). Hexagonal High-entropy Alloys. *Materials Research Letters*, *3*(1), 1–6.

Friedrich, A., Winkler, B., Juarez-Arellano, E. A., & Bayarjargal, L. (2011). Synthesis of Binary Transition Metal Nitrides, Carbides and Borides from the Elements in the Laser-Heated Diamond Anvil Cell and Their Structure-Property Relations. *Materials*, *4*(10), 1648–1692.

Gao, Y., Huang, L., Tong, Z., Liu, J., Zhang, Q., Zhang, H., Jia, Q., & Zhang, S. (2022). Low-temperature synthesis of high-entropy $(Hf_{0.2}Ti_{0.2}Mo_{0.2}Ta_{0.2}Nb_{0.2})B_2$ powders combined with theoretical forecast of its elastic and thermal properties. *Journal of the American Ceramic Society*, *105*(10), 6370–6383.

German, R.M. (2014). Sintering With External Pressure. Sintering: from Empirical Observations to Scientific Principles. Butterworth-Heinemann, 305-354. "

Ghaffari, S.A., Faghihi-Sani, M.A., Golestani-Fard, F. & Nojabayy, M. (2013). Diffusion and solid solution formation between the binary carbides of TaC, HfC and ZrC. *International Journal of Refractory Metals and Hard Materials, 41*(2013), 180-184.

Gigolotti, J. C. J., Suzuki, P. A., Nunes, C. A., & Coelho, G. C. (2012). Microstructural characterization of as-cast Hf-B alloys. *Materials Research*, *15*(2), 185–190.

Gild, J., Zhang, Y., Harrington, T., Jiang, S., Hu, T., Quinn, M. C., … Luo, J. (2016). High-Entropy Metal Diborides: A New Class of High-Entropy Materials and a New Type of Ultrahigh Temperature Ceramics. *Scientific Reports*, *6*(1), 37946. doi:10.1038/srep37946

Gild, J., Braun, J., Kaufmann, K., Marin, E., Harrington, T., Hopkins, P., … Luo, J. (2019a). A high-entropy silicide: $(Mo_{0.2}Nb_{0.2}Ta_{0.2}Ti_{0.2}W_{0.2})Si_2$. *Journal of Materiomics*, *5*(3), 337–343. doi:10.1016/j.jmat.2019.03.002

Gild, J., Kaufmann, K., Vecchio, K., & Luo, J. (2019b). Reactive flash spark plasma sintering of high-entropy ultrahigh temperature ceramics. *Scripta Materialia*, *170*, 106–110.

Gild, J., Wright, A., Quiambao-Tomko, K., Qin, M., Tomko, J. A., Shafkat bin Hoque, M., … Luo, J. (2020). Thermal conductivity and hardness of three single-phase high-entropy metal diborides fabricated by borocarbothermal reduction and spark plasma sintering. *Ceramics International*, *46*(5), 6906–6913. doi:10.1016/j.ceramint.2019.11.186

Gilman, P. S. and Benjamin, J. S. (1983). Mechanical alloying, *Annual Review of Materials Science,* 13, 279-300.

Gorsse, S., Miracle, D. B., & Senkov, O. N. (2017). Mapping the world of complex concentrated alloys. *Acta Materialia*, *135*, 177–187.

Gu, J., Zou, J., Sun, S.-K., Wang, H., Yu, S.-Y., Zhang, J., … Fu, Z. (2019). Dense and pure high-entropy metal diboride ceramics sintered from self-synthesized powders via boro/carbothermal reduction approach. *Science China Materials*, *62*(12), 1898–1909. doi:10.1007/s40843-019-9469-4.

Guillon, O., Gonzalez-Julian, J., Dargatz, B., Kessel, T., Schierning, G., Rathel, J. & Herrmann, M. (2014). Field-assisted sintering technology/spark plasma sintering: mechanisms, materials, and technology developments *Advanced Engineering Materials, 14*,830-849.

Guo, S., & Liu, C. T. (2011). Phase stability in high entropy alloys: Formation of solid-solution phase or amorphous phase. *Progress in Natural Science: Materials International*, *21*(6), 433–446.

Guo, S., Ng, C., Lu, J., & Liu, C. T. (2011). Effect of valence electron concentration on stability of FCC or BCC phase in high entropy alloys. *Journal of Applied Physics*, *109*(10), 103505.

Gutman E. M. (1998). *Mechanochemistry of Materials.* Cambridge International Publishing, Cambridge.

He, Q. F., Ding, Z. Y., Ye, Y. F., & Yang, Y. (2017). Design of High-Entropy Alloy: A Perspective from Nonideal Mixing. *JOM*, *69*(11), 2092–2098.

Heiligers, C., PRetorius, C.J. & Neethling, J.H. (2012). Interdiffusion of hafnium carbide and titanium carbide during hot-pressing. *International Journal of Refractory Metals and Hard Materials, 31*(2012), 51-55.

Iizumi K., Kudaka K., Maezawa D., Sasaki T. (2011) Mechanochemical synthesis of chromium borides**,** *Journal of Ceramic Society of Japan, 107*, 491-493.

Iyer, A. K., Zhang, Y., Scheifers, J. P., & Fokwa, B. P. T. (2019). Structural variations, relationships and properties of M_2B metal borides. *Journal of Solid State Chemistry*, *270*, 618–635.

Kanazawa, S., Kaneno, Y., Inoue, H., Kim, W.-Y., Takasugi, T. (2022). Microstructures and defect structures in $ZrCr_2$ Laves phase based intermetallic compounds. *Intermetallics, 10*(8), 783-792.

Kang, B., Lee, J., Ryu, H.J. & Hong, S.H. (2018). Ultra-high strength WNbMoTaV high-entropy alloys with fine grain structure fabricated by powder metallurgical process. *Material Science & Engineering A 712*(2018), 616-624.

Kardashova, G. D. (2020)., B., Technology of spark plasma sintering as an innovative solution of synthesis high-density of SiC ceramics. *IOP Conference Series: Materials Science and Engineering*, *848*(1), 012030.

Kavak, S., Bayrak, K. G., Bellek, M., Mertdinç, S., Muhaffel, F., Gökçe, H., … Ağaoğulları, D. (2022a). Synthesis and characterization of (HfMoTiWZr)C high entropy carbide ceramics. *Ceramics International*, *48*(6), 7695–7705. doi:10.1016/j.ceramint.2021.11.317.

Kavak, S., Bayrak, K. G., Mansoor, M., Kaba, M., Ayas, E., Balcı-Çağıran, Ö., … Ağaoğulları, D. (2022b). First principles calculations and synthesis of multi-phase $(HfTiWZr)B_2$ high entropy diboride ceramics: Microstructural, mechanical and thermal characterization. *Journal of the European Ceramic Society*, S0955221922008251. doi:10.1016/j.jeurceramsoc.2022.10.047.

Kieffer, R., & Benesovsky, F. (1958). Recent developments ın the fıeld of sılıcıdes and borıdes of the hıgh-meltıng-poınt transıtıon metals. *Powder Metallurgy*, *1*(1–2), 145–171.

Kim, H. J., Kim, W. K., Falk, M. L. and Rigney, D. A. (2007). MD simulations of microstructure evolution during high-velocity sliding between crystalline materials, *Tribology Letters,* 28, 299-306.

Kirnbauer, A., Wagner, A., Moraes, V., Primetzhofer, D., Hans, M., Schneider, J. M., … Mayrhofer, P. H. (2020). Thermal stability and mechanical properties of sputtered (Hf,Ta,V,W,Zr)-diborides. *Acta Materialia*, *200*, 559–569. doi:10.1016/j.actamat.2020.09.018

Kudaka, K., Iizumi, K., Sasaki, T., & Okada, S. (2001). Mechanochemical synthesis of MoB_2 and Mo_2B_5. *Journal of Alloys and Compounds*, *315*(1–2), 104–107.

Kumar, A., Singh, A., & Suhane, A. (2022). Mechanically alloyed high entropy alloys: Existing challenges and opportunities. *Journal of Materials Research and Technology*, *17*, 2431–2456.

Kumar, D., Maulik, O., Bagri, A. S., Prasad, Y. V. S. S., & Kumar, V. (2016). Microstructure and Characterization of Mechanically Alloyed Equiatomic AlCuCrFeMnW High Entropy Alloy. *Materials Today: Proceedings*, *3*(9), 2926–2933.

Levitas, V. (2003). Continuum mechanical fundamentals of mechanochemistry. In V. Domnich & Y. Gogotsi (Eds.), *High Pressure Surface Science and Engineering* (Vol. 20031476, pp. 161–292). Taylor & Francis.

Li, F., Cui, W., Shao, Y., Zhang, J., Du, S., Chen, Z., … Liu, G. (2022). Preparing high-entropy ceramic films from high-entropy alloy substrate. *Materials Chemistry and Physics*, *287*, 126365. doi:10.1016/j.matchemphys.2022.126365

Li, J.-H., & Tsai, M.-H. (2020). Theories for predicting simple solid solution high-entropy alloys: Classification, accuracy, and important factors impacting accuracy. *Scripta Materialia*, *188*, 80–87.

Liu, D., Wen, T., Ye, B., & Chu, Y. (2019). Synthesis of superfine high-entropy metal diboride powders. *Scripta Materialia*, *167*, 110–114. 8

Liu, D., Liu, H., Ning, S., & Chu, Y. (2020). Chrysanthemum-like high-entropy diboride nanoflowers: A new class of high-entropy nanomaterials. *Journal of Advanced Ceramics*, *9*(3), 339–348.

Liu, Y., Cheng, C., Shang, J., Wang, R., Li, P., & Zhao, J. (2015). Oxidation behavior of high-entropy alloys AlxCoCrFeNi (x=0.15, 0.4) in supercritical water and comparison with HR3C steel. *Transactions of Nonferrous Metals Society of China*, *25*(4), 1341–1351..

Long, Y., Che, J., Wu, Z., Lin, H.-T., & Zhang, F. (2021). High entropy alloy borides prepared by powder metallurgy process and the enhanced fracture toughness by addition of yttrium. *Materials Chemistry and Physics*, *257*, 123715.

Lü, L., & Lai, M. O. (1998). *Mechanical alloying*. Kluwer Academic Publishers.

Ma, M., Ye, B., Han, Y., Sun, L., He, J., & Chu, Y. (2020). High-pressure sintering of ultrafine-grained high-entropy diboride ceramics. *Journal of the American Ceramic Society*, *103*(12), 6655–6658.

Mahesh, B., Sairam, K., Sonber, J. K., Murthy, T. S. R. Ch., Nageswara Rao, G. V. S., Srinivasa Rao, T., & Chakravartty, J. K. (2015). Sinterability studies of monolithic chromium diboride (CrB_2) by spark plasma sintering. *International Journal of Refractory Metals and Hard Materials*,

Matizamhuka, W. R. (2016). Spark plasma sintering (SPS)—An advanced sintering technique for structural nanocomposite materials. *Journal of the Southern African Institute of Mining and Metallurgy*, *116*(7), 1171–1180.

Mayrhofer, P. H., Kirnbauer, A., Ertelthaler, Ph., & Koller, C. M. (2018). High-entropy ceramic thin films; A case study on transition metal diborides. *Scripta Materialia*, *149*, 93–97.

Mertdinç, S., Ağaoğulları, D., & Öveçoğlu, M. L. (2018). Mechanochemically synthesized Fe_2B nanoparticles embedded in SiO_2 nanospheres. *Ceramics International*, *44*(12), 14834–14843.

Mertdinç, S., Ağaoğulları, D., & Öveçoğlu, M. L. (2019). TaB/TaB_2 tozlarının mekanokimyasal sentezleme ile üretimi ve karakterizasyonu. *Afyon Kocatepe Üniversitesi Fen ve Mühendislik Bilimleri Dergisi, 19*(2019), 465-473.

Merz, M., Schweiss, P., Wolf, T., von Löhneysen, H., & Schuppler, S. (2014). Electronic Structure of Single-Crystalline $Mg_x Al_{1-x} B_2$ Probed by X-ray Diffraction Multipole Refinements and Polarization-Dependent X-ray Absorption Spectroscopy. *Journal of the Physical Society of Japan*, *83*(2), 024714.

Miracle, D.B., Senkov, O.N. (2017). A criticial review of high entropy alloys and related concepts. *Acta Materialia, 122*(2017), 448-511.

Mitra, R., Bajpai, A., & Biswas, K. (2022). Machine learning based approach for phase prediction in high entropy borides. *Ceramics International*, *48*(12), 16695–16706.

Monteverde, F. & Saraga, F. (2020). Entropy stabilized single-phase $(Hf,Nb,Ta,Ti,Zr)B_2$ solid solution powders obtained via carbo/boro-thermal reduction. *Journals of Alloys and Compounds, 824*, 1-11.

Monteverde, F., Saraga, F., Gaboardi, M., & Plaisier, J. R. (2021). Compositional pathways and anisotropic thermal expansion of high-entropy transition metal diborides. *Journal of the European Ceramic Society*, *41*(13), 6255–6266.

Monteverde, F., Saraga, F., Gaboardi, M., Feng, L., Hilmas, G., & Fahrenholtz, W. (2022). Quantitative inspection of grain-scale chemical inhomogeneities in high-entropy AlB_2 -type transition metal diborides. *Journal of the American Ceramic Society*, *105*(11), 6910–6923.

Munir, Z. A. & Anselmi-Tamburini, U. (1989). Self propagating exothermic reactions: The synthesis of high-temperature materials by combustion. *Material Science Reports, 3*(6), 277-358.

Munir, Z. A., Anselmi-Tamburini, U., & Ohyanagi, M. (2006). The effect of electric field and pressure on the synthesis and consolidation of materials: A review of the spark plasma sintering method. *Journal of Materials Science*, *41*(3), 763–777.

Murchie, A. C., Watts, J. L., Fahrenholtz, W. G., & Hilmas, G. E. (2022). Room-temperature mechanical properties of a high-entropy diboride. *International Journal of Applied Ceramic Technology*, *19*(4), 2293–2299.

Murty, B. S., Yeh, J. W., & Ranganathan, S. (2014). High-Entropy Alloys. In *High Entropy Alloys* (pp. 13–35). Elsevier.

Musicó, B. L., Gilbert, D., Ward, T. Z., Page, K., George, E., Yan, J., … Keppens, V. (2020). The emergent field of high entropy oxides: Design, prospects, challenges, and opportunities for tailoring material properties. *APL Materials*, *8*(4), 040912. doi:10.1063/5.0003149

Otitoju, A.T., Ugochukwu Okoye, P., Chen, G., Li, Y., Onyeka Okoye, M., & Li, S. (2020). Advanced ceramic components: Materials, fabrication, and applications. *Journal of Industrial and Engineering Chemistry*, *85*, 34–65.

Poletti, M. G., & Battezzati, L. (2014). Electronic and thermodynamic criteria for the occurrence of high entropy alloys in metallic systems. *Acta Materialia*, *75*, 297–306.

Popov, P. A., Novikov, V. V., Sidorov, A. A., & Maksimenko, E. V. (2007). Thermal conductivity of LaB6 and SmB6 in the range 6–300 K. *Inorganic Materials*, *43*(11), 1187–1191.

Post, B., Glaser, F. W., & Moskowitz, D. (1954). Transition metal diborides. *Acta Metallurgica*, *2*(1), 20–25.

Qi, C., Jiang, Y., Liu, Y., & Zhou, R. (2014). Elastic and electronic properties of XB_2 (X=V, Nb, Ta, Cr, Mo, and W) with AlB_2 structure from first principles calculations. *Ceramics International*, *40*(4), 5843–5851.

Qiao, L., Liu, Y., Gao, Y., Bi, J., Li, Y., Liu, C., … Qian, Z. (2022). First-principles prediction, fabrication and characterization of $(Hf_{0.2}Nb_{0.2}Ta_{0.2}Ti_{0.2}Zr_{0.2})B_2$ high-entropy borides. *Ceramics International*, *48*(12), 17234–17245. doi:10.1016/j.ceramint.2022.02.281

Qin, M., Gild, J., Hu, C., Wang, H., Hoque, M. S. B., Braun, J. L., … Luo, J. (2020a). Dual-Phase High-Entropy Ultra-High Temperature Ceramics. *Journal of the European Ceramic Society*, *40*(15), 5037–5050. doi:10.1016/j.jeurceramsoc.2020.05.040

Qin, M., Gild, J., Wang, H., Harrington, T., Vecchio, K. S., & Luo, J. (2020b). Dissolving and stabilizing soft WB_2 and MoB_2 phases into high-entropy borides via boron-metals reactive sintering to attain higher hardness. *Journal of the European Ceramic Society*, *40*(12), 4348–4353.

Qin, M., Yan, Q., Liu, Y., & Luo, J. (2021). A new class of high-entropy M3B4 borides. *Journal of Advanced Ceramics*, *10*(1), 166–172.

Ranganathan, S. (2003). Alloyed pleasures: Multimetallic cocktails. *CURRENT SCIENCE*, *85*(10), 3.

Reddy, V., Sonber, J. K., Sairam, K., Murthy, T. S. R. Ch., Kumar, S., Nageswara … Chakravartty, J. K. (2015). Densification and mechanical properties of CrB_2+$MoSi_2$ based novel composites. *Ceramics International*, *41*(6), 7611–7617. doi:10.1016/j.ceramint.2015.02.086

Rigney, D. A. and Hammerberg, J. E. (1999). Advanced Materials for the 21st Century. In Y. W. Chung, D. C. Dunand, P. K. Liaw, G. B. Olson (Eds.), *The 1999 Julia R. Weertman Symposium,* (Pp. 465–474). Cincinnati: TMS (OH).

Rios, J., Restrepo, A., Zuleta, A., Bolívar, F., Castaño, J., Correa, E. & Echeverria, F. Effect of ball size on the microstructure and morphology of Mg powders processed by high-energy ball milling. *Metals 2021, 11,* 1621.

Rost, C. M., Sachet, E., Borman, T., Moballegh, A., Dickey, E. C., Hou, D., … Maria, J.-P. (2015). Entropy-stabilized oxides. *Nature Communications*, *6*(1), 8485. doi:10.1038/ncomms9485

Senkov, O. N., Senkova, S. V., Woodward, C., & Miracle, D. B. (2013). Low-density, refractory multi-principal element alloys of the Cr–Nb–Ti–V–Zr system: Microstructure and phase analysis. *Acta Materialia*, *61*(5), 1545–1557.

Senkov, O.N., Miracle, D.B. & Chaput, K.J. (2018) Development and exploration of refractory high-entropy alloys-A review. *Journal of Materials Research, 33*(19), 3092-3128.

Soni, P. (2001). *Mechanical alloying: fundamentals and applications,* Cambridge International Science Publishing, Cambridge, UK.

Şimşek T., Özcan Ş. (2019). Synthesis and characterization of Mn_2B nanocrystals by mechanical alloying method, *Journal of Boron, 4,* 25-30.

Şenyurt, B., Akçamlı, N., & Ağaoğulları, D. (2021). In-situ synthesis of tungsten boride-carbide composite powders from WO_3-B_2O_3–Mg–C quaternary system via a mechanochemical route. *Ceramics International*, *47*(2), 1640–1650.

Shuang, S., Ding, Z. Y., Chung, D., Shi, S. Q., & Yang, Y. (2020). Corrosion resistant nanostructured eutectic high entropy alloy. *Corrosion Science*, *164*, 108315.

Singh, S., Wanderka, N., Murty, B. S., Glatzel, U., & Banhart, J. (2011). Decomposition in multi-component AlCoCrCuFeNi high-entropy alloy. *Acta Materialia*, *59*(1), 182–190.

Smith, S. M., Feng, L., Fahrenholtz, W. G., Hilmas, G. E., & Huang, T. (2022). High-entropy boride–carbide ceramics by sequential boro/carbothermal synthesis. *Journal of the American Ceramic Society*, *105*(9), 5543–5547.

Spear, K. E., & Liao, P. K. (1986). The B−Cr (Boron-Chromium) system. *Bulletin of Alloy Phase Diagrams*, *7*(3), 232-237.

Spear, K. E., & Liao, P. K. (1986). The B−Mn (Boron-Manganese) system. *Bulletin of Alloy Phase Diagrams*, *7*(6), 543-549.

Spear, K. E., & Liao, P. K. (1988). The B−Mo (Boron-Molybdenum) system. *Bulletin of Alloy Phase Diagrams*, *9*(4), 457–466.

Storr, B., Kodali, D., Chakrabarty, K., Baker, P. A., Rangari, V., & Catledge, S. A. (2021). Single-Step Synthesis Process for High-Entropy Transition Metal Boride Powders Using Microwave Plasma. *Ceramics*, *4*(2), 257–264.

Suárez, M., Fernández, A., Menéndez, J.L., Torrecillas, R., Kessel, H.U., Hennicke J., … Kessel T. (2013). Challenges and opportunities for spark plasma sintering: a key technology for a new generation of materials. *Sintering Applications.* doi: 10.5772/53706.

Suryanarayana, C. (2001). Mechanical alloying and milling. *Progress in Materials Science*, 184.

Suryanarayana, C., Ivanov, E., & Boldyrev, V. V. (2001). The science and technology of mechanical alloying. *Materials Science and Engineering: A*, *304–306*, 151–158.

Suryanarayana, C. (2022). Mechanical alloying: A critical review. *Materials Research Letters*, *10*(10), 619–647.

Tallarita, G., Licheri, R., Garroni, S., Barbarossa, S., Orrù, R., & Cao, G. (2020). High-entropy transition metal diborides by reactive and non-reactive spark plasma sintering: A comparative investigation. *Journal of the European Ceramic Society*, *40*(4), 942–952.

Tekoğlu, E., Öveçoğlu, M. L., & Ağaoğulları, D. (2021). Effects of milling time and reductant content on the formation of HfC-HfB_2 composite powders synthesized via a solid-state reaction route. *Ceramics International*, *47*(17), 23851–23860.

Tokita, M. (2013). Spark Plasma Sintering (SPS) Method, Systems, and Applications. In *Handbook of Advanced Ceramics* (pp. 1149–1177). Elsevier.

Tokunaga, T., Terashima, K., Ohtani, H., & Hasebe, M. (2008). Thermodynamic Analysis of the Phase Equilibria in the Fe-Zr-B System. *MATERIALS TRANSACTIONS*, *49*(11), 2534–2540.

Tong, C.-J., Chen, Y.-L., Yeh, J.-W., Lin, S.-J., Chen, S.-K., Shun, T.-T., … Chang, S.-Y. (2005). Microstructure characterization of Al x CoCrCuFeNi high-entropy alloy system with multiprincipal elements. *Metallurgical and Materials Transactions A*, *36*(4), 881–893. doi:10.1007/s11661-005-0283-0

Tsai, K.-Y., Tsai, M.-H., Yeh, J.-W. (2013) Sluggish diffusion in Co-Cr-Fe-Mn-Ni high entropy alloys. *Acta Materialia, 61*, 4887-4897.

Tsai, M.-H. (2013). Physical Properties of High Entropy Alloys. *Entropy*, *15*(12), 5338–5345.

Tsai, M.-H., & Yeh, J.-W. (2014). High-Entropy Alloys: A Critical Review. *Materials Research Letters*, *2*(3), 107–123.

Usta, M., Ozbek, I., Ipek, M., Bindal, C., & Ucisik, A. H. (2005). The characterization of borided pure tungsten. *Surface and Coatings Technology*, *194*(2–3), 330–334.

Wang, C., Ji, W., & Fu, Z. (2014). Mechanical alloying and spark plasma sintering of CoCrFeNiMnAl high-entropy alloy. *Advanced Powder Technology*, *25*(4), 1334–1338.

Wang, C., Qin, M., Lei, T., He, Y., Kisslinger, K., Rupert, T. J., … Xin, H. L. (2021). Synergic grain boundary segregation and precipitation in W- and W-Mo-containing high-entropy borides. *Journal of the European Ceramic Society*, *41*(10), 5380–5387. doi:10.1016/j.jeurceramsoc.2021.04.004

Wang, R., Tang, Y., Li, S., Ai, Y., Li, Y., Xiao, B., … Bai, S. (2020). Effect of lattice distortion on the diffusion behavior of high-entropy alloys. *Journal of AlloysandCompounds*,*825*,154099. doi:10.1016/j.jallcom.2020.154099

Wang, Y.-P., Gan, G.-Y., Wang, W., Yang, Y., & Tang, B.-Y. (2018). Ab Initio Prediction of Mechanical and Electronic Properties of Ultrahigh Temperature High-Entropy Ceramics $(Hf_{0.2}Zr_{0.2}Ta_{0.2}M_{0.2}Ti_{0.2})B_2$ (M = Nb, Mo, Cr). *Physica Status Solidi (b)*, *255*(8), 1800011.

Wieczorek-Ciurowa, K., Oleszak, D., & Gamrat, K. (2007). Mechanosynthesis and process characterization of some nanostructured intermetallics–ceramics composites. *Journal of Alloys and Compounds*, *434–435*, 501–504.

Wieczorek-Ciurowa, K. (2013). Mechanochemical synthesis of metallic–ceramic composite powders. In *High-Energy Ball Milling* (pp. 193–223).

Xu, C., Bao, K., Ma, S., Ma, Y., Wei, S., Shao, Z., … Cui, T. (2017). A first-principles investigation of a new hard multi-layered MnB_2 structure. *RSC Advances*, *7*(17), 10559–10563. doi: 10.1039/C6RA27148K.

Xu, L., Li, S., Zhang, Y., & Zhai, Y. (2012). Synthesis, properties and applications of nanoscale nitrides, borides and carbides. *Nanoscale*, *4*(16), 4900.

Yamada, S., Hirao, K., Yamauchi, Y., & Kanzaki, S. (2003). Mechanical and electrical properties of B_4C–CrB_2 ceramics fabricated by liquid phase sintering. *Ceramics International*, *29*(3), 299–304.

Yamauchi, A., Yoshimi, K., Kurokawa, K., & Hanada, S. (2007). Synthesis of Mo–Si–B in situ composites by mechanical alloying. *Journal of Alloys and Compounds*, *434–435*, 420–423.

Yang, X., & Zhang, Y. (2012). Prediction of high-entropy stabilized solid-solution in multi-component alloys. *Materials Chemistry and Physics*, *132*(2–3), 233–238.

Yang, X., Zhang, Y., & Liaw, P. K. (2012). Microstructure and Compressive Properties of $NbTiVTaAl_x$ High Entropy Alloys. *Procedia Engineering*, *36*, 292–298.

Yang, Y.-C., Liu, C., Lin, C.-Y., & Xia, Z. (2020). Core effect of local atomic configuration and design principles in AlxCoCrFeNi high-entropy alloys. *Scripta Materialia*, *178*, 181–186.

Yang, Y., Bi, J., Sun, K., Qiao, L., Liu, Y., Li, Y., … Shang, M. (2022). Novel $(Hf_{0.2}Zr_{0.2}Ta_{0.2}V_{0.2}Nb_{0.2})B_2$ high entropy diborides with superb hardness sintered by SPS under a mild condition. *Ceramics International, 48*, 30859-30867, doi: 10.1021/acs.jpclett.1c00399.

Yao, T., Wang, Y., Li, H., Lian, J., Zhang, J., & Gou, H. (2012). A universal trend of structural, mechanical and electronic properties in transition metal (M=V, Nb, and Ta) borides: First-principle calculations. *Computational Materials Science*, *65*, 302–308.

Ye, B., Fan, C., Han, Y., Ma, M., & Chu, Y. (2020). Synthesis of high-entropy diboride nanopowders via molten salt-mediated magnesiothermic reduction. *Journal of the American Ceramic Society*, *103*(9), 4738–4741.

Ye, Y. F., Wang, Q., Lu, J., Liu, C. T., & Yang, Y. (2016). High-entropy alloy: Challenges and prospects. *Materials Today*, *19*(6), 349–362.

Yeh, J.-W., Chen, S.-K., Lin, S.-J., Gan, J.-Y., Chin, T.-S., Shun, T.-T., … Chang, S.-Y. (2004). Nanostructured High-Entropy Alloys with Multiple Principal Elements: Novel Alloy Design Concepts and Outcomes. *Advanced Engineering Materials*, *6*(5), 299–303. doi:10.1002/adem.200300567

Yeh, J.-W. (2013). Alloy Design Strategies and Future Trends in High-Entropy Alloys. *JOM*, *65*(12), 1759–1771.

Yin, L., Guo, Y., & Guo, X. (2022). Cocktail effect on RT5-type (R = rare earth, T = 3d transition metal) high entropy intermetallic compounds. *Journal of Magnetism and Magnetic Materials*, *563*, 169883.

Youssef, K. M., Zaddach, A. J., Niu, C., Irving, D. L., & Koch, C. C. (2015). A Novel Low-Density, High-Hardness, High-entropy Alloy with Close-packed Single-phase Nanocrystalline Structures. *Materials Research Letters*, *3*(2), 95–99.

Zapata-Solvas, E., Jayaseelan, D. D., Lin, H. T., Brown, P., & Lee, W. E. (2013). Mechanical properties of ZrB_2- and HfB_2-based ultra-high temperature ceramics fabricated by spark plasma sintering. *Journal of the European Ceramic Society, 33*(7), 1373-1386.

Zhang, C., Zhang, F., Chen, S., & Cao, W. (2012). Computational Thermodynamics Aided High-Entropy Alloy Design. *JOM*, *64*(7), 839–845.

Zhang, R.-Z., Gucci, F., Zhu, H., Chen, K., & Reece, M. J. (2018). Data-Driven Design of Ecofriendly Thermoelectric High-Entropy Sulfides. *Inorganic Chemistry*, *57*(20), 13027–13033.

Zhang, X., Li, W., Wan, S., Feng, J., Song, M., Liu, J., … Zhang, H. (2022). Pressure dependence of the electrical conductivities of high-entropy diborides. *Journal of the European Ceramic Society*, *42*(15), 6951–6957. doi:10.1016/j.jeurceramsoc.2022.08.007

Zhang, Y., Yang, X., & Liaw, P. K. (2012). Alloy Design and Properties Optimization of High-Entropy Alloys. *JOM*, *64*(7), 830–838.

Zhang, Y., Lu, Z. P., Ma, S. G., Liaw, P. K., Tang, Z., Cheng, Y. Q., & Gao, M. C. (2014a). Guidelines in predicting phase formation of high-entropy alloys. *MRS Communications*, *4*(2), 57–62.

Zhang, Y., Zuo, T. T., Tang, Z., Gao, M. C., Dahmen, K. A., Liaw, P. K., & Lu, Z. P. (2014b). Microstructures and properties of high-entropy alloys. *Progress in Materials Science*, *61*, 1–93.

Zhang, Y., Guo, W.-M., Jiang, Z.-B., Zhu, Q.-Q., Sun, S.-K., You, Y., P… Lin, H.-T. (2019a). Dense high-entropy boride ceramics with ultra-high hardness. *Scripta Materialia*, *164*, 135–139. doi:10.1016/j.scriptamat.2019.01.021

Zhang, Y., Jiang, Z.-B., Sun, S.-K., Guo, W.-M., Chen, Q.-S., Qiu, J.-X., … Lin, H.-T. (2019b). Microstructure and mechanical properties of high-entropy borides derived from boro/carbothermal reduction. *Journal of the European Ceramic Society*, *39*(13), 3920–3924. doi:10.1016/j.jeurceramsoc.2019.05.017

Zhang, Y., Sun, S.-K., Zhang, W., You, Y., Guo, W.-M., Chen, Z.-W., … Lin, H.-T. (2020). Improved densification and hardness of high-entropy diboride ceramics from fine powders synthesized via borothermal reduction process. *Ceramics International*, *46*(9), 14299–14303. doi:10.1016/j.ceramint.2020.02.214

Zhang, Y., Sun, S.-K., Guo, W.-M., Zhang, W., Xu, L., Yuan, J.-H., Guan, D.-K., … Lin, H.-T. (2021a). Fabrication of textured $(Hf_{0.2}Zr_{0.2}Ta_{0.2}Cr_{0.2}Ti_{0.2})B_2$ high-entropy ceramics. *Journal of the European Ceramic Society*, *41*(1), 1015–1019. doi:10.1016/j.jeurceramsoc.2020.08.071

Zhang, Y., Sun, S.-K., Guo, W.-M., Xu, L., Zhang, W., & Lin, H.-T. (2021b). Optimal preparation of high-entropy boride-silicon carbide ceramics. *Journal of Advanced Ceramics*, *10*(1), 173–180.

Zhang, Z., Zhu, S., Liu, Y., Liu, L., & Ma, Z. (2022). Phase structure, mechanical properties and thermal properties of high-entropy diboride $(Hf_{0.25}Zr_{0.25}Ta_{0.25}Sc_{0.25})B_2$. *Journal of the European Ceramic Society*, *42*(13), 5303–5313.

Zhou, Y., Xiang, H., Feng, Z., & Li, Z. (2015). General Trends in Electronic Structure, Stability, Chemical Bonding and Mechanical Properties of Ultrahigh Temperature Ceramics TMB_2 (TM = transition metal). *Journal of Materials Science & Technology*, *31*(3), 285–294.

Url-1<*http://www.jnm.co.jp/en/data/melting_point.html*>, date retrieved 16.10.2022.

Url-2<*http://www.jnm.co.jp/en/data/density.html*>, date retrieved 18.10.2022.

Url-3<*http://www.jnm.co.jp/en/data/microhardness.html*>,date retrieved 20.10.2022.

Url-4<*http://www.jnm.co.jp/en/data/thermal_conductivity.html*>, date retrieved 24.10.2022.

Url-5<*http://www.jnm.co.jp/en/data/electrical_conductivity.html*>, date retrieved 03.11.2022.

Url-6<*https://materialsproject.org/materials/mp-585?chemsys=Mn-B#properties*>, date retrieved 12.11.2022.

Url-7<*https://www.webofscience.com/wos/woscc/summary/274b8979-d2bf-44db-947f-d37a3b244004-64a0cf96/relevance/1*>, date retrieved 18.11.2022

APPENDICES

APPENDIX A: Approximate XRD peak positions of the as-blended powders.

APPENDIX A

Table A.1 : Approximate XRD peak positions of the as-blended powders.

Composition / 2θ (Degree)	HEB 2	HEB 3	HEB 4	HEB 5	HEB 6	HEB 7	HEB 8	HEB 9	HEB 10	HEB 11	HEB 12	HEB 13
MnB_2	34, 46	29, 34, 46	29, 34, 46	29, 34, 46, 61	29, 34, 46, 61	29, 34, 46	34,46,61,79	34,46,61,79	34,46,61,79	34,46,61,79	34,46,61,79	34,46,61,79
MnB	40, 44, 46, 62, 81	37, 40, 44, 46, 81	37, 44	40, 81	40, 44, 81	40, 44, 81	40,44,62,81	40,44,62,81	44,62,81	44,62,81	44,62,81	44,62,81
Mn_2B	44	34, 79	78	44, 56	34, 44, 73	34	34,79	34,79	79	79	79	79
Mn_3B_4	42, 51, 62, 73, 81	46, 51, 61, 73, 81	42, 46, 51, 61, 73, 81	42, 46, 51, 62, 73, 81	37, 46, 61, 62, 73	37, 46, 61, 62, 73, 81	30,42,46,61, 62,74,81	30,42,46,61, 62,74,81	30,42,46, 51,61,62,74, 81	13,42,46,61,62,74, 81	13,30,42,46, 51,61,62,74, 81	13,30,42,46, 51,61,62,74, 81
CrB	-	34, 46, 74, 78, 81	-	31, 44, 46, 81	31, 44, 46	34, 45, 46, 74, 78, 81	30,44,49,72, 74,78,83	44,72,74,78, 83	34,36,73	34,36,73	34,36,73	34,36,73
CrB_2	-	29, 34, 46, 62, 70	-	29, 34, 46, 62, 80	29, 34, 46, 60, 62, 70, 71, 80	29, 34, 46, 60, 62, 71, 80	29,34,46,62	29,34,46,62	29,34,46,62, 71	29,34,46,62, 71	29,34,46,62, 71	29,34,46,62, 71
Cr_2B	-	30, 44, 74, 78, 83	-	30, 83	45, 75, 79, 83	30, 44, 46	30,44	44	44,49,55,75, 78,82	44,49,55,75, 78,82	44,49,55,75, 78,82	44,49,55,75, 78,82
Cr_3B_4	-	30, 41, 46, 51, 73, 81	-	30, 46, 58, 61, 62, 73, 81	36, 45, 46, 58, 61, 62, 81	30, 36, 41, 45, 46, 51, 58, 61, 62, 73, 74, 81	30,36,41,46, 58,73,81	30,36,41,46, 58,73,81	42,46,58, 59,61,73,82	13,42,46,58, 59,61,73,82	13,42,46,58, 59,61,73,82	13,42,46,58, 59,61,73,82
MoB	-	-	-	-	-	-	32,42,52	-	32,42,52	32,42,52	-	32,42,52
MoB_2	-	-	-	-	-	-	25,34,35,40, 46,49,52,61, 68,72,84	-	25,34,35,40, 46,49,52,61, 68,72	25,34,35,40, 46,49,52,61, 68,72	-	25,34,35, 46,49,52,61, 68,72,84

Table A.1 (continued) : Approximate XRD peak positions of the as-blended powders.

Composition / 2θ (Degree)	HEB 2	HEB 3	HEB 4	HEB 5	HEB 6	HEB 7	HEB 8	HEB 9	HEB 10	HEB 11	HEB 12	HEB 13
MoB_4	-	-	-	-	-	-	28,61,69	-	28,61,69	28,61,69	-	28,61,69
Mo_2B	-	-	-	-	-	-	40,72	-	31,40,72	31,40,72	-	31,40,72
Mo_2B_5	-	-	-	-	-	-	25,34,35,40, 46,49,52,61, 68,72,84	-	25,34,35,40, 46,49,52,61, 68,72	25,34,35,40, 46,49,52,61, 68,72	-	25,34,35, 46,49,52,61, 68,72,84
W_2B	-	-	-	-	-	-	-	22,32,37,40, 44,46,50,51, 66,70,71,72, 84	22,32,37,40, 44,46,50,51, 66,70,71,72	-	22,32,37,40, 44,46,50,51, 66,70,71,72, 84	22,32,37,40, 44,46,50,51, 66,70,71,72, 84
WB	-	-	-	-	-	-	-	32,42,52	32,42,52	-	32,42,52	32,42,52
W_2B_5	-	-	-	-	-	-	-	25,34,35,68	25,34,35,68	-	25,34,35,68	25,34,35,68

CURRICULUM VITAE

Name Surname : İlayda SÜZER

EDUCATION :

- **B.Sc.** : 2019, Istanbul Technical University, Faculty of Chemical and Metallurgical, Metallurgical and Materials Engineering

PROFESSIONAL EXPERIENCE AND REWARDS:

- October 2020 - Ongoing, Research Assistant, Istanbul Technical University, Chemical and Metallurgical Engineering Faculty, Department of Metallurgical and Materials Engineering.

PUBLICATIONS, PRESENTATIONS AND PATENTS ON THE THESIS:

- **Süzer İ.,** Aysel E., Mertdinç S., Gökçe H., Öveçoğlu M.L., Ağaoğulları D. 2021: Molibden Borür Tozlarının Sentezi ve Karakterizasyonu. 25. Ulusal Elektron Mikroskopi Kongresi, September 22-24, 2021 İzmir, Turkey.
- **Süzer İ.,** Aysel E., Akbari A., Mertdinç S., Öveçoğlu M.L., Ağaoğulları D. 2021: Synthesis and Characterization of Zirconium Diboride (ZrB_2) Nanoparticles. International Advanced Technologies Symposium, October 27-28 2021 Elazığ, Turkey.
- **Süzer İ.,** Aysel E., Akbari A., Mertdinç S., Öveçoğlu M.L., Ağaoğulları D. 2021: Mechanochemical Synthesis and Characterization of Hafnıum Diboride (HfB_2) Powders. International Conference on Engineering, Natural and Applied Science, November 24-26 2021, Osmaniye, Turkey.
- Aysel E., **Süzer İ.,** Ateş S., Akbari A., Mertdinç S., Öveçoğlu M.L., Ağaoğulları D. 2021: Synthesis and Characterization of Chromium Diboride (CrB_2) Nanoparticles. International Conference on Material Science and Technology in Cappadocia, November 26-28 2021, Nevşehir, Turkey.
- Akbari A., **Süzer İ.,** Aysel E., Mertdinç S., Öveçoğlu M.L., Ağaoğulları D. 2021: Mechanochemical Synthesis and Characterization of Mn-B Phases. International Conference on Advances in Engineering, Architecture, Science and Technology, December 15-17 2021, Erzurum, Turkey.

- **Süzer İ.,** Aysel E., Akbari A., Mertdinç S., Öveçoğlu M.L., Ağaoğulları D. 2021: Mechanochemical Synthesis and Characterization Investigations of W borides from WO_3, B_2O_3 and Mg by High-Energy Ball Milling. 3rd International Eurasian Conference on Science, Engineering and Technology, December 15-17 2021, Ankara, Turkey.
- **Süzer İ.,** Akbari A., Aysel E., Mertdinç S., Öveçoğlu M.L., Ağaoğulları D. 2021: Tantal Borür Tozlarının Ta_2O_5-B_2O_3-Mg Sisteminde Mekanokimyasal Sentezleme Yoluyla Sentezlenmesi. IV. Ulusal Mühendislikte Bilimsel ve Mesleki Çalışmalar Kongresi, December 23-26 2021, Turkey.
- Akbari A., **Süzer İ.,** Gürcan Bayrak K., Mertdinç S., Ayas E., Öveçoğlu M.L., Ağaoğulları D. 2022: Synthesis and Characterization of $(HfTiZrMnTa)B_2$ Ceramics. International Graduate Research Symposium, June 01-03 2022, İstanbul, Turkey.
- **Süzer İ.,** Akbari A., Mertdinç-Ülküseven S., Ateş S., Gürcan Bayrak K., Arık M.N., Ayas E., Öveçoğlu M.L., Ağaoğulları D. 2022: Production and Characterization of High Entropy Metal Borides Prepared using Different Sintering Methods. BORON22 International Boron Symposium, October 05-07 2022, İstanbul, Turkey.

OTHER PUBLICATIONS, PRESENTATIONS AND PATENTS:

- **Süzer İ.,** Mertdinç S., Aysel E., Akbari A., Gürcan Bayrak K., Ayas E., Öveçoğlu M.L., Ağaoğulları D. 2022: Production and Characterization of High Entropy $(HfTiZrMoTa)B_2$ Ceramics. International Engineering Research Symposium, March 04-06 2022, Düzce, Turkey.
- Mertdinç S., **Süzer İ.,** Aysel E., Akbari A., Gürcan Bayrak K., Ayas E., Öveçoğlu M.L., Ağaoğulları D. 2022: Synthesis of High Entropy $(HfTiZrMnCr)B_2$ Ceramics by Different Sintering Techniques. 4th International Engineering Research Symposium, March 04-06 2022, Düzce, Turkey.
- **Süzer İ.,** Mertdinç S., Aysel E., Akbari A., Gürcan Bayrak K., Ayas E., Öveçoğlu M.L., Ağaoğulları D. 2022: Powder Metallurgical Production and Characterization of $(HfTiZrWCr)B_2$ Ceramics. International Aegean Scientific Research Symposium, March 12-13 2022, Turkey.
- **Süzer İ.,** Tekinşen A.S., Özçakıcı Y.E., Ülküseven-Mertdinç S., Gürcan Bayrak K., Ayas E., Öveçoğlu M.L., Ağaoğulları D. 2022: Synthesis and Characterization of Al-x$(Hf_{0.2}Ti_{0.2}Zr_{0.2}V_{0.2}Nb_{0.2})B_2$ (x = 1, 2, 5, 10, 15 wt. %) Composites, Twentieth Young Researchers Conference, November 30-December 02 2022, Belgrade, Serbia.
- Mertdinç-Ülküseven S., Kavak S., Tekoğlu E., **Süzer İ.,** Öveçoğlu M.L., Ağaoğulları D. 2022: Optimization Studies on Powder Preparation of SiC nanowire and SiC/ZrB_2 particulate reinforced In718 powders for additive manufacturing, Twentieth Young Researchers Conference, November 30-December 02 2022, Belgrade, Serbia.